Trapping biomolecular ions
in superfluid helium droplets

Am Fritz-Haber-Institut
der Max-Planck-Gesellschaft
entstandene und

im Fachbereich Physik
der Freien Universität Berlin
eingereichte Dissertation von

Frauke Bierau

November 15, 2011

Eidesstattliche Erklärung
gemäß §7, Ziffer (4) der Promotionsordnung vom 05.02.2010 des Fachbereichs Physik an der Freien Universität Berlin.

Die Dissertation habe ich selbständig angefertigt.
Alle Hilfsmittel und Hilfen habe ich angegeben,
insbesondere habe ich die wörtlich oder dem Sinne nach
anderen Veröffentlichungen
entnommenen Stellen kenntlich gemacht.

Die Dissertation habe ich bisher weder in der gegenwärtigen
noch in einer anderen Fassung weder dem Fachbereich Physik
der Freien Universität Berlin noch einer anderen Fakultät
oder Universität vorgelegt.

Berlin, den 20.08.2011,

_____

(Frauke Bierau)

Zusammenfassung

Die Heliumtröpfchen–Methode als eine Form der Tieftemperatur–Matrixisolationstechnik ist eine wichtige und etablierte Technik der Molekül–Spektroskopie. Eingebettet in einem suprafluiden Heliumtröpfchen werden Teilchen sehr schnell intern und translatorisch auf dessen Gleichgewichtstemperatur von etwa 0.37 K abgekühlt. Dank dieser tiefen Tempe–raturen ist es möglich, selbst von großen molekularen Systemen wie C_{60} detailreiche Spektren mit hoher spektraler Auflösung und nur minimalen Störungen durch die He–liummatrix zu erhalten, welche lediglich schwach mit anderen Teilchen wechselwirkt und obendrein über einen großen spektralen Bereich optisch transparent ist. Damit ist die He–liumtröpfchen–Technik potentiell ein vielversprechendes Instrument zur Erforschung auch großer biologisch relevanter Moleküle und kann dazu beitragen, detaillierte Informationen über intrinsische Eigenschaften von zum Beispiel Proteinen oder Peptiden zu erhalten.

Das Experiment, welches im Rahmen dieser Doktorarbeit aufgebaut wurde, bietet mit Hilfe der Heliumtröpfchen–Isolationstechnik in Kombination mit diversen experi–mentellen Methoden einen neuartigen Ansatz zur Erforschung großer Biomoleküle unter wohldefinierten Bedingungen. Als Ionenquelle dient eine Elektrospray–Ionisationsquelle, mit der es möglich ist, auch große biomolekulare Komplexe auf schonende Art unter Er–haltung ihrer Struktur in die Gasphase zu bringen. Mit einem Quadrupol–Filter kann ein bestimmter Ladungszustand des Moleküls selektiert und anschließend in einer linearen Hexapol–Ionenfalle gespeichert werden.

Über die "Pickup–Technik" werden gespeicherte Ionen infolge total inelastischer mecha–nischer Kollisionen in die Tröpfchen eingebracht. So wurde das Experiment konzeptionell nach dem Vorbild von Pickup–Experimenten neutraler Teilchen gestaltet, bei denen die zu untersuchenden gasförmigen Atome oder Moleküle aus einer Kollisionszelle von hindurch–fliegenden Heliumtröpfchen aufgesammelt werden. Das experimentelle Grundgerüst kann recht flexibel mit weiteren experimentellen Techniken kombiniert werden, entweder um die zu untersuchenden Moleküle vor dem Pickup gründlicher selektieren zu können und somit die Tröpfchen mit Teilchen in einem wohldefinierten Zustand dotieren zu können oder um die dotierten Tröpfchen zu charakterisieren, zum Beispiel über Laser–Spektroskopie.

Im Falle elektrisch geladener Teilchen ist die Kollisionszelle eine Ionenfalle, in der die Ionen bei niedrigen Fallenpotentialen gespeichert werden. Für den Ionen–Pickup wird explizit die hohe kinetische Energie eines schweren Heliumtröpfchens genutzt, die ein dotiertes und so elektrisch geladenes Tröpfchen nur einen geringen Einfluss des Fallenpotentials spüren lässt, und es somit ermöglicht, dass vormals gefangene Ionen im Inneren der He–liumtröpfchen aus der Falle transportiert werden. Die Pickup–Technik kann für viele unterschiedliche Arten von Dotanden–Spezies genutzt werden, was die Heliumtröpfchen–Technik für zahlreiche neue interessante Systeme zugänglich macht.

Es ist gezeigt worden, dass große massenselektierte Ionen, bestehend aus über 1000

Atomen, effizient in Heliumtröpfchen eingelagert werden können. Die Intensitäten ionen–dotierter Heliumtröpfchen sind verhältnismäßig hoch und somit ausreichend für spektroskopische Untersuchungen der geladenen Tröpfchen, zum Beispiel mit Hilfe von infrarot (IR) Multiphoton–Absorptionstechniken (IR–MPD). Die erreichbaren Intensitäten ionen–dotierter Heliumtröpfchen hängen in erster Linien von der Teilchendichte in der Falle ab, von dem Fluss der Heliumtröpfchen durch die Falle sowie dem Kollisions–Wirkungsquerschnitt von Tröpfchen und Ionen. Bei hohen Ionendichten in der Falle und großen Wirkungsquerschnitten ist ein Pickup mehrerer Ionen pro Tröpfchen beobachtet worden, zum Beispiel hat es sich gezeigt, dass etwa 100 Phe^+–Ionen gleichzeitig in einem Tröpfchen der Größe von $\approx 3 \cdot 10^{11}$ Helium–Atomen eingebettet sein können.

Heliumtröpfchen werden in einer gepulsten isentropen Überschall–Düsenexpansion generiert. Im Rahmen dieser Doktorarbeit wurden zwei verschiedene Heliumtröpfchen–Quellen charakterisiert. Beide bestehen in ihrem Kern aus einem gepulsten Magnetventil (die erste aus einem *Parker* General valve der Serie 99, die zweite aus einem Even-Lavie–Tieftemperatur–Ventil), sie unterscheiden sich allerdings in Aufbau und Funktionsweise, in den Operationsparametern (t_{pulse}, f, U_{valve}) sowie in den Bereichen der anwendbaren Quellenparameter (P_0, T_0) zur Tröpfchenerzeugung. Auch unterscheiden sich die jeweiligen Skimmer in Öffnungsdurchmesser, Länge und Düsenabstand. Die mittleren Größen und vorliegenden Größenverteilungen der in der jeweiligen Gasexpansion generierten Tröpfchen wurden für beide Quellen mit Hilfe elektrischer Felder in senkrechter oder paralleler Richtung zum Tröpfchenstrahl bestimmt. Die Tröpfchen, die von der *Parker*–Quelle erzeugt werden, stellen sich mit mittleren Größen von über $3 \cdot 10^{11}$ Helium–Atomen als sehr groß heraus, wohingegen die von der Even-Lavie–Quelle produzierten Tröpfchen bis zu sechs Größenordnungen kleiner sind. Bei beiden Quellen liegen die erzeugten Tröpfchen in Lognormal–Größenverteilungen vor. Ferner wurden für beide Quellen die longitudinalen Tröpfchenstrahlgeschwindigkeiten und die Abhängigkeiten dieser von den Expansionsparametern untersucht, die sich als jeweils sehr unterschiedlich herausstellten. Diese Unterschiede sowohl in den Tröpfchengrößen als auch –geschwindigkeiten lassen sich vermutlich auf unterschiedliche Prozesse zurückführen, die in der Düsenstrahlexpansion zur Tröpfchenbildung führen.

Summary

Helium droplet spectroscopy is a well-established and important technique for achieving fundamental insight into the properties of embedded dopant molecules. Superfluid He droplets provide a gentle, weakly interacting, and cryogenic environment for the investigated molecules which are cooled internally and translationally to the droplet (equilibrium) temperature of ≈ 0.37 K. Measured spectra often reveal a high resolution that is comparable to the resolution observed in spectra of isolated molecules in the gas phase, even for larger species like C_{60} molecules. Therefore, it is promising to use this technique in the investigation of large biomolecules, i.e. to enable the acquisition of detailed information on the intrinsic properties of proteins and peptides.

Furthermore, obtained spectra contain information on the interaction between the dopant and the droplet and in this way, elementary properties of the He droplets themselves can be studied. This is interesting in terms of looking at, for example, superfluidity on a microscopic scale.

The experiment presented in this thesis is a new approach to investigate large biomolecules under well-defined conditions and at temperatures in the sub-Kelvin regime. The He droplet isolation technique is combined with established gas-phase techniques such as electrospray ionization and quadrupole mass filtering and provides for the possibility of studying mass–to–charge selected cold biomolecular ions in He droplets. The experiment can quite flexibly be combined with various experimental techniques and also be enhanced by additional methods to allow for more precise selection of the investigated ion species which are trapped. Ions can be incorporated in the He droplets *via* pickup, which is conceptually similar to pickup experiments performed on neutral species. Here, gas-phase ions are produced by elecrospray ionization. They are mass–to–charge selected and accumulated in a linear ion trap where they are stored by a trapping potential of a few electronvolts. Traversing He droplets can pick up the ions, remove them from the trap due to the high kinetic energy of the massive He droplets and thereby, make them accessible for further investigation by the experimental technique of choice. Having mass–to–charge or even conformation selected gas-phase ions stored in an ion trap provides the great advantage of a "clean" doping of the droplets with well-defined species. This doping technique yields higher intensities of ion-doped droplets than alternative experimental approaches for doping He droplets with large biomolecules. It has the further advantage of being applicable to a large variety of molecular species which can be incorporated in superfluid He droplets *via* pickup, such as cluster ions. Thus, the ion-pickup opens the helium droplet isolation technique to a wide range of new, interesting species.

Two pulsed He droplet sources have been characterized. Both have a solenoid valve as a main component which are different in design and operated at different parameters (t_{pulse}, f, U_{valve}) as well as at different ranges of applicable expansion parameters (P_0, T_0). The first source contains a *Parker* General valve series 99 with a 0.7 mm diameter opening in a homebuilt faceplate. It is typically operated at a 5 Hz repetition rate f with electric pulse lengths t_{pulse} of about 250 μs and an applied voltage of $U_{valve} = 240$ V. The installed skimmer is 2.5 cm long and has a 2 mm opening diameter. The other source is equipped with a cryogenic Even-Lavie valve. It has a smaller opening diameter of ≈ 100 μm, and the emitted gas pulses are much shorter, on the order of the electric pulse lengths $t_{pulse} \approx 20$ μs. Therefore, the gas flow is much reduced compared to the General valve which allows for operation of the Even-Lavie valve at a higher repetition

rate of typically 50 Hz maintaining a sufficiently low background pressure in the source chamber. The skimmer is 5 cm long and has a large opening of 4 mm.

Droplets are usually produced at $P_0 = 30$ bar for T_0 ranging from 5 K to 10 K with the *Parker* General valve and at $P_0 = 65$ bar for $T_0 = 6$–20 K with the Even-Lavie valve. The droplet sizes and size distributions in a pulse emitted from the respective source have been determined by applying parallel and vertical electrostatic acceleration fields to the charged cluster beams. For both sources, the size distribution can be described by lognormal distributions, but the mean values of the determined sizes can vary over about 6 orders of magnitude. When the droplets are doped with a large protein ion in different charge states ($CytC^{+Z}$), the mean sizes of droplets produced by the *Parker* General valve are $N_{He} \approx 3 \cdot 10^{11}$ He atoms whereas for droplets produced by the Even-Lavie valve $N_{He} \approx 1 \cdot 10^6$ He atoms. This large size difference is attributed to different processes of droplet formation in the nozzle beam expansions from the two sources.

The longitudinal beam velocities v_x have been determined and the dependence of the beam velocities on the expansion parameters (P_0, T_0, D) studied. Large differences in velocity are measured between the two valves under the same applied source temperature and pressure. For example at $T_0 = 10$ K and $P_0 = 30$ bar, a beam velocity of $v_x \approx 265$ ms^{-1} is observed for the *Parker* General valve and of $v_x \approx 360$ ms^{-1} for the Even-Lavie valve. This is also indicative of different processes leading to cluster formation in the expansion. These processes cannot be explained by the ideal gas model of isentropic beam expansions.

It is shown that mass–to–charge selected ions with masses of more than 12000 amu can be efficiently picked up from an ion trap by traversing He droplets. Even the pickup of multiple ions by single He droplets of sufficiently large sizes is likely to happen, provided there is a sufficiently high particle density in the ion trap, for example when the space charge limit is reached. For singly protonated amino acids (Phe^+) it is observed that approximately 100 ions can be embedded in a single droplet composed of 10^{12} He atoms. The achieved signal intensities of ion–doped droplets are high with peak currents of up to ≈ 20 pA that have been measured with a calibrated amplifier implying about 10^4 ion–doped He droplets per pulse. These intensities allow spectroscopic measurements on the embedded cold proteins or peptides, for example by UV-Vis spectroscopy or using infrared multi-photon dissociation techniques (IR-MPD). Laser spectroscopy of molecules in the ground state is most promising for structural investigations and for shedding light on intrinsic properties of proteins or peptides.

Contents

List of symbols

a : radius of embedded particle
A : area
Ang : angiotensin
A_S : surface area of a droplet
b : impact parameter
C : coefficient of discharge
C_{disp} : coefficient of the *London* dispersion interaction
C_n : nozzle conductance
c_p : specific heat capacity at constant pressure
CytC : cytochrome c
d : skimmer diameter
D : nozzle orifice diameter in unit μm
d_s : thickness of surface region of a cluster
d_y : distance between metal plates in deflection experiment
D_c : duty cycle
Δt : interruption time between the beginning of two successive pulses
Δv_x : longitudinal velocity distribution
E : total energy
E_b : binding energy
E_{rot} : roton energy
ESI : Electrospray Ionization
f : repetition rate
F : number of degrees of freedom
F_t : area of openings in trap endcaps and trap lenses
γ : surface tension
g : gravitational constant
G_{max} : mass flow rate
Gram^{+2}_{syn} : synthetic doubly protonated decapeptide
H : enthalpy
He : helium
$I(L)$: intensity of doped droplets after passage through the ion trap
I_0 : intensity of droplets emitted per pulse from the nozzle, $[I_0]$=droplets$\cdot$sr^{-1}s^{-1}
I_{tot} : total droplet intensity
J : rotational quantum number
k_B : Boltzmann constant
κ : ratio of specific heats $\frac{c_p}{c_v}$
λ point : $\approx$ 2.17 K

L : length of the ion trap

L_J : angular momentum

LDM : Liquid Drop Model

m_d : droplet mass

$m_{He} = 4$ amu : atomic mass of ^{4}He

n : particle density in units of particles per cm^3

N_f : final cluster size after evaporative cooling

n_{He} : number of atomic He solvation shell in droplet around dopant particle

N_{He} : number of constituent He atoms in a He droplet

N_0 : initial cluster size

$\bar{N}_q$: mean number of ions picked up by a single He droplet

N_r : number of rods in RF multipole device

$\omega(E)$: density of states

Phe$^+$: PheH$^+$: singly protonated phenylalanine ions

P_0 : applied (helium) gas pressure in expansion

q : elementary charge

Q : internal energy

Q_S : surface charge

Q_t : gas throughput

R_d: droplet radius, determined from *liquid drop model*

RF : radiofrequency

$R_{He} =$ radius He atom

R_{ion}: protein radius

ρ : particle density of liquid helium

ρ_M : mass density

S : speed ratio

S : entropy

t_{acc} : accumulation time of ions in the ion trap

t_{exp} : duration of the second part of the experimental sequence

T_∞ : terminal temperature reached in an isentropic nozzle beam expansion

t_{trap} : storage time of ions in the trap

T_i : initial cluster temperature in evaporative cooling process

T_0 : applied source expansion temperature

t_{pulse} : electric pulse length of pulsed nozzle source

t_{trap} : storage time of ions in the trap

Trp : tryptophan

U_{bias} : hexapole bias voltage

U_{cone} : voltage applied to skimmer in *ESI* process

U_{valve} : voltage applied to pulsed valve

V : volume

V_{p-p} : peak–to–peak voltage

v_x : longitudinal cluster beam velocity

v_∞ : terminal speed of a volume element in an isentropic nozzle beam expansion

x : travel direction of He droplet beam/experimental main axis

y : fractional radius of an ion in a He cluster

Z : number of elementary charges q carried by an ion

Z_p : pumping speed

x

Chapter 1

Introduction

1.1 Motivation

Achieving new insight into structural properties of biomolecules is an important task concerning their biophysical, chemical, as well as medical aspects because the global three-dimensional structure of biological molecules (for example peptides and proteins) is the key to their physiological function in a biological system.

In some cases, the folding process does not work properly and the molecule adopts a three-dimensional structure different from its native structure. The formation of misfolded proteins or peptides can lead to a malfunction of the whole biomolecular machinery and can have fatal consequences. For example, the occurrence of neurodegenerative diseases like Alzheimer's disease or Parkinson's disease is linked to the formation of proteins or peptides in misfolded structures (for example in the form of insoluble fibrils). Especially, toxic intermediate states that the molecule is adopting during the misfolding process seem to have an important impact. These processes are possibly triggered by external conditions, for example a change of the ambient temperature, pH value, or the presence of metal ions which can affect the intramolecular energetics. Understanding the structure and folding dynamics of peptides, proteins and protein complexes at a fundamental level can elucidate the environmental conditions under which these structural changes might be activated.

Studying large complex molecules like proteins or peptides is difficult since their properties are determined by a balance of many intramolecular interactions as well as intermolecular interactions with solvent molecules or other species present in their natural environment, which is mostly aqueous solution. Taking them out of solution *via* isolation in the gas phase and thereby eliminating the intermolecular interactions, is advantageous in terms of providing the possibility to probe only the intrinsic properties of the molecules of interest under well-defined conditions.

Experimental access to molecular properties is provided by various spectroscopic techniques, whereby for structural investigations vibrational spectroscopy in the infrared region is very useful. When experiments are performed at room temperature, the obtained spectra of large species are often difficult to interpret due to the high number of internally excited states and large number of populated levels. A large improvement on experimental results from spectroscopic measurements and thus, for understanding complex structures of atoms or molecules, can be achieved by performing experiments at

low temperatures. At low temperatures in the sub-kelvin range, the number of populated internal states is much reduced and molecular samples are present in well-defined structures and internal state distributions.

An important technique yielding temperatures in the low-Kelvin range is cooling the species of interest in seeded molecular beam expansions [1–4]. Spectra thus obtained from cold gas-phase molecules exhibit less congestion and provide detailed information about molecular properties. However, vibrational degrees of freedom are less efficiently cooled than rotations due to the much smaller cross section for collision–induced vibrational relaxation. This can lead to the appearance of "hot" bands in the spectrum from internally incompletely relaxed molecules which can complicate the interpretation of the spectra. A further limitation lies in the applicability of the seeded beam technique for investigating large molecular species, since it works best for smaller species such as amino acids [4–6] although large species like C_{60} molecules or peptides containing 10 amino acids have also been expanded and cooled in seeded beams [7, 8].

Molecules can also be cooled by storing them in cryogenic traps where they are internally and translationally cooled by collisions with thermalized buffer gas atoms down to ≈ 10 K [9–11]. Translationally, the trapped particles can further be cooled down to the sub-kelvin range *via* sympathetic cooling using laser–cooled atomic ions in the trap [12]. This has successfully been done for large proteins containing more than 1000 atoms which were cooled to ≈ 75 mK [13]. For spectroscopy, however, translational cooling only reduces Doppler broadening and cooling of the internal degrees of freedom is much more important.

Another very interesting and effective alternative method which provides a cryogenic ambient temperature and is applicable to a wide range of molecular species is the isolation of the species of interest in superfluid helium clusters (commonly called He droplets due to their liquid nature). This technique is of fundamental interest. It has been pioneered by Scoles and coworkers [14] as well as in the group of Toennies and has found important applications in molecular spectroscopy to date [15–19]. He clusters have an internal equilibrium temperature of ≈ 0.37 K, which is maintained *via* evaporative cooling, and embedded foreign particles become thermalized to the cluster temperature. Thereby, they cool down to their ground state. Due to the weak interactions of liquid helium, immersed dopant species can rotate freely giving in some cases rotationally resolved spectra with narrow linewidths [20, 21]. Furthermore, liquid helium itself is optically transparent from the deep UV to the far IR. All together, the unique properties and weak interactions in a superfluid make He droplets the "ultimate spectroscopic matrix" [22], offering both a high resolution comparable to gas-phase spectra and a stabilization of the investigated species in a gentle cryogenic and isothermal environment which causes few matrix perturbances and the observed broadening of spectral lines is considerably smaller than in solid rare gas matrices [23]. The remaining homogeneous broadening of rovibrational lines is attributed to relaxation processes that additionally occur when the investigated molecule is embedded in a He cluster [18]. Inhomogeneous broadening of rotational lines is attributed to a broad size distribution of He clusters as emitted from a nozzle source [24]. Rotational lines have a Lorentzian shape but the line width as well as the peak position appears to depend on the cluster size. Rovibrational excitations of a particle immersed in liquid helium are relaxed *via* coupling to the elementary excitations of the helium bath which in a finite size cluster are discrete. Thus, a rotational excitation of a dopant molecule in a He droplet can only couple to a cluster phonon when the cluster size allows for matching

of the energies of molecule and cluster [24]. For larger clusters composed of $N_{He} \approx 10^4$ He atoms, however, the rotational spectral lines of embedded molecules become independent from the cluster size and are more similar to spectral lines observed in bulk liquid helium where a continuum of phonon excitations exists [24].

Atoms or molecules can be incorporated into the droplets by pickup from a gas cell. By using this technique, small molecules [25] and biomolecules [26, 27] as well as large species such as C_{60} [28] have successfully been embedded in helium droplets. Using laser vaporization, less volatile materials such as refractory metal atoms can be evaporated and clusters can grow inside helium droplets [29, 30]. Those clusters, however, will occur in a distribution of sizes governed by Poisson statistics.

For studying molecules in He droplets a prerequisite is the ability to first bring the intact molecule into the gas phase. However, many interesting species including most larger biomolecules, can not simply be evaporated since heating usually leads to a decomposition of a protein or peptide. Employing other techniques such as laser desorption yields only low concentrations in the gas phase and furthermore gives a mixture of species such as decomposition products or molecules desorbed from the matrix which requires performing mass selection in order to exclude all unwanted species. Studying charged species in liquid He droplets is usually realized by ionization of the neutral species inside the He droplet after being picked up from a scattering cell. When particles are ionized using common experimental techniques such as electron impact or optical ionization, they are often left in an ensemble of unknown charge or quantum states and fragment species. Further interrogation of gas-phase ions requires the employment of state selective experimental techniques, for example mass filters.

In the framework of this thesis, an experiment has been set up that allows for the incorporation of large (bio)molecular ions in superfluid He droplets. Gas-phase ions are generated by electrospray ionization, are mass–to–charge selected by a quadrupole mass filter and accumulated in a hexapole linear ion trap. While the ions are being stored in the trap they can be picked up by traversing He droplets that are produced in a pulsed nozzle cluster beam expansion.

Having mass–to–charge and potentially also conformation selected gas-phase ions stored in an ion trap allows for pickup experiments with well-defined species. Doped droplets can then be further studied by the experimental technique of choice. The technique is also promising for yielding higher intensities of ion–doped droplets than alternative experimental approaches for doping He droplets, for example by crossing the He cluster beam with a seeded molecular beam. The achievable ion signal intensity depends on the beam intensity of the He droplet source, the particle density in the trap, and the detection sensitivity. The experimental setup can easily be combined with many different experimental techniques. These range from the choice of ion source (for example an electrospray ionization or laser ablation cluster source) over the applied state selective methods (for example quadrupole mass filters or ion mobility spectrometers) to the technique for further investigation of the cold ions in He droplets (for example linear absorption (*action*) spectroscopy or pump–probe dynamical spectroscopy).

In the future, the possibility of cooling large biomolecules in superfluid He droplets will allow many new and interesting experiments, such as spectroscopic investigations and possibly in the future single molecule diffraction experiments using X-ray free electron lasers [31–33] or electron diffraction experiments on aligned biomolecules [34].

In the following Chapter, an introduction to biomolecular structures and composition is given and experimental methods are presented which are often employed for structural studies of gas-phase ions. Then, in Ch. 1.3, the properties and use of liquid He droplets as cryogenic spectroscopic matrices are presented. Finally, in Ch. 1.3.2, the formation process of liquid He clusters in isentropic free-jet expansions is presented. Also, an introduction to pulsed nozzle sources is given.

1.2 Structures of biomolecules

The structure of molecules is most decisive for their chemical and physical properties. In the case of biomolecules, not only the chemical composition and the sequence of amino acids but in particular the three-dimensional shape determines the physiological function of a peptide or protein. The backbone of a protein or peptide is built by a linear sequence of amino acids which is called the *primary structure*. Folding processes into the three-dimensional geometry (the local *secondary structure* and the overall *tertiary structure*) are driven by mostly intramolecular interactions between certain atoms or functional groups as well as intermolecular interactions with the surroundings of the molecule, for example with solvent molecules. There are 20 naturally occurring amino acids that differ only
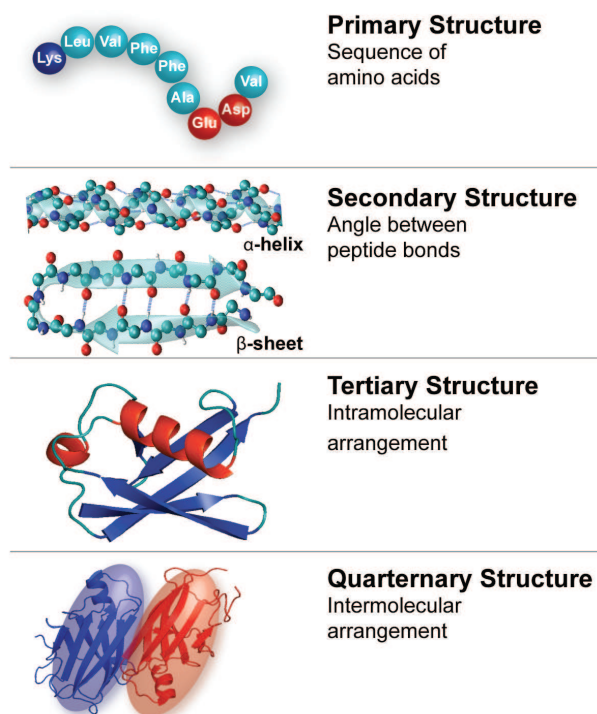
Figure 1.1: Structural elements in proteins and peptides and biomolecular complexes.

in the chemical compositions of characteristic side chains. An amino acid is basically composed of the central so-called C_α carbon atom connected to an amino group (NH_2), a carboxyl group (COOH), and a side chain which determines the chemical and structural property of the respective amino acid, and consequently, of a biomolecule as well. Amino acids bind together by peptide bonds forming the backbone chain. The backbone is commonly defined from the residue with a free amino group called N–terminus to the

final residue having a free carboxyl group which is called C–terminus. Molecules consisting of less than ≈ 50 amino acid building blocks are called peptides, longer chains are called proteins. A balance between hydrogen bonding interactions (mainly between N–H and C=O groups of the molecular backbone), steric repulsion, and electrostatic as well as dispersive interactions gives rise to the *secondary structure* of the protein which describes the three-dimensional form of local segments in the biopolymer. Local structural elements can be described by angles between peptide bonds and bond lengths. The most important examples for secondary structural elements are α–helices and β–sheets (see fig. 1.1). The adapted conformation of a protein or protein complex, and hence its physiological function, is determined by electrostatic and dispersion interactions as well as the hydrogen bonding network and the so-called hydrophobic effect. The latter is one of the most important driving forces for the folding of a protein. It refers to the burial of hydrophobic side chains in the interior of the molecule in order to minimize the number of surrounding water molecules [35, 36].

In nature, biomolecules often occur in protonated or deprotonated form in aqueous solutions. Introducing a charge in a biomolecule can cause a structural rearrangement and hence, the physiological function can depend on the charge state. Binding an ion to a molecule usually induces a significant change of the molecular structure caused by mostly intramolecular Coulomb interactions. For proteins and peptides, the introduction of (elementary) charges can lead to a stabilization or destabilization of the molecular geometry or certain structural elements due to Coulomb interactions with charged side chains of particular amino acids in the backbone sequence.

It is of highest priority for understanding molecular properties and gaining insight into structural folding dynamics that biomolecules be studied in their natural environment, which is usually aqueous solution. However, this is often difficult and *a priori* unknown interactions with solvent molecules or other species complicate the interpretation of experimental observations. To obtain information on fundamental properties of biomolecules it has proven useful to take the molecule out of its natural environment and isolate it in the gas phase. This allows one to study only intramolecular interactions while neglecting all interactions with solvent molecules. The conservation of the native solution-phase structure is not trivial in the absence of intermolecular interactions, however, it has been shown that it is possible to transfer even large biomolecular species intact from their natural solution environment into the gas phase and maintain –at least partially– the solution–phase structure when soft ionization techniques like electrospray ionization (*ESI*, see below) [37–39] or matrix assisted laser desorption ionization (*MALDI*) [40] are used.

1.2.1 Biomolecules in the gas phase

For investigation of molecules in the gas phase, only a limited number of experimental techniques is available. The mass–to–charge ratio of gas-phase ions can be measured using mass spectrometry [41]. Fragmentation studies such as collision-induced dissociation can yield information on the primary structure of biomolecules. Spectroscopy in the infrared spectral range probes the forces between the constituent atoms and can give information on local molecular structures, and the global shape and three–dimensional structure can be measured using ion mobility spectrometry [42, 43].

5

Electrospray ionization

Studying molecules in the gas phase requires as a first step an intact transition of the molecule from its native environment into the gas phase. Many interesting species such as "floppy" larger biomolecules cannot be thermally evaporated as this leads to a decomposition of the molecule. Alternative techniques for bringing biomolecules more gently into the gas phase, for example by laser desorption, often have the disadvantage that the production of gas-phase species is inherently accompanied by energy deposition into the molecule. This mostly leads to the production of gas-phase species in an ensemble of different charge states or fragment ions. A widely used soft ionization technique is electrospray ionization (*ESI*) which can successfully transfer even large proteins and protein complexes intact into the gas phase [37, 44, 45]. The biomolecules of interest are dissolved in (mostly aqueous) solution and are driven through a metal capillary (inner diameter $\approx 125~\mu$m) at a high potential of 2–4 kV with respect to a low potential counter electrode (ground). In positive ion mode[1], which was exclusively used in the framework of this thesis, positive or –more precisely– protonated ions are either present in the solution or form at the tip of the capillary [46]. As a consequence of the electrostatic field force, the ions overcome the surface tension forming the so-called *Taylor cone* which is attracted towards the low potential at the counter electrode (see fig. 1.2). Droplets are released from the Taylor cone forming a stream of solvent that is drawn out into multiple charged droplets which ultimately develop into single gas-phase ions.
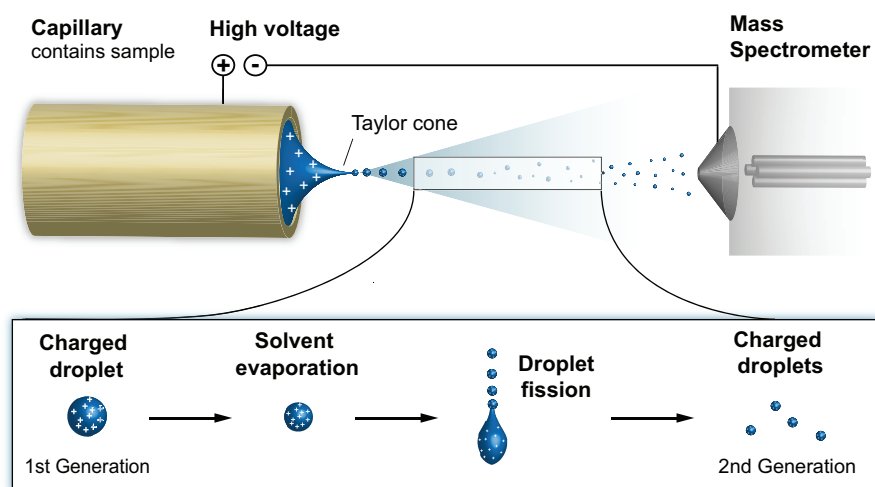

Figure 1.2: Electrospray ionization source: The sample, dissolved in (aqueous) solution, is pulled out of a metal capillary by an applied electric field towards the low potential counter electrode in a *Taylor cone*. The evolution of large solvent droplets to single protonated gas-phase ions *via* the process of Coulomb fission after reaching the *Rayleigh limit* is illustrated on the bottom. The droplets are guided into the high vacuum region through radiofrequency ion guides.

Charges usually become localized on the surface of the droplet at the largest possible distances from each other. Due to evaporation of the solvent, the droplet diameter shrinks continuously. This can be aided by simultaneous flow of (heated) N_2 gas commonly called nebulizer and desolvation gas. When the droplet reaches a certain size, the surface charge

---

[1]The polarity of the applied voltage is decisive for the nature of the gas-phase ions created.

becomes too large, and as a consequence of Coulomb repulsion, the droplet explodes into many smaller droplets distributing the charges of the "mother cluster" onto the fragment droplets. This process is called Coulomb fission, it repeats in cascades and occurs at a point called the *Rayleigh limit*. For liquid drops having a surface tension γ, the Rayleigh stability criterion puts a limit to the (constant) surface charge Q_S that a drop with radius R_d can carry before a Coulomb explosion occurs and the cluster fragments [45, 46]:

$$Q_S = 8\pi\sqrt{\epsilon_0\,\gamma\,R_d^3} \quad , \tag{1.1}$$

with ϵ_0 the vacuum electricity constant, γ the surface tension of the drop, and R_d the drop radius.

At the end of a complicated and not yet fully understood sequence of these events, the bare molecular ion is left over.

Structural investigation methods

Information on the primary structure of biomolecular ions is obtained by mass–spectrometric techniques like collision-induced dissociation (*CID*). Since the structure and three-dimensional shape of a protein or peptide is the key for the biological function and molecular recognition processes there is need for experimental techniques to access the secondary or higher order molecular structural properties. The global shape (*tertiary structure*) can be measured by ion mobility spectrometry (*IMS*). The potential energy surface of a biological molecule usually exhibits several local energy minima separated by potential barriers that lead to a variety of stable conformeric or isomeric structures which the molecule can adapt. When a molecule has high internal energy, for example at room temperature, it can overcome these potential barriers and continuously change its geometric shape back and forth. That leads to the presence of many different conformeric or isomeric structures populated at the same time in an ensemble of equal molecules. *IMS* allows for separation and selection of molecular ions with the same mass–to–charge ratio but different three-dimensional shapes. While this technique is more sensitive towards the global shape of a molecule, the local structure can better be probed by exploring spectroscopy in the infrared range of the spectrum where the energies of molecular vibrations are located. Chemical bonds and non-bonded interactions are probed directly and therefore, information on the *secondary structure* can be obtained. IR absorption spectroscopy is widely established for assignment of molecular structures for condensed-phase molecular samples. In the gas phase, however, one must employ different techniques due to the low particle density which for ionic species has an upper limit of $\approx 10^6 - 10^7$ charges per cm^3 [47] due to Coulomb repulsion and space charge effects. This density is too low to measure direct absorption. Therefore, the direct absorption of IR photons for investigating structural properties of a (bio)molecule can not be measured but instead they can be accessed using an approach commonly called "action spectroscopy" which often employs multiphoton techniques.

In direct absorption the measured quantity is the transmitted light intensity after passing an absorbing medium. That means that the measured quantity is *what the molecule does to the light.* In action spectroscopy, on the other hand, the measured quantity is *what the light does to the molecule.* That means the measured quantity is a (detectable) change in molecular properties, for example the mass, charge state, or quantum state induced by

photon absorption. While in direct absorption the sensitivity scales with the number of particles per cm^2, in action spectroscopy the sensitivity scales with the incident photons per cm^2 and is –in a first approximation– independent of the number density of sample particles.

A common technique of action spectroscopy on gas-phase biomolecular ions that is directly sensitive to the secondary structure is multiple photon dissociation in the infrared spectral range (*IR-MPD*). The absorption of many IR photons leads to an excitation of the ion and, ultimately, a heating to internal energies that are high enough to induce a dissociation of the molecule. Displaying the IR dissociation as a function of the incident wavelength results in an IR spectrum either as a depletion of the parent ion abundance or the appearance of fragment ions.

The effect of anharmonicities causes different energy normal modes to couple to each other and vibrational energy levels to become more closely spaced at higher energies. Mode coupling leads to an effect called intramolecular vibrational redistribution (*IVR*) whereby energy in a specific vibrational mode diffuses to near-resonant coupled vibrational (combination) modes. Consequently, the absorbing state becomes "de-excited" which allows for subsequent absorption of new photons at fast time scales of ≈ 1 ps.

To break a bond and therefore induce the dissociation of a molecule (the "action"), in principle, it is required to absorb at least the photon energy equivalent of the dissociation energy. For a covalent bond with a typical strength of 5 eV this corresponds to the absorption of 40 photons at 1000 cm^{-1} . But since dissociation is mainly a statistical process and the absorbed energy is distributed statistically over the molecule, a polyatomic molecule must thus absorb a much higher energy in order to break a specific bond. A rough number, depending on the size of the molecule, the energy equivalent of several times of the bond energy needs to be absorbed to induce dissociation on an experimental time scale. Therefore, to enable multiple photon dissociation processes of gas-phase ions, high photon densities are required. For example, free–electron lasers (*FEL*) have been proven to be appropriate light sources for *IR-MPD* spectroscopic experiments. The lasing medium in an *FEL* is a relativistic beam of free electrons that is injected into a resonator where the electrons are accelerated by an array of alternating undulator magnets and caused to perform a "wiggling" motion. The emitted light is strongly amplified during successive round trips through the cavity and continuous feeding by fresh electrons coming from a linear accelerator. *FEL*'s can be continuously tunable in wavelength over a wide spectral range with adjustable light intensity.

Inherent to the absorption mechanism in multi-photon techniques is a heating of the irradiated molecules to high internal energies. This has an impact on the achieved spectral resolution and results in typical spectra of "hot" molecules exhibiting broad bands with few clear characteristic features. They deviate from linear absorption spectra. Due to a large number of populated internal states and (cross-)anharmonicities the obtained absorption lines merge into broad bands that can be dynamically shifted in wavelength. That makes it difficult to assign observed vibrational bands to specific molecular transitions obtained from theoretical calculations which are mostly performed at zero Kelvin.

Messenger technique

One specific type of action spectroscopy is the so-called messenger technique. In this method, a weakly interacting species, the "messenger" (mostly rare gas atoms) is bound

to the molecule of interest (for example tightly bound covalent cluster ions) [48, 49]. Due to the low binding energy, the messenger atom easily dissociates from the investigated molecular species, allowing a significantly reduced number of absorbed photons to induce photo-dissociation. Therefore, a lower amount of heat is required to induce evaporation of the messenger and to measure an absorption spectrum using multi-photon absorption techniques.

Having a molecular species embedded in a droplet, the constituent He atoms can be used as messengers for photon absorption by the dopant. After resonant absorption, the molecule under investigation quickly transfers the excitation energy to the droplet which releases the absorbed energy mostly *via* evaporation of He atoms. Recording mass spectra of the droplet + dopant system as a function of wavelength would result in an absorption spectrum. Spectra thus obtained are expected to show narrow linewidths due to the low internal temperature of a He cluster to which an embedded particle is thermalized. Since the dopant species releases its entire internal energy to the He bath, it will return to the ground state after every resonant absorption process, which can thus be repeated many times.

1.3 Liquid helium clusters

Helium exists in two stable isotopes which are fermionic ^{3}He and bosonic ^{4}He. Both isotopes can exist as bulk liquids with binding energies of $E_b = 2.5$ K for ^{3}He and 7.17 K for ^{4}He [19] and as finite size clusters having lower binding energies than in the bulk material. The ^{4}He isotope liquid exhibits superfluidity, and all the following is restricted to this isotope. Helium is the only element that is liquid even at zero Kelvin as long as the pressure stays below 25 bar. This is due to the tiny mass of a helium atom and the high zero-point energy. As the smallest rare gas atom, it has also the lowest atomic polarizability and it interacts with other rare gas atoms only through weak van der Waals interactions (He–He interaction <1 μeV (binding energy of the only bound state) [50]). These properties lead to the occurrence of a phenomenon called superfluidity. It is a second form of the liquid phase which forms at temperatures below the so-called λ–transition at $\approx$ 2.17 K. A superfluid flows with zero viscosity and is characterized by an almost infinitely high heat conductivity. The occurrence of superfluidity can be explained by looking at the dispersion relation of superfluid helium (fig. 1.3) which has been obtained by inelastic neutron scattering measurements [50]. It reflects the combinations of energy $\hbar\omega(\vec{k})$ and momentum $p = \hbar\vec{k}$ (of the collision partners) for which elementary modes exist in a He cluster. At low energies, the dispersion relation is linear, and the corresponding bulk modes in the superfluid are phonons as longitudinal density fluctuations, in analogy to acoustic phonons in a solid crystal. At higher energies, the dispersion relation shows a characteristic maximum ("maxon"), which is followed by the "roton" minimum. In the region of the minimum, the dispersion curve can be described by a quadratic relation as $\hbar\omega = E_{\rm rot} + p^2/(2\,\mu_{\rm rot})$ with $\mu_{\rm rot} = 0.16$ m$_{\rm He}$ the effective mass of the roton [50]. The energy $E_{\rm rot} = 8.65$ K provides a gap in the excitations which is regarded as the basis for superfluidity [52]. Due to this energy gap, it follows from energy and momentum conservation, that an excitation in the superfluid can only be excited under certain conditions. Any particle can move through superfluid helium without any "mechanical" friction as long as it does not couple to a helium elementary mode,
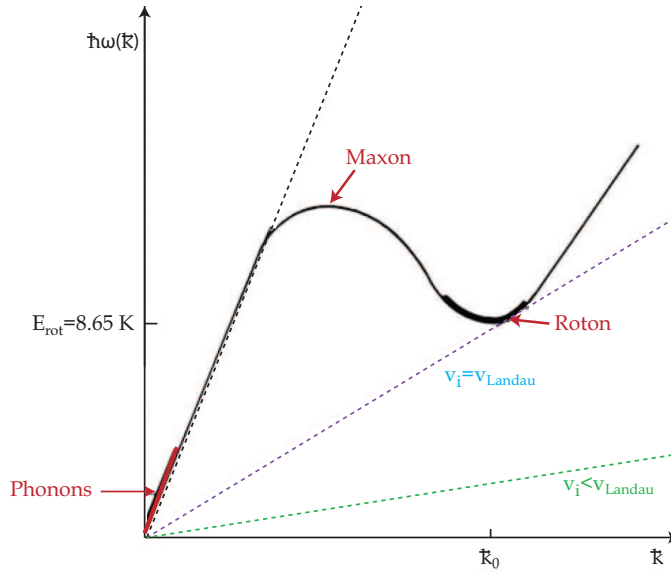
Figure 1.3: Dispersion relation of liquid helium [50]. The energy $\hbar\omega(\vec{k})$ is displayed over the wave vector $\vec{k}$. The dispersion relation is characterized by a linear part at low energies, which is analogous to acoustic phonons in a crystalline solid, and by a maximum of the curve at the so-called maxon, which is followed by a minimum, the so-called roton. The blue dotted line reflects the energy–momentum relation of a particle which moves with the critical Landau velocity v_{Landau} [51] through the superfluid and is able to excite a roton. The green dotted line reflects particles with velocities $v_i < v_{\mathrm{Landau}}$ which can move through superfluid helium without any friction.

causing the helium to become viscous. Due to the minimum in the dispersion curve, a critical velocity can be defined by $v_{\mathrm{Landau}} = E_{\mathrm{rot}}/p \approx 60 \ \mathrm{ms}^{-1}$ as the minimal velocity which is required to excite a roton with energy E_{rot}. This critical velocity can be derived from the dispersion curve as the line of flattest slope through the origin which intersects the dispersion curve (blue dotted line in fig. 1.3). That means that frictionless motion through superfluid helium is only possible when the relative velocity between the particle and the superfluid does not exceed the Landau velocity (green dotted line in fig. 1.3). Otherwise, the helium becomes viscous and exerts a drag force on the particle.

Another characteristic for a superfluid is the occurrence of second sound as a temperature wave [52, 53]. Contrary to a first sound pressure wave, whose components are moving in phase with one another, in the second sound wave the normalfluid (hot) and the superfluid (cold) components move out of phase in opposite directions. Due to the temperature difference between the two components a temperature drop is caused by an increase of the superfluid component concentration and a temperature rise when the normalfluid component concentration is increased. Due to the simultaneous presence of the two condensed phases liquid helium is often treated in a two-fluid model.

It has been considered whether superfluidity can also occur in finite size clusters [54–57]. It is found that the cluster size has to be greater than a temperature dependent coherence ("healing length") which is on the order of a few Å for temperatures $T < 1$ K for this to occur [15].

He clusters are liquid and have an internal pressure that is smaller than 250 mbar (for He clusters composed of 10^6 He atoms) [58]. The *Liquid drop model (LDM)* from nuclear physics is often used to describe liquid He clusters in the size range of $N_{\mathrm{He}} \geq 10^3$ [15, 59]. In the *LDM*, a droplet in the ground state is supposed to be spherical with a sharp outer

edge. The radius R_d of a droplet is determined by the number of He atoms N_{He} as [15]:

$$R_d = \sqrt[3]{\frac{3N}{4\pi\rho}} = 2.22 N_{He}^{\frac{1}{3}} \text{Å} \quad . \tag{1.2}$$

The particle density in a He droplet has a value that is close to the bulk value of liquid He with $\rho = 0.022$ atoms $\cdot$ Å^{-3}. Approaching the cluster surface, the density decreases and ultimately reaches a value of 90%–10% of the bulk particle density over the surface region of thickness $d_S \approx 10$ Å for ^{4}He [60].

The collective elementary excitations of a superfluid He droplet are classified as compressional bulk modes, so-called *rotons*, and surface capillary waves called *ripplons* which are the lowest energy modes. The energies of both bulk and surface modes are dependent on the number of He atoms N_{He} composing the cluster [61].
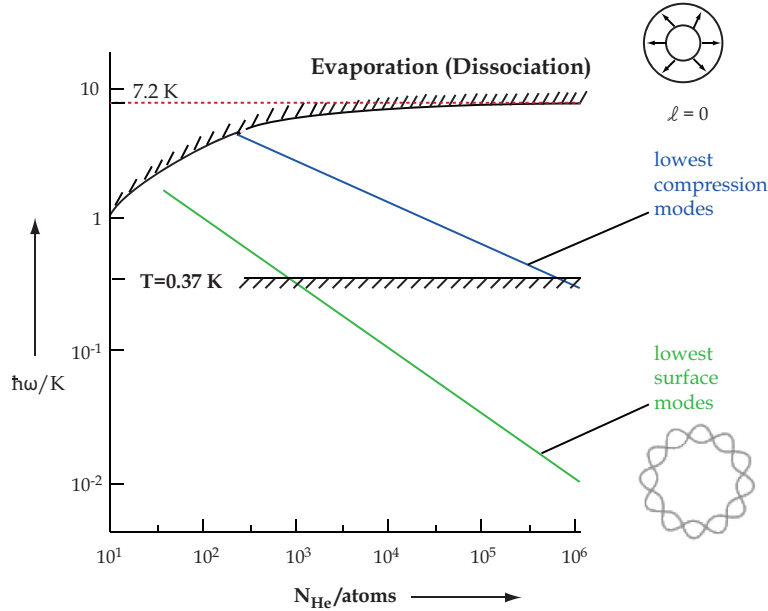

Figure 1.4: Energies (in Kelvin) of elementary excitations of a He$_N$ cluster as a function of the number N_{He} of constituent atoms. The upper curve corresponds to the dissociation energy when a He atom is evaporated from the cluster. The figure (modified) is taken from ref. [15].

The energies of the elementary excitations are shown in fig. 1.4 as a function of the number N_{He} of constituent He atoms in a cluster. Collective modes are found for clusters containing more than ≈ 80 He atoms and are excited only as ripplons in clusters having sizes between $N_{He} = 10^3$–10^6 constituent He atoms at the cluster temperature of 0.37 K (horizontal line); in larger clusters, also bulk modes are excited at this temperature. The compressional modes are not excited at the low internal cluster temperature since their energies are too high (see fig. 1.4). However, they are excited at 0.37 K when the clusters contain more than 10^6 atoms. The upper curve shows the dissociation energy at which a He atom will be evaporated from a cluster of size N_{He}.

Bulk liquid helium –for example in a jar– is not particularly well suited for dissolving molecules as these would quickly sink to the bottom or possibly aggregate or stick to the walls. Thus there is a need for finding alternative techniques to study molecules in liquid helium and the breakthrough happened about twenty years ago when the first experiments

were performed on molecules captured by He clusters in vacuum [15, 22].

Probably the earliest observation of He droplets was that made by Kamerlingh Onnes in a "Joule free expansion" in 1908 [62]. He droplets can be formed in free-jet expansions [63] of high-pressure, pre-cooled He gas. This technique is used by many groups to produce continuous or pulsed cluster beams[2], obtaining clusters in a wide range of sizes, from $N_{He} = 10^3$–10^{12} He atoms.

1.3.1 Superfluid ^{4}He clusters as cryogenic spectroscopic matrices

Spectroscopic studies of foreign species embedded in liquid He droplets as "the ultimate spectroscopic matrix" [22] is an important and well-established technique. The cryogenic environmental temperature provides for dopant species to be present in the ground state with only a few populated internal states. A He droplet is a dissipative system which releases all absorbed energy mostly *via* evaporating He atoms from its surface and in this way, maintains its internal equilibrium temperature of ≈ 0.37 K. An embedded foreign species transfers the entire energy contained to the He droplet once it is picked up and is cooled very fast to the droplet temperature. That also means that, after resonant absorption, the embedded molecule gives the excitation energy to the dissipative He droplet environment and relaxes internally. As a large droplet has a large heat capacity it can efficiently control and equilibrate the temperature of the droplet+dopant system [15]. Thus, since in a multiple photon absorption process the liquid helium environment will cause the absorbing molecule to relax between each single photon absorption event and therefore, basically all absorptions will start from the vibrational ground state, the resulting optical spectra appear more like linear absorption spectra exhibiting narrow absorption bands instead of hot molecule spectra. The first spectra of molecules in superfluid He clusters were measured by Scoles *et al.*, followed by Toennies *et al.* in infrared spectroscopic studies on SF_6 [20, 66], and by UV–Vis absorption spectra of glyoxal $C_2H_2O_2$ molecules [67]. Rotationally resolved infrared spectra of the HCN dimer [68] and of guanine [69] were measured by Miller *et al.*. High-resolution vibrational spectra were also measured on tryptophan and tyrosine by Vilesov *et al.* [26]. Electronic transitions in larger organic molecules were investigated in the group of Slenczka [70, 71]. Such studies also reveal the interaction between the embedded species and the He cluster, in particular the influence of the electron–phonon coupling and the occurrence of so-called phonon wings. The growth of metal clusters in He droplets is reviewed in [72]; the dynamics of ionized metal clusters grown in He droplets have been studied in pump–probe experiments using femtosecond high–intense laser pulses by Meiwes–Broer *et al.* [30, 73]. The growth of van der Waals complexes in helium droplets is performed and studied by M. Havenith *et al.* [74]. In the group of Stienkemeier, alkali metal ions attached to He droplets are laser probed [75, 76] and the ultrafast dynamics of vibrational wave packets excited in small ionized alkali oligomers is studied in pump–probe experiments [77]. Embedded molecules and molecular complexes can rotate freely inside ^{4}He droplets. Recorded IR spectra often show a well-resolved rotational fine structure. This can be seen in fig. 1.5 which shows rovibrational spectra of $OC^{32}S$ molecules embedded in superfluid ^{4}He droplets composed

---

[2]Macroscopic droplets with diameters between 2 μm and 2 cm are, for example, formed in capillaries or as "mist" by rapid pumping on the liquid and subsequent levitation in magnetic or laser dipolar traps [17, 64, 65]. They can be observed by optical means like microscopes.
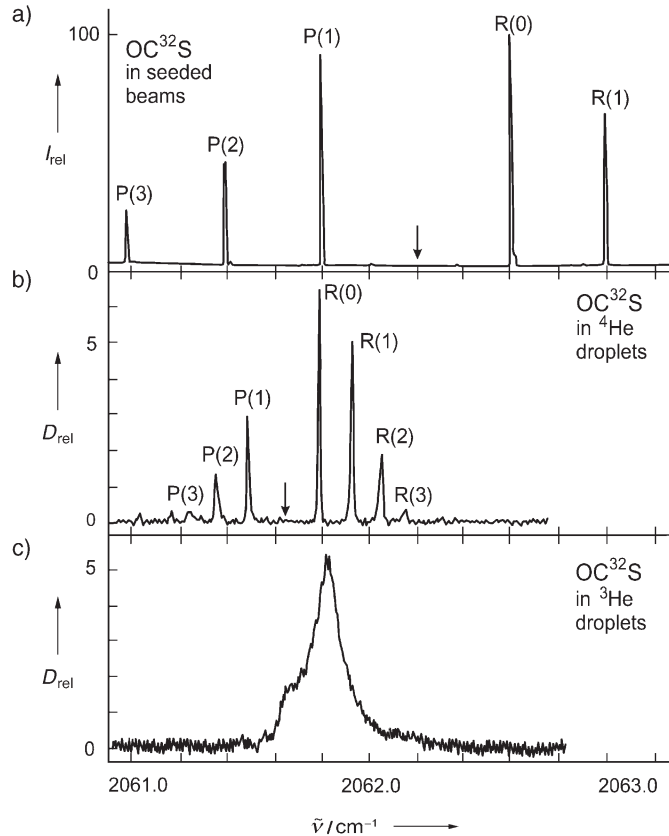
Figure 1.5: Comparison of IR spectra of $OC^{32}S$ molecules in different environments: The IR absorption as a function of wavenumber is shown in the top panel for gas-phase $OC^{32}S$ molecules expanded in an Ar seeded beam, the center panel $OC^{32}S$ embedded in superfluid ^{4}He droplets, and the bottom panel $OC^{32}S$ embedded in ^{3}He droplets. The different lines correspond to various rotational transitions (P and R branches), the position of the (missing) Q-branch is indicated by arrows. The spectra shown were taken from ref. [15]).

of about 6000 He atoms [25], compared to spectra obtained in Ar seeded beams and in non-superfluid ^{3}He droplets [54]. As can be seen, the resolution and measured line widths are comparable in the two upper spectra, whereas the spectrum in the bottom panel has a considerably reduced resolution showing only one broad band. Therefore, the high resolution that can be obtained in ^{4}He droplets is (at least partly) attributed to superfluidity. Furthermore, compared to molecules that are isolated in solid matrices, no "crystal field effect" (local distortions) is observed in He droplets [15]. Especially for molecules with large moments of inertia like $OC^{32}S$, it is observed that the line spacings are significantly reduced compared to a free rotor in the gas phase (see fig. 1.5). This is attributed to the normalfluid component of bosonic helium that binds to the dopant molecule in a monatomic or biatomic shell, leading to an increased moment of inertia and, as a consequence, to a smaller rotational constant B [15]. Since the rotational energy levels are given by $E_{rot} = BJ(J+1)$ with J the angular momentum quantum number, a reduced line spacing indicates a reduction in the rotational constant. Furthermore, IR spectra of molecules which are analyzed in superfluid He clusters often show that the vibrational origin is red–shifted by a few wavenumbers (-0.56 cm^{-1} for $OC^{32}S$ and -2.22 cm^{-1} for HF molecules) compared to the band positions in the gas phase. These energy shifts are attributed to a closer spacing of the vibrational ground state and the (first) excited state

13

in a He droplet which is mainly caused by enhanced attractive interaction forces (electrostatic induction and dispersion) between the chromophore of the vibrationally excited molecule and the surrounding He atoms compared to the molecule in the ground state [15, 68]. However, the symmetry of molecular vibrations is usually not affected by the liquid helium environment.
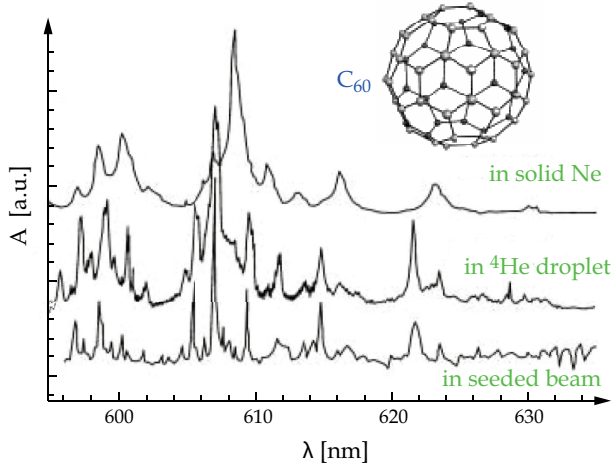

Figure 1.6: Visible absorption spectra of C_{60} in different environments. The electronic absorption as a function of the wavelength of the incident light is shown in the uppermost spectrum for C_{60} embedded in a solid Ne matrix, below for C_{60} embedded in superfluid ^{4}He droplets, and at the bottom for C_{60} in a helium–seeded pulsed molecular beam in the gas phase. The spectra are shown with an offset due to clarity (spectra taken from ref. [15]).

It is seen that rovibrational excitations of molecules immersed in He droplets do usually not lead to a stronger interaction between the droplet and the excited species than when the particle is in its ground state. In other words, performing rovibrational spectroscopic measurements does, in general, not lead to a perturbation of the He clusters through excitation of the dopant species and the internal cluster states are usually conserved. On the contrary, UV-Vis spectroscopic measurements for investigation of electronic transitions of dopant molecules can possibly lead to a simultaneous excitation of the internal modes of the He clusters. This is presumed to result in significant changes of the repulsive interactions between the dopant species and the surrounding He atoms and consequently, to a change in the equilibrium configuration of the He solvation shell around the solute. However, most electronic excitation spectra (for example LIF spectra) of several organic molecules or C_{60} in superfluid He droplets show surprisingly small shifts of the band positions compared to a free molecule. In fig. 1.6, electronic absorption spectra of C_{60} molecules in different environments are shown: embedded in a solid neon matrix ([78], top), in ^{4}He droplets of an average size of $N_{He} = 10^4$ He atoms ([28], center), and isolated in the gas phase in a He–seeded pulsed molecular beam ([7], bottom) [15]. Furthermore, for large molecules embedded in superfluid He droplets, recent spectroscopic studies have yielded spectra of even higher resolution, compared to those obtained for the bare gas-phase molecule in a molecular beam setup, [79], because of a lower rotational temperature and a narrower rotational band–contour.

The cooling rate and the internal droplet temperature of ≈ 0.37 K can be estimated from measured spectroscopic line widths and line intensities, respectively, due to a Boltzmann distribution of populated states [15]. The experimentally obtained droplet temper-

14

ature is in good agreement with the theoretically determined temperature of a He cluster [80] which indicates that the rotational degrees of freedom are fully equilibrated in the liquid helium bath [15].

When a foreign particle is picked up by a He droplet, it can either stay on the surface or move into the interior of the droplet. Whether a dopant particle becomes located in the droplet center or on the surface depends on interactions between the outer electrons of the foreign species and the He atoms and can be determined by a dimensionless parameter λ [15]. This parameter links the gain in energy from the interaction with the He as a solvent and the energy needed to create a He cavity [15]. For $\lambda < 1.9$, the dopant is predicted to reside on the cluster surface whereby for $\lambda > 1.9$, it becomes solvated and immersed in the cluster.

Usually, open-shell atoms and molecules (Na, O_2) become localized on the cluster surface in a *bubble* solvation structure [50]. This can be experimentally observed by –for example– performing UV-Vis spectroscopic measurements which show that UV–Vis excitation energies are often blue-shifted when a particle is solvated in a *bubble*.

1.3.2 Formation of He droplets in free-jet nozzle expansions

Liquid He droplets can be formed *via* expanding He gas in a free jet under high pressure P_0 and low temperature T_0 into vacuum. It is presumed in the expansion that no energy is exchanged between the expanding gas volume and its environment or, in other words, that the occurring particle–particle interactions dominate over particle–surface interactions by many orders of magnitude. This is well satisfied close to the symmetry axis of the beam, given the high jet densities and low background pressure in the vacuum chambers. These conditions allow for an adiabatic treatment of the free-jet expansion. A further advantage
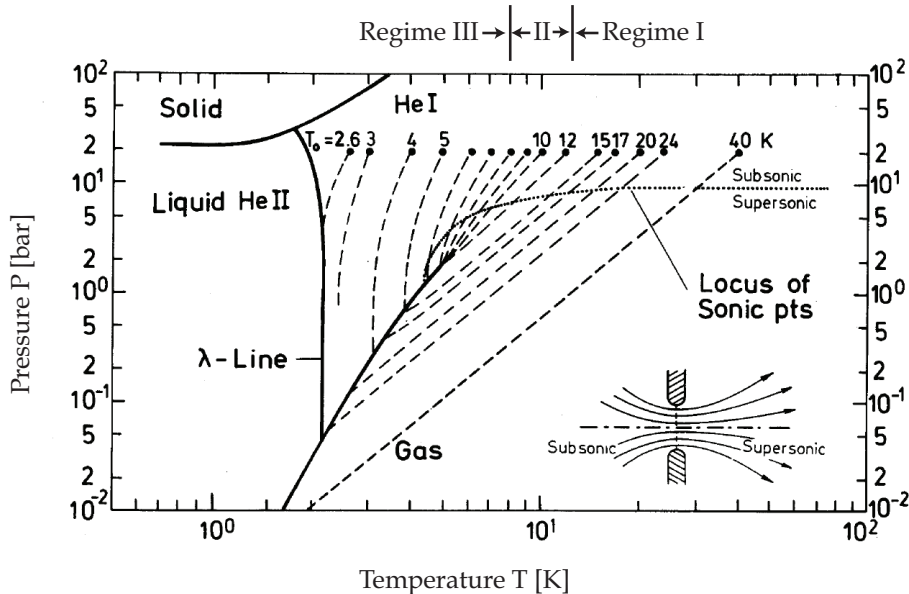

Figure 1.7: Phase diagram of ^{4}He. Dotted lines show isentropes on which an expanding gas volume can progress with constant entropy characterized by the relation $P_0 T_0^{\kappa/(1-\kappa)} = $ constant. The figure is taken from ref. [58].

is given when the expansion process is presumed to be reversible. This allows for an

isentropic treatment and hence, for a description of the beam evolution by means of the initial stagnation conditions [81]. Under the assumption of a constant entropy, the enthalpy of the expanding fluid of the expanding system can be evaluated as a function of the stagnation conditions (P_0, T_0) and the final beam temperature T_∞ [81]. The resulting expressions for the flow properties like the terminal beam velocity $\langle v_f \rangle$ are very close to those obtained for adiabatic expansions [81].

The isentrope on which the expansion will proceed in the phase diagram is defined by the initial source conditions P_0 and T_0, the gas is cooled by passing through adiabatic changes of states along the respective isentropic line [15] (see fig. 1.7).

Descriptions for (mostly continuous) free-jet expansions are given in the fundamental text books from G. Scoles [1] and H. Pauly [2], which also present models to describe condensation processes leading to cluster formation in terms of thermodynamic and kinetic processes. The resulting cluster sizes and size distributions as well as the average beam flux can be controlled by the source conditions P_0, T_0 and the nozzle parameters like geometry and orifice diameter D.

Isentropic free-jet expansions

An isentropic expansion is characterized by its temporal evolution along lines of constant entropy $\Delta S = 0$ in the phase diagram. The isentropes are defined by the relation $P_0 T_0^{(\kappa/(1-\kappa))} = $ constant with $\kappa = c_p/c_V$ the ratio of specific heat capacities which is characteristic for the medium (for helium: $\kappa = 5/3$). This means that, in order to remain on the same isentrope, a change in P_0 must be compensated by the respective change in T_0 [82].

When an isentropic beam expansion is treated as an ideal gas, the flowing medium (gas) is considered as an ensemble of many non-interacting molecules in permanent motion. Interaction in terms of energy and momentum exchange takes place only at close distances between the particles [2]. The energy of a single molecule is approximated as the sum of translational (kinetic) energy, rotational energy, and vibrational energy [2]. In the ideal gas approximation, effects like friction, heat transfer, and external forces as well as cluster formation processes are neglected. These are treated later on in Ch. 1.3.3 when real fluid properties and interaction between particles are considered. The kinetic theory of gases is based upon the fundamental ideal gas equation of state (Boyle-Mariotte's law)

$$PV = Nk_B T \quad , \tag{1.3}$$

The thermodynamic laws valid for isentropic processes when going from a temperature T_1 to a temperature T_2 in terms of the flow properties gas pressure P, mass density ρ_M, and temperature T are the following:

$$\frac{P_2}{P_1} = \left(\frac{T_2}{T_1}\right)^{\kappa/(\kappa-1)} \qquad \frac{\rho_{M,2}}{\rho_{M,1}} = \left(\frac{T_2}{T_1}\right)^{1/(\kappa-1)} \qquad \Rightarrow \qquad \frac{P_2}{P_1} = \left(\frac{\rho_{M,2}}{\rho_{M,1}}\right)^{\kappa} \quad . \tag{1.4}$$

In its early stage at high particle densities, the expansion can be treated by equilibrium thermodynamics for a continuous medium [2]. Changes in flow properties occur on distance scales that are large compared to the mean free path of the gas molecules and local equilibrium is adjusted instantaneously. At thermodynamic equilibrium, particles exchange energy *via* collisions until every degree of freedom of the particles in the system

has the same average energy, according to the equipartition principle. Colliding particles are then present in a Maxwellian distribution of relative velocities [2]. After moving further into vacuum, the gas rapidly becomes diluted for increasing distance x from the nozzle which is accompanied by a continuous temperature decrease.

A decrease in particle density corresponds to an increase in mean free path which finally becomes large compared to the dimension of the expanding system (namely, a gas volume element in thermodynamic equilibrium). This implies a decrease of collision rate and collisional cooling of internal states until they cease completely at too low particle density n. This is called free molecular flow region where no collisions occur that lead to (internal) relaxation of the expanding particles and thus, no local equilibrium exists [1, 2]. The evolution of a free-jet expansion can thus be divided by a transition region into a flow at thermodynamic equilibrium conditions and a flow at non-equilibrium conditions. The transition region is characterized by the occurrence of incomplete relaxation processes and can be described by collision rates within the kinetic theory of gases by an approximative solution of the Boltzmann equation [2]. An illustrative concept for treating processes under conditions where relaxation processes are "freezing" out is provided by the method of the "sudden–freeze radius" or "quitting surface" [1].

Upstream of the quitting surface, the expanding gas volume is at local equilibrium and can be treated as an isentropic continuous medium and downstream in the free-molecular flow region, particle collisions for energetic relaxation cease and the gas volume has reached its final temperature T_∞. However, in case of condensed beams, when clusters are formed at high particle densities before the quitting surface is reached, the formed clusters can cool down further by energy–loss processes (evaporation). The location of the quitting surface or sudden–freeze radius with reference to the distance from the nozzle can be calculated through the measured final speed ratio S [83]. For example, the sudden–freeze for He clusters formed in continuous expansions is located at ≈ 1000 orifice diameters
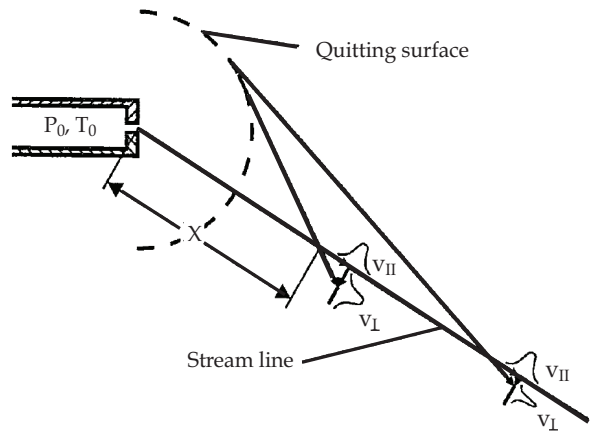

Figure 1.8: Quitting surface in a free-jet gas expansion (figure taken from ref. [2]). The quitting surface divides the two stages of an adiabatic free jet which are that of a continuous medium and of free molecular flow.

D from the source [15]. Then, the resulting beam consists of a mixture of He atoms and clusters in a certain size distribution [15, 58, 84]. Isentropic beam expansions can be realized through nozzles of different geometric shape and cross–sectional area. The nozzle geometry is decisive for the kinetic flow properties of the emitted beam.

Molecular beam velocities and velocity distributions

The average velocity of a monatomic gas volume reached in a continuous isentropic expansion of an ideal gas is mainly determined by the expansion temperature and the mass of the expanded gas. It is derived using the isentropic laws given in eq. (1.4) on the basis of energy conservation and given for an ideal monatomic gas with $\kappa = 5/3$ by [1, 2]:

$$v_x = \sqrt{2\frac{\kappa}{\kappa-1}\frac{k_B T_0}{m}} = \sqrt{\frac{5k_B T_0}{m}} \quad , \tag{1.5}$$

with k_B the Boltzmann constant, T_0 the applied source temperature, and m the atomic mass of the expanded gas.

The velocity distribution in a free-jet gas expansion is non–isotropic in an expanded gas volume element. This can be understood by the sudden-freeze model [2]. According to this, collisions take place only before the quitting surface is reached. Further downstream, the distribution of parallel velocities remains constant. The perpendicular velocities, on the contrary, continue to decrease with increasing distance from the source caused by geometric effects [2]. The final longitudinal velocity distribution Δv_x can be predicted in terms of the stagnation conditions and gas properties regarding the evolutionary stage of the expansion. It is characterized by the Mach number M which is defined as the ratio of flow velocity to the local speed of sound. The Mach number is still valid in the transition region and can be expressed in terms of the speed ratio $S = v_x/\Delta v_x$ which is a measure for the distribution of relative velocities of the gas particles in a volume element among each other at thermodynamic equilibrium [2, 83]. The volume element itself moves with a translational velocity v_∞ that is determined by the source temperature T_0. The relative velocities of the particles in the volume element, however, are determined by the source temperature and the pressure in the reservoir. The speed ratio S is expected to be largest (corresponding to a narrow velocity distribution Δv_x) for cold gaseous beams expanded at high pressure P_0, when no condensation is taking place. For large speed ratios S the final beam temperature T_∞ will be considerably lower than T_0.

1.3.3 Real fluid corrections

In the ideal gas model, particle–particle interactions are neglected and therefore, it can not be applied to predictions of flow properties at high particle densities which are present in the source at low temperature T_0 and high pressure P_0. These, however, are important prerequisites for condensation effects and cluster formation.

Macroscopic models are derived in ref. [81, 85–87] for describing properties of expansions of real gases. The fluid beams are described in terms of thermodynamic quantities such as the Helmholtz free energy, the enthalpy, and the entropy.

Looking at the phase diagram of helium (fig. 1.7), the phase state of the expanded fluid is determined by the initial state of the fluid (T_0,P_0) in the source which defines the isentrope on which the expansion is progressing. At very low source temperatures T_0 the beam is already liquid before passing the nozzle throat and a liquid beam is expanded. Clusters are formed through the break-up of a superheated liquid beam [58], comparable to a "spray" resulting from Rayleigh oscillations [15]. A model is proposed which describes the fragmentation of a fluid in a spherical expansion in a hydrodynamic approach and proposes an expression for the cluster size [86]. The beam velocity of a liquid beam can be derived from hydrodynamics. Considering an incompressible (i.e. when the changes in density of the fluid upon changes in pressure or temperature are negligible) and irrotational fluid in steady flow without friction, it results from conservation of energy that the sum of internal energy, kinetic energy, and potential energy is constant along a

flow streamline at any point for horizontal flow [88, 89]:

$$\frac{\partial}{\partial x} = \left(\frac{mv^2}{2} + \frac{mP_0}{\rho_M} + m\,g\,h \right) = 0 \quad , \tag{1.6}$$

with ρ_M the mass density of the fluid at a certain temperature and pressure P_0, m the mass of the particles composing the fluid, g the gravitational constant, and h the distance that the fluid is traveling in perpendicular direction to the beam flow. Here, gravitation will be neglected. From the resulting equation, the velocity of a liquid beam which is flowing out of a reservoir under a pressure P_0 and is passing through an orifice can be derived as [90]:

$$v = C\sqrt{2P_0/\rho_{M,0}} \quad . \tag{1.7}$$

C is the so-called discharge coefficient ($0 < C < 1$), which is a measure for the friction exerted by the orifice the fluid is flowing through. A value of $C \approx 1$ is taken for smooth orifices. Eq. (1.7) is called Bernoulli equation, it is a special formulation of Euler's equation. In so-called supercritical expansions, all isentropes pass through or close to the critical point. In this region, there is no clear separation of liquid and gas phase which is characterized by large density fluctuations [58]. Cluster formation is predicted to result from the separation of the gas and the liquid phase [91].

In ref. [81], a macroscopic approach is presented that is applicable to a large number of fluids, including all rare gases and all aggregation states, and to a wide range of expansion parameters (T_0, P_0). An expression for the mean beam velocity is derived as a function of the residual enthalpy $H \equiv U + PV$ in the expanding fluid which includes the liquid–vapor phase boundary and the critical point. Both the initial state of the fluid in the reservoir and the final aggregation state in the free jet will affect the terminal beam velocity which results mainly from the enthalpy change during the expansion as $v_\infty \sim \Delta H = H_0 - H_f$. For comparison, the ideal gas expression in eq. (1.5) determines the terminal beam velocity as a function of only the source temperature T_0 and the molecular weight M, whereas a dependence on the source pressure P_0 is not included.

The terminal velocity v_∞ is maximal when the change of enthalpy from the initial to the final state is largest, and since the degree of condensation is the major factor that determines the change of enthalpy, the highest beam velocity is achieved when the expanded fluid –at least partially– condenses. The vapor and liquid regions of a jet are characterized by two distinct residual enthalpies $H_v > H_l$ which differ by the enthalpy of vaporization[3]. Therefore, the formation of clusters due to condensation in a gas expansion leads to a lowering of the residual enthalpy and furthermore, the condensation energy gives an additional contribution to the directed translational motion of the expanding jet. This results in a significantly higher terminal beam velocity v_∞ of a cold condensed beam compared to a cold but gaseous beam [81].

In general, any fluid has the largest value of the residual enthalpy H at its triple point [81]. It decreases for increasing pressures due to a higher number of particle–particle interactions. This results in a reduced total initial energy that is available for conversion into directed translational center–of–mass motion and thus, a lower terminal beam velocity for increasing source pressures P_0. But at the same time, an increased source pressure

---

[3]The enthalpy of vaporization and the enthalpy of condensation are equal but have an inverse sign.

enhances the particle–particle interactions during the expansion and hence, the efficiency of collisional cooling as well as the importance of nucleation processes in an evolving jet [81]. The increase in beam velocity for increasing source pressure P_0 due to the heat of condensation released is in competition with the decrease in beam velocity due to a reduced total energy. For increasing temperature T_0, the enthalpy H increases constantly.

In an isentropic expansion, it is possible to determine the residual enthalpy H as a function of the initial stagnation conditions and the final temperature T_∞ through the entropy S_0. The relevance of cluster formation i.e. the relative intensities of the gaseous and condensed portion of a beam for a certain thermodynamic state $(T_0,\ P_0)$ of the expanding fluid can be determined by calculation of the initial entropy $S_0(T_0,\ P_0)$ which specifies if and at what temperature a given expansion will reach the two-phase region. Hereby, a low pressure P_0 corresponds to a high entropy S_0. Further, the terminal beam temperature T_∞ in an isentropic expansion can be determined using the entropy S_0 giving an upper limit for T_∞ by the saturation temperature of the fluid. It predicts that the lowest final temperatures can be reached in cold gaseous beams when no condensation occurs since the released heat of condensation in cluster formation processes diminishes the energy that is available for conversion [81].

Beam intensity

The mass of flowing gas per unit time through a nozzle with opening diameter D can be obtained for a given flow velocity v_x and gas mass density ρ_M by [2]

$$G = \pi \left(\frac{D}{2}\right)^2 v_x \rho_M \quad , \tag{1.8}$$

with G in units of kg·s^{-1}.
Using the flow properties of an isentropic expansion given in eq. (1.4) and the equation of state, eq. (1.3), an expression for the maximal mass flow rate G_{max} in a gas dynamic beam of an ideal gas is derived in ref. [2].
For practical applications, the total mass rate G_{max} of gas that can be removed from a vacuum chamber by a pump with pumping speed Z_p is acquired when inserting the total mass of gas $g = m\,N$ contained in a volume V at a background pressure P and ambient temperature T into the ideal gas equation of state:

$$g \;=\; \frac{m\,P\,V}{k_B T} \tag{1.9}$$

$$\Rightarrow \quad G_{max} \;=\; \frac{m}{k_B T} P Z_p \quad . \tag{1.10}$$

The total flux I_{tot} of a nozzle beam (in units of particles per steradian and unit time) follows from the maximum mass flow rate as

$$I_{\text{tot}} = \frac{G_{max}}{m_{\text{He}}} \quad , \tag{1.11}$$

and the centerline intensity I(0) (in units of particles per steradian and unit time) can be

calculated as

$$I(0) = \frac{\gamma}{\pi} I_{\text{tot}} \quad , \tag{1.12}$$

where $\gamma(\kappa)$ is the so-called peaking factor with $\gamma(\kappa) = 1.91$ for $\kappa = \frac{5}{3}$ (He) [2].

1.3.4 Cluster formation

Cluster formation in adiabatic nozzle beam expansions following condensation of the expanded gas was at first observed by Becker *et al.* in 1956 [63]. Cluster beams are characterized by high mass flow rates and highly uniform speeds [82]. They occur if the gas is sufficiently cooled before or during passage of the sonic point, and clusters can be formed *via* condensation which is understood as the liquefaction of a cooled gas beam [82].

Cluster formation due to condensation can be explained by a macroscopic and a microscopic model. In the macroscopic picture, the onset of condensation is thought to depend on the thermodynamic state of the system and on the kinetics of the adiabatic expansion. In fig. 1.9 the course of a condensed beam expansion is illustrated. The free-jet expansion starts at a certain point T_0, P_0 (point *(A)*) in the phase diagram, follows the respective isentrope over the phase separation line $P_V(T)$ (point *(B)*) with P_V the vapor pressure of a plane liquid surface [2]. In the liquid phase regime, the expanded systems becomes supersaturated. A gas volume condenses when it reaches a state of supersaturation. The supersaturation ratio increases on the further course into the liquid regime until, finally, the supersaturated state breaks down (point *(C)*) and condensation processes set in. The gas converts to a liquid and clusters are formed. Afterwards, the expansion returns to the equilibrium vapor pressure $P_V(T)$.
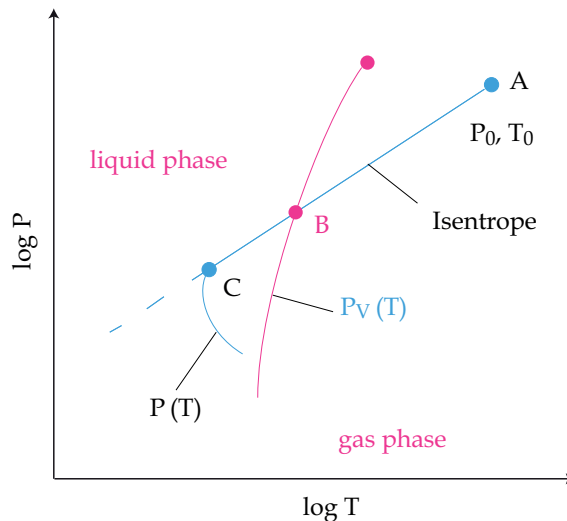

Figure 1.9: Scheme of the expansion curve $P(T)$ and the vapor pressure curve $P_V(T)$ in a double logarithmic diagram (figure taken from ref. [2]).

In the microscopic model, cluster formation is treated on the basis of nucleation theory. Dimers, as condensation nuclei, are supposed to form before or during passage of the sonic point. Further atoms can be attached with a statistical "sticking probability" [59]

leading to cluster growth from the successive accumulation of monomers [2]. Dimer formation requires three-body collisions due to momentum and energy conservation and occurs only at high particle densities in close proximity to the nozzle. When during the further course of the expansion the cluster number density increases compared to the monomer density, cluster growth resulting from cluster–cluster collisions becomes more important. An exact theoretical treatment of cluster formation processes is complicated. It is possible to describe cluster growth or decay on the basis of coupled rate equations. Collisional cross sections leading to cluster formation in free-jet beam expansions can be determined within the kinetic gas theory. The most simple treatment is to assume a hard-sphere model for the intermolecular potential but more accurate results for collision processes can be achieved by considering for example the Lennard-Jones interaction potential [2]. It predicts enhanced clustering in ideal planar rather than in axisymmetric expansions [2].

Whereas beam intensities scale with $P_0 D^2 T_0^{-1/2}$, the formation of clusters scales with the three-body collision rate Z_3 like $P_0^2 D T_0^{-2}$ [2, 82]. This implies that nucleation processes and cluster growth can be enhanced by making D larger or P_0 higher.

Expansion parameters

The properties and temporal evolution of molecular beam expansions and the processes leading to cluster formation and growth are defined by the initial stagnation conditions in the source as well as by the nozzle geometry and diameter D. On the course of the expansion, the gas travels along a specific isentrope and is passing through a range of states in the phase diagram [91]. The traveled distance before reaching the quitting surface is determined by the number of occurring collisions, i.e. by the collisional cross section[4] and the nozzle expansion parameters [58]. This means that variations of the source conditions according to the thermodynamic isentropic law $P_0 T_0^{\kappa/(1-\kappa)}$ do not change the thermodynamic quantities like gas temperature, T, or number density, n, for a given state of supersaturation [82].

For isentropic nozzle expansions of rare gases it is known that applying high gas pressures P_0 and low source temperatures T_0 favours the occurrence of condensation processes. High initial pressures and low temperatures lead to both larger cluster sizes and higher mass fluxes because the gas saturation line $P_V(T)$ is crossed at higher gas densities [82]. The nozzle geometry is decisive for the dynamics of the expansion and determines the flow field gradients as present before or during passage of the sonic point. Smaller nozzles are known to make faster expansions, due to a faster change in the flow field gradients, for example in the temperature gradient dT [82]. This has an influence on the velocity with which the expansion is passing through different states on the isentrope, meaning that in faster expansions it takes shorter transit times dt for the expanded gas volume to pass through a certain temperature interval $[T, dT]$ [82]. In other words, the slower the expansion the longer the transit time dt for which the gas remains in a specific state n, T on the isentrope [82]. It includes that slow expansions lead to the formation of larger droplets since –according to the standard condensation theory– more condensation nuclei of a particular state n, T, P can be formed and more mass is added to already existing cluster cores [82]. A possible scaling law for beams of clusters of the same size

---

[4]For helium, the quantum mechanical collisional cross section should be considered which is larger than the classical one, due to the large quantum effects present in helium [2].

for fixed T_0 is derived for rare gas clusters (except helium) as $P_0 D^q$=constant with $q > 0$ [82]. In order to obtain equal cluster sizes, it is thus required to compensate a smaller nozzle orifice diameter D by an increase in pressure P_0.

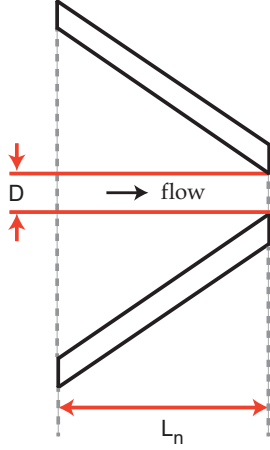The geometry and diameter D of the nozzle have an influence on the beam velocity. An isentropic expansion can be described by the thermodynamic variables of an ideal gas as a function of the source parameters [82]. To describe the influence of the expansion parameters on the cluster formation processes of rare gases, expressions are derived on the basis of the equation of state (1.3) and the thermodynamic isentropic laws (eq. (1.4)) for a given ratio of specific heats κ. This treatment, however, is restricted to processes that occur in a zone within a distance dx downstream from the nozzle where the fraction of condensed gas is still negligibly small [82]. Depending on the nozzle and the initial source temperature applied, the beam temperature is decreased by a magnitude dT along a certain distance dx traveled [82]. The transit time dt it takes a given expansion to achieve a temperature change in an interval $[T, dT]$ can be determined from the flow velocity $v_x = x/dt$ as given in eq. (1.5) and is linearly proportional to the nozzle orifice diameter D and to the respective temperature change dT. In ref. [82], expressions for the transit time and the temperature change in pulsed expansions of rare gases (except helium) are derived for different nozzle geometries. After transition of the quitting surface, further cooling of the formed clusters is achieved *via* evaporative cooling. The cluster temperature finally reached depends on the interatomic forces and the depth of the interaction potential of the specific gas [57]. The weaker the binding energies between the constituent atoms in a cluster, the lower the final cluster temperature T_∞ [57]. Therefore, He clusters with the weakest interaction forces have the lowest temperatures among the rare gas clusters. Cluster cooling mechanisms and temperatures are further discussed in Ch. 2.5.1.

Figure 1.10: Illustration of a sonic nozzle with opening diameter D and length L_n.

Clustering occurs only after passage of the nozzle throat (the sonic point) which results in an aligning of the velocities of all particles contained in the expanded gas volume into one direction. During passage through the sonic point, slow particles are pushed by faster ones and fast particles are slowed down by slower ones leading to a unified particle velocity[5] in the ensemble. However, in a cluster beam a large variety of particles of different masses can be present leading to a variety of Maxwell distributions. However, in a related study [92] it was found that the particle velocity in a condensed beam is a function of cluster size N_{He} and decreases for increasing cluster sizes (a decrease of $\approx 5\%$ of the longitudinal velocity v_x is measured for an increase in cluster size by one order of magnitude).

Furthermore, the anisotropic velocity distribution can lead to an inhomogeneous distribution of differently sized particles in a cluster beam. Then, heavier clusters would

---

[5] A non-equilibrium phenomenon commonly called "velocity slippage" describes the observation that in an expansion of a gas mixture (for example in seeded beams), the particle velocities are not necessarily uniform due to different orientations of the molecules relative to the flow direction. This depends on the molecular angular momentum [1, 2].

be concentrated closer to the beam centerline whereas lighter particles can be located further towards the outer parts of the beam, because they have larger perpendicular velocity components (with respect to the beam direction) than the heavy particles [2].

1.3.5 Pulsed nozzle expansions

Pulsed nozzle beams can be realized by using electromechanical valves. Their operation mode is characterized by a repetition rate f, a pulse duration t_{pulse} (of an ideal rectangular pulse), and an interruption interval Δt which is the time interval between the starting times of two successive pulses and is typically long compared to the pulse length t_{pulse}. These parameters result in the definition of the duty cycle D_c:

$$D_c = \frac{t_{pulse}}{\Delta t} = f \cdot t_{pulse} \quad . \tag{1.13}$$

Since the dominating difference between the flow properties of a continuous and a pulsed nozzle expansion is given by the duty cycle, it is possible to obtain the flow properties of a pulsed expansion by multiplying the respective quantities such as mass flow rates and beam intensities as derived for continuous expansions with D_c. Whereas for continuous nozzle beams, the background pressure P in the vacuum chamber is practically given by the applied expansion pressure P_0 and the pumping speed Z_p of the evacuating pumps, it is a function of time $P = P(t)$ in case of pulsed expansions. When the valve opens at a specific (initial) time t_0, the pressure in the vacuum chamber increases to a peak value P_i which is determined by the source pressure P_0, the nozzle
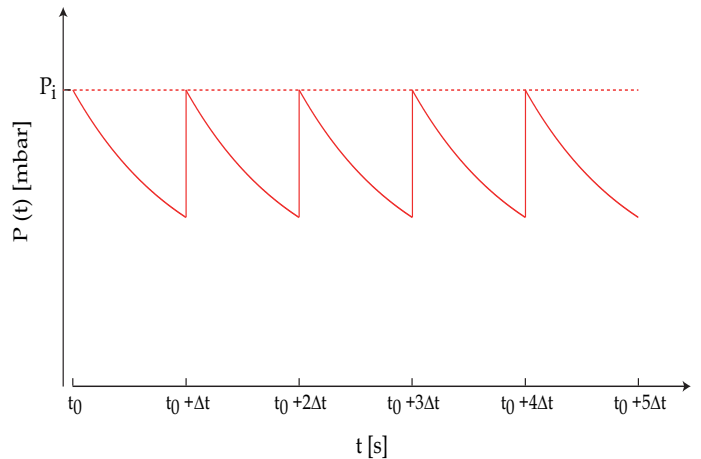

Figure 1.11: Time-dependent background pressure caused by pulsed nozzle expansions. When the valve opens, the pressure increases to a peak value P_i and decreases exponentially until the valve opens the next time after a period Δt.

conductance C_n[6], the valve opening time t_{pulse}, and the chamber volume V. This is all expressed by a factor B. The background pressure $P(t)$ is assumed to decay exponentially with time (see fig. 1.11). The characteristic decay time $\tau = V/Z_p$ depends on the chamber volume V and the pumping speed Z_p. Then, at a given instant t after the last pulse, the momentary background pressure $P = P(t)$ is determined by the superposition of the background pressure caused by the actual valve opening and the pressures that have been caused by the preceding pulses. This can be described as:

---

[6]C_n is the conductance of the nozzle. In the viscous flow region –as is present in molecular beam expansions– the conductance can be determined by $C = 32600 \cdot 10^{-4}(P_0 D^4)/(\eta L_n)$
with D the nozzle orifice diameter [cm], η the viscosity of the medium (with $[\eta]=\mu$P, 1 Poise=1 P = 0.1 Pa $\cdot s$), L_n the length of the nozzle [cm], P_0 the expansion pressure [torr] [93].

$$
\begin{aligned}
P(t) &= B\Big(\exp(-t/\tau) + \exp(-(t+\Delta t)/\tau) + \exp(-(t+2\Delta t)/\tau) + ... \Big) \\
&= \sum_{n=0}^{\infty} P_n(t) = B\exp(-t/\tau) \sum_{n=0}^{\infty} \Big[\exp(-\Delta t/\tau) \Big]^n \\
&= B \cdot \frac{\exp(-t/\tau)}{1 - \exp(-\Delta t/\tau)} = B \cdot \frac{\exp(\Delta t - t/\tau)}{\exp(\Delta t/\tau) - 1} \quad ,
\end{aligned}
\tag{1.14}
$$

with $B = (P_0\,C_n\,t_{pulse})/V = (P_0\,C_n\,D_c)/(Z_p\,\Delta t)$.

In pulsed nozzle expansions, the resulting longitudinal velocity spread Δv_x is given by a convolution of the inherent thermal velocity distribution and a velocity spread that is caused by imperfections of the valve opening. In reality, the opening of a pulsed valve deviates from an ideal rectangular behavior due to the finite times it takes the moving parts to open and close the valve [2]. During the opening and closing phases of the valve the expansion is hindered by the valve plug and quasi-steady flow is reached only with delay which causes the occurrence of pressure gradients in the expanding gas and results in a distribution of particle velocities.

1.4   Summary

In this Chapter, a motivation for setting up an experiment which allows for studying large isolated biomolecules at cryogenic temperatures is given. The He droplet technique is introduced as a very well adequate technique for cooling the investigated molecules to sub-Kelvin temperatures. Superfluid ^{4}He droplets which serve as matrices for embedded dopant particles are produced in isentropic nozzle beam expansions.

Chapter 2

Ionic species in liquid helium droplets

Studying charged species embedded in liquid He droplets is important as it can allow for probing different aspects of superfluidity in finite systems (for example achieving an experimental verification of the critical Landau velocity [94–96]), for gaining insight into the microscopic interaction between an ionic impurity and the He environment, as well as for observing the intrinsic properties of the ion in an ultracold environment.

In this chapter, the interaction of ions with a liquid helium environment is considered. First, the generation of charged bare He clusters and their fragmentation dynamics after electron impact or optical ionization are introduced in Ch. 2.1. This helps to explain the features observed in the mass spectra of He cluster fragment ions after electron-impact ionization, which are presented in Ch. 4.1.

In Ch. 2.2, the principle of the pickup of ions from an ion trap is described and compared to the pickup of neutral particles from a gas cell. The pickup process itself is examined which is accompanied by an energy release through the dissipative He environment.

After this, the interaction between an ion and its environment when it is immersed in liquid helium is considered. The ion-He interaction potential and the solvation structure of a positive ion are introduced in Ch. 2.3. The energy of solvation of a large multiply charged ion, representing a protonated protein, is determined by a macroscopic approach in Ch. 2.3.3.

Then, in Ch. 2.4 the binding strength of the ion-droplet interaction is considered and the magnitude of the electric force required to pull an ion out of a droplet by an electrostatic field of strength $\left|\vec{E}\right|$ is calculated. Finally, in Ch. 2.5 the change in droplet temperature due to the heat transfer from an embedded dopant particle to the droplet is treated. The subsequent thermal evaporative cooling mechanism and a statistical model of a He droplet as a microcanonical ensemble are introduced.

2.1 Generation of charged He droplets by electron impact or photoionization

In most experiments on charged droplets, ionization occurs *via* electron impact or photoionization [97]. The fragmentation dynamics of ionized doped or bare He clusters is studied to obtain a better understanding of the mechanisms that are responsible for

energy dissipation inside a He droplet and of cooling processes [97–99]. In general, the introduction of a (positive) charge in a He cluster can be a large perturbation [98]. Whereas the neutral He–He interaction has a binding energy of ≈ 5 cm^{-1} (cf. fig. 1.4), the He–He$^+$ ion is bound by $20\,000$ cm^{-1} [100]. For comparison, the binding energy of the He–Na$^+$ interaction is determined to be ≈ 35 meV [101] and the binding energy of the He–Cl$^-$ cluster to be ≈ 14 meV [101]. Many dynamical processes initiated by cluster ionization are observed to be influenced by the cluster sizes [97], for example cooling mechanisms [99, 102] and charge migration. Microscopically, charge migration is described as a dynamical hole-hopping process (see below). Time scales of the steps involved in a dynamical process are also observed to depend on the cluster size, for example the hopping frequency of a charge is determined to be higher in larger clusters [97, 103]. Halberstadt and Janda [97] calculated the hopping frequency to range from 28 ps^{-1} for a 20-atom He cluster to 54 ps^{-1} for a 200-atom cluster. The mean hopping distance, however, is determined to be 3.1 Å, independent of the cluster size [97]. Scheidemann *et al.* [103] estimated the time scale for resonant charge hopping to be 10^{-14} s and for charge localization to be 10^{-12} s. Furthermore, they give an estimation for the possible hopping distance of ≈ 500 Å during the random walk before the charge becomes localized. The cluster size has thus an influence on the ionization probability of a dopant species [97].

2.1.1 Fragmentation dynamics of ionized He$_N$ clusters

The ionization of a cluster leading to cluster fragmentation is a dynamical process that involves several elementary steps [97, 98, 103–106]. (1) At first, a random single He atom is ionized by the incoming electron. Usually, the initial ionization occurs at a He atomic site close to the cluster surface and probably not in direct contact to a dopant species [107]. Ionization means the sudden removal of an electron from an individual He atom, equivalent to the introduction of a positively-charged electron hole which immediately (within 10–100 fs) delocalizes over several atoms or atom pairs. (2) That is followed by a series of rapid charge hops between adjacent He atoms, equivalent to a diffusion of the hole in the helium bath. (3) The resonant hole migration is terminated when the charge becomes localized on either a dopant molecule or by self-trapping on a positive He$_2^+$ core [103], forming a He$_N^+$ ion in a solvation shell. In both cases, a considerable amount of energy is released to the droplet, leading to extensive evaporation [18]. (4) If more than one dopant molecule is deposited into the cluster, the attractive forces between them cause a fast coagulation (≈ 1 ns) of the dopant molecules in the cluster center. These sub-clusters usually survive ionization processes as intact entities [104].

The dynamics of the coupled electronic and nuclear coordinates of doped and non-doped He$_N^+$ clusters are studied by a combination of classical and quantum mechanical methods which include both the large zero-point energy of He atoms and –in the case of doped clusters– all the non-adiabatic couplings between the potential energy surfaces (*PES*) of the ionized dopant [98, 99]. Methods employed are the mean-field approach, which works especially well for large clusters, and surface hopping dynamics which includes together hole hopping, hole localization and the self-trapped hole which is commonly called the *snowball* solvation structure (see Ch. 2.3.1), and subsequent cluster fragmentation [97–99].

2.1.2 Mass spectra of He cluster fragment ions

Recording mass spectra of cluster fragment ions after electron impact or photoionization results in spectra which usually exhibit peaks of bare He ions at m/q ratios which are multiples of 4 amu and, in the case of doped clusters, mass peaks of the dopant species, of dopant fragment ions, or possibly complexes of the dopant species. Some He_N^+ fragment ions often appear at significantly higher abundances in the mass spectra than others; the origins of these are briefly explained in the following. Apart from these aspects, the intensities of mass peaks from larger cluster fragments are observed to decrease gradually but have significant abundances up to He_{50}^+ [98]. In general, the required energy of an electron to ionize a He cluster and not to remain attached to it needs to be high enough to be able to excite the electron to the conduction band of liquid helium [84]. Thus, the minimal energy required is the sum of the atomic ionization energy (24.6 eV) and the energy gap to the conduction band (1.1 eV) minus the energy of polarization of the surrounding He atoms (≈ 0.15 eV), resulting in a required ionization energy of $E_{ion} \geq 25.6$ eV [84].

Mass spectra of (small) He clusters containing 10^3–10^4 He atoms show the He dimer ion He_2^+ as the most stable fragment ion [108]. This is attributed to the ejection of He_2^+ ions from the cluster before full vibrational relaxation of the cluster is completed (see below). The formation of the He dimer ion can occur *via* different mechanisms [84, 99]. When it derives from small clusters, it results from a direct cluster ionization followed by snowball formation around the He_N^+ molecular ion under ejection of both electrons. The binding energy is released to the thermal modes of the cluster which then thermalizes *via* evaporative cooling.

From larger clusters, however, the He_2^+ ion is predicted to result from a two-step ionization process [84]. At first, an exciton is formed by an impinging electron with sufficient energy (≥ 21 eV); it is then trapped in a *bubble* solvation structure on the cluster surface. When the excited He* atom captures a second He atom from the cluster, the vibrationally excited molecular state $a^3\Sigma_u^+$ (He_2^*) is formed. This can easily be ejected from the cluster due to its translational energy. Outside of the cluster, it can either be ionized by a second electron or *via* surface or field ionization in the vicinity of a hot surface or by a strong electric field [84]. One known feature observed in the mass spectra of clusters formed in nozzle beam expansions is the occurrence of so-called *magic* clusters of sizes N_{He} showing especially high signal intensities due to a particular cluster stability [109]. The strong binding occurring in the magic clusters is caused by the strong quantum effects present in helium [83]. For He clusters, magic numbers for cluster sizes $N_{He} = 3, 7, 10, 14, 30$ are observed for small He clusters in the size range of $He_{N=2-100}$ [109].

2.1.3 Resonant hole hopping

The motion of the charge *via* resonant hole hopping is driven mostly by electrostatic polarization forces, where the hole experiences a polarization bias to migrate to the cluster center [98, 110]. The driving force for charge migration in the cluster is further regarded in the semi-classical model developed by Lehmann and introduced later in Ch. 2.3.5. Microscopically, hole hopping can be understood in terms of sequential hops from one atom pair where the hole is localized for a short time followed by rapid delocalization over at most three atoms at a time, and a hop to the next atom pair. This occurs on time scales of 10–200 fs [98]. The direction of the single hops is dictated by contractions

of interatomic distances due to polarization forces and small fluctuations in the cluster symmetry are decisive for the direction of charge migration. The He_3^+ ion involved in a single charge hopping step is found not to be a linear symmetric triatomic ion (as predicted by *ab initio* calculations [98]), but rather a linear ion with the charge localized on two atoms and a weakly bound third atom, He_2^+–He.

Resonant hole hopping can be either adiabatic as a charge migration along an excited electronic surface, or non-adiabatic as a charge hop to lower energy surfaces. Both adiabatic and non-adiabatic hole hopping cause a conversion of vibrational energy into kinetic translational energy, as known in bulk liquid helium [98]:

$$He_2^+(\nu) + He \qquad \Rightarrow \qquad He(T) + He_2^+(T', \nu' < \nu) \quad ,$$

with ν the vibrational quantum number of the diatomic pair at which the charge has been localized before the hop and T, T' the translational kinetic energies released. The kinetic energy T carried by the monatomic part of the product leads to the ejection of fast neutral atoms, while the energy T' of the charged diatomic unit can lead to the ejection of He_2^+ from the cluster [98]. The energy release due to ν–T transfer leads to vibrational relaxation of the cluster and serves to evaporate most or all He atoms from the remaining ion core [104]. Energy loss during the random walk precludes a reversal of the process. Once a non-adiabatic charge transfer to the lowest electronic surface occurs, hole localization and self-trapping is initiated [98].

In large clusters, both adiabatic charge migration and non-adiabatic hops to lower *PES* can occur. The ν–T transfer accompanying the charge migration is supposed to lead to full vibrational relaxation of the clusters as long as no hole self-trapping followed by ejection of a charged unit occurs. In particular for large clusters, it is established that a complete vibrational relaxation down to the stable He_3^+ fragment –bare or (partially) solvated by neutrals– as positive ion core takes place [98]. In smaller clusters, however, the ejection of He_2^+ ions might occur before the vibrational relaxation is completed [98]. Once charge localization begins, only a few more hole hops can take place until the vibrational ground state $\nu=0$ is reached within ≈ 5 ps [97]. There are two main competitive charge localization processes. The random walk of the electron hole can be terminated by the formation of the dimer ion He_2^+, or it continues until it reaches the foreign species and ends by formation of the dopant ion. The ionization of the dopant species takes place when the charge hops into the vicinity of the impurity species and charge transfer occurs before the He dimer ion He_2^+ has been formed and ejected. This competition determines whether a dopant ion will be observed in a fragment mass spectrum where it usually becomes the most intense peak [104, 105].

2.2   Doping He droplets *via* ion pickup

In most of the pickup experiments of foreign particles by liquid He droplets, use is made of the special ability of He droplets to incorporate any molecular species following mechanical collisions with a very high probability [15]. In the top panel of fig. 2.1, a scheme of a typical experimental apparatus for the pickup of neutral gas-phase particles is shown. A (skimmed) beam of He droplets, formed in an isentropic nozzle beam expansion, passes through a gas cell and collects every particle it collides with. In the approximation of a
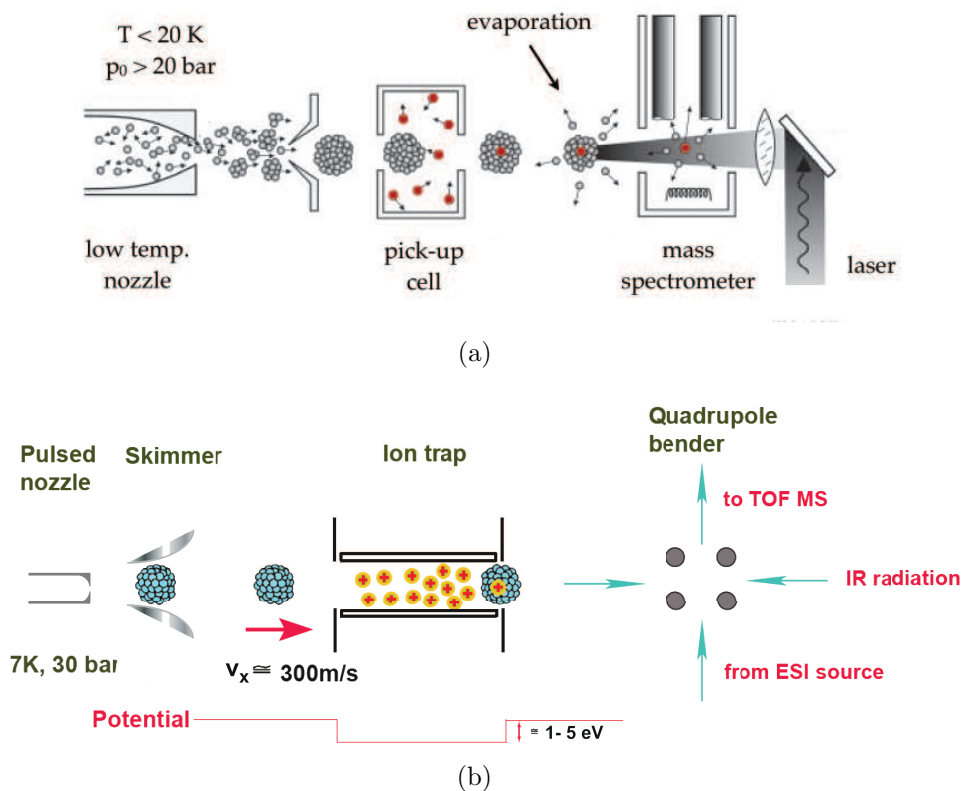
(a)

(b)

Figure 2.1: (Top panel) Standard setup for pickup experiments of neutral molecules from a gas cell by liquid He droplets (figure taken from ref. [111]). (Bottom panel) Illustration of the experimental setup for ion pickup by He droplets: Mass–to–charge selected (biomolecular) ions are accumulated and stored in a linear ion trap. In the longitudinal direction, trapping is achieved by low electrostatic potentials of a few eV at the two trap electrodes (*endcaps*). When an ion is picked up and trapped inside a He droplet, it can exit the trap due to the high kinetic energy of the droplet, which exceeds the trapping potential. The ion-doped droplets can then be further interrogated.

constant pickup cross section, the probability for picking up of k particles follows a Poisson distribution [15]. Gas-phase particles are usually produced by thermal evaporation of the species of interest in the pickup cell. A picked-up particle quickly transfers all its internal energy and the center-of-mass collision energy to the droplet *via* coupling to the elementary cluster modes. In this way, the particle is cooled down to the droplet temperature of ≈ 0.37 K (see Ch. 2.5.1). After exiting the scattering region, doped droplets can be interrogated further by applying the respective experimental method of choice, for example laser spectroscopy. Investigation of ions in He droplets is often performed by ionization of neutral particles when they are already incorporated in the He droplets. An alternative approach for studying ions in He droplets is the doping of droplets directly with ions. The experimental implementation for the ion pickup by He droplets is conceptually similar to the pickup technique for neutral particles. This can be seen by comparing the top and bottom panels of fig. 2.1. In both, there is a pre-cooled solenoid valve, a skimmer to cut out the central part of the beam, and a pickup cell which is a (linear) ion trap in the case of charged particles. In an ion trap, particles are radially confined by a radiofrequency field and longitudinally by DC stopping electrodes at each end. A crucial difference to the pickup experiments of neutral particles from a gas cell is

the explicit use that is made of the high kinetic energy of the He droplets. Although the droplets move slowly ($\approx$ 200–300 ms^{-1}), their mass can be large and thus their kinetic energy also that is given by:

$$E_{kin} = \frac{1}{2} N_{He} m_{He} v_x^2 \approx \frac{1}{2} N_{He} \cdot 1.8 \, \text{meV} \quad , \tag{2.1}$$

where 1.8 meV is the kinetic energy of a single He atom which moves with a velocity of $v_x = 300$ m s^{-1}. When a droplet picks up an ion, the kinetic energy of the doped droplet will exceed the longitudinal trapping potential energy and, once they are inside a He droplet, the ions can leave the trap. In fig. 2.2, a pictorial representation of two different dopant species (an amino acid and a protein) embedded in He droplets of three different sizes ($N_{He} = 10^4$, 10^6, and 10^{12}) is shown (to scale), illustrating the occupied volume of the droplet interior by the embedded molecule. Considering the van der Waals radius of a He atom to be 140 pm [112], the approximate number of He layers that surround the respective dopant species in the droplet center is indicated. For Phe$^+$ ions[1], the number of He atom shells around the ion is 34 for $N_{He} = 10^4$, 158 for $N_{He} = 10^6$, and 15857 for $N_{He} = 10^{12}$. For CytC^{+Z} ions, the number of He atom shells is 22, 146 and 15845, respectively.
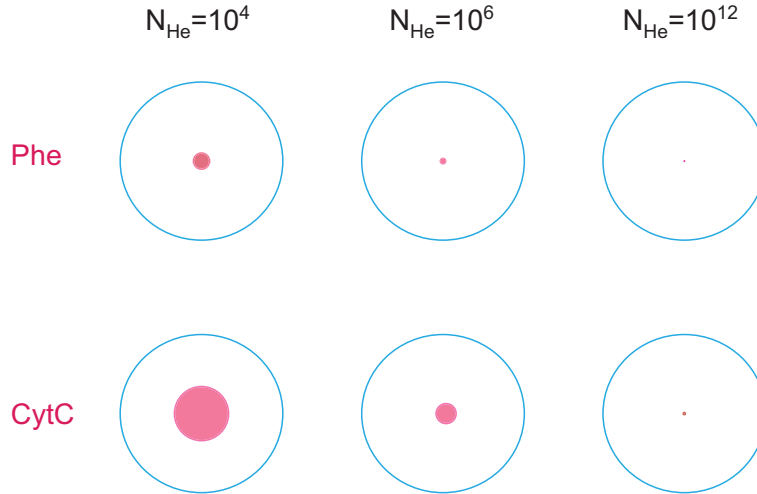
Figure 2.2: Molecular ions Phe$^+$ (top) and CytC^{+Z} (bottom) in (He)$_N$ clusters for $N_{He} = 10^4$, 10^6, 10^{12}. In the case of Phe$^+$, the approximate number of He atom shells around the ion is 34 for $N_{He} = 10^4$, 158 for $N_{He} = 10^6$, and 15857 for $N_{He} = 10^{12}$. For CytC^{+Z} ions embedded in He droplets, the number of He atom shells is 22, 146 and 15845, respectively.

2.2.1 Expected ion-doped He droplet signal

To obtain an estimate for the expected signal intensity $I(L)$ of ion-doped He droplets for a given pulsed nozzle expansion after passing a scattering chamber, the Lambert-Beer law is used. Usually, it is employed for determining the intensity of the fraction of the transmitted light of a given initial beam intensity after passing through an absorbing medium. Here, the same exponential law is used to determine the growth of the intensity of the fraction of doped ("scattered") droplets $I(L)$ from an initial intensity I_0 of droplets

---

[1]Protonated species, cf. Ch. 3.3.

which pass through a scattering cell of length L. The intensity $I(L)$ depends on the particle number density n of ions in the trap, on the collisional cross section σ with a stored ion, and the length L of the trap. However, doped droplets are produced against zero background, as non-doped droplets are not detected. The signal for droplets that pick up one ion can be obtained from:

$$I(L) = I_0 \left[1 - \exp(-\sigma \cdot n \cdot L) \right] \quad . \tag{2.2}$$

Thus for $\sigma \cdot L \cdot n \ll 1$, eq. (2.2) reduces to

$$I(L) \approx \sigma \, n \, L \cdot I_0 \quad . \tag{2.3}$$

When $\sigma \cdot L \cdot n$ approaches the value 1, however, the probability for multiple pickup increases (see Ch. 2.2.3) and the above expression for single pickup is no longer valid. To determine the number of doped droplets per pulse for pulsed nozzle expansions, the intensity of doped droplets $I(L)$ as given in eq. (2.2) must be multiplied by the duty cycle D_c (see eq. (1.13)). From an initially emitted intensity of droplets of a nozzle beam source I_{tot}, which is given in units of inverse solid angle and inverse second, meaning that –in a spherical expansion– droplets are emitted in all directions, only the fraction of the droplets close to the beam axis will finally traverse the trap after passage of the skimmer and the trap openings.

Before the signal intensity $I(L)$ of ion-doped He droplets can be calculated, the initial beam intensity I_0 needs to be specified more accurately. Passing a skimmer leads to cutting out of the central portion of the beam, which is then the only part of the beam that potentially enters the trap. Since only droplets being emitted close to the beam axis will potentially enter the scattering region, it is sufficient to restrict ourselves from the intensity I_{tot} of droplets as emitted from the source to only the beam intensity in the forward direction, I_0 [1, 2].
The solid angle that is subtended by the droplet beam at the trap exit after a distance s_x from the nozzle of orifice diameter D is given by:

$$\Omega = \frac{A_{cal}}{s_x^2} = \frac{\pi \left(\frac{D}{2} \right)^2}{s_x^2} \quad ,$$

with $A_{cal} = \pi (D/2)^2 = 3.8 \cdot 10^{-3}$ cm^2 the segment area of a sphere with radius s_x, corresponding to the solid angle Ω. This finally leads to an expression for the "scattered" signal intensity as (see eq. (1.12)):

$$I(L) = I_0 \cdot \left[1 - \exp(-\sigma \cdot L \cdot n) \right] = \frac{\gamma}{\pi} \cdot I_{tot} \cdot D_c \cdot \Omega \cdot \left[1 - \exp(-\sigma \cdot L \cdot n) \right] \quad , \tag{2.4}$$

where D_c is the duty cycle of the pulsed expansion. Eq. (2.4) can be used to determine the number of ion-doped droplets obtained for a given nozzle operating at a duty cycle D_c and emitting clusters at a total intensity I_{tot}, which travel through an ion trap of length L where particles of a number density n are stored.

As an example, $I(L)$ is calculated here for typical parameters and values, assuming that only one ion per droplet is picked up. The solid angle Ω subtended by the cluster beam at the exit of the scattering chamber, i.e. at a distance of ≈ 55 cm from the nozzle (in case of the long trap, see Ch. 3.1.3), is determined to $\Omega = 1.3 \cdot 10^{-6}\, sr$. Together with a typical beam intensity of $I_{tot} = 10^{16}$ droplets $sr^{-1}s^{-1}$ as reported in the literature for a similar nozzle [15, 113] and a duty cycle of $D_c = 1.25 \cdot 10^{-3}$ given by a repetition rate of 5 Hz and a typical pulse opening time $t_{pulse} = 250\, \mu s$, a beam intensity in the forward direction of $I_0 \approx 1 \cdot 10^7$ droplets per pulse is calculated. Now, the signal intensity $I(L)$ of ion-doped He droplets can be determined. Droplets composed of $N_{He} = 10^5$ He atoms with a radius of 10.3 nm have a collisional cross section of $\sigma = \pi\, R_d^2 = 3.3 \cdot 10^{-12}$ cm^2; they traverse the ion trap of length $L = 30$ cm, filled with ions at a particle density presumed to be at the space charge limit, $n = 10^6$ cm^{-3}. This yields a scattered intensity of $I(L) \approx 1 \cdot 10^5$ ion-doped droplets per pulse.

Such intensities should be sufficient to investigate the dopant ions *via* action spectroscopy (in which the wavelength-dependent response of the chromophore upon light exposure is monitored), for which only few ions per pulse are needed [114].

2.2.2 Energy release

In the pickup process, one of the colliding partners (the ion) transfers its entire energy to the collision partner (the droplet). The transferred energy in the pickup process is the sum of the kinetic energy E_{kin} in the center–of–mass frame and the internal energy Q of the ion [104]. The pickup process represents a so-called "capture reaction" as a total inelastic collision. After the collision, both particles move as one unit in a center–of–mass system. That includes the fact that an elastic collision can in principle not lead to particle pickup.

The kinetic energy in the center-of-mass system is given by

$$E_{kin} \;=\; \frac{1}{2}\mu v_{\mathrm{rel}}^2 \quad , \text{with} \tag{2.5}$$

$$\mu \;=\; \frac{m_d m_{ion}}{m_d + m_{ion}} \quad \text{the reduced mass and} \tag{2.6}$$

$$v_{\mathrm{rel}} \;=\; v_{ion} - v_x \quad \text{the relative velocity} \tag{2.7}$$

of the collision partners with v_{ion} the (average) thermal velocity of the ion and v_x the longitudinal droplet beam velocity of typically 300–400 ms^{-1} [113] which is usually dominant. Especially in the case of large proteins, the thermal velocity is small with $v_{ion} \approx 20$–30 ms^{-1} and can be neglected compared to v_x. In the system of a He droplet colliding with a molecular ion, it can be assumed that the droplet mass is much larger than the ion mass ($m_d \gg m_{ion}$) and therefore, the reduced mass is mainly determined by the smaller mass $\mu \approx m_{ion}$. Therefore, the center–of–mass collision energy deposited in a droplet in case of large droplets and light ions is approximately given by $\frac{1}{2}m_{ion}v_x^2$.

The internal degrees of freedom of molecular rotations and vibrations make contributions to the internal energy. A (non-linear) molecule containing N atoms ($N \geq 3$) has

$F = 3N - 6$ degrees of freedom, from which about one third to one half of them are populated at room temperature [115]. Only low-energy modes (for example bending modes) are excited at room temperature, but not high-frequency modes such as X–H stretching modes. In the literature, values for the heat capacity are given for L–phenylalanine in water, as ≈ 2364 J/(kg·K) [116, 117], and for cytochrome c, as ≈ 2080 J/(kg·K).

The absorption of energy by a He droplet leads to the release of a certain amount of energy *via* evaporating He atoms from the droplet surface that can be estimated from a rule of thumb of ≈ 1600 ^{4}He atoms per 1 eV of heat released [15] when it is considered that every He atom evaporated carries away its binding energy to the droplet of ≈ 7.2 K. Here, the energy release caused by the collision and internal energy transfer is determined for three classes of foreign biomolecular species, considering a medium-sized He droplet of $N_{He} = 10^6$ He atoms moving with a beam velocity $v_x = 350$ ms^{-1}: a single amino acid, a smaller peptide containing ≈ 10 amino acids (≈ 100 atoms) and a real protein composed of ≈ 1000 atoms. For each dopant type, the resulting number of evaporated-off He atoms required in order to dissipate the kinetic and potential energy as well as the solvation energy of the ion in the He bath as obtained from the rule of thumb is given in table 2.1.

Table 2.1: For three different types of dopant molecules composed of the number of atoms indicated, the energy released in the pickup process is calculated. It is given by the sum of the kinetic energy E_{kin} of the center-of-mass system (eq. (2.7)) and the heat Q that is stored in the molecule. The resulting number $N_{He,ev}$ of evaporated He atoms is derived using the rule of thumb which states that ≈ 1600 He atoms are evaporated per eV of absorbed energy [15], given by the sum of $E_{kin} + Q$. The rule of thumb corresponds to the release of ≈ 7.2 K per He atom evaporated.

Species	# atoms	E_{kin} [eV]	Q [eV]	$N_{He,ev}$
amino acid	15	$95 \cdot 10^{-3}$	0.33	680
peptide	100	$630 \cdot 10^{-3}$	3	5800
protein	1000	7.6	30	60 000

2.2.3 Particle pickup

The mean number of ions being picked up by a He droplet of radius R_d that traverses a scattering cell of length L filled with particles of radii R_{ion} is calculated. The pickup probability $P(n, \sigma)$ for particles by a single droplet is determined by the geometric dimensions of the colliding particles, thus the collisional cross section of the colliding particles $\sigma = \pi (R_d + R_{ion})^2$, and the number density n in the scattering chamber, it follows a Poisson distribution [15]. Especially in the case of large droplets, the collisional cross section is dominated by the droplet radius, $\sigma \approx \pi R_d^2$. In fig. 2.3, an illustration of a He droplet with diameter $2R_d$ is shown which picks up all ions located within its geometrical capture cross section σ, illustrated by a "tube" in dotted lines. The mean number $\bar{N}_q$ of particles that are picked up with a probability $P(n, \sigma)$ is calculated as:

$$\bar{N}_q = \sigma \cdot L \cdot n \approx \pi R_d^2 \cdot L \cdot n = \pi \left(2.22 \cdot N_{He}^{1/3} \right)^2 \cdot L \cdot n \quad , \tag{2.8}$$

with L the length of the scattering chamber. An upper limit for the particle density n
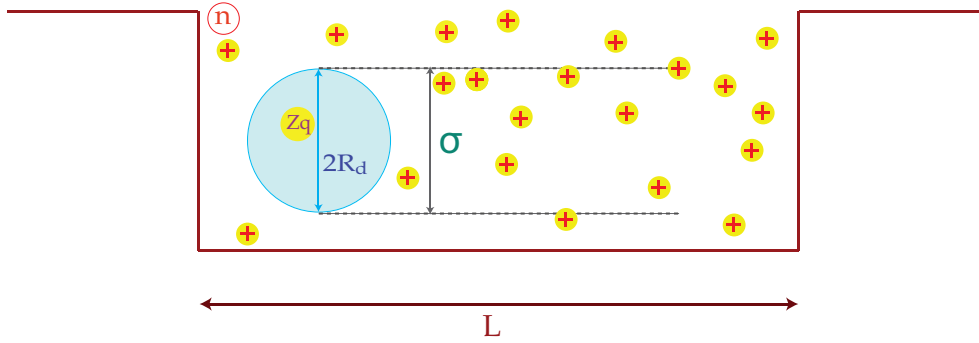
Figure 2.3: Scheme of the pickup of multiple ions by one (spherical) He cluster passing through a scattering cell filled with positive ions at a number density n ($\approx$ space charge limit). All ions that collide physically with a He droplet of diameter $2R_d$ and collisional cross section σ which corresponds to the "tube" in dotted lines are incorporated in the droplet and contribute to the charge Zq that is then carried by the droplet.
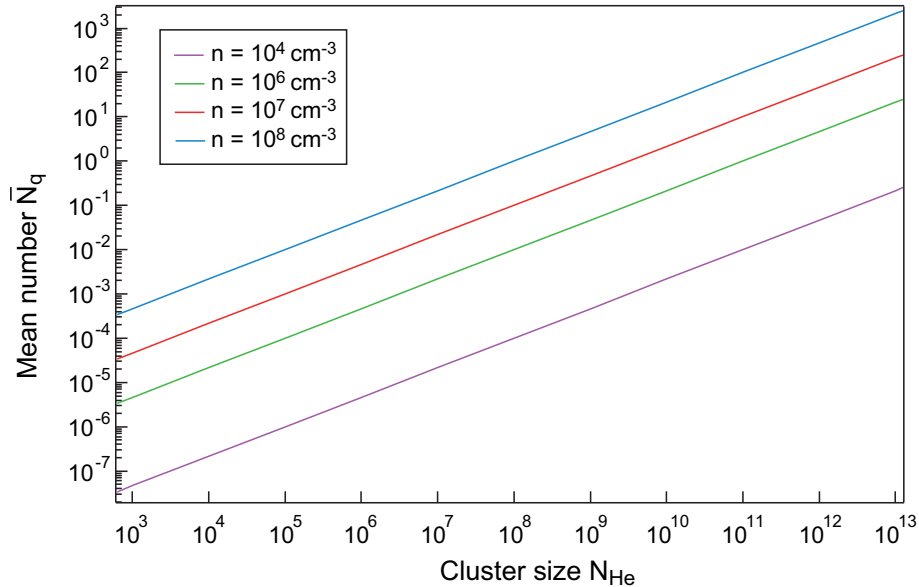

Figure 2.4: The mean number $\bar{N}_q$ of particles that are picked up by a He droplet, as given by eq. (2.8) is shown as a function of cluster size N_{He} and thus of the collisional cross section σ. The He droplets traverse a gas cell of length $L = 30$ cm filled with particles at a number density n. $\bar{N}_q$ is displayed for four different particle densities n regarded.

in the trap is given by the space charge limit. The mean numbers $\bar{N}_q$ of (subsequently) picked up particles by a single He droplet of size N_{He} from a trap of length L containing elementary charges q stored at a particle density n are determined using eq. (2.8) and shown in fig. 2.4.

2.2.4   Pickup of multiple ions by one droplet

The question arises as to whether a He droplet that has picked up an ion from the trap can possibly pick up more ions *via* (mechanical) collisions in the scattering chamber. In principle, three requirements have to be met. The first is whether a collision between a charged droplet and a charged particle occurs or if the ion is already repelled from

the loaded droplet at large distances due to Coulomb repulsion. The second question is whether a droplet of a size N_{He} can carry more than one ion on its surface or in the interior, or if a total charge $Q_S = \bar{N}_q \cdot Z \cdot q$ will instead lead to a fragmentation of the cluster as a consequence of Coulomb repulsion. If these two prerequisites are fulfilled, the question remains as to whether the particle density in the trap is sufficiently high to allow multiple collisions between droplets and ions. The change in the geometrical cross section of the droplets after particle pickup due to He atom evaporation is neglected here.

A doped He droplet, carrying the charge Zq, can be treated as a charged sphere with an electrostatic potential E_{pot}. In the (semi)classical problem of Rutherford scattering, it is possible to predict the scattering angle and the path of a scattered (point) particle [118]. Rutherford scattering is now invoked to treat the Coulomb repulsion of an ion-doped He droplet and other ions in the trap [119] in an effective one-body problem. Only the relative motion of the two particles is regarded; they interact through a central force, while all external forces are neglected. The center of mass of the two-body system is presumed to move uniformly and its total energy E is obtained by

$$E = \frac{1}{2}\mu v_{\text{rel}}^2 + \frac{L_J^2}{2\mu r^2} + \frac{\zeta}{r} \quad , \tag{2.9}$$

with r the radial distance between the ions,

$$
\begin{aligned}
L_J &= \mu\, v\, b \quad \text{the angular momentum and} \\
b &= \frac{L_J}{2\,\mu\,\sqrt{E}} \quad \text{the impact parameter} \quad .
\end{aligned}
$$

The expression ζ is given by

$$\zeta = \frac{Z_1 Z_2 q^2}{4\pi\epsilon_0\epsilon_r} \geq 0 \quad , \tag{2.10}$$

with Z_1 and Z_2 the numbers of elementary charges q carried by each ion. The turning point or distance of closest approach, r_c, is defined by the condition $v_{\text{rel}} = \dot{r} = 0$.
It follows for the total energy:

$$E = \frac{L^2}{2\mu r_c^2} + \frac{\zeta}{r_c} \quad . \tag{2.11}$$

To obtain the distance of closest approach r_c from eq. (2.11), the following quadratic equation is solved:

$$r_c^2 \left[1 - \frac{\zeta}{Er_c}\right] - b^2 = 0 \quad , \tag{2.12}$$

with the positive solution:

$$r_c = r_c(b) = \frac{\zeta}{2E} + \frac{1}{2}\sqrt{\left(\frac{\zeta}{E}\right)^2 + 4\,b^2} \quad . \tag{2.13}$$

Note that in case of oppositely charged ions, the first term in eq. (2.13) becomes negative.

If the size of the doped droplet with radius R_d is smaller than the distance of closest approach ($R_d < r_c$), any second ion will be precluded from coming into contact with the doped droplet and hence, no ion "double-occupancy" (or any higher occupancy) of the droplet will occur. The minimal distance of closest approach $r_c(b = 0)$ is determined for
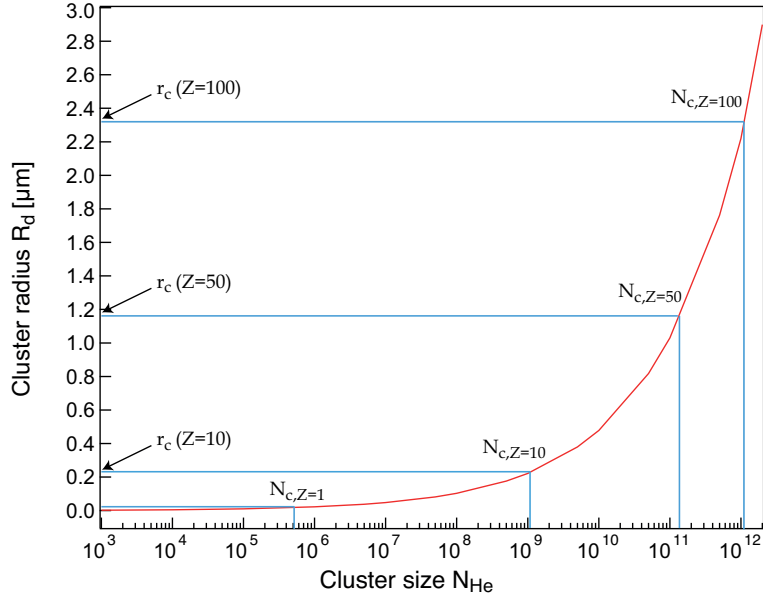
Figure 2.5: The cluster radius R_d is shown as a function of the number of constituent atoms N_{He}. The horizontal blue lines reflect the minimal distance of closest approach $r_c(b = 0)$ for different numbers of elementary charges Zq already contained in the droplet and a beam velocity of v_x=322 ms^{-1} (as experimentally determined with the *Parker* General valve for $T_0 = 10$ K, $P_0 = 30$ bar). All droplets having sizes of corresponding radii $R_d > r_c$ can pick up additional charges, all droplets with $R_d < r_c$ are precluded from multiple pickup.

a molecular beam velocity $v_x = 322$ ms^{-1} (corresponding to $T_0 = 10$ K) and for a singly protonated amino acid having a mass of 165 amu (cf. Phe$^+$).

In fig. 2.5, the cluster radius R_d is shown as a function of the cluster size N_{He} given as the number of constituent He atoms. Horizontal blue lines reflect the minimal distance of closest approach $r_c(b = 0)$ for different numbers of elementary charges Zq (picked up singly-protonated Phe$^+$ ions) that are already contained in the droplet. A pickup of more than one ion by the same He droplet containing the charge $Z q$ (here: $Z =1$), as mentioned above, can be excluded for clusters having radii of $R_d < r_c$. This holds for all droplet radii N_{He} below the blue line or on the left of the corresponding vertical blue line. However, all droplets having sizes corresponding to radii of $R_d > r_c$ can pick up additional charges.

Coulomb repulsion in a multiply charged liquid He droplet

When a He droplet picks up multiple ions, they will probably tend to be located at the largest possible distance between each other, due to Coulomb repulsion. In a limited-sized He cluster, the greatest separation can be obtained on the cluster surface. The electrostatic potential E_{pot} of a He droplet doped with Z ions that are distributed on its surface is displayed in fig. 2.6 on the left. For increasing cluster dimensions, it is likely that from a certain size on, ions can also be distributed (more) homogeneously within the volume of the large cluster. The corresponding electrostatic potential of this limiting case is shown
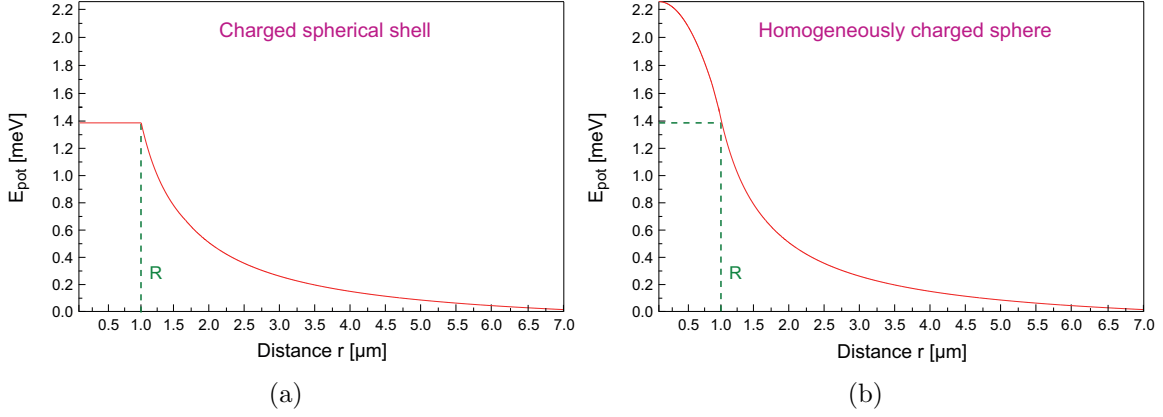
Figure 2.6: Electrostatic potential E_{pot} of a charged sphere for (a) when the charge is located only on the surface and (b) a homogeneously distributed charge throughout the whole sphere. The potential is displayed as a function of the radial distance r from the center of the sphere.

on the right side of fig. 2.6.

In order to predict whether a He cluster can contain a number Z of charges q or if it breaks into fragments due to Coulomb repulsion, the *Rayleigh limit* is calculated. It is frequently used to describe the dynamics of highly-charged droplets generated in electrospray ionization (see Ch. 1.2.1). In the case of charged He droplets, the *Rayleigh limit*
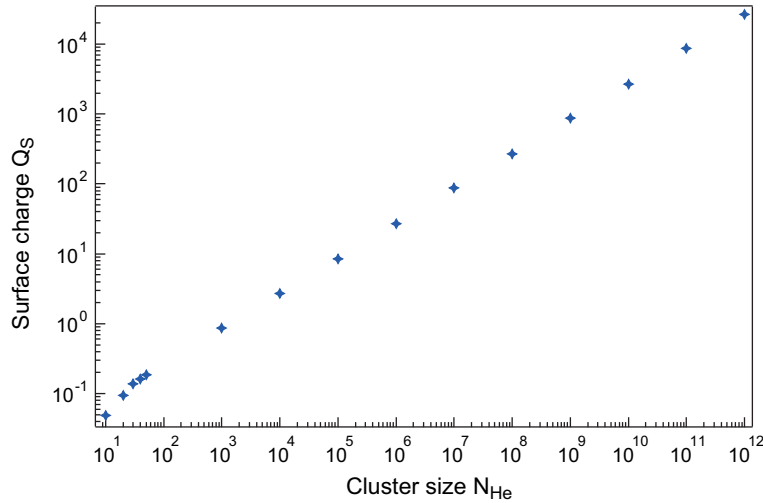
Figure 2.7: Surface charge Q_S that can be contained on the surface of a liquid drop with surface tension γ that is composed of N_{He} particles without fragmentation.

is determined using eq. (1.1), and the maximal charge $Q_S = Z\,q$ that a cluster of size N_{He} can carry on its surface (or in the bulk) is displayed in fig. 2.7 for a range of cluster sizes N_{He}. The surface tension γ of a He droplet is used as a function of droplet size N_{He} as $\gamma = 0.10 - 0.35$ erg cm^{-2} for cluster sizes $N_{He} = 10$–50 He atoms as derived in [120, 121]. For larger droplets, the constant value for a planar He surface of $\gamma = 0.35$ erg cm^{-2} is taken. It is questionable if the theory holds for very few charges, as they cannot be distributed evenly over a sphere. For a higher number of charges, however, the *Rayleigh* criterion might be applicable and predicts that already a droplet containing only 10^3 atoms can hold ≈ 10 (elementary) charges.

In any case, under our experimental conditions Rayleigh stability is not the limiting factor. Provided that the ion density in the trap is large enough, it was shown in Ch. 2.2.4 that, for example, to pick up 10 charges, the droplet has to contain more than 10^9 He atoms at which Rayleigh stability is given.

2.3 Interaction potential

The intermolecular potential between particles is of fundamental interest for understanding the dynamic and static properties of gaseous, liquid, or solid systems. However, it is often a difficult task to obtain good descriptions for an interaction potential, in particular for large systems like biomolecules.

In the case of charged particles dissolved in liquid helium, various models are used to describe the solvation energetics and to obtain an expression for the ion-He interaction potential [96, 122–124]. In this Chapter, the interactions that occur when a charged particle is immersed in bulk liquid helium are regarded. The forces acting cause the formation of a distinct solvation structure which, in the case of positive ions, is commonly called a *snowball*.

When ions are embedded in clusters of liquid helium, a change in the interaction forces occurs that is induced by finite size effects. A model potential of a particle in a He droplet is presented in Ch. 2.3.2. In a continuum theory, the solvation energy of an ion in a non-polar dielectric can be derived from thermodynamic macroscopic properties of the solvent and solute as the change in the Gibbs free energy [125]. It is determined for a large, Z–fold protonated protein in the size range of 1000 atoms that becomes dissolved in liquid helium. Finally, the electrostatic driving force that is acting on an electric charge inside a He cluster is determined in Ch. 2.3.5 as derived in a dielectric model from K. Lehmann [110].

2.3.1 Ions in bulk liquid helium

In the absence of static dipole or higher order multipole moments, the interaction occurring between an electric charge and a He atom is determined by induction and polarization forces, although the polarizability of He is very small, at $\alpha = 0.20$ Å^3. At large internuclear distances R, when no charge overlap occurs, the attractive ion-He atom interaction is given by the sum of charge-induced dipole interactions and the van der Waals interactions as described by:

$$U(R) \;\; = \;\; U_{ind} + U_{vdW} \quad \text{with}$$

$$U_{ind}(R) \;\; = \;\; -\frac{\alpha(Zq)^2}{(\epsilon_0 \epsilon_r)^2 R^4} \tag{2.14}$$

with α denoting the atomic polarizability, Z the number of elementary charges q, ϵ_0 the vacuum dielectric constant, ϵ_r the dielectric constant of the medium, and R the interatomic distance [126]. The van der Waals interactions U_{vdW} depend on the dipole or higher multipole atomic polarizability of helium for atomic ions. They contribute less than 25 % to the interaction potential in the well region and even less outside [101]. The total van der Waals interaction is composed of three terms which make contributions to

the Helmholtz free energy: the randomly oriented dipole-dipole interaction (*Keesom*), the dipole induction interaction (*Debye*), and the dispersion interaction (*London*) which is often the dominant one [126].

The *London* dispersion interaction is the only one present for helium; it is given by:

$$U_{vdW}(R) = -\frac{C_{disp}}{R^6} \quad , \tag{2.15}$$

with C_{disp} the van der Waals coefficient for the dispersion [126]. Experimental techniques to probe the ion-atom interaction for larger internuclear distances R are, for example, ion mobility measurements [127] which deliver the potential parameters by a direct inversion of the measured data. For small R (close to the potential well), data for the interatomic interaction strength can be obtained from beam-scattering experiments by virial– as well as transport coefficient measurements [128].

At shorter distances, charge overlap starts to become more and more important and the ion-neutral interaction potential needs to be extended to include repulsive terms. For short internuclear distances, the potential is purely repulsive which is attributed largely to Pauli exchange forces with a contribution from electrostatic repulsion.

Solvation structure

In presence of an ionic impurity, the attraction between ^{4}He atoms and the charge leads to a strong modulation of the local environment of the ion in the liquid. The effect of coagulation of the solvent atoms around the impurity is commonly referred to as *electrostriction* [122], which describes a field-induced deformation of a dielectric or electrical insulator responding to an electrical field [129]. Two different effects are known to occur. Negative impurities like electrons or He$^-$ form a cavity called a "*bubble*". It is given by an effect of local repulsion arising from the Pauli exclusion principle that leads to a steric separation distance between two electrons. *Bubbles* are usually located on the cluster surface, leading to a deformation of the surface in the form of a "dimple" with a diameter of 1.7 nm [15, 64].

A positive impurity, however, causes the surrounding He atoms in its close vicinity to become strongly localized and to form a solid solvation structure of compressed He atoms called a "*snowball*". The snowball is much smaller than the bubble structure, with a typi–cal diameter of 0.6 nm [15] and, as a solid entity, moves within the superfluid He cluster. Hereby, the He layers in immediate proximity are strongly bound and compressed around the ion core so that they become effectively solid, and consequently, the local density in the first shells becomes so high that a local ordered structure is created. For example, a cubic local order is formed in the case of Li$^+$, and a face-centered cubic structure for K$^+$ [96, 130].

In ref. [15], a dimensionless parameter, the dopant-He pair potential has been proposed in order to determine whether an impurity species becomes embedded in the droplet center (heliophilic) or at the surface (heliophobic). It reflects the net change in energy due to the interaction of the dissolved particle with the He atoms, and the energy needed to create a cavity. By generating radial density profiles and angular correlations of the first shell atoms, it is possible to determine the extent of particle localization as well as the kind of local order [96]. It turns out that the microscopic structure of the snowball is characteristic for the ion core, since it results from the competing interactions between a

He atom and the impurity (Na$^+$, K$^+$: the first shell is essentially localized, so the *snowball* is "solid"; Li$^+$, Cs$^+$: He atoms readily exchange with the others). According to the *snowball* model developed by Atkins [53], the effective mass of the snowball depends on the specific identity of the ion core. It is known that particles dissolved in liquid helium exhibit a reduced mobility with which they move inside the droplet. For example, in the case of alkali ions, the mobility can be smaller than that of the He$^+$ ion and decreases as the atomic number of core ions increases or *vice versa* [131].

For neutral impurities, a known effect is the binding of a shell of normal fluid He to the dopant molecule, which leads to an increase of its moment of inertia. This is experimentally observed by a reduced rotational constant in spectroscopic measurements [15].

2.3.2   Ions in He clusters

Given that an ion immersed in a He cluster, its motion will be limited by potential barriers at the cluster surface. They are mainly caused by polarization charges that develop on the cluster surface, induced by the electric charge (see Ch. 2.3.5).

In a quantum-mechanical approach, the dynamics of an ion in a droplet can be modeled according to the well-known quantum mechanical particle–in–a–box problem [61]. The motion of a particle trapped in a liquid He cluster is proposed to be frictionless but limited by the cluster surface that forms the box boundaries of the spherical well potential. For light particles embedded in smaller clusters, the geometric dimensions of the cluster are comparable to the de Broglie wavelength of the particle. Therefore, a trapped molecule is assumed to behave as a non-classical particle with discrete energy levels. A particle in such a box can occupy only discrete energy states which are determined by the volume available for free motion and by the form of the effective potential [61]. The reduced mass μ of a particle in a box is rather an effective mass which is different from the mass of the free particle for two reasons [61]. First, it is increased by the *snowball* solvation structure surrounding the particle due to induction and dispersion forces. The second effect is the friction acting on a particle which moves through a fluid of density ρ. Classically, a sphere of mass m in a fluid behaves as if it has an effective mass $m_{eff} = m + 0.5\,\rho\,V$ with V the volume of the fluid displaced by the migrating sphere [61].

A simplification of the particle–in–a–box model is the assumption of infinitely high potential walls given by the cluster surface boundary. In reality, the walls are formed in an extended surface region of ≈ 10 Å thickness. Over this region, the particle density decreases from 90%–10% of the bulk density [60]. Assuming box walls of a finite height would hence lead to a smooth step in the interaction potential.

2.3.3   Energy of solvation

In a macroscopic approach, the individual ion-He interaction is neglected when determining the solvation energy of a (charged) particle in a solvent medium. The solvent (here: the He droplet) is treated as a continuous bath with dielectric constant ϵ_r in which the dopant species is immersed. The process of solvation is dominated by electrostatics, it results mainly in an electrostatic force exerted on the solvent molecules by the solute due to interactions with the charges, permanent or induced dipoles or higher order multipoles. The energy released is calculated as the difference in solvation energy of a

particle in vacuum (mainly electrostatic) and in a dielectric solvent [132].

When a molecule is immersed in a solvent, the polarization of the surrounding solvent molecules induces the formation of a "solvation cage" around the solute [133, 134]. Hence, the solvation energy is basically given by the energy release due to the reorganization of the perturbed molecular solvent structure and the additional interaction energies between the solute and the solvent molecules, which can be locally strong [134].

The solvation energy of a particle in a solvent can be derived in a continuum model using a formalism derived by Onsager which is also often referred to as the Born-Onsager model [135–137]. In an implicit treatment of the solvation process, the solvent is represented by a dielectric continuum in which the solute is immersed, whereas in an explicit description, the particularities of the respective real fluid configuration are considered [138].

The continuum approach takes the solute molecule as introduced into a homogeneous polarizable solvent medium characterized by a dielectric constant ϵ_r on which it induces a "reaction field", corresponding to the subsequent reorganization of the dielectric [133, 139]. The solvent then interacts with the dipole moment μ of the dissolved particle and creates a "cavity" around the solute which is treated as a sphere with a point dipole at its center. In non-polar solvents, the solute becomes stabilized due to a lowering of the free energy of solvation ΔG_{sol} that is associated with the binding of solvent molecules to an immersed neutral or charged particle [125] as:

$$\Delta G_{sol} = -N_A \cdot \frac{\mu^2}{4\pi\epsilon_0\, a^3} \cdot \frac{\epsilon_r - 1}{2\epsilon_r + 1} \quad, \tag{2.16}$$

with μ = the dipole moment of the dissolved molecule and a the radius of the solvation cage.

In the case of charged solute species, the expression for the free energy of solvation ΔG_{sol} in eq. (2.16) is modified by an additive Born term[2] to take charge-induced effects into account [125]. This term is obtained from the Born equation and is calculated as the electrical work that has to be performed in order to transfer a charge from vacuum into a medium with dielectric constant ϵ_r. The ion is treated as a hard sphere of radius R_{ion} and charge $Z\,q$, which leads to an electrostatic potential at its surface given by:

$$\Phi = -\frac{Z\,q}{8\,\pi\epsilon_0\epsilon_r R_{ion}} \quad, \tag{2.17}$$

resulting in a change in the free energy of solvation ΔG_{sol} as follows [125]:

$$\Delta G_{sol} = -\frac{Z^2 q^2 N_A}{8\,\pi\epsilon_0 R_{ion}}\left(1 - \frac{1}{\epsilon_r}\right) \quad. \tag{2.18}$$

Z is the number of charges q, N_A the Avogadro constant, ϵ_r the dielectric constant, and R_{ion} the distance between the charge and the solvent molecule (here corresponding to the

---

[2]Born's self-energy term considers the contribution of a charge to the free energy of a system which consists of a charge Zq embedded in a cavity of radius a and dielectric constant ϵ_r from solvent molecules [134, 140].

radius of the ion). The change in free energy ΔG_{sol} is mainly influenced by three factors which are the charge Zq of the dissolved particle, its dipole or higher order multipole moments, and the reciprocal distance between the center of the ion and the oppositely charged "pole" of the (induced) dipole [140].

2.3.4 Biomolecules in liquid He droplets

In Ch. 2.3.1, the ion-He interaction potential is introduced[3]. The total attractive interaction between a protein and a He atom is given by the sum of charge-induced dipole interactions and van der Waals interactions $U(R) = U_{ind} + U_{vdW}$ and can be determined by the sum of all pair potentials [122, 141] $U(R)$ of the ion and all surrounding He atoms. The protein and the He atoms are all modeled as hard spheres with radii given by $R_{ion} = 1.7$ nm, similar to globular CytC^{+Z} ions in solution, and the helium van der Waals radius of $R_{\mathrm{He}} = 1.4$ Å [112]. The interaction energy between a protein ion and the He atoms in each solvation shell n_{He} in the neighborhood is now calculated as:

$$U(n_{\mathrm{He}}) \;=\; \sum_{n_{\mathrm{He}}=0} U_{ind}(R, n_{\mathrm{He}}) + U_{vdW}(R, n_{\mathrm{He}}) \quad \text{where} \qquad (2.19)$$

$$U_{ind}(R, n_{\mathrm{He}}) \;=\; U_{ind}(R_{ion} + 2(n_{\mathrm{He}} - 1) \cdot R_{He}) \quad . \qquad (2.20)$$

$$(2.21)$$

Here, however, the contributions from the van der Waals interactions are neglected due to the rapid fall-off of the interaction with increasing distance and only the contributions from the charge-induced dipole interactions are considered, they are derived by eq. (2.14). This is illustrated in fig. 2.8.

The value obtained for U_{ind} in a shell n_{He} corresponding to a specific distance R, n_{He} is then multiplied by the number of He atoms contained in the respective solvation shell which is calculated using the volume density of bulk liquid helium ($\rho = 0.022$ rA^{-3}). This gives the number of He atoms in a volume $V = 2R_{He} \cdot$ A, with A $= \pi(R_{ion} + 2(n-1)R_{He})^2$.

The values for the total solvation energies are determined for a protein with different charges Zq as the sum of the contributions from the first three solvation shells; shells further outward are assumed to have minor contributions due to the rapid fall-off of the interaction strength with increasing distance, especially when a screening of the ion charge by the previous He atom shells comes into play (which is neglected here, however). Nevertheless, the value for the charge-induced dipole interaction is here also calculated for a shell further apart $n_{\mathrm{He}} = 10$ as it might better reflect the binding energy between the dissolved ion (in its *snowball*) and the He droplet. All calculated values are given in table 2.2.

This calculation of the solvation energy of a large (spherical) particle in a He bath as the sum of all individual ion-He interactions is, however, rather crude. It should rather represent an upper limit for the solvation energy. The assumption of the total charge being located in the center of the protein is a large simplification, leading to a negligence of (possibly strong) charge effects from individual atoms close to the surface in a protonated protein on the surrounding He atoms, which also affect the (individual)

---

[3]The repulsive part of the potential is mainly caused by the Pauli exclusion principle of the outer electrons of the impurity molecule, which repel those of the surrounding He atoms. It is not considered further here.

Table 2.2: The calculated energies released when a particle carrying a charge Zq becomes solvated in a liquid helium bath. This was carried out for different numbers Z of charges, once as the sum $\Sigma(n_{He}, U_{ind})$ over the first three shells and for $n_{He} = 10$ and, alternatively, as the change in the free energy of solvation ΔG_{sol} using the thermodynamic approach (eq. (2.16) and eq. (2.18)).

Z	n_{He}	U_{ind} [eV]	ΔG_{sol} [eV]
0	1	/	0.184
	2	/	
	3	/	
	10	/	
1	1	0.006	0.020
	2	0.005	
	3	0.004	
	10	0.001	
	$\Sigma(n_{He}=1\text{–}3)$	0.015	
2	1	0.025	0.081
	2	0.019	
	3	0.015	
	10	0.005	
	$\Sigma(n_{He}=1\text{–}3)$	0.059	
5	1	0.156	0.504
	2	0.119	
	3	0.093	
	10	0.029	
	$\Sigma(n_{He}=1\text{–}3)$	0.368	
10	1	0.626	2.017
	2	0.474	
	3	0.372	
	10	0.114	
	$\Sigma(n_{He}=1\text{–}3)$	1.472	
15	1	1.408	4.539
	2	1.067	
	3	0.837	
	10	0.257	
	$\Sigma(n_{He}=1\text{–}3)$	3.312	
20	1	2.503	8.069
	2	1.897	
	3	1.487	
	10	0.457	
	$\Sigma(n_{He}=1\text{–}3)$	5.887	
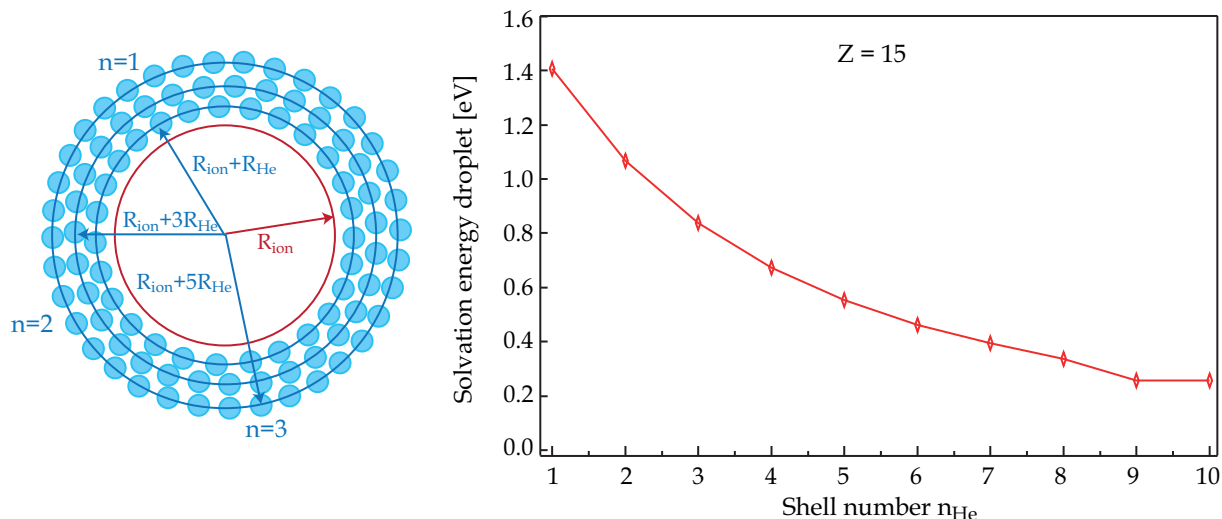
Figure 2.8: (Electrostatic) potential in a He droplet as a sum of all individual ion-He interactions as the charged-induced dipole interactions between the ion of radius R_{ion} and the He atoms contained in a shell n_{He}. The illustration on the left shows how the number of He atoms contained in a shell n_{He} with radius $R_{ion} + 2(n-1)R_{He}$ are calculated. On the right, the interaction potential is displayed for each solvation shell up to $n_{He} = 10$.

ion-He distances. Furthermore, the density of the droplet is assumed to be that of bulk liquid helium, as in the liquid-drop model. However, the actual density in a He droplet is a function of droplet size [142] and decreases with decreasing droplet size and the actual density in the shells is also dependent on the individual dopant particle [143] as well as on the dopant-He interaction forces present. Also, modulations of the helium density around the solute are neglected. Moreover, the first one or two shells are known to be more tightly bound to a positively charged dopant particle and compressed, becoming solid rather than liquid (see above in Ch. 2.3.1). Therefore, for the first and perhaps the second shell, it should be appropriate to calculate the number of atoms using the density of solid helium; it is given by ≈ 0.028 atoms$\cdot$ Å^{-3} [144]. However here, for all shells alike the uniform particle density of superfluid helium is employed.

Now, the solvation energy for large ions is calculated using the combined Born-Onsager continuum model (see eq. (2.16)) given in ref. [133], which is extended by an electrostatic Born term. When a globular protein with a radius of $R=17$ Å and a dipole moment of $\mu \approx 300$ D (given for a cytochrome c ion from equine heart in [145], where about 3.5 D are counted per peptide bond) is immersed in liquid He; in ref. [146], the value for the dipole moment of CytC^{+2} or CytC^{+3} is indicated as 200–300 D. The radius a of the solvation cage is taken equal as the radius of the ion. For the dielectric constant of liquid helium at low temperatures of ≈ 1.5 K a value of $\epsilon_r \approx 1.05$ is taken [147, 148]. Inserting these values, the change in the free Gibbs energy upon dissolving a neutral protein ion $Zq = 0$ of ≈ 184 meV is obtained. Then, electrically charged particles are considered and ΔG_{sol} is determined by eq. (2.18) for a protein carrying different charges Zq. All values obtained are also given in table 2.2.

When comparing these values with the respective values obtained by the previous method for the same charge Zq, it is seen that they agree well with each other, even though they do not have precisely the same physical meaning. $\Sigma(n_{He}, U_{ind})$ gives the enthalpy which differs from the free Gibbs energy ΔG_{sol} mainly by the entropy. At temperatures close

45

to 0 K, this might however be neglected and in the calculation here, temperature effects are only considered through the value of the dielectric constant in case of the calculation using the continuum model. The agreement is better for smaller total charges contained in the protein. For $Z \geq 10$, the two values show increasing differences and the values obtained from the macroscopic approach become rather large.

2.3.5   Driving force of an ion in a He droplet

The translational motion of an ion that has entered a ^{4}He droplet is determined by the (long range) electrostatic interaction between the charge and the helium bath. It was first calculated by Antoniewicz *et al.* [149] and then recalculated by Lehmann [110] in a semiclassical approach that models the He droplet as a dielectric sphere. The interaction
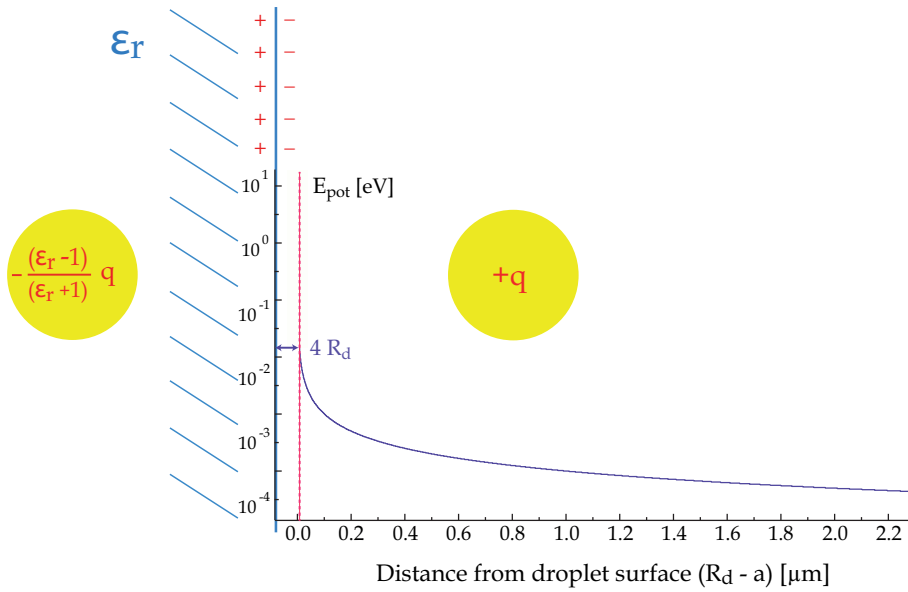
Figure 2.9: A charge $+q$ close to a boundary with a medium of dielectric constant ϵ_r induces an image charge of $-(\epsilon_r - 1)/(\epsilon_r + 1)\, q$ beyond this interface [150], here in case the charge is in vacuum ($\epsilon_r = 1$) and shown for a planar interface. In the dielectric model from Lehmann, the interface between vacuum and (bulk) liquid helium with dielectricity constant ϵ_r is given by the spherical cluster surface. The charge inside the cluster feels a repulsive force exerted by the polarization charge that it induces on the cluster surface as the dielectric response. The shown graph gives the repulsive electrostatic energy E_{pot} as derived from the electrostatic model in ref. [110]. It falls off with increasing distance $(R_d - a)$ from the cluster surface.

can be described by a charge that induces a polarization charge on the cluster surface as "dielectric response" which acts then as a repulsive force on the ion. The effective electrostatic confinement potential describes the influence of the polarization charge on the motion of an ion in a He cluster. For example, the migration path through the cluster of ions created by electron impact ionization or an entering electron (hole) will be strongly biased by this potential [110]. It is derived in ref. [110] by the mirror-charge method. All charge-induced dipole interactions between the ion and the missing He atom beyond the cluster surface are summarized as a function of the distance of the charge from the cluster surface. As a reference state, the electrostatic potential of an ion in bulk liquid helium is taken, defining the zero point of the potential [110]. This is illustrated in fig. 2.9: An electric charge q induces an image charge beyond the boundary with the dielectric medium

of dielectric constant ϵ_r.

The starting point for the calculation in ref. [110] is the electrostatic field of a charge q that is located at the distance R from the droplet surface:

$$\left|\vec{E}(R)\right| = \frac{q}{4\pi\epsilon_0\epsilon_r R^2} \quad , \tag{2.22}$$

and the repulsive potential E_{pot} is ultimately derived in [110] as:

$$E_{pot} = \frac{q^2}{4\pi\epsilon_0 R_d} \cdot \frac{\epsilon_r - 1}{2\epsilon_r^2} F_0\left(\frac{a}{R_d}\right) \quad . \tag{2.23}$$

F_0 is a function of the "fractional radius" $y := \frac{a}{R_d}$ of the impurity species, which reflects the ratio of the distance a of the ion from the droplet center and the droplet radius R_d. It is given by the following expression:

$$F_0(y) = \frac{1}{4}\left(\frac{2}{1-y^2} + \frac{1}{y}\log\frac{1+y}{1-y}\right) \approx 1 + \frac{2}{3}y^2 + \frac{3}{5}y^4 + ... \tag{2.24}$$

The graph shown in fig. 2.9 reflects the calculated effective repulsive potential E_{pot} as given by eq. (2.23) for a singly-charged particle which is located in the cluster center at a distance $(R_d - a)$ from the cluster surface. R_d is the droplet radius and a is the distance of the charge from the cluster center [110]. An increasing droplet radius is equivalent to an increasing distance of the charge from the polarization charge on the cluster surface and, thus, the magnitude of the repulsive force decreases rapidly with increasing distance $(R_d - a)$ from the cluster surface (i.e. for larger droplets R_d). From the dielectric model, it results that the most stable position for an ion is at the center of the cluster, providing the largest distance from the surface polarization charge [110]. In fact, it is found [15, 16] that the minimum energy position for most foreign particles in a He droplet is the droplet center (with the exception of alkali atoms and a few other species) [76].

However, the expression for the repulsive potential given in eq. (2.23) is derived for ions which are localized close to the cluster center. The series for $F_0[y]$ in eq. (2.24) is expanded around $y = 0$ and goes to infinity for $y \to 1$. Therefore, the repulsive potential cannot be obtained for ions located directly at the cluster surface with $y = 1$; only approximative values for the potential at a value of $y \approx 1$, hence for ions close to the surface can be determined by eq. (2.23). Antoniewicz *et al.* cut off the potential at distances from the droplet surfaces that are comparable to twice the geometric size of the ion [149]. Then, the effective potential can be determined for a value of y close to 1, which is taken here as the distance from the cluster surface of four times the radius of the ion as:

$$y_{surf} = \frac{R_d - 4 R_{ion}}{R_d} \quad . \tag{2.25}$$

The repulsive potential for an ion with a charge Zq which is located at the cluster center ($y = 0$) or close to the surface ($y = y_{surf}$) is now determined for clusters of three different sizes N_{He}, inserting the value for the dielectric constant of He at 3 K of $\epsilon_r = 1.05646$ like in ref. [110]. At first, it is calculated for a singly charged amino acid embedded in a cluster composed of $N_{He} = 10^4$ He atoms. The value derived for E_{pot} is ≈ 7.6 meV at the

cluster center and ≈ 26.7 meV close to the surface.

Then, the value is determined for clusters composed of $N_{He} = 10^6$ and 10^{12} He atoms which are doped with a globular protein having a geometric diameter of 3.4 nm and carrying $Z = 10$ elementary charges. The values for E_{pot} are determined to ≈ 164.0 meV and ≈ 1.7 meV in the cluster center of a 10^6 and 10^{12} cluster, respectively. The values for the repulsive potential when the protein ion is located close to the cluster surface are ≈ 373.7 meV for a 10^6 cluster and 137.2 meV for a 10^{12} cluster.

In accordance with ref. [110], the repulsion is stronger when the charge is close to the cluster surface as compared to the cluster center and thus, the effective potential pushes the ion towards the droplet center. Obviously, the magnitude of the repulsive forces is much larger for highly charged particles.

The difference in potential between cluster center and surface is larger for the 10^6 clusters than for the very large 10^{12} clusters. Presumably, this is due to the ratio of the geometric diameters of protein and cluster R_{ion}/R_d, which is considerably larger for the 10^6 than for the 10^{12} clusters. Therefore, the repulsive forces on an ion in the cluster center exerted from the polarization charge on the surface of a 10^6 cluster are stronger than those of a 10^{12} cluster. For the latter case, the repulsive potential is very weak, corresponding to the rapid fall-off of the potential as a function of distance from the cluster surface. Large droplets are supposed to have a more extended region in the cluster interior with a flat potential, and an embedded ion feels less of the repulsive forces from the surface polarization charge as compared to smaller clusters.

2.4 Is it possible to extract an ion from a droplet?

One might wonder how, in principle, a foreign particle can be caught by a superfluid He cluster in a pickup process and is not spilled out of the droplet straightaway on the opposite edge after a frictionless passage through the cluster. However, the zero viscosity of a superfluid holds only for particles moving at velocities less than the Landau velocity through the superfluid. At higher (relative) velocities, the superfluid becomes viscous due to the excitation of rotons or phonons in the liquid helium. In a phenomenological model, the helium environment can be simulated as a frictional force that acts on a foreign species when its velocity exceeds the critical Landau velocity [99]. Therefore, a particle entering a He droplet after pickup is slowed down by the non-viscous helium due to the high relative velocity (≈ 300–400 m s^{-1}) at which the particle collides with the He droplet in the pickup process, and it thus becomes trapped in the cluster.

It remains an open question whether, once a charged particle is dissolved in a liquid He droplet, the binding of the particle to the cluster is strong and the particle is stored stably inside the cluster, or if it can (easily) be separated from the droplet in an experiment. The attractive ion-He interaction is given by charge-induced dipole interactions with contributions from the van der Waals interactions (see Ch. 2.3.1). Since helium, as the smallest rare gas atom, has a very low polarizability, the interaction forces are presumed to be weak.

In the following, it is considered whether it is possible to extract a dissolved ion from a He droplet by applying electric fields. Then, experimental observations regarding the ejection of ions upon electron impact or optical excitation are presented.

2.4.1 Extraction by applying high electric fields

The potential of the (individual) ion-He interaction is presented in Ch. 2.3. The total
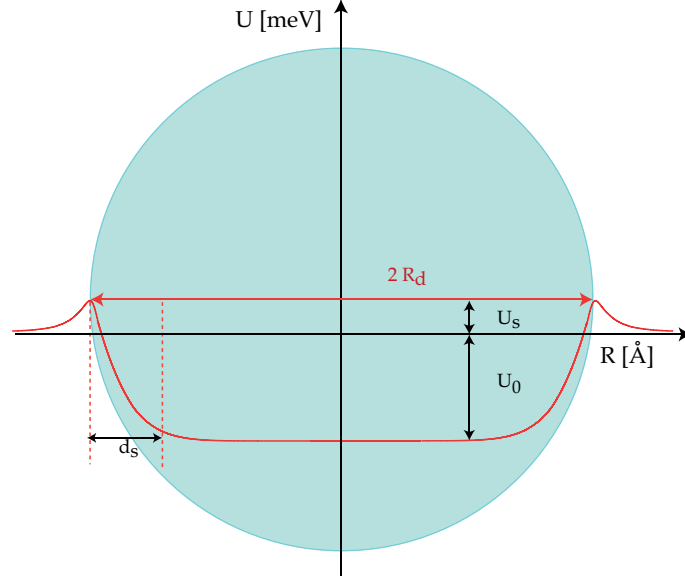
Figure 2.10: (Electrostatic) potential for a particle in a He droplet as a sum of all individual ion-He interactions.

interaction potential in a He cluster of the dopant and the helium bath, however, is given by the sum of all individual interactions between the ion and the He atoms in the surrounding solvation shells. The ion is moving (freely) inside the cluster in a potential that is presumably flat in the cluster interior and exhibits barriers at the cluster surface, due to, for example, electrostatic repulsion from polarization charges on the surface of the dielectric cluster (cf. Ch. 2.3.5). An illustration of the cluster potential is depicted in fig. 2.10. The potential well depth is then given by the solvation energy of the ion in the cluster (cf. Ch. 2.3.4), and the height of the surface barriers can be obtained as a function of distance R from the cluster surface using the mirror charge method. Outside of the cluster, the potential rapidly falls to zero. When an ion is extracted from a droplet it is likely that it will be separated from the droplet in the tightly bound *snowball* or at least being partly solvated.

When an electric field $\vec{E}$ pulls on the ion in the droplet with a force $\vec{F}_{el}$, the competitive forces acting in opposite directions are the restoring force $\vec{F}_B$ and the classical inertia $\vec{F}_t$. In equilibrium, the total force $\vec{F}_{tot}$ must be zero:

$$\vec{F}_{tot} = \vec{F}_{el} - \vec{F}_t - \vec{F}_B = 0 \quad . \tag{2.26}$$

Regarding dynamical equilibrium allows for neglecting inertia, and since the forces considered are directed either in the same or in opposite directions it is sufficient to treat only the absolute values of the acting forces in a one-dimensional treatment. In order to extract an ion from the cluster, the electric force exerted by a (homogeneous) electric field must exceed the binding force throughout the whole droplet:

$$|\vec{F}_{el}| > |\vec{F}_B| \quad , \tag{2.27}$$

and hence, when $|\vec{F}_{el}|$ is larger than the binding force at the point of maximal force $|\vec{F}_{max}|$, ion and droplet will be separated. The maximal (restoring) force, corresponding to a maximal change in the interaction potential, is obtained through the null value of the second derivative of the interaction potential $U(R)$. The required electric force must thus pull the ion out of the potential well and over the potential barrier at the surface.

The ion-He cluster potential can be described within two limiting cases. One is given by a rectangular potential with finite walls. The infinite slope of the potential at the cluster surface, however, does not allow for a calculation of the force acting there. The second limiting model potential is that of a linear potential and thus a constant force throughout the whole cluster. This gives a lower limit to the restoring force that acts on the ion within the cluster. The force in the case of a linear potential is derived by

$$-\frac{d}{dR}U(R) = -\frac{d}{dR}\left(\left[1 - \frac{R}{R_d}\right] \cdot U_0 + \frac{R}{R_d} \cdot U_S\right) \quad , \tag{2.28}$$

where U_0 is the (constant) potential in the cluster interior, R_d the cluster radius, and U_S the height of the surface potential barrier. The value of U_0 as the solvation energy of the ion in the droplet is estimated by three different values $U_0 =100$ meV, 1 eV, and 10 eV defining a range which should definitely cover the realistic value of the solvation energy. The value for U_S is taken from the dielectric model in Ch. 2.3.5, with a barrier height of ≈ 5 meV for a single charge close to the surface of a 10^6 He cluster. Inserting these values, the minimal electric field strength required to separate a singly charged ion from a droplet is given by $|\vec{E}| = F/q \approx 4.3 \cdot 10^4\,V/cm$, $\approx 4.5 \cdot 10^5\,V/cm$, and $\approx 4.5 \cdot 10^6\,V/cm$, respectively. These values are all of them very high, showing that, although the binding can be weak, quite high electric fields are required to extract a dissolved ion from a He droplet.

2.4.2 Violent ejection mechanism

Resulting from fragmentation studies of ionized He clusters, it has been discovered that cooling of ions in liquid He droplets is not exclusively achieved by a purely thermal process (evaporative cooling) [99, 151]. Additionally, a non-thermal and more violent mechanism is proposed, which leads to the impulsive ejection of He_2^+ ions or the dopant species from the cluster. The ejection of He_2^+ ions is attributed to the release of translational energy after vibrational energy transfer from an ionized He atom [98]. An indicator for the impulsive ejection mechanism was the observation of a large amount of energy, about 22 cm^{-1} per atom, that is removed by the first several thousand He atoms from clusters composed of 10^3–10^4 He atoms [152]. This amount of energy is significantly larger than expected [98, 153] and is four times higher than the atomic binding energy of ≈ 5 cm^{-1} per atom which is removed by a purely thermal cooling process [99, 102].

Experimental studies were performed by different groups dealing with the occurrence of He dimer ions He_2^+ or larger oligomer ions He_N^+ ejected from He clusters after electron impact ionization, which were indicative for a non-thermal cooling mechanism of charged particles in liquid He clusters [151, 154]. Theoretical studies to obtain a further understanding of the mechanisms for cooling and energy relaxation inside a He droplet were performed by Bonhommeau *et al.*, their results are also in accordance with an impulsive ejection mechanism for cooling in He droplets [99, 107]. In order to explain the impulsive ejection mechanism in ionized He clusters, a model was proposed by Gspann *et al.*

[153]. According to this model, the strong electrostatic interaction and polarization forces between a charged particle and the He atoms leads to a strong attraction of He atoms towards the ionic impurity. Electrostriction results in a temporarily depleted region a bit further outwards which becomes heated due to the release of polarization energy and ultimately, in a rapid local heating of the firmly bound He atoms in the *snowball*. If this process takes place in the vicinity of the cluster surface, the minicluster ion that is bound to the cluster by electrostriction might be expelled from its parent cluster as a hot "gas bubble" [153].

Recent experiments performed by Drabbels *et al.* revealed that an impulsive ejection of ions from a He cluster also occurs after vibrational excitation of an embedded molecular ion [102]. IR absorption spectra from cold aniline ions dissolved in He droplets are recorded by taking mass spectra of bare aniline ions as a function of incident IR wavelength. The observations in this experiment are indicative of the ejection of a "hot" dopant ion from a He cluster due to vibrational excitation of initially cold ions. Drabbels *et al.* propose an explanation that is similar to the model of Gspann: the vibrational energy is assumed to become localized in the *snowball* solvation structure of the ion before it is distributed over the whole droplet. The subsequent fast heating of the *snowball* as a local high-pressure gas bubble can lead to droplet fission. It is presumed that either ion solvation or vibrational excitation of an ion in a He droplet are mainly responsible for the ejection mechanism, but to date, there are no final conclusions about the underlying nature of the process [102]. In order to obtain a better insight into the ejection process, it is promising to study cold ions rather than ions having high internal energies as are usually present after electron impact ionization.

Also in the experiments on vibrationally excited molecular ions, a dependence of the ejection process on the cluster size is observed [102] since the ion yield of impurity ions ejected from a He cluster is observed to decrease rapidly for increasing cluster size. The model proposed can help to explain this observation. In large clusters the radial distance from the location of the impurity (in the cluster center) to the surface is large, and the release of polarization energy might be accomplished before the hot "gas bubble" reaches the cluster surface and is ejected from the cluster.

For performing IR spectroscopic experiments on ions dissolved in liquid He droplets, an ejection of the vibrationally excited dopant ion from the droplet could be of direct practical use. Since a bare ion is significantly lighter than the droplet+ion system, it could facilitate both the manipulation of the ion by electric fields and the detection process to a significant extent.

2.5 Cooling in He droplets

When a foreign particle is picked up by a He droplet and transfers its entire energy and angular momentum to the droplet, there are three processes initiated in order to transport the heat from the dopant interior to the cluster surface.
First, there is the intramolecular heat transfer in the molecule itself, from its interior to the interface with the He bath. This is due to the mechanism of internal vibrational redistribution (IVR), which takes place on fast time scales of ≈ 1 ps [155]. Here, the heat transport *via IVR* is faster for large molecules with a high density of states.
The second step of heat transport is the transfer from the boundary of the dopant molecule

to the cluster or, more explicitly, to the solvation shell of the cluster, which is a less well-known process but, however, is presumably fast, too.

Finally, the heat is transferred from the dopant location in the cluster (often the droplet center) to the cluster surface. This transport is mainly determined by the heat conductivity of the solvent, which is extraordinarily high in superfluid helium ($\geq 900\,000\,W/(\text{mol}\cdot \text{K})$).

2.5.1 Evaporation and cooling rate

Both the formation of liquid He clusters and the cooling mechanism after picking up a foreign species invoke the thermal process of evaporative cooling for the release of energy. In nozzle beam expansions, when the pressure in the expansion drops below the equilibrium vapor pressure of the droplets and collisional cooling ceases (downstream of the quitting surface), further cooling of the clusters is achieved by evaporating He atoms from their surfaces and thereby removing energy from the cluster [18]. The mechanism and time scale for equilibrating the center-of-mass motion of a picked-up impurity particle involves the exchange of energy and angular momentum with the elementary excitation modes of the cluster which are compressional bulk modes or *ripplons* as quantized surface capillary waves [110] (see. Ch. 1.3).

The final cluster temperature that can be reached in a condensed beam is determined by the vapor pressure of the expanded species and the flight time in the beam [28], the cluster temperature keeps decreasing due to the evaporative mechanism, until no more atoms can be evaporated from the surface [57, 156], implying that the final cluster temperature depends on the binding energy of the constituent atoms. Therefore, it is predicted that liquid He clusters, having the smallest binding energy of 7.2 K per atom (as in bulk liquid helium), can reach the lowest temperatures.

The key for an efficient cooling mechanism is the rapid energy exchange between the dopant particle and the helium bath [17]. Time scales are assumed to be dependent on the coupling of the foreign molecular (ground) state to the (thermal) elementary modes of the cluster. The coupling works best for low energy modes since helium does not have a high density of states at higher energies. For example, the cooling of vibrationally excited HF molecules in He droplets is rather inefficient and relaxation takes more than 0.5 ms due to a large energy gap between the populated internal states of HF and the helium internal energy modes [157].

Cluster temperature rise after energy absorption

After a pickup process or the absorption of energy by the dopant species with subsequent energy transfer to the helium bath, the cluster is heated to a temperature $T_2 > 0.37$ K. The absorbed energy is rapidly dissipated over all energy states of the cluster and then the cooling process is initiated. The cooling process ceases when the cluster has returned to thermodynamic equilibrium at ≈ 0.37 K, including a cooling of the embedded impurity species to this temperature. In classical thermodynamics, the temperature change of a body of a mass m_d upon transfer of an energy amount Q is determined by the heat capacity of the system as:

$$\Delta T = T_2 - T_1 = \frac{Q}{m_d\, c_p(T)} \quad , \tag{2.29}$$
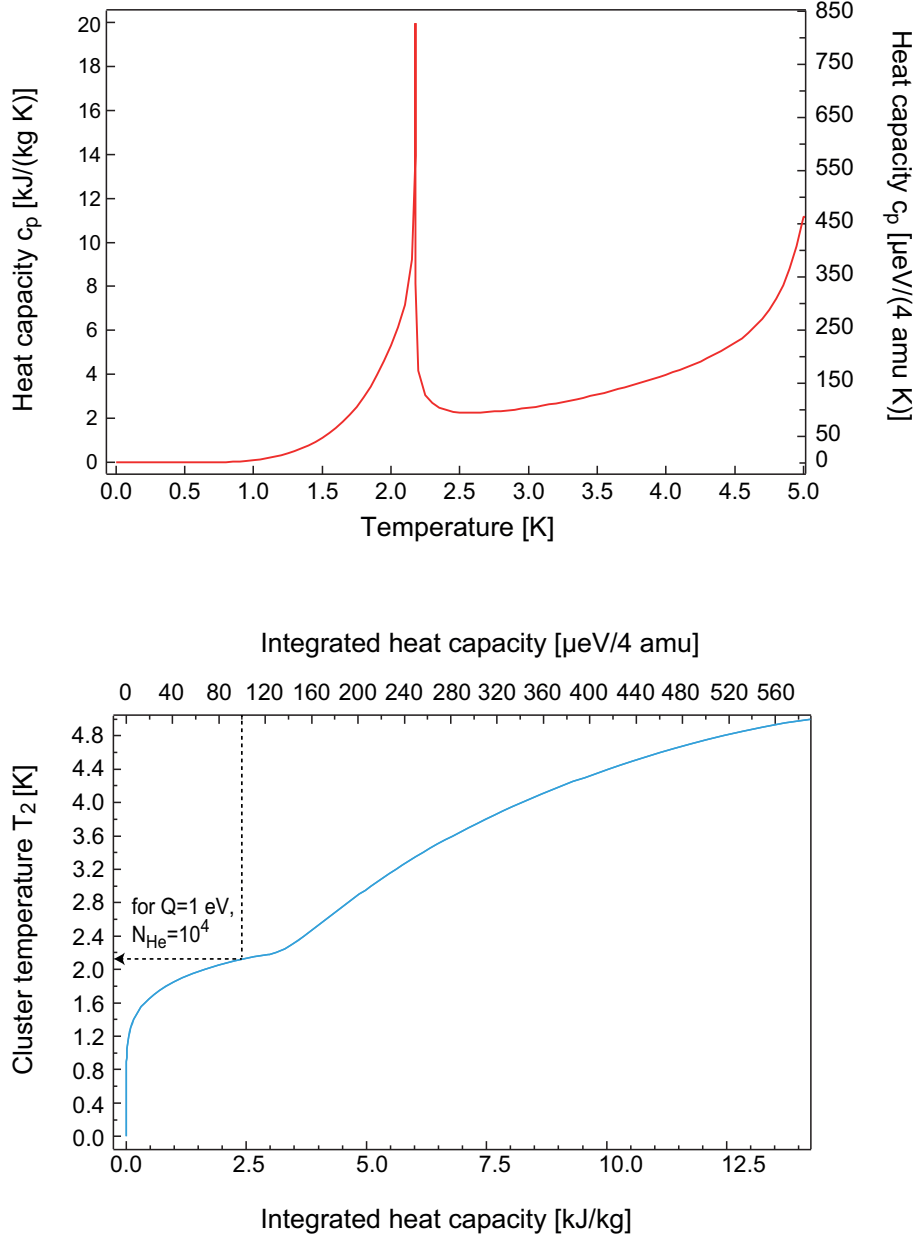
Figure 2.11: (Top panel) Heat capacity of helium at saturated vapor pressure as given in ref. [158, 159]. On the left axis, c_p is given in SI units, on the right axis in units of eV per He atom. (Bottom panel) The temperature dependent heat capacity is numerically integrated and inversely shown, i.e. the corresponding temperature is displayed as a function of the fraction of energy amount Q/m_d (cluster mass). The bottom axis shows the integral in SI units, the top in units of μeV per 4 amu, the mass of a He atom. The temperature T_2 reached in a cluster of mass m_d after absorbing a heat amount Q can then be determined graphically, here shown by the black dashed line for the absorption of 1 eV by a cluster composed of $N_{He} = 10^4$ He atoms.

where Q is the amount of energy transferred and c_p the specific heat capacity at constant pressure. The cluster temperature T_2 reached after heat absorption can then be determined by

$$T_2 = \frac{Q + c_p\, m_d T_1}{c_p\, m_d} \quad , \tag{2.30}$$

53

Table 2.3: Temperature T_2 of He clusters of three different cluster sizes N_{He} when, after absorbing a quantity of heat Q, the internal cluster temperature of $T_1 \approx 0.37$ K is increased.

N_{He}	Q [eV]	T_2 [K]
10^4	1	2.15
10^4	30	≈ 90
10^6	1	1.07
10^6	30	1.78
10^{12}	1	≈ 0
10^{12}	30	0.65

presuming that the heat capacity is independent of the temperature. However, this is often not the case. Helium, for example, has a heat capacity which is a strong function of temperature. The specific heat capacity at saturated vapor pressure is shown in the top panel of fig. 2.11; it exhibits a characteristic discontinuity at the λ transition whose shape actually is the origin for the term "λ point". Values for the heat capacity of liquid helium at saturated vapor pressure are taken from [158, 159]. In the case of a temperature-dependent heat capacity, one has

$$c_p = \left(\frac{\partial H}{\partial T}\right)_p \quad \text{and} \tag{2.31}$$

$$Q = \Delta H = \int_{T_1}^{T_2} m_d \, c_p(T) dT \quad , \tag{2.32}$$

where H is the enthalpy. In the bottom panel of fig. 2.11, the temperature is displayed $vs.$ the integrated heat capacity c_p which corresponds to Q/m_d from eq. (2.32). On the bottom axis, the integrated heat capacity is given in units of kJ/kg [160], on the top axis in eV/(4 amu) which allows for determining the final cluster temperature T_2 after heat absorption. Here, the heat capacity of liquid helium at a temperature close to 0 K ($T_1 \approx 0.37$ K) is also close to zero. The value obtained when dividing a given energy amount Q that is transferred to a cluster (for example the internal energy of a dopant) by the cluster mass m_d defines the x value for which the corresponding y value and hence the cluster temperature T_2 is given by the curve (the respective integrated heat capacity). For example, transferring an energy amount of 1 eV to a 10^4 cluster will lead to a rise of the cluster temperature to about 2.15 K, as illustrated by the black dashed line in the figure. The temperature T_2 is determined for clusters of three different sizes which each absorb a heat amount of $Q = 1$ eV or $Q = 30$ eV (corresponding to the internal energy of a CytC^{+Z} ion); they are given in table 2.3. This shows that the temperature of smaller clusters containing 10^4 atoms are raised almost over the λ transition after absorbing heat quantities of 1 eV, whereas very heavy clusters containing more than 10^{12} He atoms do not increase their temperatures noticeably after absorbing $Q = 30$ eV of energy. The value for T_2 of a small cluster reached after absorption of $Q = 30$ eV is very high[4] being almost

---

[4]this value is not covered in the range shown in fig. 2.11, but obtained including further values for the temperature dependent enthalpy from [158, 159].

100 K; this implies that it is rather impossible for a cluster having a size of $N_{He} = 10^4$ He atoms to absorb such high amounts of energy without being evaporated completely.

We note that the change in cluster mass Δm_d is neglected here. When He atoms are evaporated, the droplet mass decreases and so will the heat capacity c_p.

A statistical model

An explicit treatment of the many-body evaporation problem can be carried out by real-time quantum dynamics involving techniques such as for example Monte Carlo methods of various types, but this is a complex and difficult problem [17, 161]. An alternative treatment is a thermodynamic approach, where the He droplet is treated as a microcanonical ensemble with the total energy as conserved quantity. Brink and Stringari developed a statistical model to describe a He cluster and determined the internal equilibrium cluster temperature to be ≈ 0.3 K [59], which has been confirmed experimentally. For example, Hartmann *et al.* demonstrated that solvated molecules in liquid He droplets have rotational populations that can be well described by Boltzmann distributions with temperatures around (0.37 ± 0.02) K [21]. In the thermodynamic treatment, it is possible to express the evaporation rate by statistical unimolecular rate constants [162, 163]. However, a complete treatment must also include the conservation of angular momentum, which was carried out later by Lehmann and Dokter [164]. They obtain similar results for the final droplet temperature as Brink and Stringari.

The statistical model of He$_N$ clusters by Brink and Stringari is based on the liquid drop model [165] (cf. Ch. 1.3), it is derived in ref. [59]. The treatment includes an explicit calculation of the density of states (DOS) $\omega(E)$ for a given excitation energy E of a He droplet as a microcanonical ensemble. The starting point for the calculation of the density of states is the partition function for a population of phonon-type thermally excited elementary excitations of the cluster. The whole formalism is derived under two conditions, which are firstly, a restriction to conditions at which only surface modes are excited. This applies to clusters in the size range of $N_{He} = 10^3$–10^6 He atoms at a cluster temperature below 1 K. The second condition is that the cluster temperature is greater than the spacing of the energy levels of the thermal cluster modes, which is on the order of 0.1–0.4 K.

From the expression derived for the density of states they deduce the temperature evolution and evaporation rate of the He clusters starting from the *Weisskopf* formula, which has also been used by Klots [163] to derive evaporation rates and rate equations for a microcanonical ensemble. The *Weisskopf* formula describes the probability per unit time for a cluster He$_N$ with energy E_N to emit an atom with kinetic energy ϵ yielding a cluster He$_{N-1}$ with the energy $E_{N-1} = E_N - E_0 - \epsilon$. Here, E_0 is the (cluster size dependent) binding energy of an atom evaporated from a large ^{4}He cluster. Originally, the *Weisskopf* formula is developed to give statistical descriptions of nuclear processes and to derive expressions for the emission probability of neutrons or charged particles by highly excited heavy nuclei under the presumption that all involved energies are large compared to the lowest excitation energies of the nuclei [166]. The emission probabilities in the Weisskopf formalism are derived similarly as those for the probability of evaporating a particle from a cold drop [166]. An integration of the *Weisskopf* formula with the cluster energy yields the total evaporation rate $\Gamma \equiv \frac{dN}{dt}$, that is related to the average lifetime of an atom be-

fore it evaporates from a cluster surface at temperature T [2, 59]. This lifetime depends on the cluster size through a (minor) size dependence of the chemical potential. At low temperatures $T \to 0$, however, the chemical potential μ reduces to the binding energy $-E_0$. This finally leads to an expression for the evaporation rate Γ which then results in an expression for describing the temporal evolution of the cluster temperature $T(t)$ as a consequence of the evaporation process:

$$\Gamma = g \frac{m_{\text{He}}\,\sigma}{\pi^2}\,T^2 \exp\left[-\frac{E_0}{T}\right] \quad , \tag{2.33}$$

with g the spin degeneracy of the emitted particle ($g = 1$ for ^{4}He) and m_{He} the atomic mass of helium. The cluster size dependence for the evaporation rate is given by the cross section σ of the cluster.

As a remark, the units used in this treatment are for $\hbar = k_B = 1$, lengths are measured in Angstroms, energies in Kelvin, and time in units of $\hbar/k_B$.

For each emitted He atom, an energy amount E_0 is removed from the cluster and the temporal change in cluster energy is determined by the temporal change in cluster size as:

$$\frac{dE}{dt} = -E_0 \frac{dN}{dt} \quad . \tag{2.34}$$

Using the microcanonical relationship between the excitation energy E of an N_{He} cluster and the cluster temperature T results in a differential equation for the thermal evolution of large ^{4}He clusters ($g=1$, $\mu \approx E_0$) as [59]:

$$\frac{dT}{dt} = -\frac{9}{28\pi\alpha} m_{\text{He}}\, r_0^2 E_0\, T^{\frac{2}{3}} \exp\left[-\frac{E_0}{T}\right] \quad , \tag{2.35}$$

with $\alpha = 0.39 \text{ K}^{-4/3}$ and $r_0 = 2.22$ Å [59]. This equation is **independent** of the cluster size.

The differential equations (2.33) and (2.35) allow the computation of the temporal evolution of the number N_{He} of constituent He atoms and the cluster temperature, respectively. They are solved for various initial temperatures $T_i = 0.5$ K, 0.7 K, 1 K, and 2 K, and $N_0 = 10^3$, 10^4, and 10^6. The initial temperature T_i can be considered as (for example) the temperature at the sudden freeze radius of a condensed beam which characterizes the distance from the nozzle when collisional cooling and condensation cease in an isentropic expansion and cluster cooling continues by evaporation only (see Ch. 1.3.2). The result is that when starting from the same initial temperature T_i, the evaporation rate Γ for every initial cluster size N_0 has an identical behavior (not shown), meaning that the clusters have the same time evolution during the evaporative cooling process: Almost all the boiled-off He atoms are emitted at the very beginning of the evaporation and afterwards, N_{He} stays almost constant and the respective final cluster size N_f is reached after identical time periods. A difference in evaporation rate $\Gamma(t)$ depending on the initial cluster size N_0 can thus not be observed. Exemplarily, the evolution of the number of constituent atoms $N(t)$ for two different initial cluster sizes $N_0 = 10^3$ (small cluster) and $N_0 = 10^6$ (large cluster) are shown in fig. 2.12 for the first stage of evaporative cooling (0.01 ms).
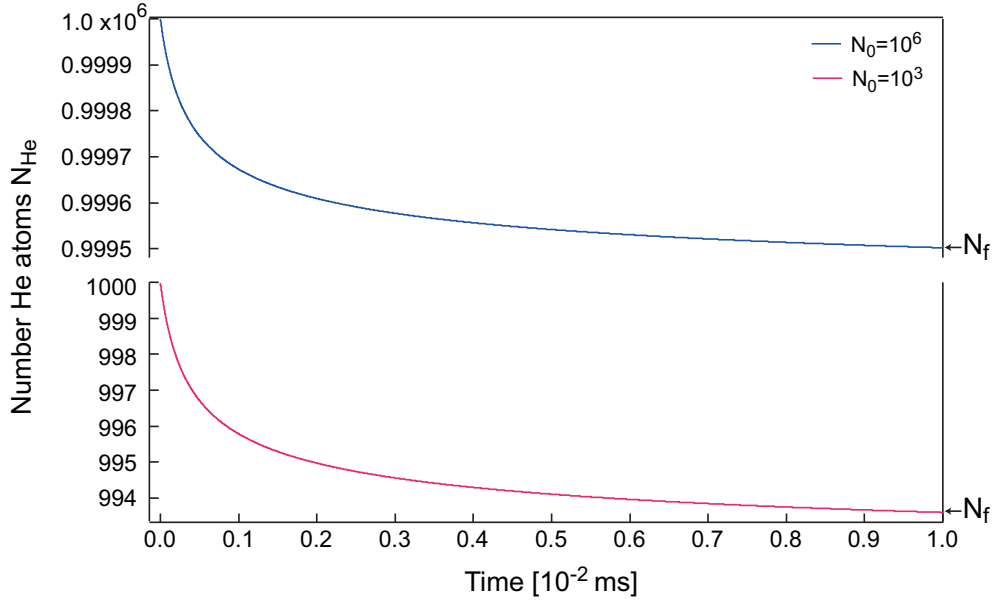
Figure 2.12: Temporal evolution $N(t)$ of the constituent atoms for He clusters of an initial size $N_0=10^3$ (representing small clusters, bottom panel) and $N_0=10^6$ (representing larger clusters, top panel) in the first stage of the evaporative cooling process. The initial temperature is $T_i=1$ K in both cases. On a scale ranging from the final cluster size N_f at which the cluster equilibrates, to N_0, it can be seen that the behavior is identical.

The differential equation (2.35) does not have a dependence on the cluster size as, for example, E_0 is not independent of the droplet size as it is presumed in the statistical model. Indeed, when it is solved for different cluster sizes N_0 at equal initial temperatures T_i, the functions obtained as solutions $T(t)$ all exhibit the same behavior (not shown). Cooling processes and the lowest temperature that can be reached in a cluster are closely related to the binding energy (per atom), which is lower for small clusters [17]. In the *LDM*, the reduction of binding energy is given by a cluster size dependent factor for the surface energy correction [167]. Cooling and evaporation rates of (liquid) clusters at a given temperature are determined by unimolecular rate constants. These rates are functions of the cluster size through the heat capacity of the cluster which is a function of the cluster mass[5] and temperature [162, 168]. This is of fundamental importance for thermal processes taking place in a He cluster. Time scales for evaporative cooling are further determined by the finite velocity at which a phonon travels through the cluster (for example from the center to the surface)[6], which is normally considered to be the speed of sound [17].

In general, the behavior of (small) clusters is different from that of bulk material at low temperatures because surface modes dominate their thermal properties. Moreover, the relative contribution from the surface energy to the thermal cluster excitation energy E with respect to the bulk contribution is a function of the size and temperature of a cluster [59].

In fig. 2.13, the solution function $T(t)$ of the differential equation (2.35) for $N_0 = 10^3$

---

[5]More accurately, the heat capacity per atom depends on the mass (or size) of the cluster.
[6]This becomes then more important for larger clusters or higher temperatures
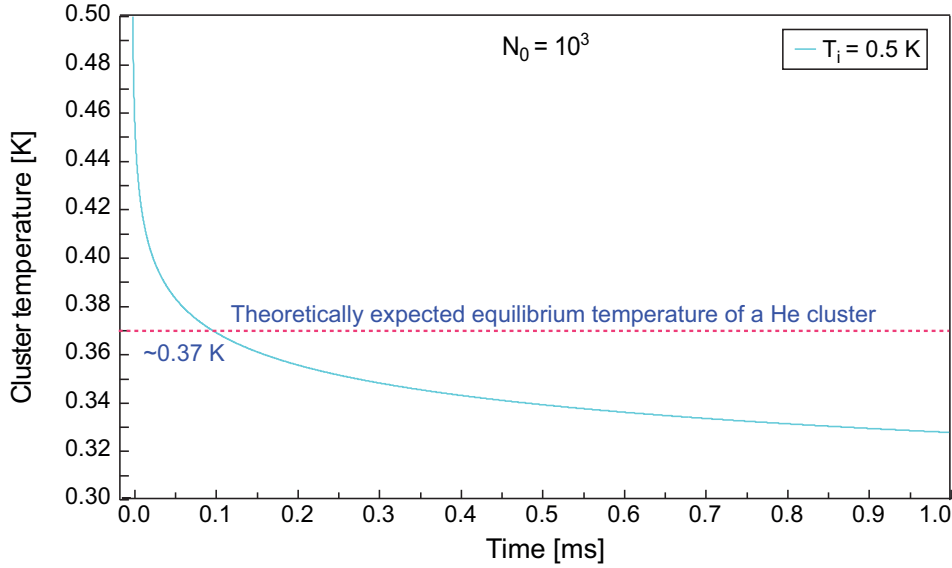
Figure 2.13: Temperature evolution $T(t)$ of a cluster containing 10^3 He atoms in the first millisecond of the cooling process. The initial temperature is $T_i = 0.5$ K. The dashed horizontal line indicates the known cluster temperature of ≈ 0.37 K.

He atoms and $T_i = 0.5$ K is displayed on an experimental time scale. The cluster temperature rapidly decreases in the very first stage, and reaches a temperature of ≈ 0.3 K after 1 ms which is close to the known internal equilibrium temperature of a ^{4}He cluster having a size of $N_{He} \approx 10^3$ He atoms of $T \approx 0.37$ K [15, 17, 169]. It can be seen that the statistical model describes the cluster temperature evolution quite well.

Energy removed

The question arises as to how many He atoms need to be evaporated in order to release the absorbed energy and to cool down the cluster+dopant system.
In fig. 2.14, the ratio of the final cluster size N_f reached after $t = 1$ s of evaporation to the initial cluster size N_0 is displayed as a function of the initial temperature T_i. Evidently, the relative loss of He atoms is larger for the smaller clusters, but this is reasonable due to the constant number of boiled-off He atoms for equal amounts of energy absorbed.
An estimation of the energy removed by evaporating the outermost layer of He atoms of a cluster can be obtained on the basis of the *liquid drop model* (see Ch. 1.3). The surface area of a He cluster is determined as $A_S = 4\pi R_d^2$. The volume of a monoatomic layer then follows by multiplying A_S with the approximate "diameter" of a He atom of $d_{He}=$ 280 pm [112], and the number of He atoms contained in the shell is obtained from the bulk density of liquid helium. However, the density considered in the LDM is predicted to decrease to 90%–10% of the bulk value of $\rho = 0.022$ atoms Å^{-3} [15] over the surface area with a thickness of ≈ 10 Å. When for each evaporated atom, an energy amount equal to its binding energy of 7.2 K is assumed, the amount of energy E_S removed by evaporating the first monoatomic shell of the cluster is obtained as given in table (2.4). E_S is determined for three different droplet sizes $N_{He} = 10^4$, 10^6, and 10^{12} He atoms.

In conclusion, the statistical model developed in ref. [59] is found to be able to predict the initial temporal evolution of the cluster temperature $T(t)$ and the evaporation rate
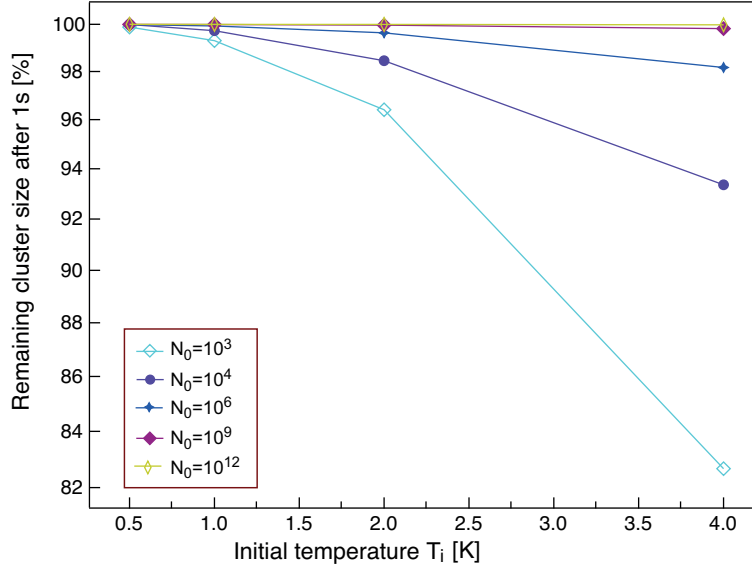
Figure 2.14: The ratio of the number N_f of He atoms in a He cluster that remain after 1 s of evaporative cooling to the initial number N_0 of constituent He atoms is shown as a function of the initial temperature T_{init}.

Table 2.4: The amount of heat released *via* evaporating the outermost shell of He atoms from the cluster is determined for three different cluster sizes N_{He}. N_S is the number of atoms contained in the outermost droplet shell of surface area A_S. On evaporation, each He atom carries away its binding energy of ≈ 7.2 K, which leads to a total energy E_S released when N_S atoms are evaporated.

N_{He}	A_S [Å^2]	N_S	E_S [eV]
10^4	$2.9 \cdot 10^4$	166	0.1
10^6	$6.2 \cdot 10^5$	3546	2.2
10^{12}	$2.1 \cdot 10^9$	$1.2 \cdot 10^7$	$7.8 \cdot 10^7$

$\Gamma(t)$ in terms of the rapid boil-off of most of the evaporated He atoms in the first stage of the cooling process ($\approx 10^{-8}$–10^{-7} s). This is also predicted by theories and observed in experiments [15, 17]. However, this is no longer true for longer times $t > 1$ ms, when the predicted temperature evolution $T(t)$ deviates from other results. While the temperature is predicted to stop decreasing when the cluster has reached thermodynamic equilibrium, as commonly stated in the literature, here the temperature rather continues dropping steadily. Therefore, for a correct prediction of $T(t)$, other mathematical methods such as Monte Carlo calculations should be employed.

Furthermore, a difference in cooling or evaporation rate depending on the initial cluster size N_0 is not obtained from the results of the statistical model.

2.6   Summary

This chapter treats the (thermodynamic and microscopic) properties of charged superfluid He clusters which are generated either by electron impact ionization or *via* ion pickup and subsequent dynamic processes. The probability for ion pickup processes is determined depending on the collisional cross section and the particle density in the scattering cell

(ion trap). The ion-He interaction is considered and the solvation energy released when a multiply charged large (protein) ion is immersed in a superfluid He droplet is calculated. Cooling mechanisms of He droplets and dopant+droplet systems are discussed.

Chapter 3

Experimental

The experiment we set up provides for the possibility to study mass–to–charge selected biomolecular ions at sub–Kelvin temperatures in order to obtain insight into molecular properties of large proteins. The He droplet technique is used for cooling of the species investigated.

This chapter starts with a motivation for carrying out an experiment of this kind. Then, the experimental setup is presented and the individual components are described. In Ch. 3.2, the experimental sequence employed is introduced. Then, an introduction to the molecular species that are chosen as foreign dopant particles of the He droplets is given in Ch. 3.3. The results from the characterization of the ion trap and the two He droplet sources are presented in Ch. 3.4.

3.1   Experimental setup

Fundamental idea

The aim was to set up an experiment which permits us to obtain detailed information on the properties of large biomolecules. It is realized by a combination of an ion source for the generation of intact biomolecular ions in the gas phase, various mass spectrometric techniques, a linear ion trap, and a pulsed He droplet source.

The basic experimental procedure starts with the generation of gas-phase ions *via* electrospray ionization, which are then mass–to–charge selected by a quadrupole mass filter and accumulated in a linear hexapole ion trap. After the trap has been filled with ions, the He droplet beam is turned on, passes through the trap, and the stored ions are picked up by superfluid He droplets. Doped droplets exiting the trap can be further investigated by, for example, laser spectroscopy. We employ a pulsed He droplet source which is expected to form large droplets at high droplet intensities per pulse [113]. Large droplets are needed for picking up and cooling large charged molecules, in order to accommodate the release of the energy transferred from the species incorporated. All internal and kinetic energy of the molecule as well as the solvation energy upon immersing the particle in liquid helium is released into the thermal modes of the He cluster and is usually removed from the cluster *via* evaporation of He atoms from its surface. Upon evaporation, each atom takes away its binding energy in the cluster, of ≈ 7.2 K, which results in an effective cooling of the cluster itself and of the dopant embedded.

The experiment provides for the investigation of large biomolecules which are

present in a well-defined state at the moment of interrogation. This is realized by several parameters allowing for manipulation and control of the gas-phase ions: In the electrospray process, the charge distribution and oligomeric state of the ions which enter the high vacuum region is selected, while during transfer through the different pressure regions, the kinetic energy of the gas-phase ions can be defined. A specific mass–to–charge ratio can be selected using a quadrupole mass filter and, perhaps in the future, a certain conformation might be selected by using ion-mobility mass spectrometry (see Ch. 5). The ion beam can be focussed and manipulated by ion optical elements and deflected by 90° with a quadrupole bender which acts as an energy filter. Then, the beam is injected into an ion trap in which the ions are slowed down *via* collisions with buffer gas and accumulated. The ion trap serves as a pickup cell for doping the He droplets which traverse it after they are produced in a pulsed-gas expansion. Incorporated in the droplets, the ions are translationally and internally cooled down to the internal He cluster temperature of ≈ 0.37 K. This provides for a thermostatic control over the temperature of the ions being investigated. As the kinetic energy of the doped droplets exceeds the longitudinal trapping potential, they can leave the trap to be further investigated. For this purpose, the experiment can flexibly be combined with various experimental techniques. A scheme of the experimental setup
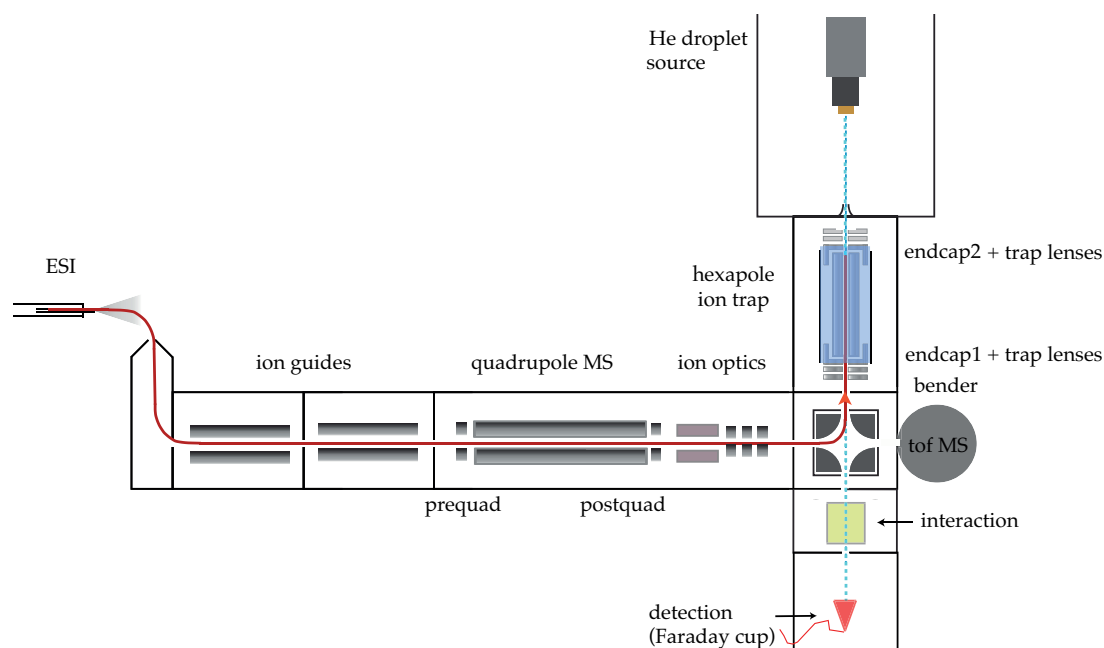
Figure 3.1: Scheme of the experimental setup. Ions are brought into the gas phase *via* electrospray ionization, are mass–to–charge selected by a quadrupole MS and stored in an ion trap from which they can be picked up by He droplets. The droplet beam is shown as a blue dotted line. Experiments on the ion + droplet complex can be performed in the *interaction region*, for example by applying electrostatic fields in order to determine the droplet size distribution (for further details see text). After some distance downstream, the direct ion current is measured. The central axis of the experiment is defined by the skimmer of the source chamber, the trap openings, and the bender lenses. The red trace depicts the flight path of the ions from the *ESI* source to the hexapole trap.

is shown in fig. 3.1. It is composed of four main parts, which are a mass spectrometer (MS), an ion trap, a helium droplet source and a stage for further investigation and detection. In the following, the "central experimental axis" is defined by the pinholes

between the He droplet source and the detection region, i.e. by the skimmer in the droplet source chamber, the trap openings, and the bender lenses. The red line depicts the flight path of the ions through the apparatus, the blue dotted line the He droplet beam.

The part of the setup from ion production to detection in a time-of-flight mass spectrometer is a modified version of a commercial *Q-tof Ultima MS* from *Waters Corporation* equipped with an electrospray ion source, two ring-electrode ion guides, a quadrupole mass filter and a high-resolution time-of-flight mass spectrometer with a double reflectron. The *Q-tof Ultima MS* is modified by installing ion-optical elements behind the quadrupole and an electrostatic quadrupole deflector. The individual components are described in the following.

3.1.1   The modified QTof Ultima

A *QTof Ultima* from *Waters Inc.* has been modified becoming the front part of the experimental setup. As the instrument was delivered, it was fully equipped with vacuum pumps, though all power supplies and electronics still had to be installed. These were either manufactured in the electronic workshop of the Fritz Haber Institute, or already existing equipment is installed, for example an RF power supply from *Extrel* for driving the quadrupole.
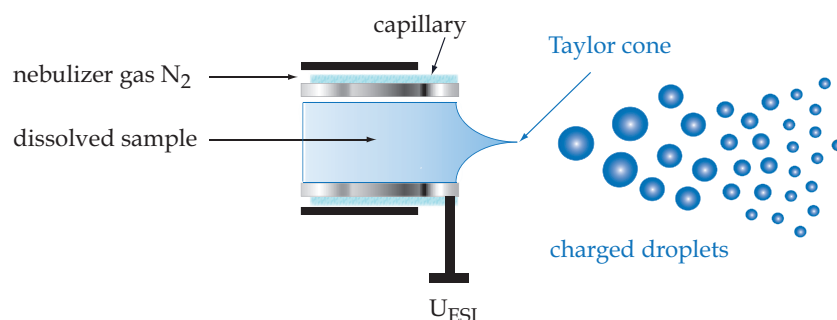
Figure 3.2: Electrospray ionization source. The sample solution is pulled by an electric field of 2–4 kV out of a metal capillary, accompanied by formation of the so-called *Taylor cone* at the tip, from which charged droplets are emitted.

Intact and multiply charged peptides and proteins are produced by electrospray ionization (see Ch. 1.2.1). The instrument is equipped with a so-called Z-spray source where the ions are first deflected by 90° from the capillary into a cone. Then, the ions are deflected again by 90° and enter the first ion guide. The Z-spray source allows only charged particles to enter the high-vacuum region, while most neutral particles and solvent molecules will hit a metal plate opposite the capillary in the straight-ahead direction.
The electrospray process can be used to control the charge distribution and the oligomeric state of the ions produced and can be controlled in a first step through the composition of the solution which contains the dissolved molecules, and in a second step by the applied voltage to the capillary. Furthermore, the cone voltage determines the charge states which are transmitted and also the oligomeric state, since a high cone voltage can lead to fragmentation of the gas-phase ions.
The dissolved sample is sprayed at a typical flow rate of 5–15 μl/min through a metal

capillary with an inner diameter of $\approx 100\,\mu m$ to which a high voltage of 2–4 kV is applied. The entrance cone of the vacuum chamber is set to a voltage of typically ≈ 30–120 V with respect to ground. This so-called cone voltage has an influence on the charge state distribution of the electrosprayed molecules [170]. Heated desolvation (120°C) and nebulizer gas (typically N_2) at flow rates of around 300 l/min and 22 l/min, respectively, flow together with the sample spray in order to promote evaporation of the solvent in the *ESI* process.

After the ions are brought into the gas phase by the electrospray process, they pass through two differentially-pumped stages with background pressures of 11 mbar and 1 mbar, respectively. The ion beam is radially confined by radiofrequency fields in an ion transfer system in both pressure stages before it reaches the high vacuum region at $\approx 1{\cdot}10^{-6}$ mbar. The ion transfer system consists of two ring-electrode ion guides which are composed of a stack of thin electrodes (0.5 mm thick) with a circular central opening diameter of 5 mm. The electrode assemblies are each terminated at the far end by an

Figure 3.3: Photo of a ring-electrode ion guide.

end cap with a pinhole of ≈ 1.5 mm opening diameter, leading to the next lower pressure region (see fig. 3.3). During passage through the ion guides, collisional cooling takes place and the gas-phase ions are thermalized by collisions with background gas molecules to a well-defined (thermal) kinetic energy.

The ring-electrode ion guides are driven by a commercial radiofrequency source (*Ardara*) with two RF outputs generating a maximal RF amplitude of about 500 V$_{pp}$. One of the outputs emits radiofrequency radiation at 1.4 MHz, the other at 2.8 MHz. After leaving the ring-electrode ion guides, the ion beam passes through a quadrupole mass filter which is driven by an *Extrel* power supply operating at 880 kHz. At the end of each quadrupole rod, there are installed four short rods, the so-called *pre–/post–*quadrupole rods, which run in RF-only mode and serve to shield the quadrupole towards the outside and thus generate a more homogeneous field at the edges. Furthermore, they have a focussing effect on the ion beam and, in the experimental setup, they can be used for determining the ion energies by blocking the ions with an electric field of increasing strength until no more ions are transmitted.

After the quadrupole, the original *QTof Ultima* is extended by ion-optical elements. First, there is an Einzel lens installed for focussing the ion beam; it is followed by two pairs of deflection plates for manipulation of the ion beam in x and y direction and to

permit corrections for vertical and horizontal deviations of the beam direction. Behind the deflection plates, the ions pass through a grounded drift tube that screens the ion beam from stray fields until they reach the quadrupole bender region.

A quadrupole deflector works basically as an energy filter [171]. Charged particles with a certain kinetic energy can be deflected by 90° in an electrostatic field in the interior of the bender. The appropriate potential energy landscape is generated by the voltages applied to four hyperbolic electrodes (A, B, C, and D) which are located at the edges of the bender chamber (see fig. 3.4) and form two pairs of diagonally opposite electrodes set to the same potential (AC and BD). The potential difference $U(AC) - U(BD)$ is decisive for transmitting ions of a certain energy which enter the bender region and are deflected around the so-called inner pole (the negative pole in case of positively-charged ions) in order to properly exit the bender after being deflected. Central in the four walls of the bender chamber are four circular electrodes as entrance/exit lenses in each direction (L_1, L_2, L_3, and L_4) with apertures having an inner diameter of ≈ 1 cm. They are insulated from the grounded walls by small sapphire pellets and voltages can be applied to them in order to focus the transmitted ion beam. Stainless steel tubes are installed behind each of the lenses to screen the ions from stray electromagnetic fields on their flight to the respective succeeding device: Ions which come from the *ESI* source and pass through the bender in the straight-ahead direction (when no voltages are applied to the bender electrodes) will enter the time-of-flight mass spectrometer for analyzing purposes. After being deflected by 90° the ions are injected into the hexapole linear ion trap and accumulated. In fig. 3.4, trajectories of ions are shown which pass through the bender
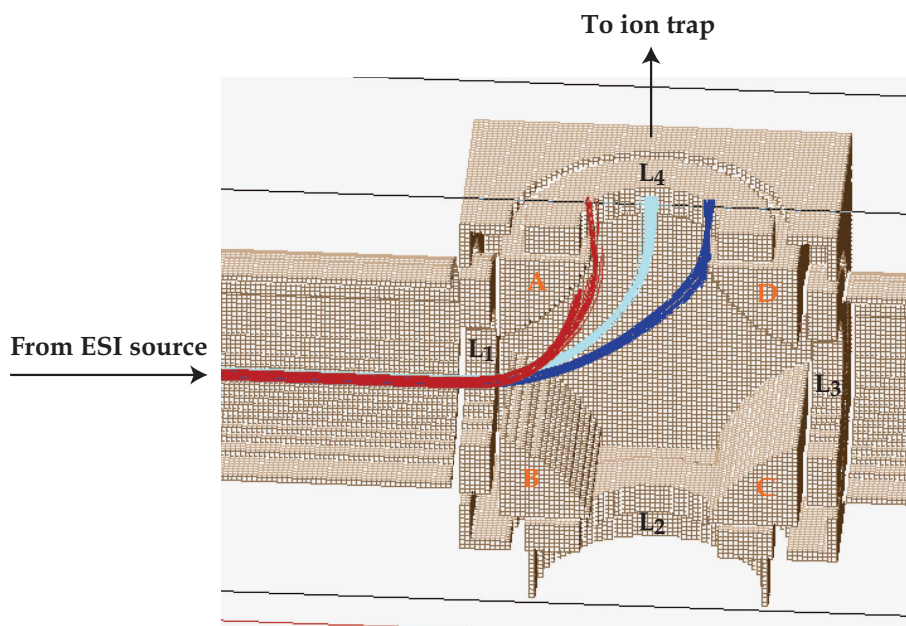
Figure 3.4: Ion trajectories in the quadrupole deflector. The traces are generated by *Simion* [172]. The traces in cyan show the trajectories of ions which can pass through the bender with the appropriate settings for the respective ion energies. The blue traces show the ion trajectories when the potential difference between the two electrode pairs is too low, the red traces show the ion trajectories when the potential difference between the two electrode pairs is too high.

for different settings. The trajectories are generated using the ion simulation program *Simion* 8.0 [172]. The particles defined have similar properties to protonated Phe$^+$ ions.

Some 200 positively-charged ions, each having a mass of 165 amu are generated and are emitted from a circular source in a Gaussian distribution of kinetic energies with a mean value of 30 eV and a FWHM of 5 eV. They enter the quadrupole deflector from the left-hand side. The cyan lines show the trajectories for the appropriate electrode settings to deflect the ions by 90° (the angle is measured between the direction from which the ions enter the bender and the axis of the exit lens with respect to the center of the bender) for the ions defined with a voltage difference AC–BD of 99 V. The blue traces show the trajectories of ions when the voltage difference is too small to guide the ion packet correctly through the bender. The incoming ions are deflected by an angle larger than 90°, and the ions cannot exit the bender through lens L_4, but instead collide with electrode D. The red traces show the opposite case. The voltage difference is too large, the ions are deflected by an angle which is too small, and collide with electrode A.

Ion detection

The time-of-flight mass spectrometer is assembled as shown in fig. 3.5. Incoming ions enter through a stack of electrodes that are denoted as *pusher*, *puller*, and V_1 electrode. There are two reflectrons for mass separation that are set to the same potential, which (in
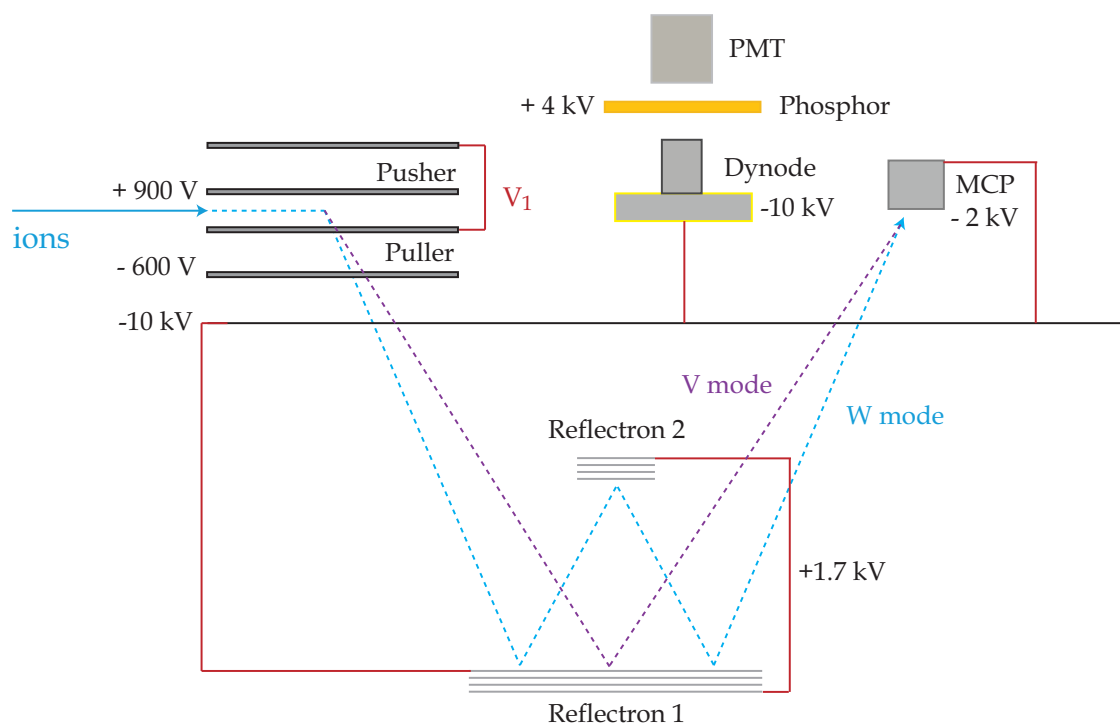
Figure 3.5: Trajectories of ions in the *QTof* time–of–flight mass spectrometer with double reflectron.

positive ion mode) lies above the flight tube potential of –10 kV. Two different detectors are installed in the time-of-flight mass spectrometer. One is a microchannel plate (*MCP*) detector for detection of mass-to-charge selected ions that have passed one (*V mode*) or both of the (*W mode*) reflectrons. The other one is an assembly that consists of a gold-coated plate on which incoming ions that are not injected into the time-of-flight mass spectrometer are accelerated by a voltage of –10 kV. Secondary electrons are released and accelerated onto a phosphor screen that is held at a voltage of +4 kV. Emitted photons

are detected by a photomultiplier tube (*PMT*). This detector is used for recording mass spectra by scanning the preselecting quadrupole mass filter over a certain m/q ratio range. When ions enter the time-of-flight mass spectrometer, they can be processed, in principle, in two different ways. Either they continue their flight straight on and are detected in the *PMT* detector assembly without mass-to-charge selection. Or else, they are deflected vertically towards the first reflectron when *pusher* and *puller* are operated in pulsed mode. Pusher and puller plates are switched by high-voltage switches (*Behlke*) with a maximal rate of 1 kHz between the voltage V_1 and 900 V (*pusher*) or –640 V (*puller*), respectively. The voltage V_1 determines the angle under which the ions enter the reflectron. This determines whether the ions pass only the first reflectron and then fly straight on to the *MCP* detector, in the so-called *V mode*; or pass both reflectrons in the *W mode*, yielding higher mass resolution $\left(\frac{m}{\Delta m} \text{ up to 15 000}\right)$. The ion signal detected is amplified using a current-to-voltage converter (*Philips* model 6954) and recorded on a digitizer card. In the experiments presented in this thesis, two different digitizers are used (*acqiris DC 211, DC 440*), differing mainly in the achievable resolution (DC 211: 8 bit, bandwidth 1 GHz, sample rate 4 GS/s; DC 440: 12 bit, bandwidth up to 300 MHz, sample rate up to 400 MS/s) and in the number of points that can be recorded.

3.1.2 (Pre)amplifiers

For detection and amplification of ion signals from doped He droplets, different detectors and amplifiers are used. One is a conversion dynode-type, the so-called *Daly* detector [173]. Charged particles are accelerated towards an off-axis metal block (aluminum) that is set to a high voltage (–20 kV). Secondary electrons are released and accelerated towards the sensitive surface of an electron multiplier which is held at a voltage +17 kV with respect to the aluminum block at a distance of $\approx$ 5–6 cm. The advantage of this type of detector is its sensitivity and fast detection speed. This should allow for observing transients of charged particles having pulse widths that presumably reveal the "real" longitudinal velocity distribution Δv_x without additional broadening of the signal pulse due to the detector electronics. A disadvantage, however, is that the detection sensitivity of a Daly detector is mass dependent, with lower sensitivity for heavy particles.

When a Faraday-type metal detector is used to detect the incident current of ion-doped He droplets, the signal is amplified by one of the two amplifiers as presented in the following. For more details, see the respective manuals [174, 175]. They work on different operation principles; the circuit diagrams are shown in fig. 3.6. In the top panel (a), a current-to-voltage amplifier is displayed, which has a calibrated maximal gain of 10^{11} V/A and a gain-dependent maximal bandwidth of 1.1 kHz (*FEMTO* DLPCA-200). It can be seen in the diagram that current-to-voltage conversion is effected by an operational amplifier (op-amp) [174]. The two main measurement modes are "*High speed (H)*" and "*Low noise (L)*". Parallel resistances R_ρ=1k...1GΩ enable the measurement at different sensitivities and thus at different detection speeds. In general, enhancing the sensitivity of the measurement is always at a cost in the time constant of detector response. For the *FEMTO* DLPCA-200 the rise/fall time constant for a gain setting of 10^5V/A, for example, is 700 ns (at *High speed* setting "H") and for 10^{11}V/A it is 300 μs [174]. The bandwidth limiter can be used to set the upper cutoff frequency from 500 kHz down to 10 Hz. Further features are a toggle to choose between AC or DC input coupling, an internally applied DC bias, and –parallel to the op-amp series– an overload
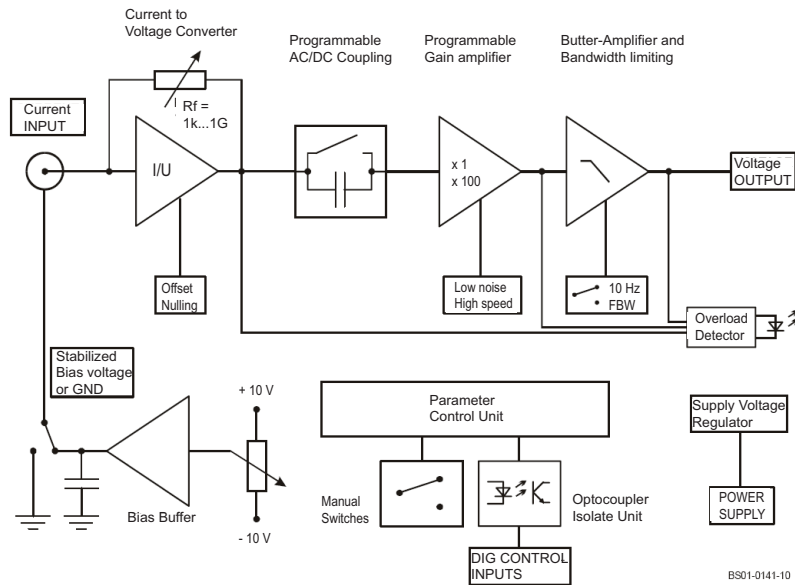
(a)
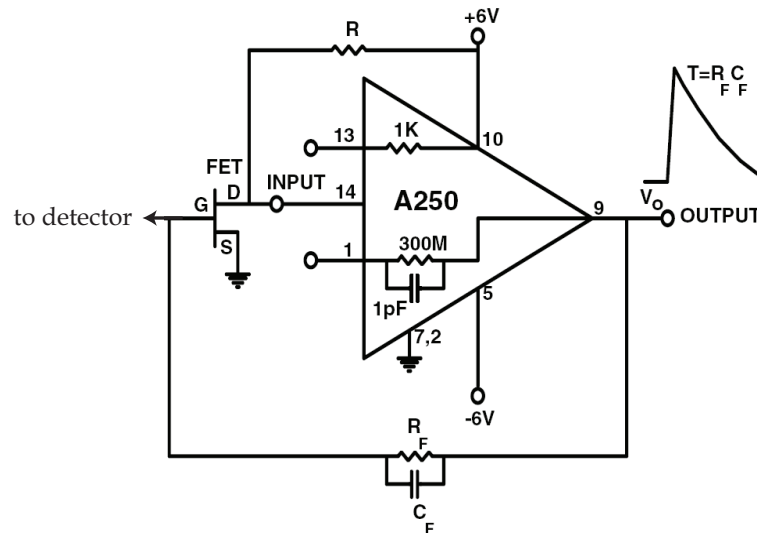
(b)

Figure 3.6: Schematic circuit diagram of the amplifiers used (a) *FEMTO* DLPCA [174] and (b) *Amptek* A250 [175].

detector to protect the detector from high input currents. The use of extra-shielded low noise cables between detector and preamp helps to enhance the signal-to-noise ratio.

The other amplifier in use provides a better signal-to-noise ratio and a high sensitivity at a fast response at the same time. The detector response to an incident ion event is fast, of the order of nanoseconds (< 20 ns), whereas the trailing edge is much slower ($\approx 300\ \mu$s) [175].

Its working principle is based on a solid state field-effect transistor (*FET*) which is used for weak-signal amplification. Additionally, the *AMPTEK* A250 contains a so-called feedback capacity C_f and resistance R_f, which can be used to adjust the current passing through the FET. The capacitance C_f is inversely proportional to the sensitivity and has

a typical value of $C_f < 1$ pF for low-noise applications [175]. The gain can be enhanced by inserting a smaller capacitor. The feedback resistor R_f defines the time constant of the response function by returning the output of the integrating loop to the baseline (see fig. 3.6). It has a typical value of $R_f > 1\,G\Omega$ for low-noise applications [175]. In our setup, a feedback capacitor of $C_f = 0.1$ pF (*American Technical ceramics*, Mod. 700 B0R1BW–500X, 0.1 pF) and resistor of $1\,G\Omega$ (*ELTEC Instruments* Model 104, $1\,G\Omega$) are inserted. One possibility to enhance the signal–to–noise ratio and sensitivity is to cool the FET to temperatures down to 133 K, where it has maximal transconductance, and hence reducing the detector leakage current and noise [175].

The *AMPTEK* A250 preamplifier has no calibrated gain. It is connected to an additional amplifier (*Ortec–Brookdeal*) with a tunable amplification factor and tunable bandwidth of the transmitted frequencies.

3.1.3 Ion accumulation and storage: Hexapole ion trap

Linear ion traps

A detailed review on RF devices is given by Gerlich [176] and explicitly concerning multipole linear ion traps by Douglas *et al.* [177]. Two-dimensional multipole linear traps are expected to yield high ion injection efficiencies and ion storage capacities, compared to three-dimensional Paul traps. Ions are radially confined by a two-dimensional time-dependent electric field and longitudinally by DC voltages that are applied to longitudinal electrodes [177]. These can be simple circular electrodes with (circular or elliptic) openings. The trap is composed of an array of parallel rods that are symmetrically placed on
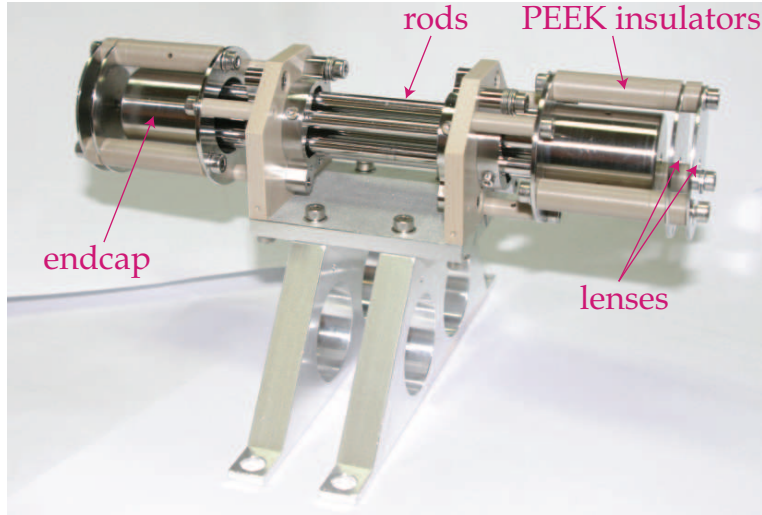
Figure 3.7: Photo of the short trap. The metal enclosure as mentioned in the text is not shown on the picture.

a bore hole of radius r_0. Time-dependent voltage alternating at a radio frequency (RF) Ω and with an amplitude V is applied to the system of rods, giving one RF phase alternating on every second rod. The RF can oscillate around an offset voltage that is applied to the whole rod array and defines the hexapole bias voltage. Ions in RF fields perform a "wiggling" free motion in each orthogonal direction x and y along the central trap axis

[177]. In general, the motions of particles in multipole fields are strongly coupled in the x and y direction. The only exception is the motion in pure quadrupole fields where the two directions can be decoupled and treated independently [177]. Ion trajectories in RF multipole fields can be described by an effective mechanical potential as a function of distance from the central rod axis which is proportional to $r^{N_r - 2}$ with r the distance from the trap axis and N_r the number of rods. In the case of a hexapole trap, the effective potential is thus proportional to r^4. The ion motion is not harmonic, and the frequency of motion depends on its amplitude. Higher order multipole effective potentials are flat close to the central axis and increase with stronger slope on approaching the rods [177].

Trap operation

The experiments presented in this thesis were performed using two different linear hexapole ion traps. They are both composed of six rods with a diameter of 5 mm that are placed on a 14.1 mm diameter circle[1] and longitudinal trapping electrodes called *endcaps* at each end. They are both equipped with a grounded metal enclosure within which He buffer gas is injected to support ion trapping. Common to both traps are also two pairs of plates used as ion lenses which are installed in front of each of the *endcaps*. The first version of the trap has rods of a length $L = 14.5$ cm and circular openings of 1.5 mm radius in the *endcaps* and lenses; it is denoted as "short trap" in the following.
The second trap has rods of double length $L = 30$ cm and longer elliptical holes in the *endcaps* and lenses. These allow for correction of deviations between the trap axis and the central axis of the experiment. The orifices in the *endcaps* are 6 mm long and 4 mm high, those in the lenses are 6 mm long and 3 mm high. The trap is operated with 1.7 MHz RF at a voltage of ≈ 250 V_{p-p} amplitude that is oscillating around an offset given by the hexapole bias voltage U_{bias}. The RF voltage is produced by a commercial radio setup, where a radio transceiver emits an RF output that is fed to a transformer [179]. The secondary winding of the coil is directly connected to the rod system of the trap, each second rod to one RF phase. Additionally, to tune the resonance frequency in the secondary circuit, a coil with a tunable inductivity of up to 36.6 H is connected parallel to the secondary winding of the transformer. The longitudinal trapping electrodes are kept 1–10 V above the rod DC level and thus define the trap depth as the difference between *endcap* and hexapole bias voltage with a potential energy of:

$$E_{pot} = q \cdot (U_{endcap} - U_{\text{bias}}) \tag{3.1}$$

The electrostatic potential keeps ions with lower kinetic energy stored in the trap, which means that for higher ion charges the trapping potential becomes deeper.

In order to efficiently store ions, we inject helium buffer gas into (the enclosure of) the hexapole trap, so that the measured background pressure in the trap chamber averages $\approx 1.2 \cdot 10^{-5}$ mbar. Presumably, the ion density in the trap reaches the space charge limit of approximately 10^6–10^7 ions $\cdot$ cm^{-3} if the accumulation time t_{acc} is long enough. Ions in the trap are thermalized to the hexapole bias potential by collisions with the buffer gas atoms. Each collision removes up to $1/2\,\mu v_{rel}^2$ from the ion. Therefore, the translational energy of the trapped ions is then determined by the hexapole bias voltage. The cooling of incoming ions in the trap by He buffer gas atoms is schematically shown in fig. 3.9.

---

[1]in order to obtain the optimal potential distributions in the trap, it is found that the ratio of rod radius to the distance from the symmetry axis should be 0.5375, giving an approach an ideal geometry [177, 178].
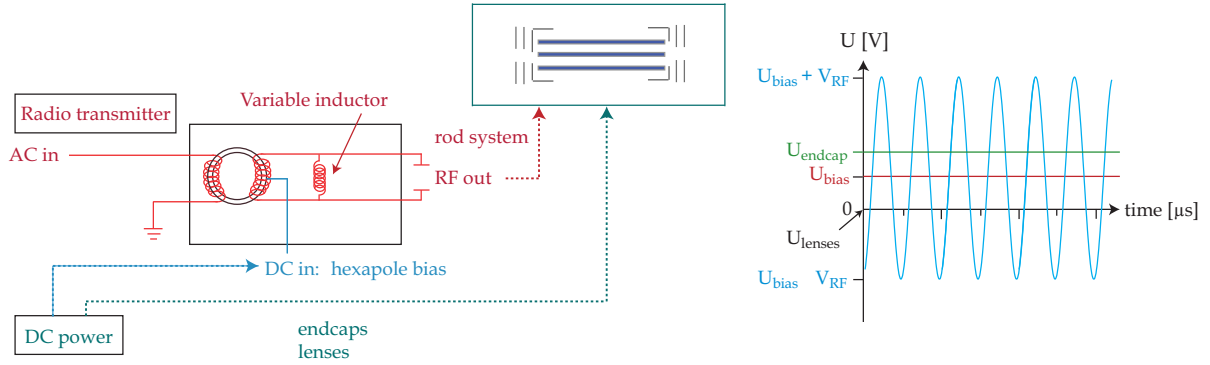
Figure 3.8: RF transmit to trap. AC voltage oscillating at radio frequency is fed to the primary circuit of a transformer. The transformed RF voltage is directly connected to the rod system of the trap, each RF phase alternates on the rods. The DC voltage as offset for the RF voltage is fed into the secondary coil of the transformer *via* a contact in the middle of the coil. The coil parallel to the transformer serves as impedance matching. DC voltages for the *endcaps* and lenses are provided by low voltage power supplies. On the right in the figure, a scheme of the potentials in the trap is shown (not on a realistic scale). The RF oscillates around the DC hexapole bias voltage U_{bias}, the potential of the longitudinal trapping voltages are higher than U_{bias}, and the lenses are grounded.
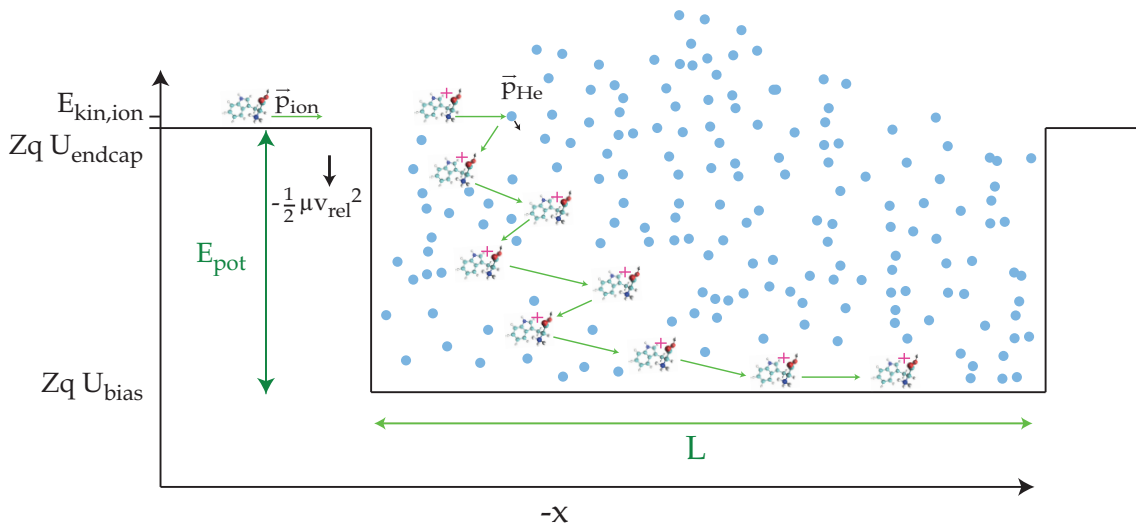
Figure 3.9: Accumulation and trapping of ions which enter the hexapole trap. A trapping potential of $E_{pot} = Zq \cdot (U_{endcap} - U_{bias})$ is applied. Entering ions are translationally cooled by elastic collisions with He buffer gas atoms. In each collision, an energy of up to $1/2\, \mu v_{rel}^2$ is removed from the ion.

Effusion

When He buffer gas is pulsed into the enclosure of the trap, a pressure rise in the trap chamber can be observed after a delay of around 1–2 s. This delay is mainly caused by the time it takes the buffer gas atoms to effuse from the trap interior through the pinholes in the longitudinal trapping electrodes into the trap chamber, where they are detected as a background pressure rise. The question arises as to what buffer gas pressure is effectively required for a sufficient cooling of the incoming ions during ion accumulation in order to trap them. This pressure is assumed to be considerably higher than the measured pressure rise in the trap vacuum chamber; it is calculated here.

By means of the pressure rise ΔP in the trap chamber, the mass flow rate G can be

determined using eq. (1.10), giving the total mass of flowing gas per unit time at a given throughput in a vacuum chamber. The throughput $Q = \Delta P \, Z_p$ is determined by the observed pressure rise and the pumping speed Z_p of the pumps evacuating the trap chamber:

$$G = \frac{m_{\text{He}}}{k_B T} Z_p \Delta P = \ 1.0 \ \cdot \ 10^{-9}\,\text{kg s}^{-1} \quad , \tag{3.2}$$

with $\Delta P = 1.2 \cdot 10^{-5}$ mbar and the sum of the pumping speeds of the turbomolecular pumps used taken to be $500 \, \text{l s}^{-1}$. With the mass flow rate G, the number of particles N (mostly He atoms) that are flowing per time unit can be determined:

$$N(t) = \frac{G}{m_{\text{He}}} = \ 1.5 \cdot 10^{17}\text{s}^{-1} \quad . \tag{3.3}$$

$N(t)$ thus corresponds to the number of He atoms that has been effused from the trap through the orifices in the two *endcaps* and the lenses per unit time. This number can be calculated as the average number of thermal gas molecules of mass m that are impinging on a pinhole with area A in a wall per unit time as a function of particle number density $n = \frac{N_0}{V}$ [2], where N_0 is the total number of particles contained in a volume V [2]. Every particle that hits the pinhole will leave the volume V, which is the trap volume in this case. The area A is given here by the diameters of the orifices in the two *endcaps*, which each have an area of $F_t = \pi \, a \cdot b = 1.4 \cdot 10^{-5}\,\text{m}^2$, where a, b are the semiaxes of an ellipse with $a = 3$ mm and $b = 1.5$ mm.
The wall collision rate Z is given by:

$$Z = \frac{\text{number of wall collisions}}{\text{area} \cdot \text{time}} = \frac{N(t)}{V} \sqrt{\frac{k_B T}{2\pi \, m}} \quad . \tag{3.4}$$

The effusion rate ZA is defined by [2]:

$$ZA = -\frac{dN}{dt} = \frac{2\,F_t \cdot N(t)}{V} \sqrt{\frac{k_B T}{2\pi \, m_{\text{He}}}} \quad , \tag{3.5}$$

where V is the volume contained in the trap enclosure. The effusion rate is given by the number N of particles per unit time as determined by eq. (3.3). Eq. (3.5) defines a differential equation for the number of particles that impinge on the area A and leave the trap. The solution is a simple exponential function for $N(t)$:

$$N(t) \ = \ N_0 \exp\left(-\frac{t}{\tau}\right) \quad \text{with} \tag{3.6}$$

$$\tag{3.7}$$

$$\tau \ = \ \frac{V}{2\,F_t} \sqrt{\frac{2\pi m_{\text{He}}}{k_B T}} \quad , \tag{3.8}$$

the time constant for the effusion process and N_0 correspond to the initial number of He atoms contained in the trap before effusion occurs and are thus the interesting quantities. N_0 is determined under the condition that (at room temperature) after approximately
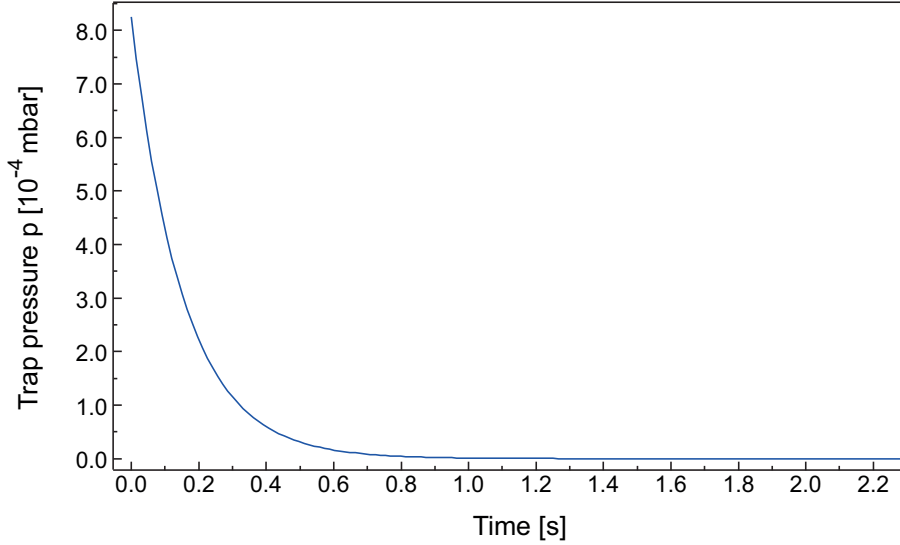
Figure 3.10: Temporal evolution of the gas pressure in the trap. It decreases as a function of time due to effusion.

1 s, the number of He atoms effused corresponds to the pressure observed in the trap chamber.

Taking values for the pinhole area $F_t = 1.4 \cdot 10^{-5} \mathrm{m}^2$ as given above, the volume of the trap enclosure of $V = 2.2 \cdot 10^{-3} \mathrm{m}^3$, and the atomic mass of helium gives a value for the time constant of $\tau = 0.15$ s. The number of particles that effuse from the trap interior per unit time as a function of time is then obtained from eq. (3.8) as:

$$N(t) = 2.8 \cdot 10^{21} \exp(-6.56\, t) \quad . \tag{3.9}$$

This, in turn, gives an initial particle density of buffer gas atoms in the trap interior (inside the enclosure) of $n = 6.2 \cdot 10^{18}$ atoms $\cdot$ cm^{-3} from multiplying the N_0 as determined by the trap volume V. Transforming the particle number density into pressure, an initial buffer gas pressure in the trap of $P_0 = 8.2 \cdot 10^{-4}$ mbar is obtained. It is almost two orders of magnitude higher than the measured pressure in the trap chamber. In fig. 3.10, the temporal decrease of the trapping buffer gas pressure present in an ion trap is shown for the calculated time constant τ.

3.1.4 Pulsed helium droplet source

In our experiments, helium droplets are produced in a pulsed isentropic free-jet expansion of 99.999% pure He gas under high pressure and low temperature into vacuum.
Formation of cold cluster beams requires a cryogenic valve cooled by a cryostat down to temperatures of a few Kelvin, a high-pressure clean He gas supply, a vacuum system with appropriate pumps, a beam skimmer, and a mechanism for aligning the He droplet source. The emitted gas flux is mainly determined by the applied gas pressure, the orifice diameter of the nozzle, and the time duration of gas expansion.

Continuous He droplet sources give high beam fluxes and therefore, they require pumps with high pumping speed to remove the emitted gas. Pulsed sources, on the contrary, are popular since they also give high peak fluxes but lead to comparatively low background pressures. This also allows for using valves with considerably larger diameter orifices than the often used $D = 5$ μm orifices of continuous sources. This is favorable for the cluster formation process since it leads to a slower expansion (see Ch. 1.3.4) and is further advantageous since larger opening diameters have a reduced probability of being clogged by impurities present in the helium gas which are frozen out at the cryogenic temperatures used. Another advantage is that pulsed devices can be readily combined with other pulsed techniques that are often employed in experimental setups, for example pulsed lasers, for further investigation of the doped droplets. A disadvantage, however, is that the initial expansion conditions P_0 and T_0 in pulsed expansions are not so well defined as in static continuous expansions due to the short periods of quasi-steady flux conditions during the opening and closing process. Additionally, heat production through moving parts and pressure gradients in the opening process lead to further reduced controllability *via* the initial stagnation conditions in terms of beam intensities and cluster sizes formed in the expansion .

To obtain information about cold molecules embedded in He droplets, it is preferable to use small droplets. Heavy charged particles are both difficult to manipulate with moderate electric fields and also, detection becomes difficult since the sensitivity of standard charged-particle detectors, which use the impact-induced release of secondary electrons as a first step, decreases rapidly for large m/q ratios.
Therefore, the challenge is to produce helium droplets in the optimal size range.

3.1.5 Components of the He droplet source

The main components of the helium droplet source are a pulsed valve that can be operated at cryogenic temperatures, a skimmer which separates the central part of the beam at a specified distance from the nozzle, a cryocooler and heater as well as a He gas bottle with reducer valve for providing the required source conditions (T_0, P_0). Experiments presented in this thesis were performed using two different valves installed in the He droplet source; they are described in detail in Ch. 3.1.6 and Ch. 3.1.7. The first one is a solenoid-type pulsed *Parker* General valve, the second one is an Even-Lavie valve [180] which contains also a solenoid but operating on a different working principle. Each valve is encased in a copper holding device that is directly mounted on the second stage of the cryostat. In fig. 3.11, the assembled *Parker* General valve mounted on the cold head is shown. At a distance of ≈ 5 cm downstream from the nozzle, the central part of the cluster beam is cut out by a skimmer (*Beam Dynamics*, model 2, orifice

diameter $D = 2$ mm) and it then enters the ion trap.

Helium gas under high pressure is supplied by a He gas bottle containing 99.999% pure He gas and equipped with a pressure reducing valve that allows for regulating the applied He gas pressure up to $P_0 = 100$ bar to the nozzle. The He gas is supplied by a $\frac{1}{16}$" stainless steel tube which is wrapped around the cold head and thermally anchored to the first stage of the cold head to provide efficient precooling of the gas. For cooling
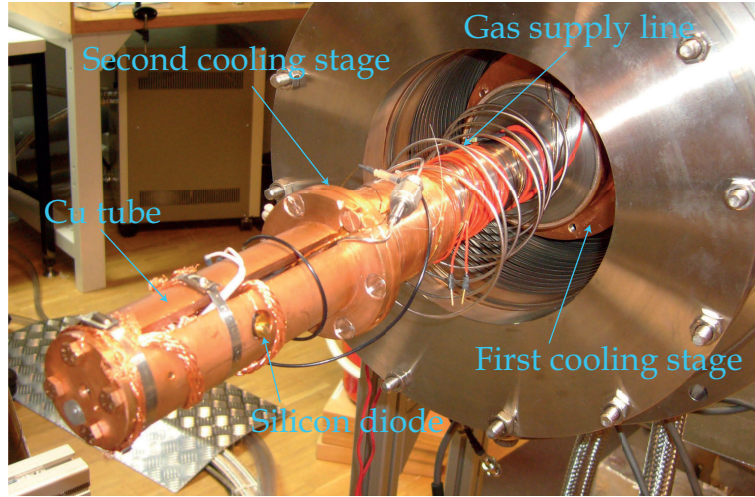
Figure 3.11: Photo of the assembled *Parker* General valve encased in the copper tube mounting, equipped with a Cu cover head to improve the cooling of the nozzle by the cryostat.

of the nozzle, a closed-cycle helium cryocooler (*Sumitomo* RDK 408D2) was used with a cooling power of 40 W at the first stage (30 K) and of 1 W at the second stage (≈ 4 K). The time required to cool the bare cold head down to the final temperature of ≈ 5 K at the 2nd stage is about 45 minutes, while the first stage reaches its final temperature of ≈ 30 K after around 30 minutes. However, with an attached mass the required time for cooling to the final temperature becomes longer and is roughly 90–100 minutes with the pulsed valve assemblies mounted. The expansion temperature T_0 is adjustable between 4.7 K and 30 K using a cartridge heater (*Watlow* 50 V, C1G-8638 155 W). The actual operation temperature is measured by a silicon diode temperature sensor (*Lakeshore* DT 670 CU) which is inserted into the faceplate. Heater and source temperature can be controlled and monitored by a commercial temperature controller (*Lakeshore* 331) using fully automatic proportional-integral-derivative (*PID*) control or partial manually set parameters. Temperature fluctuations of up to 1 K are observed in the operating cycle of the intake/exhaust of the cold head (≈ 1.3 Hz) which are possibly due to heating of the He gas. The fluctuations become more pronounced at higher applied stagnation pressure and higher repetition rate f due to heat production of the moving parts. The cold head is mounted to the vacuum chamber flange *via* a stainless steel bellows which allows for adjustment of the skimmer-to-nozzle distance through compressing or extending its length. This is done by means of a simple alignment device shown fig. 3.12. It consists of three threaded stainless steel ferrules which are connected to the front vacuum chamber flange on the one side and on the other side to the flange onto which the cold head is mounted. The ferrules have a clockwise thread on the one side and a counter-clockwise thread on the other side, requiring the use of right-handed tapered screws for the one and
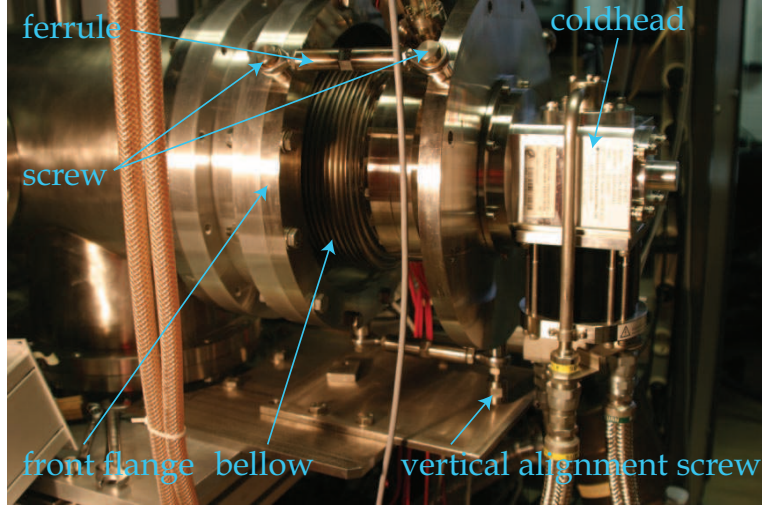
Figure 3.12: The adjustment device installed between the vacuum chamber and the flange on which the cold head is mounted is shown on the photo. It is used to compress or decompress the bellows through which the cold head is connected to the source chamber. In this way, the skimmer-to-nozzle distance can be changed within ≈ 3 cm and the nozzle plane as determined by the three ferrules (see text) can be tilted with respect to the vacuum chamber flange.

left-handed tapered screws on the other side. Thus, rotating the ferrule in a clockwise or counter-clockwise direction leads to further screwing-in of both screws into the ferrule or, respectively, screwing-out of both at the same time. The screws can be introduced into the ferrules at a flexible length within ≈ 1.5 cm each. The variability of this length allows for compressing or decompressing the bellows, which leads to a change of the distance between skimmer and nozzle. The three ferrules + screw assemblies define a plane for the nozzle and thus the emitted beam. Changing the length of one of them results in a tilting of the nozzle plane and thus allows for adjustment of the nozzle with respect to the skimmer and the global axis of the experiment. For adjustment of the vertical position of the nozzle, a screw under the cold head flange can be used. It provides for aligning the emitted beam in the parallel direction to the experimental axis without tilting.

The source vacuum chamber is evacuated by a turbomolecular pump with a pumping speed of 2400 ls^{-1} for He (*Varian*, Turbo-V 3k-T), backed by two rotating forepumps with a pumping speed Z_p of 25 m^3/h each, which, after ≈ 12 hours pumping, reaches a base pressure of $\approx 5 \cdot 10^{-7}$ mbar at a forepump pressure of $\approx 1 \cdot 10^{-3}$ mbar. The pumpout time constant $\tau = \frac{V}{Z_p}$ is estimated to be $\tau \approx 0.019\,s$ with the source chamber volume of $V = 0.5\,m \cdot \pi \cdot (0.17\,m)^2 \approx 0.5\,m^3$. When the cryocooler is running, the steady-state pressure is further lowered by 1-2 orders of magnitude due to cryopumping.

The valve opening length t_{puls} and the repetition rate need to be adjusted to control the gas flux into the source chamber, which must not lead to a pressure rise higher than $1 \cdot 10^{-4}$ mbar and a forepump pressure of $1 \cdot 10^{-2}$ mbar.

Cryogenic requirements

To enhance the thermal contact from the nozzle holder to the coldfinger, Apiezon^R grease is applied to the nozzle holder flange. A Ni-coated Cu heat shield is mounted on the first stage of the cryostat to screen the valve from black-body radiation. It is crucial for effective cooling to minimize the heat transfer from the surroundings to the valve. In case

of the *Parker* General valve, manganin (cryogenic) wire is used for electrical leads due to its low thermal conductivity [181].

For the *Parker* General valve, the resistivity of coil and leads together is 84 Ω at room temperature and decreases to 15 Ω at low temperatures due to the higher electrical conductivity of copper at low temperatures. For the Even-Lavie valve, thin copper wires of ≈ 0.5 mm diameter are used as electrical leads; the electrical resistivity of the coil with the wires and contacts is 0.6 Ω, and no significant decrease is observed at low temperatures. For this valve, the total electrical resistance between the power supply and the valve appears to be critical for correct valve performance. Similar copper wires are used for supply of the cartridge heater to heat the nozzle to a specific source temperature T_0.

3.1.6 *Parker* General valve droplet source

The first valve as a central part of the He droplet source described here is a solenoid-type[2] pulsed valve (*Parker* General valve Series 99) shown in fig. 3.14. The difficulty in using pulsed solenoid valves as He droplet sources is to operate them at cryogenic temperatures. Materials are required which can withstand ultralow temperatures without cracking and still keep the valve sealed. Kel-F (polychlorotrifluoroethylene, PTCFE) turned out to have acceptable low-temperature properties and behavior.
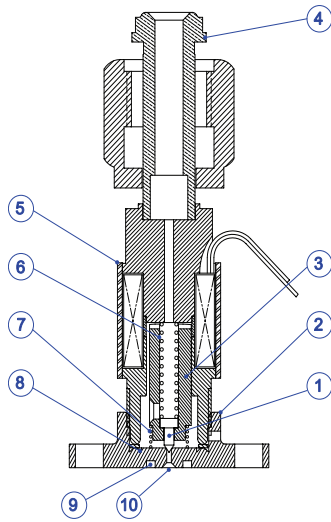
The valve used in this study consists of a faceplate, the valve body and a $\frac{1}{4}$" VCR tube fitting to facilitate the connection to a gas supply line. In fig. 3.13, a schematic drawing of the interior of the *Parker* General valve is shown. The valve is encased in a copper tube, which is mounted on the second stage of the *Sumitomo* closed-cycle cryocooler (see fig. 3.11). The valve body encloses a copper wire coil which drives a ferromagnetic rod (armature) and simultaneously, the poppet. At rest, the poppet is pinched into the faceplate orifice and thus seals the valve while it is not activated. The pulse driver generates an electric pulse which makes a current flow through the coil, and the resulting magnetic field causes the displacement of the armature and consequently a mechanical opening of the valve. The valve opening can be controlled by adjusting the amplitude of the voltage U_{valve} applied and the electric pulse duration t_{pulse}. Our model of the *Parker* General valve Series 99 allows for applying a maximal long-term voltage of 24 V_{DC} and a current of 500 mA. When operating the valve with only short current pulses, the maximal (peak) voltage applied can be increased to a considerably higher value, between 200–300 V. The buffer spring is used to return the armature to its resting state, when no electric power is applied.

Figure 3.13: Interior of the General valve Series 99 [182]: (1) poppet, (2) valve body, (3) armature, (4) VCR fitting, (5) coil assembly, (6) main spring, (7) buffer spring, (8) gasket, (9) orifice on centerline.

---

[2]A solenoid is an electromechanical device which is actuated by a current pulse that generates a magnetic field and exerts a force on a movable ferromagnetic core. Its mode of operation is based on the conversion of electromagnetic energy into mechanical (kinetic) energy.
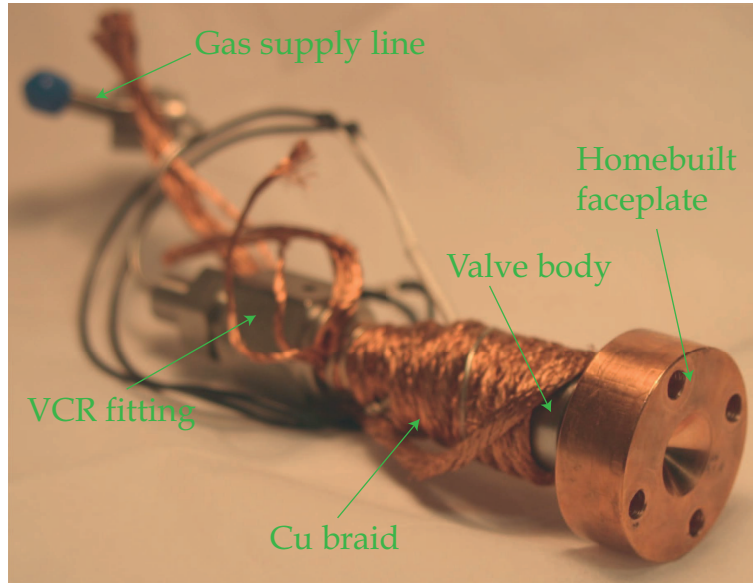
Figure 3.14: Photo of *Parker* He droplet source source equipped with the homebuilt Cu faceplate.

The faceplate provides both the sealing and cooling of the valve and contains the valve orifice on its centerline. To improve the cooling of the nozzle, its original stainless steel faceplate is replaced by a homebuilt copper faceplate which provides better heat conduction from the cold finger to the valve. In fig. 3.15, a schematic drawing of the front and rear side of the new faceplate is shown. The valve orifice is a ≈ 0.7 mm diameter tapered hole followed by a 1 cm long cone of 90° opening angle, as can be seen in the front view of the
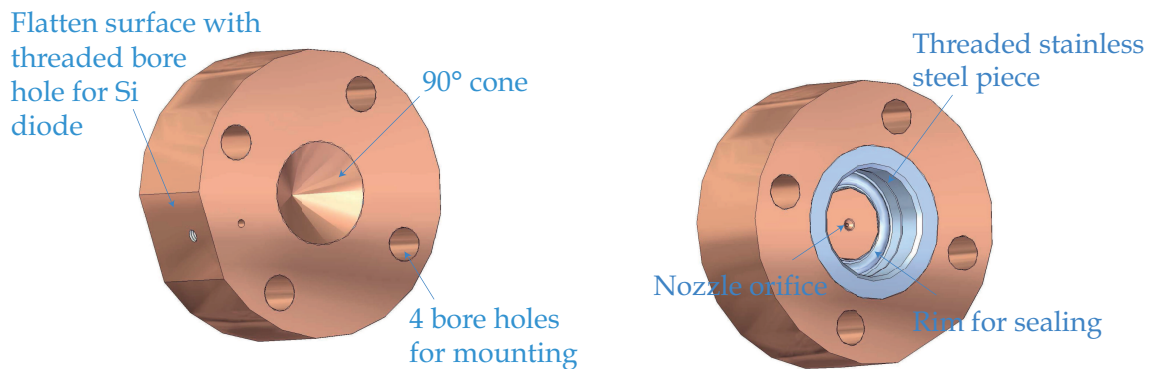
Figure 3.15: Modified faceplate of the front and rear sides. On the front side, the 90° cone is visible. A flattened area on the surface of the cylinder serves as mounting point for the Si diode. The faceplate is affixed to the valve body by four screws. On the rear side, the threaded stainless steel part is inserted to ensure leak-tight closing of the valve. The valve is sealed by metal (Ni) gaskets into which a metal flange is pressed.

faceplate. A sectional view of the geometry of the different faceplates is given in fig. 3.16. In fig. 3.16, the original *Parker* faceplate is shown including two modifications. In the faceplate as delivered from the company, there is a 0.25 mm constriction in the 0.50 mm opening channel. This causes heating of the gas during the initial stages of adiabatic cooling and hence may perturb the cluster formation. Removing the constriction by introducing a cone with an opening angle of 90° was observed to aid the cooling [113], resulting in a notable enhancement of droplet intensities. Moreover, Ellis *et al.* [183]

observed that a further modification of the faceplate in the form of a short straight ≈ 1 mm channel immediately after the cone might facilitate control of the sizes and size distributions of clusters formed in pulsed expansions with the expansion parameters T_0, P_0. Copper is soft and a faceplate of pure copper cannot be mounted gas-tight to the valve body. Therefore, a threaded stainless steel ring is inserted into the copper to permit sealing to the main valve body. To further improve the cooling, a Cu braid is wrapped around the valve body and fixed to the Cu tube. In order to achieve proper sealing of the valve, it is necessary to stack multiple Ni gaskets of different thicknesses (in our case it required one 0.4 mm and another 0.5 mm thick), because the appropriate distance between valve body and faceplate has to be maintained to assure that the proper force is exerted on the armature by the buffer spring. For operating the pulsed valve, a homebuilt pulse driver was used, similar to the commercial IOTA One pulse driver (*Parker*). After receiving a TTL trigger signal, it generates an electric pulse of a voltage between 130–300 V_{DC} and a duration of 40 - 300 μs. Typically, the *Parker* General valve is operated at a valve voltage of $U_{valve} = 240$ V with ≈ 200 μs long electric pulses at a 4 Hz repetition rate.

3.1.7 Even-Lavie valve

The Even-Lavie valve is an electromechanical high-pressure jet source which produces gas pulses by moving a metallic plunger instead of a poppet. It is designed for operating at cryogenic temperatures so that energy dissipation and power consumption are minimized when the valve is operating. Therefore, it enables the production of helium clusters at high repetition rates and intensities. A detailed description of the cryogenic pulsed helium droplet source is given in [184, 185]. The valve interior can be seen in fig. 3.17 which shows a sectional drawing and a schematic illustration of the components. The numbered parts mentioned in the following correspond to the numbers given in fig. 3.17. The Even-Lavie valve is delivered[3] ready to be mounted onto the low-temperature stage of the cryostat. The valve housing consists of a cylindrical copper body on a gold-coated Cu flange to ensure good thermal contact to the cold finger, which can be additionally enhanced by the application of Apiezon[R] grease. The housing is further equipped with a heater, a sensor mounting clamp, and a cooling facility for the gas tube to precool the gas before the

Figure 3.16: Schematic drawing of differently shaped nozzle faceplates: Starting point is the original *Parker* General valve series 99 faceplate. The green dotted line indicates the cone with an opening angle of 90 ° as described in ref. [113]. The grey line along the cone defines the nozzle shape as adapted. The red line shows the short (≈ 1 mm) straight channel introduced to achieve better control over cluster sizes as described in ref. [183]; this shape served as a model for the design of our faceplate.

expansion. The valve body contains a low-inductance copper coil (3 μH) and components

[3]The Even-Lavie valve was developed at the School of Chemistry, Tel Aviv University, and is manufactured by Atad Ltd. [180].
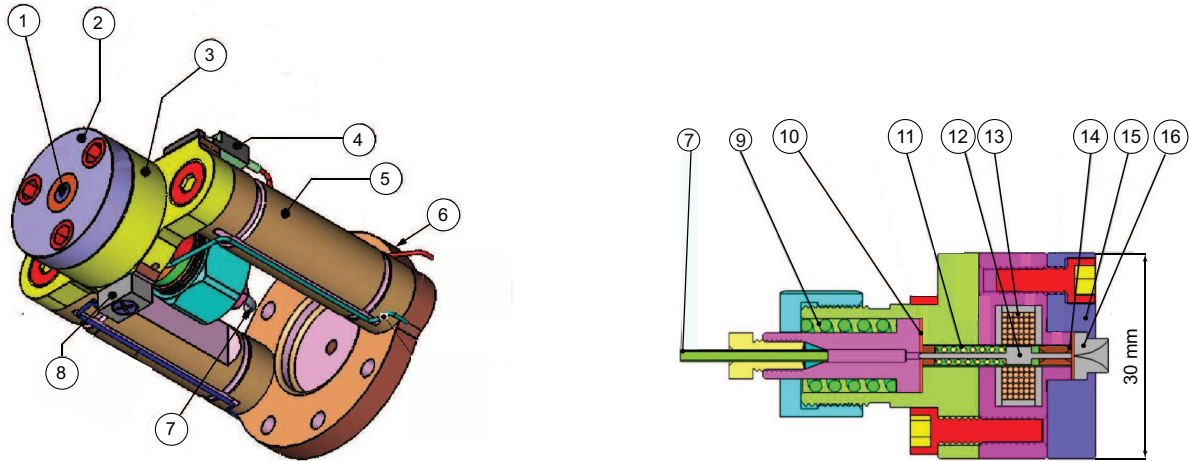
Figure 3.17: Components of the Even-Lavie valve [180]: (1) orifice, (2) nozzle front flange,(3) valve body (copper), (4) HPR heater, (5) Cu columns, (6) base flange to mount on cold finger, (7) tube gas inlet ($\frac{1}{16}$"), (8) diode sensor clamp, (9) tightening spring and pressure relief valve,(10) Kapton foil gasket, (11) return spring, (12) reciprocating plunger (magnetic stainless steel alloy), (13) Kapton-insulated Cu coil, (14) Kapton foil gasket, (15) front flange and valve body, (16) conical nozzle (stainless steel).

of the electromagnet. The nozzle orifice is conical and has a 100 μm diameter opening. At rest position, sealing is achieved by pressing the plunger against the front Kapton
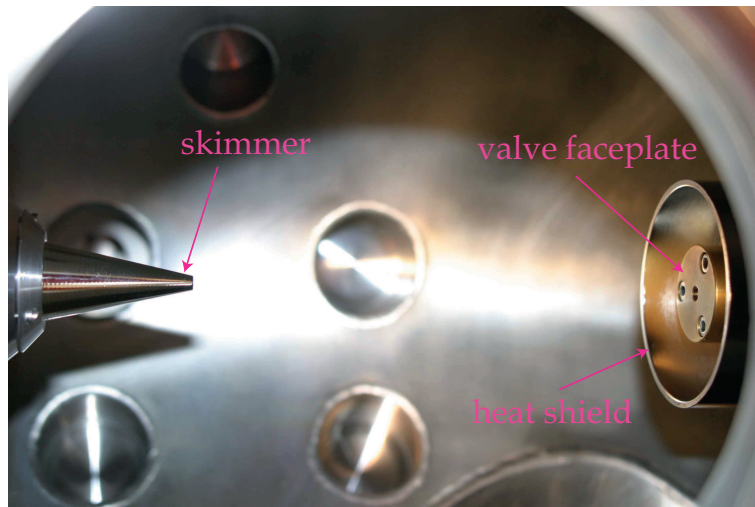
Figure 3.18: Photo of the new skimmer and the Even-Lavie valve at a larger nozzle-to-skimmer distance of $\approx$ 17 cm. On the right-hand side, the Even-Lavie valve front flange enclosed in the radiation shield can be seen; the new skimmer is on the left-hand side of the photo.

gasket (14) on the nozzle flange by both the return spring (11) and the applied gas pressure P_0. When electrical power is applied, a short high-current pulse[4] of 7–15 A is sent to the solenoid. This generates a strong magnetic field ($\approx$ 3 T) in the center of the solenoid for a short time (a few μs) which causes the plunger to be pulled back against the return spring. The valve is opened for the set electrical pulse duration t_{pulse} ($\approx$ 10$-$20 μs) which corresponds approximately to the mechanical opening. When

---

[4]The current is generated by discharging a capacitor in the power pulse driver which is switched by a solid state bipolar transistor.

the electrical power is switched off, the plunger is pushed back to its sealing position by the return spring. The Even-Lavie cryogenic valve can be operated over a wide temperature range from 4-380 K and gas pressure range from 0-100 bar. Restrictions in the applied expansion pressure are due to forepumping requirements and the pumping capacity. The repetition rate is –in principle– continuously adjustable between single shot and 1 kHz, but the heat dissipation developed in the coil when operating the valve at a repetition rate f > 500 Hz is too strong for producing He droplets [180, 184]. The electric pulse length is usually set between 10–20 μs and is adjusted individually with respect to the applied expansion parameters T_0, P_0. In fig. 3.33, a strong increase in source chamber pressure for opening times t_{pulse} longer than 18.5 μs can be seen. This can possibly be attributed to a magnetization of the plunger as a consequence of the long-duration high current flow, which leads to an incomplete closing of the valve [180].

The changes in the experimental setup, compared to operation with the *Parker* General valve, mainly apply to the nozzle-skimmer distance which is recommended to be $\approx$ 30 cm in order to avoid the formation of shock waves at the skimmer caused by the high-intensity He beam. A longer skimmer (*Beam dynamics* Model 50.8) with a 4 mm diameter opening was installed. This ensures, at the same time, a high gas density behind the skimmer in the trap chamber.

3.2   Experimental sequence

A typical cycle starts by loading the trap with ions that are continuously produced by the electrospray ionization source and which are mass-to-charge selected by a quadrupole mass filter (see fig. 3.1). The bender voltages (electrodes and lenses) are optimized for deflecting ions coming from the ion source by 90° towards the hexapole ion trap (setting *bender (1)*). During ion accumulation, He buffer gas is pulsed into the trap in order to translationally cool injected ions. Ions enter with a kinetic energy just barely above the trapping potential energy and are cooled *via* collisions with He buffer gas atoms so that they cannot overcome the trapping potential any longer, and remain in the trap (see fig. 3.9). After a few seconds, depending on the ion current, the number of ions in the trap stops increasing, presumably when the space-charge limit ($10^6 - 10^7\, q\cdot$ cm^{-3}) is reached. During storage, the ions adopt the potential energy given by the hexapole bias voltage U_{bias}. When the accumulation of ions is finished after t_{acc}, the voltages at the *pre-/post*-quadrupole rods are set to a value that is higher than the ion energy (typically $U_{\mathrm{pre-/post}} \approx$ 45 V) to stop ions entering from the continuously running ESI source. At the same time, the bender is either switched to a setting appropriate to deflect the ions coming from the trap towards the time-of-flight MS (in version (a)) of the experimental sequence, setting *bender (2)*, see fig. 3.19) or else it is switched off for straight passage of arriving ions (in version (b)) of the experimental sequence).

The second part of the experimental cycle has two versions. Version (a) provides for measuring the trap content after a certain storage time t_{trap} of ions in the trap. This includes the observation of trap depletion due to removal of ions which are picked up by He droplets. Version (b) allows for measuring the ion signal of charged droplets on a Faraday-type metal detector as an electric current (see fig. 3.19). Employing version (a) of the sequence, the trap is "opened" after the storage time t_{trap} by setting the trap entrance
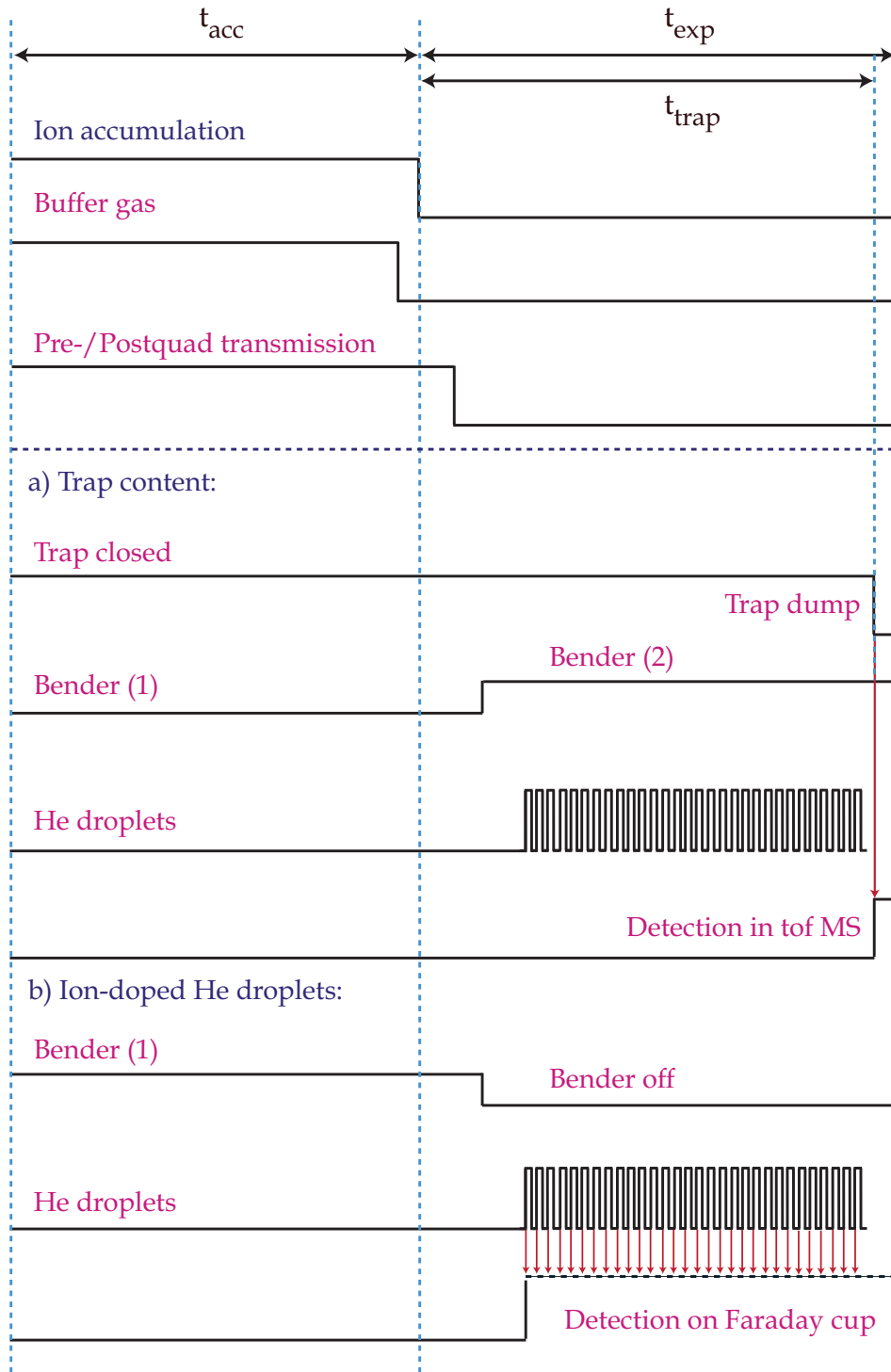
Figure 3.19: Experimental sequence employed for pickup experiments in two different versions, depending on whether the trap content is to be measured ("*trap depletion*", see Ch. 4.2.1), or the ion signal of charged droplets ("*time–of–flight profiles*"; see Ch. 4.2.2). The sequence is illustrated as a logic scheme, *i.e.* "up" refers to activation of the respective step (binary *(1)*), "down" to deactivation of the step (binary *(0)*). While the process of ion accumulation from gas-phase ions in the hexapole ion trap during the time t_{acc} is the same for both experiments, changes are made in the second part of the cycle during the time t_{exp}. The injection of buffer gas is stopped shortly before ion accumulation is completed in order to allow for pumping away the buffer gas before the He droplet source is turned on. Too many collisions in the trap are destructive of the cluster beam. For further explanations see text.

electrode (*endcap 1*) to a voltage below the hexapole bias voltage. As a consequence, the ions can diffuse out of the trap, are accelerated from the trap bias potential to ground, then are deflected by the bender by 90° and can be detected in the time-of-flight mass spectrometer with either the MCP detector or the PMT detector assembly (see below in Ch. 3.1.1). The ion signal thus obtained serves as the base signal for the trap content at the respective experimental settings. A depletion of the trap can be measured when the He droplet source is switched on while ions are being stored in the trap. The measured trap content is observed to be reduced with respect to the base signal when ions have been removed from the trap due to pickup. This is referred to as the depleted ion signal in the following. After detection, the bender is switched back to the former settings, the voltage at the *pre–/post*–quadrupole rods is reset to U = 0 V to allow ions coming from the ESI source to pass the quadrupole mass filter, and the experimental cycle is repeated from the beginning.

Version (b) of the experimental sequence in employed in order to measure ion-doped droplets in a direct way. After ion accumulation, the *pre-/post*-quadrupole rod voltages are set to 45 V and, at the same time, the bender is switched off (0 V) to allow for straight passage of charged particles coming from the trap. Then, the He droplet source valve receives trigger pulses and emits He droplets which traverse the trap during ion storage. When a droplet picks up an ion, it becomes an electrically charged particle and can be detected as an electrical current on a Faraday-type copper detector that is installed in the direction of the He droplet beam behind the bender. Data acquisition using a digitizer and a digital oscilloscope is triggered by the He droplet source valve opening, so time-of-flight profiles of ion-doped droplets are recorded as a function of time after valve opening[5].

When t_{exp} has elapsed, the cycle is repeated after reloading the trap.

3.3 Species investigated

The experiments are performed on He droplets doped with molecular ions which can be classified into three categories in terms of size and hence number of degrees of freedom. The first class is formed by single amino acids, such as protonated singly-charged phenylalanine (Phe^+) and tryptophan (Trp^+); the second covers (small) peptides composed of about 10 amino acids, corresponding to masses on the order of ≈ 1000 amu, for example doubly-protonated angiotensin II and a synthetic decapeptide denoted as $Gram_{syn}^{+2}$. The third category includes real proteins weighing more than 10 000 amu, such as cytochrome c in a variety of charge states.

A remark about the notation: The abbreviations used for the molecular species all refer to protonated species; this means that Phe^+ corresponds to $PheH^+$, Trp^+ to $TrpH^+$, $CytC^{+Z}$ to $CytC(Z \cdot H^+)$, Ang^{+2} to $Ang(2 \cdot H^+)$.

---

[5]In effect, the recording of the time of flight is triggered not by the real valve opening but by the electronic trigger signal to the pulsed valve. For the *Parker* General valve, the delay between receiving an electronic trigger and mechanical valve opening is typically around 200 μs.

3.3.1 Single amino acids: Phenylalanine and tryptophan

Phenylalanine is an essential non-polar amino acid which is composed of 23 atoms and has a molar mass of 165 g·mol^{-1}. Phenylalanine is dissolved in a 500 μM solution composed of 70:30 H$_2$O:MeOH and $\approx$ 2.5‰ AcOH in this experiment to obtain singly-protonated molecules in the gas phase. L-tryptophan is an amino acid which is essential in the human

(a)   (b)
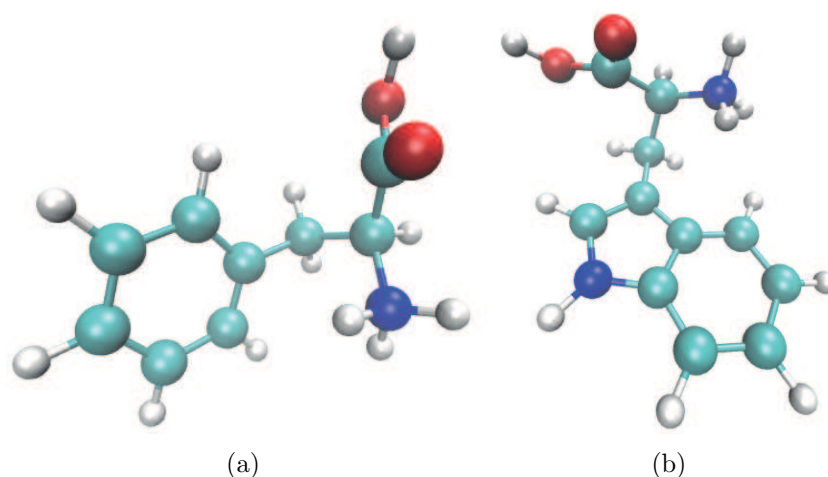
Figure 3.20: Structure of protonated (a) phenylalanine (Phe$^+$) and (b) tryptophan (Trp$^+$).

diet. It consists of 28 atoms and has a molar mass of 204 g·mol^{-1}. The structure of tryptophan is interesting since it exhibits two aromatic rings which makes it a good absorber for photons in the UV range with a broader red-shifted absorption band compared to phenylalanine.

L-tryptophan is not soluble in pure water, so the stock solution is composed of 50:50% MeOH:H$_2$O. This is diluted to usually a 200 μM solution of 50:50% MeOH:H$_2$O with $\approx$ 2‰ acetic acid (AcOH).

3.3.2 Peptides: Angiotensin, Gram$_{syn}^{+2}$

Angiotensin II is composed of 8 amino acids and has an average molar mass of 1296 g·mol^{-1} [186]. It is a hormone that controls the arterial pressure in the human body and drives up the blood pressure. The secondary structure of angiotensin II is shown on the left in fig. 3.21. To investigate this peptide in the gas phase, a 30 μM solution of 50:50% MeOH:H$_2$O with about 0.1‰ AcOH is electrosprayed. A second medium-sized peptide is the synthetic species called Gram$_{syn}^{+Z}$; its structure is drawn on the right in fig. 3.21. It is composed of 10 amino acids having a mass of $\approx$ 1200 amu, and has the same amino acid sequence as the naturally occurring cyclic decapeptide *gramicidin S* ("S" stands for "soviet") [187], cyclo–(Pro–Val–Orn–Leu–dPhe^6)^2, with the main difference that in the synthetic species, the ring is cut between a Val and an Orn. *Gramicidin S* is known to adopt a β-sheet structure as doubly-protonated ion in the gas phase. The species

---

[6]Three letter code of amino acids: proline–valine–ornithine–leucine–d-phenylalanine
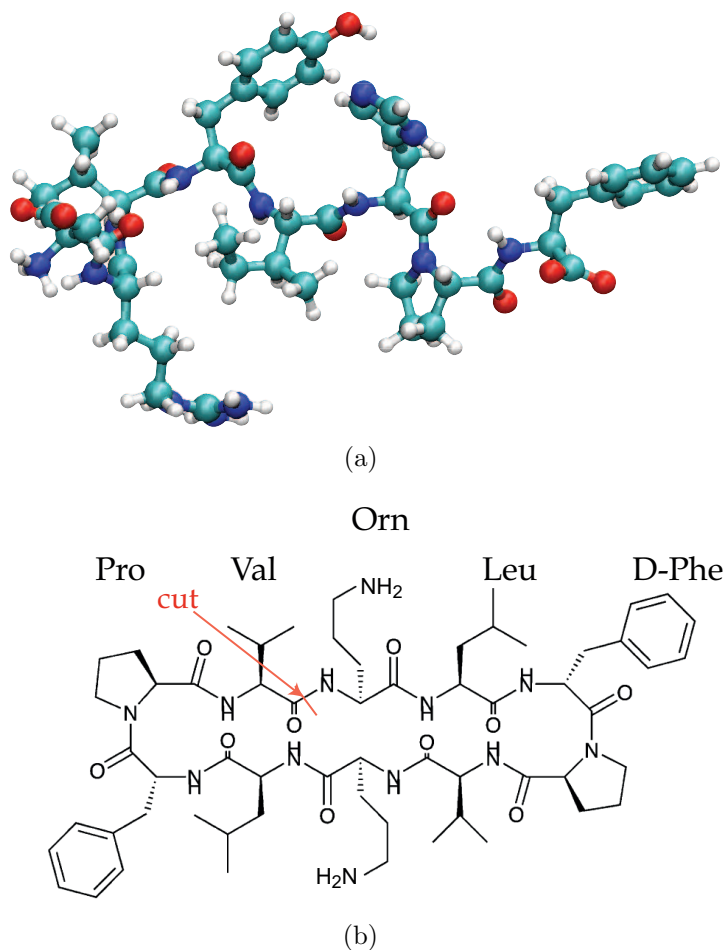
Figure 3.21: Structure of the peptides angiotensin (a) and of the naturally occurring decapeptide gramicidin S (b). The arrow indicates where the ring is cut in the synthetic peptide Gram$_{syn}$. The structure of gramicidin S is taken from ref. [187].

Gram$_{syn}^{+2}$ has been synthesized after solid phase peptide synthesis using $Fmoc$ strategy[7] in the chemistry department of the Freie Universität Berlin by K. Pagel in the group of B. Koksch. For investigations in the gas phase, it is dissolved in a 50 μM solution with 50:50 MeOH:H$_2$O and $\approx$ 3‰ AcOH and transferred into the gas phase *via* electrospray.

3.3.3 Protein: Cytochrome c

As a candidate for a real protein, cytochrome c from equine heart was chosen; it contains around 1000 atoms. One biological function of cytochrome c is that of an electron transporter of molecular oxygen in the respiratory chain, as it is capable of undergoing oxidation and reduction. It consists of 104 amino acids and has an average molar mass of 12327 g·mol^{-1}. In the solution phase, it is known to adopt a mainly α-helical conformation [189] which it can retain in the gas phase, provided that it is present in a low charge state. The observed distribution of charge states ranges from +7 up to +17 after electrospray ionization [190].

---

[7]$Fmoc$ stands for Fluorenylmethyloxycarbonyl chloride.
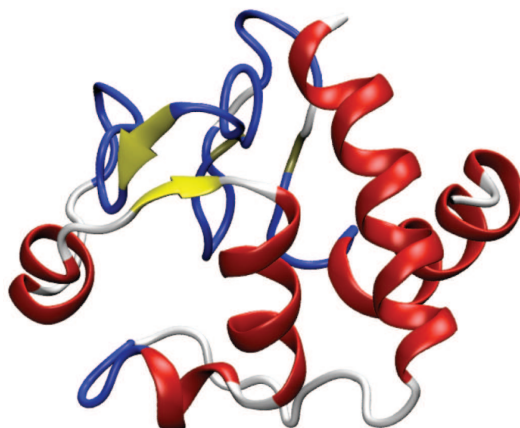
Figure 3.22: Structure of cytochrome c ($CytC^{+Z}$) as obtained by x-ray diffraction, in a cartoon representation [188].

We dissolved $CytC^{+Z}$ in an aqueous 50 μM solution in 50:50 H_2O:MeOH and $\approx 3‰$ acetic acid for electrospray and, usually –depending on the charge state desired– applied a cone voltage of about 100 V.

3.4 Results

3.4.1 Characterization of the trap

Trapping of ions is carried out in such a way that ions coming from the ESI source enter the trap with minimal kinetic energy. This is achieved by setting the potential at the trap entrance *endcap1* just slightly below the energy of the incoming ions ($E_{ion} \approx$ 25–35 eV). Collisions with buffer gas atoms further cool down the ions so that after a few collisions, they cannot overcome the potential barrier of the longitudinal trapping electrodes any longer. The accumulation efficiency depends on the amount of injected buffer gas. In fig. 3.23, the ion signal obtained after trap dumping is shown as a function of the buffer gas pressure that is injected into the trap during ion accumulation. Important to note is that the displayed ambient pressure on the $x-$axis of the figure is that measured by the pressure gauge in the trap vacuum chamber and **not** the gas pressure that is effectively present in the trap itself, which is presumably about 1–2 orders of magnitude higher (see Ch. 3.1.3). Buffer gas atoms injected into the trap during ion accumulation can be detected by a background pressure rise in the trap vacuum chamber after a short delay ($\approx$ 1-2 s) due to effusion of gas particles through the trap openings. A calculation to obtain the real buffer gas density in the trap deduced from the increase of the background pressure in the trap vacuum chamber is performed above in Ch. 3.1.3. It is observed that below a certain buffer gas pressure, no ion signal can be measured. That means that in order to accumulate and store ions in the trap, a minimum gas pressure providing for collisional cooling is required. In the graph it can be seen that an increasing gas density and hence, too many collisions with buffer gas atoms, causes the ion signal intensity to decrease. This can possibly be attributed to scattering of the ions in the high pressure region just before the trap entrance that causes a reduced injection efficiency. The error bars shown in fig. 3.23 along the horizontal axis are caused by fluctuations of the effective buffer
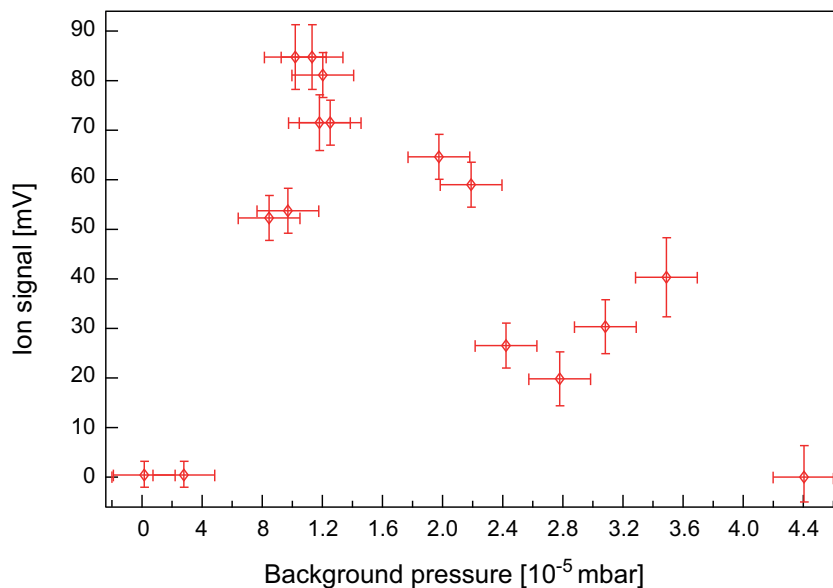
Figure 3.23: The average trap content is shown as a function of the background gas pressure in the trap during ion accumulation. However, the background gas pressure rise ΔP indicated was measured in the trap chamber during ion accumulation, which is observed after a short time delay when buffer gas is injected into the trap enclosure. The ions are accumulated for $t_{acc} = 10$ s and are stored for $t_{trap} = 30$ s. Then, the trap is dumped and the trap content is measured using the PMT detector assembly. Error bars in the horizontal axis are caused by fluctuations of the effective buffer gas density in pulsed operation due to effusing gas atoms. In the vertical axis, the error bars account for the fluctuations in ion yield obtained from different measurements.

gas pressure obtained with pulsed valves (see Ch. 1.3.5). In the vertical direction, the error bars account for observed statistical fluctuations in ion signal intensity over different measurements. The trap content as detected with the PMT detector assembly is shown in fig. 3.24 (top panel). CytC^{+Z} ions are accumulated in the trap for $t_{acc} = 10$ s, then the trap is dumped after a storage time of $t_{trap} = 80$ s by setting the longitudinal entrance electrode *endcap1* to 0 V, which is lower than the trap bias voltage of $U_{bias} \approx 26$ V. In the bottom panel of fig. 3.24, the measured trap content of accumulated Phe$^+$ ions is shown as a function of the accumulation time t_{acc}. The ions are stored for $t_{trap} = 100$ s before dumping the trap, and the integrated ion signal of the trap content as measured in the PMT detector assembly is shown. It is observed that the signal intensity does not increase significantly with longer accumulation time for $t_{acc} > 6$ s, indicating that the space charge limit of 10^6-$10^7 \, q \cdot \text{cm}^{-3}$ has already been reached at that time. Ions can be stored in the trap with high stability for many minutes[8]. This finds a practical application in terms of the refilling frequency of the trap with fresh ions from the *ESI* source. Once the trap is filled with ions up to the space charge limit, it can be assumed that they are available for pickup during one entire experimental cycle. Moreover, since ions are observed to remain stable in the trap, it is possible to obtain the same ion yield of charged droplets when the trap is not refilled after each cycle (*i.e.* if the trap is not dumped meanwhile). This allows for extending the second part of the experimental cycle to longer times t_{exp} with respect to the accumulation part when employing version (b) of the sequence (see fig. 3.19), which

---

[8]It is observed for trapping times up to 15 minutes that the trap content is not reduced significantly. Those 15 minutes correspond to the maximal delay that can be selected in *Stanford Research* delay generators which are used as experimental clocks.
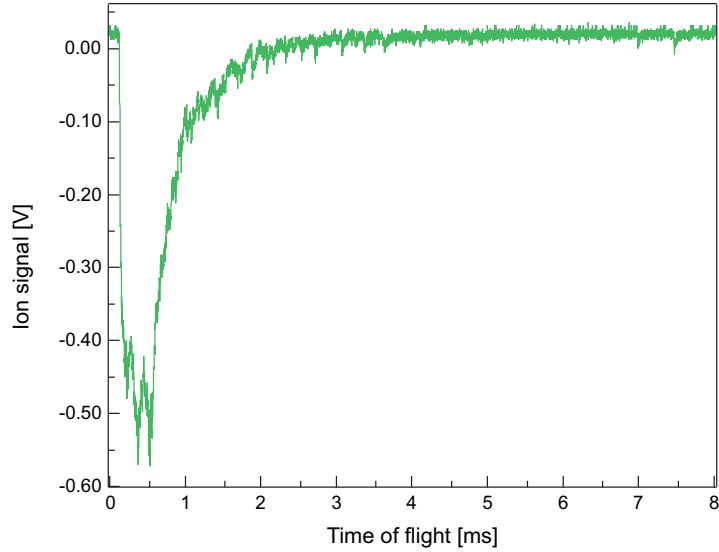
(a)
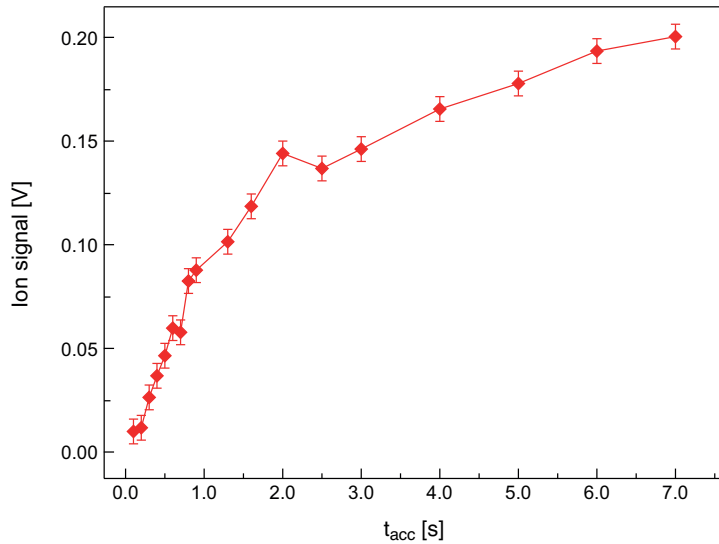
(b)

Figure 3.24: (Top panel) Trap content for CytC^{+Z} ions (not mass-to-charge selected) is shown as a function of the time of flight from the trap to the detector (PMT detector assembly). The trap content signal is measured after a storage time of $t_{trap} = 80$ s. (Bottom panel) The integrated ion signal as obtained from measuring the content of the trap filled with Phe$^+$ ions is shown as a function of accumulation time t_{acc}. Ions have been stored for $t_{trap} = 100$ s. The signal intensity does not increase significantly with longer accumulation times for $t_{acc} > 6$ s, when presumably the space charge limit of 10^6-10^7 $q \cdot$ cm^{-3} has been reached.

is advantageous for the duty cycle of the experiment and the achievable ion signal per unit time. In fig. 3.25, the gain in ion signal intensity is shown after exchanging the short trap for the long trap. Time-of-flight profiles of ion–doped He droplets that are produced at $T_0 = 7$ K, $P_0 = 30$ bar with the *Parker* General valve are shown. CytC^{+14} ions are accumulated in the trap for $t_{acc} = 10$ s and He droplets are generated for $t_{exp} = 10$ s. The trace obtained when the long trap is used reflects an average over 50 measurements, while the trace obtained with the short trap corresponds to an average over 200 measurements. An enormous enhancement of the ion signal of almost a factor of 10 is achieved due to
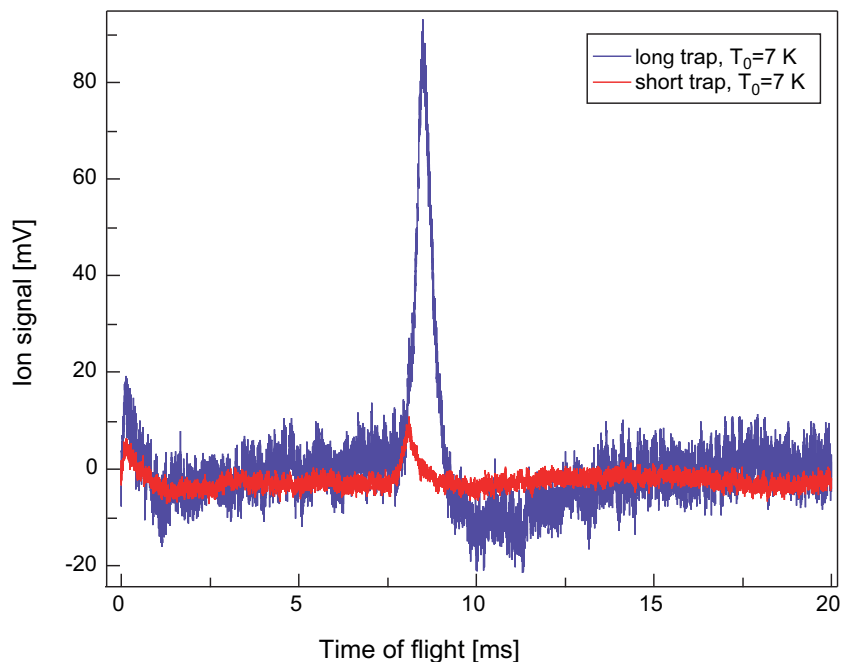
Figure 3.25: Time-of-flight profiles of He droplets doped with $CytC^{+14}$ ions as detected with a Faraday-type metal detector and amplified with the *Amptek* amplifier (for further explanation see Ch. 4.2.2). Ions are accumulated either in the short trap (red trace) or in the longer trap (violet trace). A large increase in ion signal is observed after exchanging the traps and realignment of the trap and the He droplet source with respect to the central experimental axis.

the trap exchange and a realignment of the trap and the He droplet source with respect to the central experimental axis at the same time.

Trap losses

In fig 3.26, a time-of-flight mass spectrum of $CytC^{+14}$ ions is shown after storage for 30 s in the trap (upper panel) and after a storage time of 90 s (lower panel). The mass-to-charge resolved spectrum is detected with the MCP detector in *W-mode* measurement. It is observed that for the longer trapping time, the signal intensity of the $CytC^{+14}$ peak is reduced, accompanied by an enhanced population of the lower charge state of +13. The observed change in charge-state distribution deprotonation can possibly be attributed to mass discrimination effects that are known for linear ion traps and often result in ion ejection [177]. These effects could be either shifts towards populating lower charge states due to "charge stripping" [191] or ion depletion from the trap as a consequence of ejection or fragmentation. Both mechanisms are observed to occur when the trap is filled with too many ions up to the space charge limit and Coulomb repulsion possibly affects the stability of the stored ions. A shorter ion accumulation time t_{acc} –such that the space charge limit is not reached– can help to avoid ion ejection. Non-optimal trap operating parameters (voltages) can also be decisive for limiting effective ion accumulation and storage [177]. Another mass discrimination effect is charge transfer to background gas molecules, especially when there is a significant remaining amount of solvent molecules present in the trap [177]. This can be reduced by applying lower flow rates in the *ESI* process or by shortening the accumulation time. When the mass-to-charge ratio of the trapped molecules is decreased due to deprotonation, the effective trapping potential well
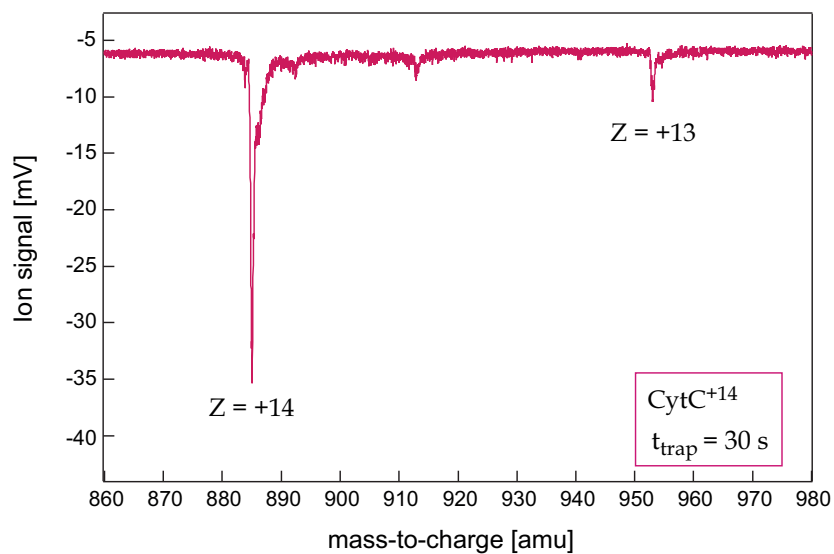
(a)
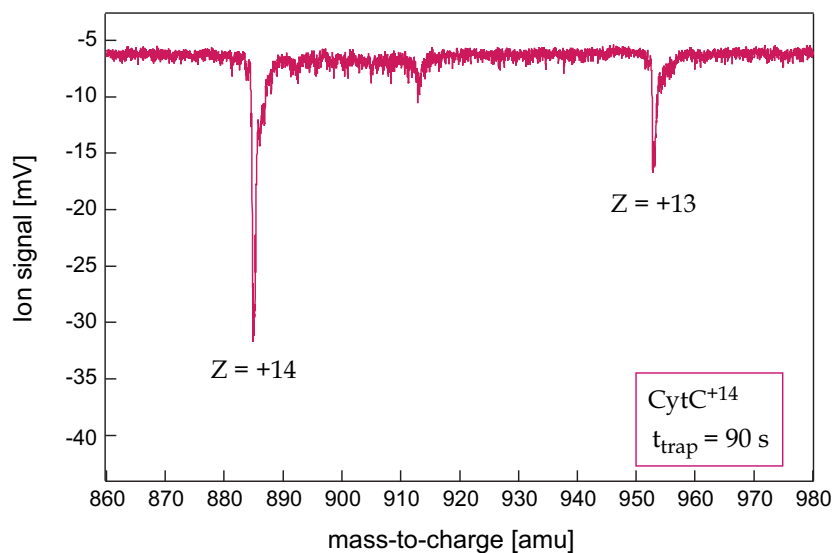
(b)

Figure 3.26: Mass spectra of $CytC^{+Z}$ ions after storing in the trap for (a) 30 s and (b) 90 s. It is observed that at longer storage times of 90 s (compared to 30 s), the signal of ions in charge state $Z = +14$ is depleted. This is accompanied by the appearance of the lower charge state $Z = +13$. After $t_{exp} = 90$ s, the appearance of lower charge states is more distinct than for shorter storage times of $t_{exp} = 30$ s.

depth qU decreases and trapping becomes less effective.

Applying higher voltages U_{cone} between the capillary and skimmer often results in removal of loosely bound charges (protons, alkali ions, etc.) from the species investigated, an effect which is commonly called "charge stripping" [192]. This can possibly explain an observation made for $CytC^{+Z}$ ions that are generated *via* electrospray ionization at different applied voltages U_{cone} at the cone. For a lower cone voltage of $U_{cone} = 75$ V, the charge distribution is observed to possess maximal intensity at the charge state $+14$, compared to a higher cone voltage of 200 V where the central charge state with highest intensity is shifted to $+10$ (shown in fig. 3.27).

Charge stripping leads to an enhanced presence of lower mass-to-charge ratios of gas-

phase ions after electrospraying at high voltages. A multiply charged molecule –as often
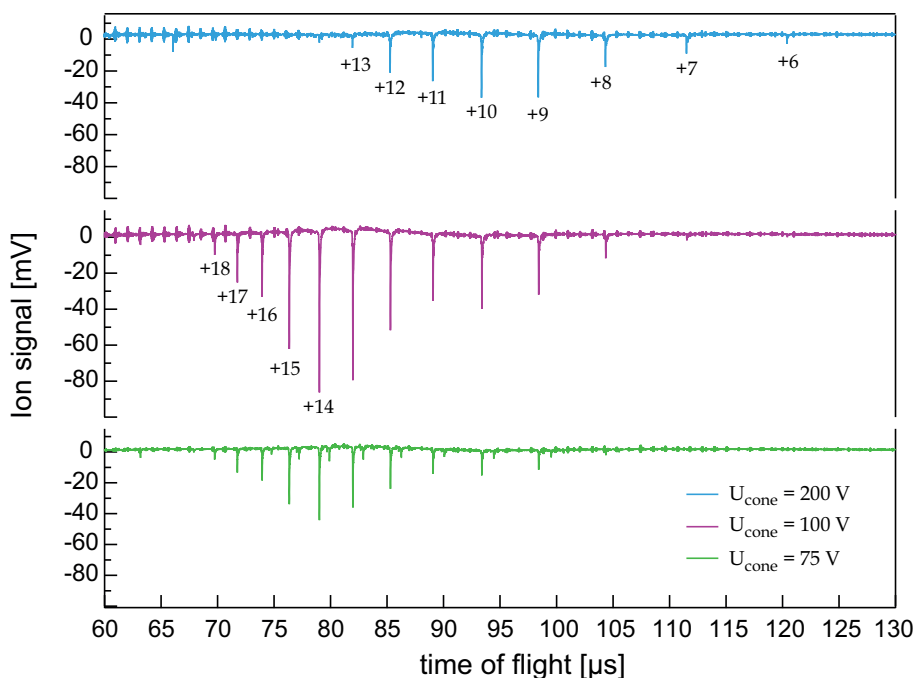
Figure 3.27: Mass spectra recorded from charge state distribution of $CytC^{+Z}$ ions after electrospray for different cone voltages U_{cone} applied. It can be seen that at high cone voltages of 200 V, the production of lower charge states is favored compared to the distribution obtained at lower cone voltages. This effect is presumably due to "charge stripping of loosely-bound protons during the electrospray process.

present after electrospray– that carries a higher number of charges than it has in its native environment can be in a state of enhanced strain due to Coulomb repulsion between the charges. To allow for the largest possible distance between the charges, the molecules start to unfold and to adopt a less globular and more stretched three-dimensional structure which deviates from their native structure. When a multiply-charged ion carrying many protons (as in the case of $CytC^{+14}$ or $CytC^{+17}$) is stored in an ion trap for a longer period, it may happen that it loses protons *via* collisions with neutral particles (buffer gas) [191]. The number of protons and the rate of collision should depend on the buffer gas density and the storage time in the trap.

3.4.2 Characterization of the He droplet source

Parker General valve

The valve performance as a pulsed cluster beam source was studied by observing the He dimer ion signal after electron impact ionization of undoped clusters and recording time-of-flight profiles of doped droplets (see Ch. 4). Transients of the He_2^+ ion as a function of applied source temperature T_0 and electrical pulse length t_{pulse} are detected by an electron multiplier detector and monitored on a digital oscilloscope. They give information on the longitudinal beam velocity v_x and velocity spread Δv_x. The observed background pressure increase is a measure of the particle flux as emitted from the source. It is used as an indicator for correct assembling and performance of the valve. In operation, the background pressure in the source chamber usually rises from $\approx 2 \cdot 10^{-8}$ mbar
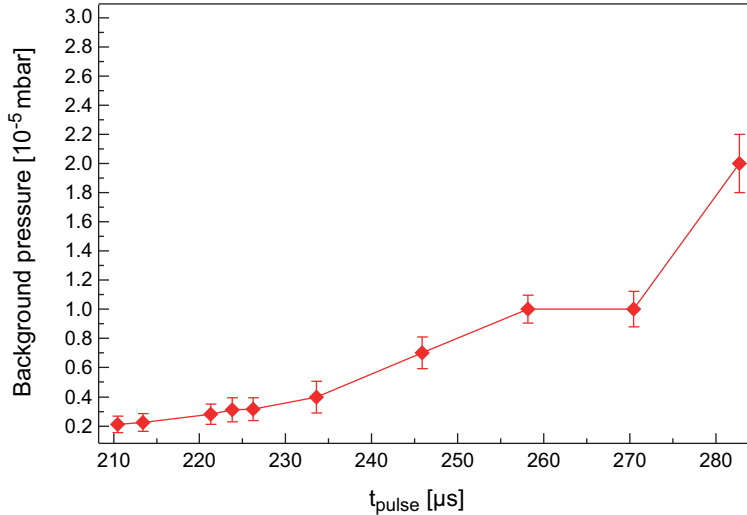
Figure 3.28: Background pressure in the He droplet source chamber as a function of the valve opening time t_{pulse} at an applied voltage U_{valve}=240 V.

base pressure[9] up to $\approx 3 \cdot 10^{-5}$ mbar. In fig. 3.28, it can be seen that the droplet flux increases by an order of magnitude when the electrical pulse length is increased from 210 μs to 290 μs. The temporal profile of the He gas pulse is mainly determined by the combination of pulse duration t_{pulse} and applied voltage U_{valve} to fully open the valve. A minimal voltage of $U_{valve} = 200$ V must be applied at pulse lengths between $\approx$ 220–280 μs. Setting higher voltages of up to $U_{valve} = 320$ V allows us to reduce the pulse lengths to $\approx$ 160–200 μs. Fig. 3.29 shows the temporal development of the He dimer peak profile depending on the valve opening time t_{pulse} at an applied voltage of U_{valve}=280 V. If the pulse length is too short (and, at the same time, the voltage U_{valve} not sufficiently high), no He$_2^+$ signal is observed (threshold pulse length $\approx$ 150 μs). At t_{pulse}=176 μs, a gas pulse arises which exhibits a small shoulder on its right side that becomes more pronounced at a longer pulse length of t_{pulse}=190 μs. It is observed, that the time structure of the pulse changes for increasing electric pulse lengths and is found to have optimal at t_{pulse}=225 μs. Together with an applied valve voltage U_{valve}=280 V, this is established to be the valve operating parameters usually employed in all experiments performed with the *Parker* General valve. Recording time-of-flight profiles of the He monomer signal He$^+$ produced at a valve opening time of $t_{pulse} \geq 260$ μs and voltage U_{valve}=250 V, the occurrence of a large gas "blob" is observed, which presumably is caused by uncontrolled bouncing of the poppet and ejection of a large amount of He gas (see fig. 3.30). This can be suppressed by reducing the valve opening times, and it is observed only for quadrupole settings which transmit the atomic He$^+$ ion, not for the dimer or larger cluster fragment ions.

Fig. 3.31 shows the beam velocity (red line and dots, left axis) as a function of the applied source temperature T_0 between 4.5 K and 13 K, together with the respective observed He dimer signal intensity (green diamonds, right axis). An increase in the beam velocity is observed for increasing temperatures T_0. The dimer signal intensity is maximal for expansion temperatures between 6–8 K and decreases at higher T_0, vanishing for T_0 >11.5 K.

---

[9]with cryocooling
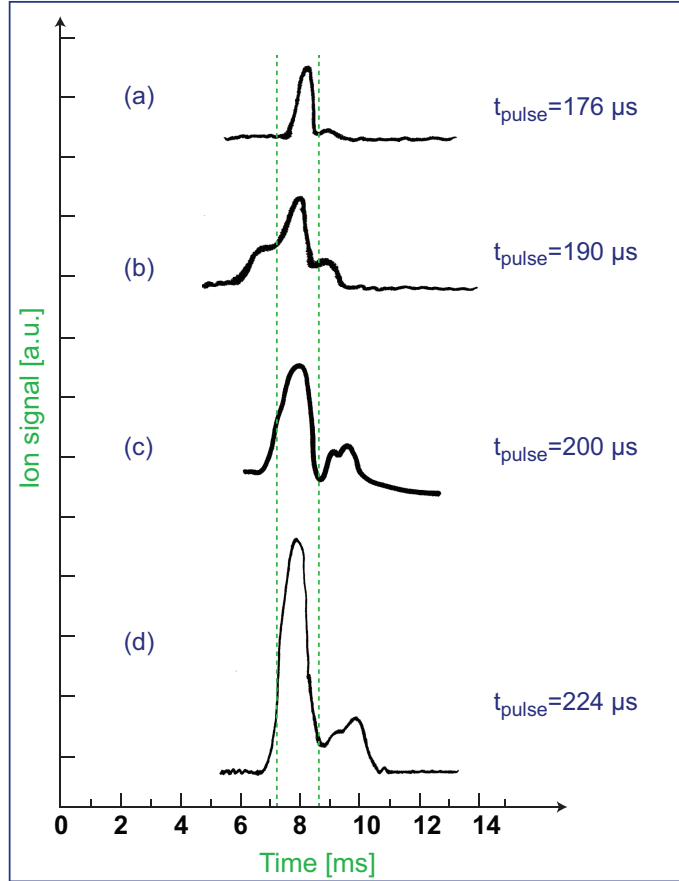
Figure 3.29: Evolution of the temporal pulse profile as a function of the applied (electronic) pulse lengths t_{pulse}. The detected ion signal is shown (in arbitrary units, offset for clarity) when the quadrupole is set for transmission of the He dimer ion He_2^+. The zero point of the time axis is given by the electronic trigger to the pulsed valve, the applied (electronic) pulse durations t_{pulse} are indicated below the respective signal pulse. The pulse shape and number of peaks appearing are observed to change depending on the valve opening time t_{pulse}. The dimer ion signal is not observed for pulse lengths shorter than 176 μs. At longer pulse lengths, the He_2^+ signal is present (between the two dashed green lines) and is observed to be followed by a second gas pulse, which might be caused by a recoil of the poppet.

It should be noted that there is a time delay of typically $\approx$ 200 μs between receiving the trigger signal and the actual valve opening. That means that the real flight time of the gas pulse is $\approx$ 200 μs shorter than observed on the oscilloscope.

When observing the He monomer He^+, the ion signal can be detected over the whole temperature range from room temperature to low temperatures. This shows that the appearance of the He dimer signal is related to cluster formation, which only occurs at low temperatures (and high pressures P_0).

For beams containing large clusters, a narrow distribution Δv_x of velocities in the longitudinal direction is expected [1, 82], in particular He cluster beams are assumed to have a sharp velocity distribution of $\Delta v/v \approx 0.01 - 0.03$ in continuous expansions [15]. A high speed ratio is also observed in pulsed cluster expansions using a similar He droplet source [113]. The temporal spread of the pulses detected is quantified by the full width at half maximum (FWHM). The longitudinal velocity distribution Δv_x in

93
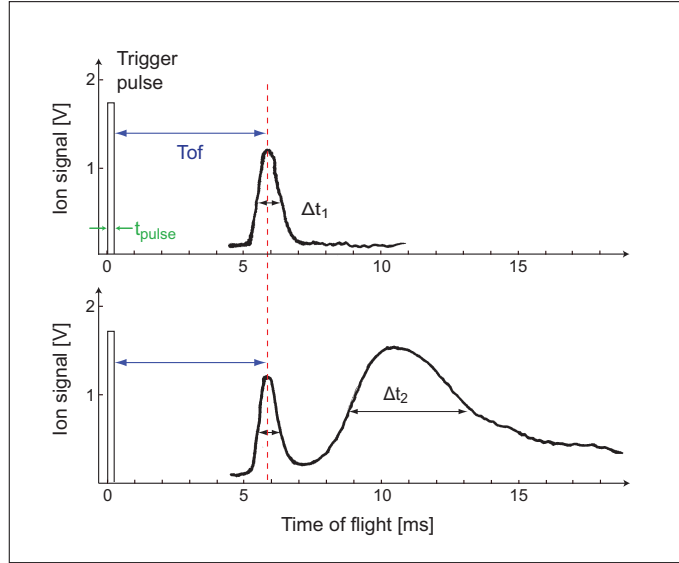
Figure 3.30: Time-of-flight profiles of the He monomer ion for two different valve opening times (a) $t_{pulse} = 190$ μs and (b) $t_{pulse} = 290$ μs. A broad gas pulse arises for longer valve opening times ($t_{pulse} > 250$ μs at an applied voltage of $U_{valve} = 300$ V.), with an increased flight time of several ms longer than the monomer ion signal (He$^+$), which follows the He gas pulse in case the mass filter is set to transmit the He monomer ion. The second gas pulse is presumably caused by a recoil of the poppet at longer electric pulse lengths and valve opening times. The time profile is shown for gas pulses produced at $T_0 = 6$ K and $P_0 = 25$ bar. The He$^+$ gas pulse has a width (FWHM) of around 1 ms, the second gas pulse has a broad width of at least 4 ms.
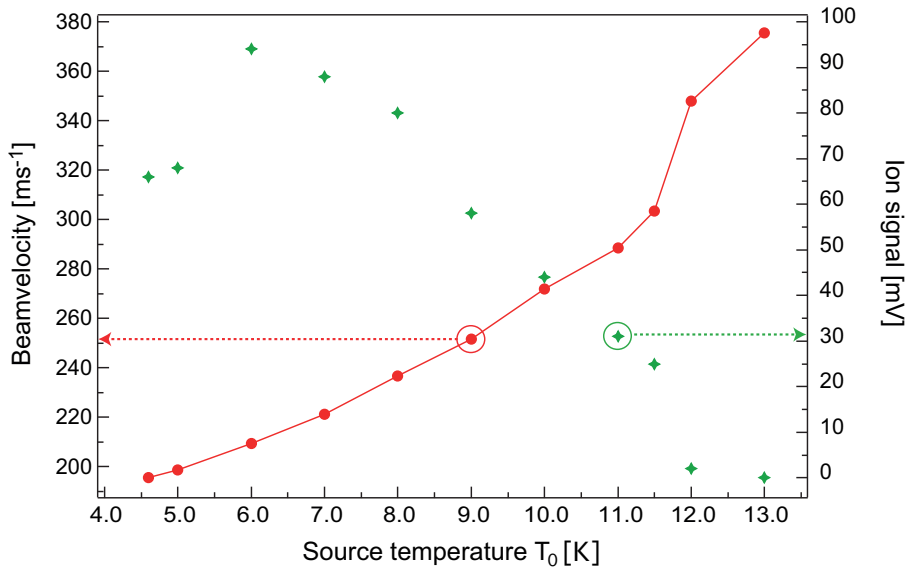
Figure 3.31: Dependence of the beam velocity v_x of the He gas pulse on the expansion temperature T_0 when using the *Parker* droplet source. He droplets are produced at $P_0 = 30$ bar and a pulse duration $t_{pulse} \approx 250$ μs with an applied voltage of $U_{valve} = 240$ V. Clusters are ionized *via* electron impact, and the signal of the He dimer ion He$_2^+$ is recorded as a function of time after the electronic trigger to the pulsed valve.

pulsed cluster beams is given by a convolution of the thermal velocity spread as present in nozzle beam expansions and a velocity spread caused by the opening process of the valve. In real valves, the poppet pull-back is not instantaneous and deviates from an

ideal rectangular process [2]. Formation of quasi-steady flow, which occurs when the valve is fully opened, is delayed during the opening and closing process. In these stages, the expansion is hindered by the valve plug [2]. This causes gas density fluctuations and results in a broader (Gaussian) spread of beam velocities. Additionally, the heat production caused by the moving parts can make a contribution to the velocity spread. So a higher repetition rate f leads to an increased valve temperature T_0 and therefore to higher beam velocities. One possibility to determine the temporal profile of the emitted gas pulse is to measure the pulse directly in front of the nozzle (for example using a fast ion gauge), where it is not yet broadened by the velocity spread Δv_x. This was, unfortunately, not done in our experiments.

The beam velocity v_x observed ($v_x = 220$ ms^{-1} for $T_0 = 7$ K) and the (electric) pulse duration t_{pulse}, which is approximatively corresponding to the mechanical valve opening, allow for an estimation of the longitudinal spatial length s_x of the gas pulse at the nozzle (without a longitudinal spread of the packet due to the velocity spread Δv_x) and we find:

$$s_x = v_x \cdot t_{pulse} \approx 220\, ms^{-1} \cdot 200\, \mu s = 4.4\, cm \quad . \tag{3.10}$$
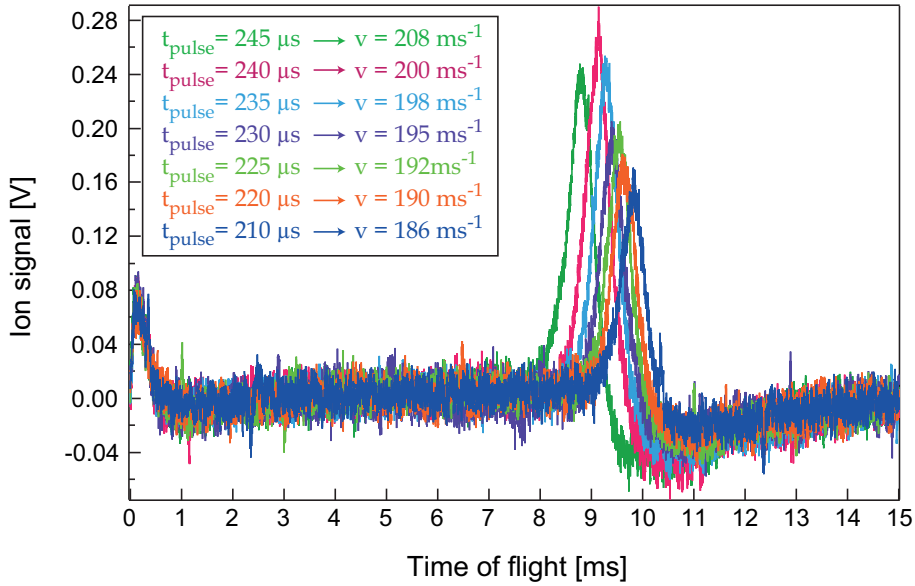
Figure 3.32: Dependence of the beam velocity on the valve opening time t_{pulse} at a voltage of $U_{valve} = 240$ V. He droplets are produced with the *Parker* General valve He droplet source at $T_0 = 5$ K, $P_0 = 30$ bar and doped with CytC^{+Z} ions (not mass-to-charge selected).

It is observed that the arrival time of the detected gas pulse (here: ion-doped He droplets) shifts to earlier times (corresponding to a higher beam velocity v_x) when the electronic pulse length t_{pulse} is longer. In fig. 3.32, time-of-flight profiles of He droplets produced at a source temperature of $T_0 = 5$ K and pressure $P_0 = 30$ bar, and doped with CytC^{+Z} ions (not mass-to-charge selected) are shown. The valve voltage is $U_{valve} = 244$ V and the applied electrical pulse length is varied from $t_{pulse} = 210$ μs to 245 μs. The corresponding longitudinal beam velocity v_x is observed to increase from 186 ms^{-1} to 208 ms^{-1} at otherwise unchanged expansion conditions. The increasing velocities can

probably be attributed to a change of the valve electronic properties and consequently, of the mechanical valve opening. Longer electric pulse lengths seem to lead to faster beams, possibly due to better expansion conditions. Another possible reason is that at longer opening times, the clustering process might be favored. At quasi-steady flow in the mechanical valve opening process of a pulsed expansion, the particle flux and cluster growth are known to work best [2]. Clustering is also known to lead to higher beam velocities due to the release of condensation enthalpy, which heats and accelerates a molecular beam.

Even–Lavie valve

The Even-Lavie valve was likewise characterized as a He droplet source and it was seen that its performance is significantly different from that of the General valve (see Ch. 3.4.2). The background pressure rise when operating the valve at different electric pulse lengths
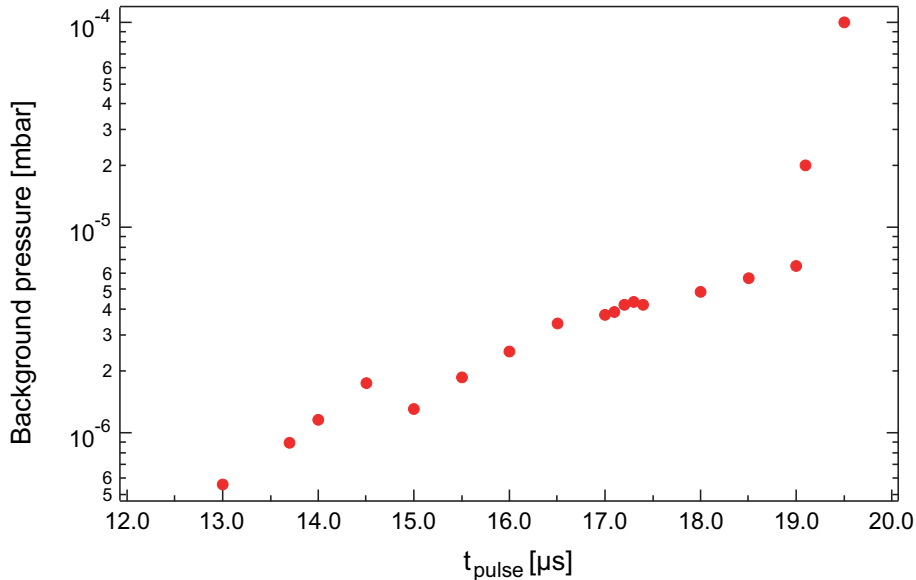
Figure 3.33: Background pressure rise in source chamber when the Even-Lavie valve is operated at different pulse opening times t_{pulse}. The background pressure displayed was measured in one data series at source conditions $T_0 = 6$ K, $P_0 = 30$ bar, and a repetition rate $f = 10$ Hz.

t_{pulse} is shown in fig. 3.33. The valve was operated at a frequency $f = 10$ Hz and expansion parameters $P_0 = 30$ bar and $T_0 = 6$ K. A strong increase in background pressure up to $\approx 1 \cdot 10^{-4}$ mbar is monitored for electric pulse lengths longer than 18 μs. The much shorter pulse length and hence, smaller amount of gas emitted per pulse, allows for a significantly higher repetition rate for operating the valve which will be set to ≈ 50 Hz in most of the following experiments. The range of applicable stagnation temperatures T_0 is larger (compared to the other droplet source) and clusters are produced for source temperatures up to ≈ 25 K. This has been observed in mass spectra of cluster fragments after electron impact ionization (see Ch. 4.1). Time-of-flight profiles of ion-doped clusters produced by the Even-Lavie source are recorded, and the measured beam velocities are shown in fig. 3.34 as a function of applied source temperature T_0, together with the respective intensity of the He_2^+ signal intensity. As expected, the beam velocity increases for higher source temperatures but at the same time, the signal intensity decreases for decreasing temperatures.
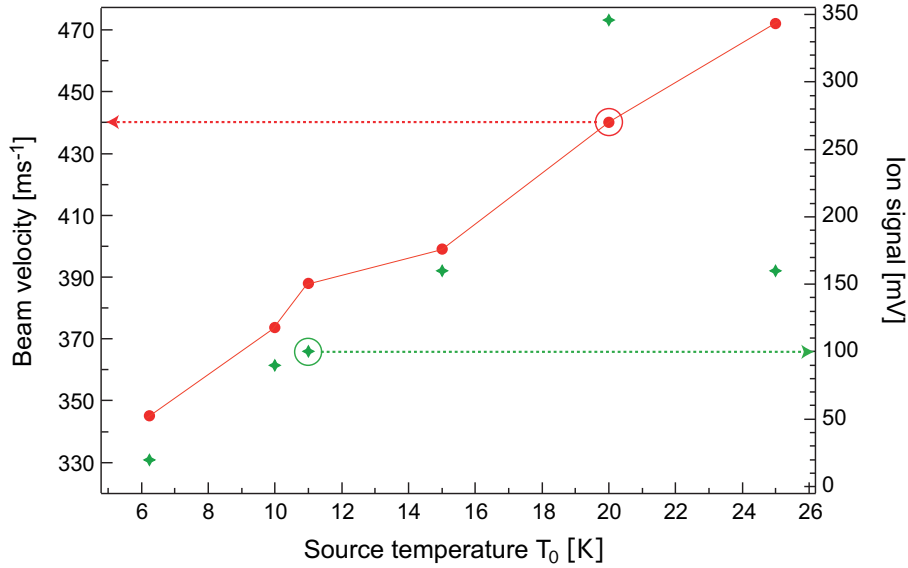
Figure 3.34: Dependence of the beam velocity on the expansion temperature T_0 for cluster beams produced with the Even-Lavie valve. He droplets are produced at $P_0 = 30$ bar stagnation pressure, a repetition rate of $f = 50$ Hz, and a pulse duration $t_{pulse} \approx 15$ μs. Clusters are ionized *via* electron impact, and the signal of the He dimer ion He_2^+ is recorded as a function of time after the electronic trigger to the pulsed valve.

This effect cannot be explained by the temperature dependence of the mass flow rate from nozzle beam expansions which scale like $P_0 D^2 T_0^{-1/2}$ [2] and either by that of the three-body collision rate Z_3 which scales like $P_0^2 D$ T_0^{-2} [2] since both formulas predict an increase for decreasing temperature. Low expansion temperatures lead to the production of larger clusters but at the same time, to a smaller number of droplets per pulse. Fewer droplets presumably result in a smaller number of He_2^+ ions generated by electron impact ionization that make a contribution to the ion signal. On the other hand, large droplets have large geometrical cross sections and might be ionized by more than one electron, which possibly leads to an ejection of multiple He_2^+ ions from a large cluster. However, a reduced absolute number of droplets produced at low temperatures can possibly explain the decrease in ion signal compared to the He_2^+ ion signal obtained at higher temperatures and thus, for a larger number of small droplets (at the same ionizer settings).
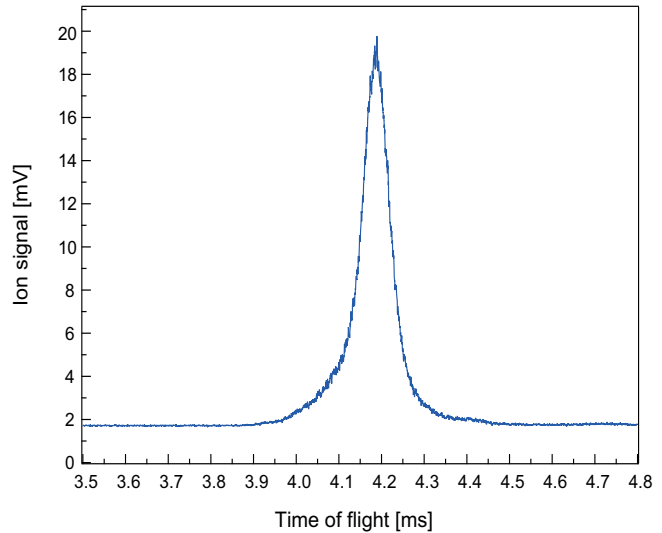
Figure 3.35: Time-of-flight profile of an ion-doped He droplet pulse emitted from the Even-Lavie source and detected by the Daly detector. The pulse width (FWHM) of ≈ 90 μs presumably represents a pulse width close to the real one, i.e. that is not broadened by the amplifier.

Compared to the velocities observed for cluster beams expanded using the *Parker* General

valve (see fig. 3.31), it results from the beam velocity measurements that for similar expansion conditions (P_0,T_0), the beam velocity is significantly higher. This is also observed in case of beams of doped droplets and will be regarded in Ch. 4.4.

In fig. 3.35, the time-of-flight profile of a gas pulse emitted from the Even-Lavie valve is shown. The pulse shapes were characterized for different nozzle geometries and expanded gases in ref. [180]. At a longitudinal beam velocity v_x of 400 ms^{-1}, the measured speed ratio S was found to be ≈ 46.

3.5   Summary

In this Chapter, the experiment is presented and the single components of the setup are described. Also, the experimental sequence employed and the investigated molecular species are introduced. The hexapole ion trap as well as the pulsed He droplet source are characterized and the results are presented.

Chapter 4

Charged helium droplets

In this Chapter, the results of the experiments performed on charged He droplets produced by the two different He droplet sources are presented and further analyzed. At first, mass spectra of undoped He cluster fragment ions created by electron impact ionization are shown in Ch. 4.1. They are the first indicators for successful cluster production by the two sources. In Ch. 4.2, the experimental results obtained on doped He droplets are presented. These results are the first experimental proofs for the successful doping of He droplets *via* pickup of mass-to-charge selected ions from an ion trap. In Ch. 4.3, the mean sizes and size distributions of the emitted He droplets are determined with the aid of acceleration by perpendicular or parallel (with respect to the droplet beam direction) electrostatic fields. The gas dynamic properties of the cluster beam are studied in Ch. 4.4, for example the beam intensity and the dependence of the observed beam velocities on the droplet source parameters.

4.1   Bare He droplets

The detection of bare droplets is accomplished by mass spectrometry. A commercial quadrupole mass spectrometer (*Extrel*) with an integrated electron-impact ionizer is used. The transients are observed on a digital oscilloscope, and the time of flight of the helium gas pulse is measured from the trigger signal to the valve until the moment of detection. The beam velocity is determined by the measured flight time divided by the flight distance from the nozzle to the ionizer region[1].

The ions are detected using an off-axis electron multiplier, which provides a gain of 10^4–10^7 times the incident ion current and can be enhanced by an analog current-to-voltage preamplifier with a sensitivity of $10^7 - 10^9$ V/A. The electron multiplier is operated in combination with a conversion dynode (4 kV). Secondary electrons are generated on the dynode surface and are accelerated to the electron multiplier. The acquired signal is then transferred to a digital oscilloscope. The quadrupole voltages can be remote controlled by a computer using a home-built software called "iMess". A 0–10 V ramp drives the scan unit of the quadrupole that corresponds to the ratio of the RF amplitude and the

---

[1]Note that this is not the full distance to the detector; rather, after electron impact, the cluster (fragment) ions are accelerated by ≈ 50 V and move with high velocity from the ionizer to the detector in a flight time that is comparably short. This time can thus be neglected in determining the time-of-flight of the He clusters, especially considering the observed pulse width of ≈ 500 μs (FWHM) and the achievable accuracy for determination of the time of flight in the experiment.

DC voltage U_{RF}/U_{DC} which are applied to the rods and thereby controls the transmitted mass-to-charge ratio (see Ch. 3).
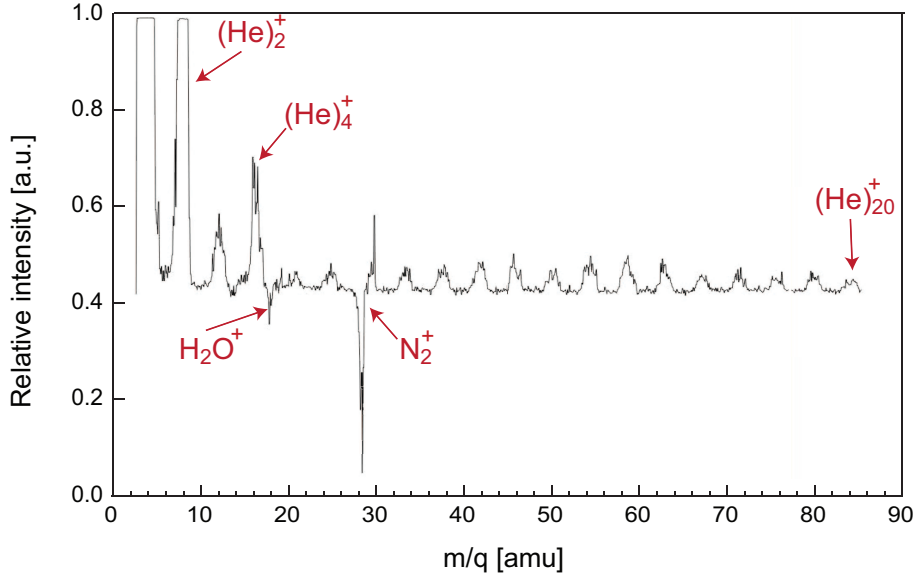
Figure 4.1: Mass spectra of bare He cluster fragment ions produced by the *Parker* He droplet source after electron impact ionization. He droplets are produced at $P_0 = 30$ bar, $T_0 = 6$ K, and the ionizer energy is $E_{el} = 100$ eV. The mass spectrometer settings and alignment of the He droplet source are optimized for the He dimer He_2^+ ion signal. The intensities displayed are normalized to the highest mass peaks (He^+ and He_2^+). For further explanations of the observed features in the mass spectrum see text.

For analog signal acquisition a *Stanford Research Instruments* (*SRS*) Gated integrator and boxcar averager is used [193]. This device is designed to acquire and analyze fast repetitive analog signals.
The gated integrator integrates and amplifies only a signal which coincides with the opening of a time gate which is adjustable in width between 100 ps–150 μs and can be set with a delay relative to the respective trigger signal. The temporal width of the gate is shorter than the observed width of the emitted gas pulse, so a gate of ≈ 1 ms opening time would be more convenient for this experiment. The output of the integrator is averaged over n trigger pulses and thus the signal-to-noise ratio is improved by a factor of $\sqrt{n}$.

Fig. 4.1 shows a mass spectrum of He droplet fragments after electron-impact ionization. He droplets are produced by the *Parker* General valve at $T_0 = 6$ K and $P_0 = 30$ bar at a repetition rate of $f = 4$ Hz, and an electrical pulse length $t_{pulse} = 230$ μs at an applied voltage of $U_{valve} = 240$ V. The electron energy E_{el} is 100 eV, the spectrum is recorded for one time at a scan speed of 0.001 Vs^{-1}, corresponding to ≈ 0.2 amu s^{-1}. The quadrupole settings as well as the droplet source alignment to the experimental axis are adjusted using the He dimer He_2^+ ion signal as optimized quantity. Typical ion intensities obtained are ≈ 1.2 V for the He monomer and ≈ 70 mV for the dimer.
In the mass spectrum obtained, He_N^+ ions are observed up to a size of He_{20}^+. Some of the mass peaks appear at significantly higher abundances than the average intensity, for example the He monomer and the dimer ion appear at saturated intensities. The next highest intensity has the ion signal of the tetramer ion He_4^+, which is almost double that of the trimer ion He_3^+ signal. An at first striking feature of the mass spectrum is the

presence of two very pronounced dips in the baseline occurring at the m/q ratios of H_2O^+ and N_2^+. The origins of all mass peaks and the last-mentioned features are explained in the discussion below.
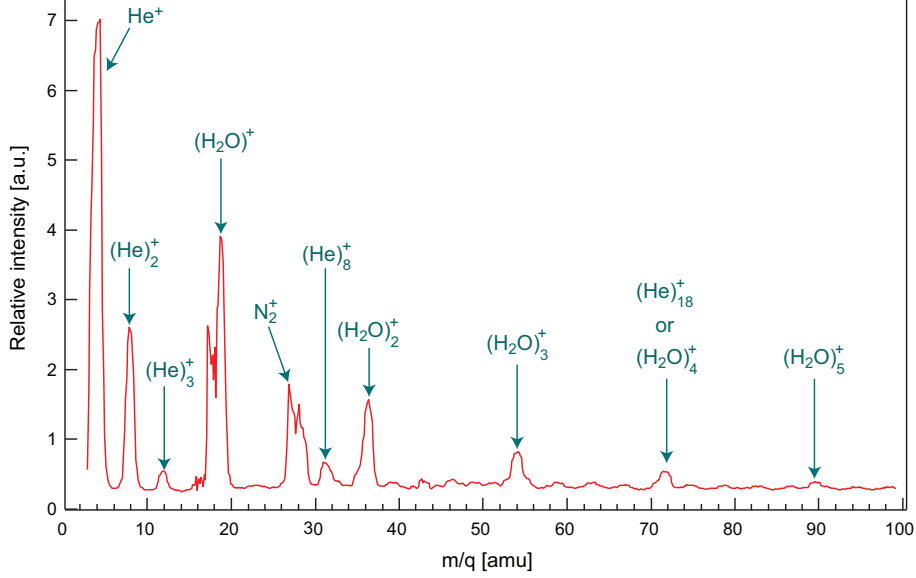
Figure 4.2: Mass spectrum of He droplet fragments from Even-Lavie source after electron impact ionization. He droplets are produced at $P_0 = 30$ bar and $T_0 = 15$ K at a repetition rate $f = 10$ Hz with pulse lengths $t_{pulse} = 16.7$ μs, the electron energy for ionization is 50 eV. The mass spectrum shown is an average of 5 measurements.

Fig. 4.2 shows a mass spectrum of He droplet fragment ions after electron-impact ionization when using the Even-Lavie valve in the He droplet source. The He monomer and dimer ion peaks are dominant; also larger cluster fragments are present up to $He_{N=8}$, but for larger N the mass spectrum is dominated by ionized water clusters (here up to $(H_2O)_5$). The baseline of the mass spectrum in fig. 4.2 possibly indicates the presence of larger cluster fragments since it exhibits a wave-like structure; however, at much reduced relative intensities compared to the intensities of the water clusters. The "dips" in the 18 amu and 28 amu peaks structures correspond to the baseline dips observed in the mass spectrum of the General valve.

Discussion

He_2^+ is supposed to be the fragment ion with highest abundance after electron impact which –compared to the monomer ion– can emerge from cluster fragmentation only (see Ch. 2.1.1). The trimer ion signal He_3^+ also appears in high abundance. This is explained by dynamic charge hopping processes and ν–T transfer[98]. According to this theory, the He_3^+ ion is the positive ion core that remains after fragmentation and complete vibrational relaxation of a large He cluster as the most stable cluster fragment.

The tetramer ion He_4^+ often appears in particularly high abundance in fragment mass spectra of He clusters. This cannot be attributed to an especially high stability like for "magic" cluster sizes as reported in ref. [194], because the atomic binding energy in

the tetramer cluster ion is only 0.03 eV and is thus low compared to the binding energy of 0.17 eV present in a He trimer cluster [58]. Therefore, a different, more complex formation process needs to be considered [58]. The He_4^+ ion is observed only when the electron ionization energies are higher than 37 eV, which indicates that might be formed by the simultaneous creation of two metastable $^3S_1$ atomic excitations [84, 92]. Furthermore, it appears only at low temperatures and high pressures and is therefore assumed to be related to liquid beam expansions in the "*Regime III*" [58, 84] in phase space (see Ch. 1.3.2).

The large baseline fluctuations ("breakdowns") at 18 and 28 amu are not of physical nature. They are rather caused by the measurment technique using the boxcar averager in an AC coupled mode. The boxcar synchronizes the acquisition time with the arriving signal wave. The input is AC coupled which means that only pulsed waveforms are transmitted while the continuous component of the signal wave is blocked. When scanning over N_2 or H_2O, which are statically present as residual gases, the baseline is caused to fluctuate with time due to temporal changes of transmitted and blocked m/q ratios. In this way, an "artificial" AC component is created which is then treated as part of the transmitted signal. Water and nitrogen are prominent residual gases in vacuum chambers[2], and therefore usually make a large contribution to the background signal. In our experiment, N_2 has a high abundance since in the *ESI* process, nitrogen is used as desolvation and nebulizer gas (see Ch. 3.1.1). Performing the mass scanning at slower scan speed can help to suppress this effect.

The main difference between the fragments mass spectra measured using the two different valves is the presence of water cluster $(H_2O)_N$ ions in the mass spectrum of clusters produced by the Even-Lavie, valve which are missing in that produced by the General valve. The detection of water clusters can be used as an indicator for He droplets having travelled through the apparatus. Water clusters can form in the droplets as aggregates of successively agglomerated up H_2O molecules. One possibility is that the water molecule aggregates in large clusters can be very large and complexes of several hundred to thousands of water molecules are formed. Those "ice" complexes can therefore be quite heavy and would be beyond the scanned mass range in these measurements.

Note that the probability for the simultaneous pickup of charged and neutral particles is given as the product of probabilities, $P_{ion} \cdot P_{neutral}$. The aim is to pick up as few impurity particles –especially water molecules– per He droplet as possible. For this purpose, a low background pressure is essential. In particular, large He droplets with large cross sections are theoretically able to pick up a great number of water molecules which presumably aggregate in the droplet center and form an ice shell around the dopant molecule. An estimate of the number of H_2O molecules picked up by a He droplet composed of $N_{He} = 10^{12}$ atoms (a droplet size that is observed for the *Parker* General valve source, see Ch. 4.3.1) is given in the following.

The partial pressure of H_2O usually makes a large contribution to the total background gas pressure in a vacuum apparatus. Under the prerequisite that there is no leak or

---

[2]If vacuum chambers are neither baked nor cooled in order to remove water. The high abundance of water is due to an OH layer on chamber components that evaporates at background pressures of around $1 \cdot 10^{-6}$ mbar in high vacuum at room temperature.

other steady gas supply to the chamber, it is assumed that the contribution of hydrogen and water to the residual gases in a non-baked vacuum chamber at room temperature comprises about 80–90 % after several days of pumping (when heavier particles are usually already removed). Most of the standard vacuum pumps have a low pumping efficiency for light particles, especially for hydrogen. Removing water from a vacuum apparatus is difficult too, and it can take a long time to evacuate an apparatus from water because it desorbs only slowly from the inner walls of a vacuum chamber at decreasing pressure. The hydrogen contribution to the background pressure is neglected here.

In an experimental setup like ours, however, with a large opening of the electrospray ionization source at the entrance, it is assumed that other residual gases (for example nitrogen) make a larger contribution to the background gas and, therefore, the percentage of water should correspondingly be reduced. Estimating a percentage of ≈ 50 % gives a partial pressure of $5 \cdot 10^{-8}$ mbar at a total pressure of $\approx 1 \cdot 10^{-7}$ mbar, which corresponds to a particle density of $\approx 4 \cdot 10^8$ particles per cm^{-3}. A large He droplet composed of 10^{12} He atoms has a collisional cross section of $\sigma \approx 1.3 \cdot 10^{-7}$ cm^2. With a distance of ≈ 200 cm from the nozzle to the detector and the given partial pressure of H_2O molecules in our chamber, an estimation of the mean number of water molecules picked up yields $\bar{N} = \sigma \cdot n \cdot L \approx 10400$.

However, the desired mean number is preferably less than one water molecule per droplet, in order to acquire experimental results for the pure, not water-dissolved, dopant particle. This can be promoted by a low temperature environment for doped He droplets in the vacuum apparatus, for example a cooled ion trap at liquid nitrogen temperature. The vapor pressure of water decreases rapidly with decreasing temperature, reaching a value of less than 10^{-12} mbar at liquid-nitrogen temperature [195]. Therefore, when the chamber is cooled to ≈ 70 K, no water should be able enter the gas phase in high vacuum at a background pressure of $\approx 1 \cdot 10^{-7}$ mbar. Usually, parent ion peaks of dopant molecules become the most intense peaks in a (fragment) mass spectrum of ionized clusters [104]. However, according to the theory of charge migration and fragmentation dynamics in a He cluster, these processes are dependent on the cluster size. The probability for charge transfer from a He atom to an embedded foreign species is higher for smaller clusters and rapidly decreases for large clusters [97]. Therefore, the lack of a signal from water cluster ions in the fragment mass spectrum of droplets produced by the General valve in fig. 4.1 might be indicative of the formation of very large clusters by the *Parker* General valve.

4.2   Ion-doped liquid He droplets

Charged droplets are obtained *via* pickup of ions from a linear hexapole ion trap, as described in Ch. 2.2. The experimental setup introduced in Ch. 3 is used with slight variations of the components or experimental sequence which will be indicated. There are two different basic sequences employed. One is used to measure the trap content (see Ch. 4.2.1), the other to measure the current of ion-doped He droplets. Each experimental sequence has two parts. In the first part, gas-phase ions are accumulated in the trap for a duration of t_{acc}, which is identical for both types of experiment. The difference occurs in the second part of the cycle, when ions are being stored in the trap and usually, He droplets are produced and traverse the trap. In the one version (measurement of trap content), the trap is dumped after a certain storage time t_{trap} and ions diffusing from the

trap are detected in the time-of-flight mass spectrometer, whereas in the other version of the cycle the ion-doped droplets are directly measured as an electric current on a Faraday-type metal detector.

In the experiments described, two different hexapole traps were used; they are introduced in Ch. 3.1.3. They differ mainly in length and therefore in the absolute number of ions that can be stored in the trap at one time. In the following, the first trap is denoted as the short trap, the second as the long trap. The experimental cycles employed are introduced in Ch. 3.2.

4.2.1 Depletion of the trap content

The first indication that ions can be removed from the trap by liquid He droplets was found by indirect detection: By the depletion and thus "missing" of a fraction of stored ions in a trap that is the result of a series of traversing He droplets. This is shown in
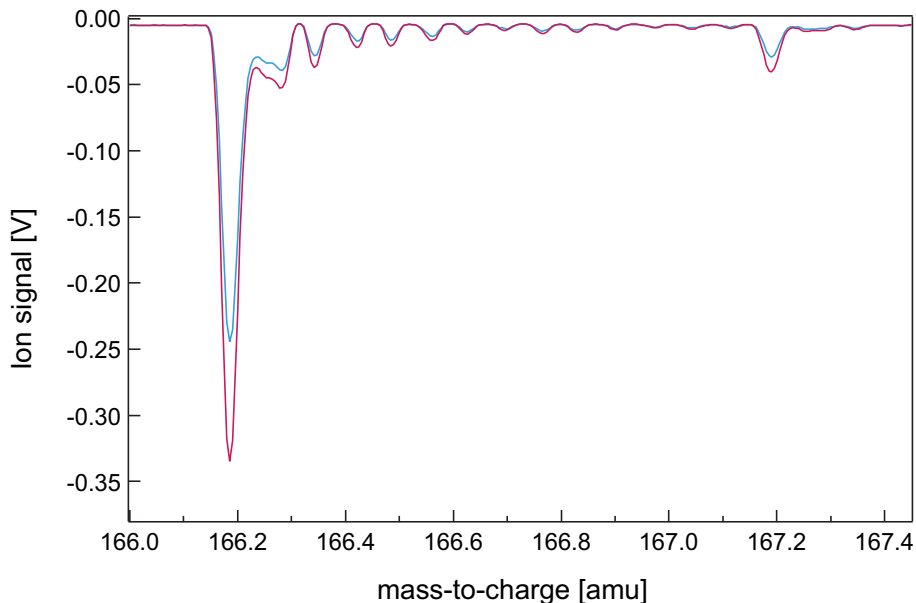
Figure 4.3: Base and depleted trap content. Mass-to-charge resolved spectra of Phe^+ ions after certain storage times as detected in the time-of-flight mass spectrometer after passing the double reflectron and being detected by the MCP detector. The base ion signal (red) is detected in the time-of-flight mass spectrometer after $t_{trap} = 30$ s storage and subsequent dumping of the trap. The depleted trap content (blue) is obtained after sending He droplet pulses for 30 s at a repetition rate $f = 4$ Hz through the trap (produced at $T_0 = 7$ K, $P_0 = 30$ bar). Protonated phenylalanine has a mass of 166 amu, and the small peak at 167 amu can be attributed to the fraction of C_{13} atoms in the sample.

fig. 4.3. Displayed in red is the base signal of Phe^+ ions that have been accumulated and stored in the trap for a time $t_{acc} = 30$ s and $t_{trap} = 30$ s.
Afterwards, the trap is dumped and the ions can diffuse out of the trap. They are deflected in the quadrupole bender by 90° and are detected in the time-of-flight mass spectrometer with mass-to-charge resolution using the double reflectron assembly. In blue, the depleted trap content ion signal of Phe^+ ions is shown. Ions are accumulated and stored in the trap for the same time t_{acc}, but during the storage time of 30 s, He droplet pulses pass through the trap at a repetition rate of $f = 4$ Hz. It is observed that the ion signal is reduced by ≈ 30 %. The experimental sequence employed is sketched

in fig. 3.19. In fig. 4.4, the trap content is displayed as a function of the number of droplet pulses which are produced during the storage time t_{trap} of ions in the trap. For each point on the graph, Phe$^+$ ions have been accumulated for $t_{acc} = 10$ s, and after the storage time, the trap was dumped and the ion signal measured in the time-of-flight mass spectrometer using the PMT detector assembly. The base trap content is displayed as circles (red), the depleted trap content is shown as diamonds (blue). Obviously, the ion yield is diminished when He droplets have passed through the trap, and this is more pronounced for increasing storage times t_{trap}. A simple kick-out of ions by He droplets *via* elastic collisions can be ruled out because the collision energies are usually below the trapping potential (see table 2.1). A control experiment was performed with a "warm" beam of atomic helium that is expanded at $T_0 = 30$ K (when no clustering is expected). This beam traverses the trap during ion storage and indeed, no depletion of the trap content is observed after dumping the trap. The absence of a signal depletion for an atomic He beam confirms that the observed diminishing of the ion signal must be an effect of He clusters. This means that an ion is picked up and transported out of the trap by a He droplet. Therefore, the signal depletion is interpreted as a consequence of ion-pickup by (sufficiently large) He clusters.

In Ch. 4.2.2, the results for directly measured ion-doped He droplets are presented; they confirm this interpretation of the depletion experiments.

The decrease in ion signal intensity per unit time and hence, the decrease in the number of ions contained in the trap N is assumed to be a consequence of a removal of ions from the trap, which are picked up and transported by He droplets. Thus, the number of ions removed from the trap per unit time is determined by the number of pickup events per unit time, corresponding to the effective number of collisions which take place during ion storage. The pickup probability depends on the (initial) particle density n in the trap, which is assumed to be constant when ions are accumulated for equal times t_{acc} at equal ion fluxes from the *ESI* source, on the trap length L, the collisional cross section σ of a droplet and an ion (dominated by the geometrical cross section of the droplet), and on the flux of He droplets I_0 which are passing through the trap (see Ch. 2.2.1) as:

$$\frac{dn}{dt} = -n\,L\,\sigma\,I_0 \quad , \tag{4.1}$$

with n the ion density in the trap, L the trap length, σ the collisional cross section, and I_0 the droplet flux in units of droplets $\cdot$ cm^{-3} $\cdot$ s^{-1}. This differential is solved by an exponential function as $n(t) = n_0\,e^{-L\,\sigma\,I_0\,t}$.

From the graph it can be seen that half of the ion signal is depleted after ≈ 300 droplet pulses. Assuming the space charge limit with $n = 10^6$ cm^{-3} and estimating a maximum total number $N = n \cdot V$ of ions contained in the trap by assuming an upper limit for the trap volume as the space between the rods (which, however, is an extreme upper limit) of $V \approx 20$ cm^3 results in a number N of about $2 \cdot 10^7$ ions in the trap. Thus, using the observed half-value period of 300 pulses after which 50 % of the $N = n/2 \cdot V$ ions are removed from the trap results in a rate of $1.3 \cdot 10^5$ ions removed per second and, with a repetition rate of 4 Hz, this corresponds to $\approx 3 \cdot 10^4$ ions removed per He droplet pulse. This seems to represent a low pickup efficiency. One reason might be a lower particle density in the trap, since the space charge limit might not be reached during the 10 s accumulation time. Another possible reason is a misalignment of the He droplet source

with respect to the trap, leading to a small intensity I_0 of droplets traversing the trap. A realignment of the droplet source when the longer trap was installed was indeed observed to yield a large gain in ion signal (see fig. 3.25). Furthermore, the approximation for the intensity of doped droplets $I(L) \approx n\,L\,\sigma\,I_0$ might not be valid under the given experimental conditions. In Ch. 4.3, the droplet sizes are determined and it turns out that the droplets produced by the *Parker* General valve can be very large. Having large cross sections σ enhances the probability for the pickup of multiple ions by a single droplet (see Ch. 2.2.4) and thus, the intensity of doped droplets $I(L)$ is rather given by the exact form of eq. (2.2).
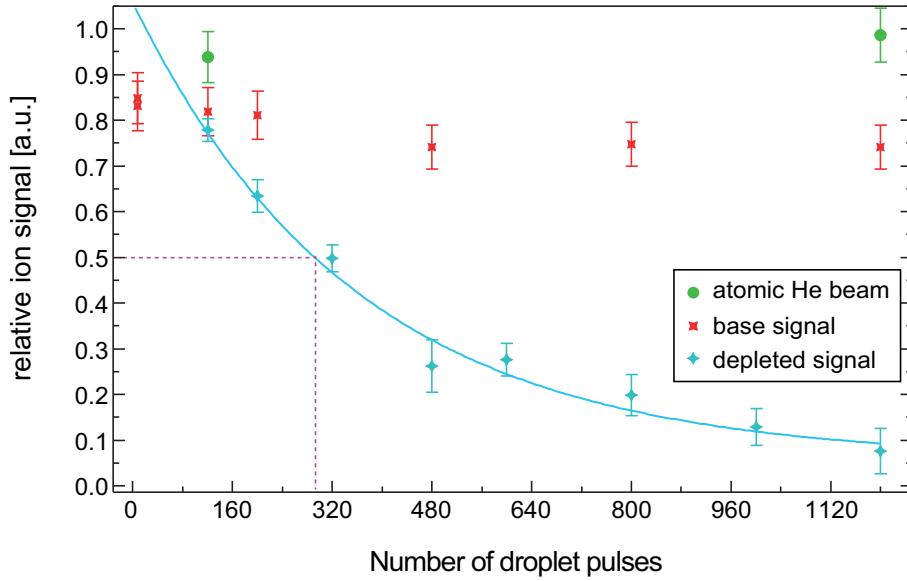
Figure 4.4: Base and depleted trap content as a function of the number of He droplets produced during the storage time t_{trap} of ions in the trap, as detected in the PMT detector assembly. Phe$^+$ ions are accumulated for $t_{acc} = 10$ s in the shorter trap ($L = 14.5$ cm). He droplets are produced at $T_0 = 6$ K and $P_0 = 30$ bar. The data shown were taken in a one-day series. Each point represents the peak intensity of the ion trap content signal as observed on the oscilloscope, while red points reflect the base signal and dark blue rectangles the depleted ion signal. Green diamonds show the ion signal after an atomic He beam produced at $T_0 = 30$ K has traversed the trap. Error bars account for fluctuations of the ion signal as well as the possible inaccuracy of signal read-out on the oscilloscope.

When an atomic He beam produced at $T_0 = 30$ K traverses the hexapole trap, the ion base signal is observed to increase slightly (see open diamonds (green) in fig. 4.4). This can presumably be attributed to the higher background pressure in the trap chamber due to the He gas beam which is observed to rise to about $5 \cdot 10^{-6}$ mbar when the He droplet source is turned on. During ion accumulation, the background pressure in the trap is determined by the injected He buffer gas. When the injection is stopped, He atoms effuse out of the trap into the vacuum chamber and are pumped away. When, during ion storage, additional He gas enters the trap (as in case of an atomic beam emitted from the droplet source), it might promote the trapping efficiency due to further collisional cooling of the thermally moving trapped ions.

The depletion of the trap content was measured as a function of the applied source temperature T_0 at three different gas pressures P_0 of 20 bar, 30 bar, and 40 bar in a one-day series. CytC^{+14} ions were accumulated in the short trap for $t_{acc} = 10$ s, He
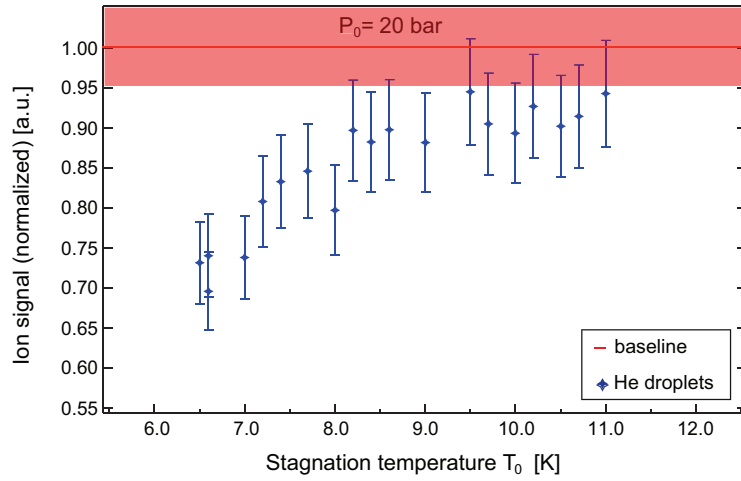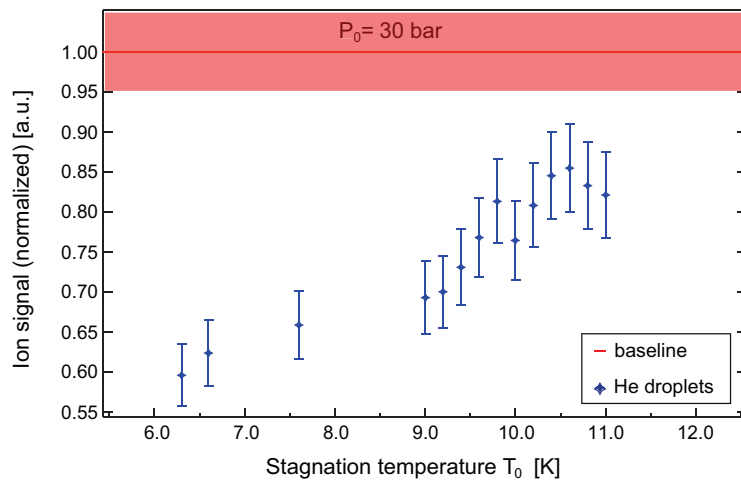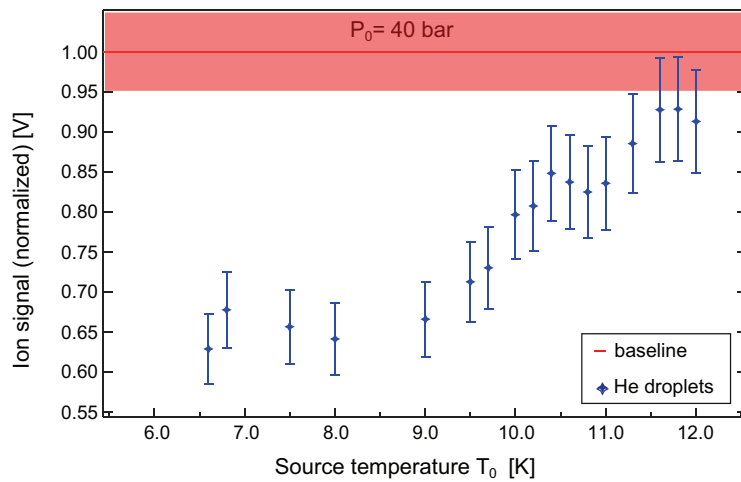
Figure 4.5: Trap content as a function of initial stagnation temperature T_0 for CytC ions at different pressures P_0 (a) 20 bar, (b) 30 bar and (c) 40 bar. He droplets are produced for $t_{exp} = 30$ s at a repetition rate of $f = 4$ Hz using the *Parker* General valve
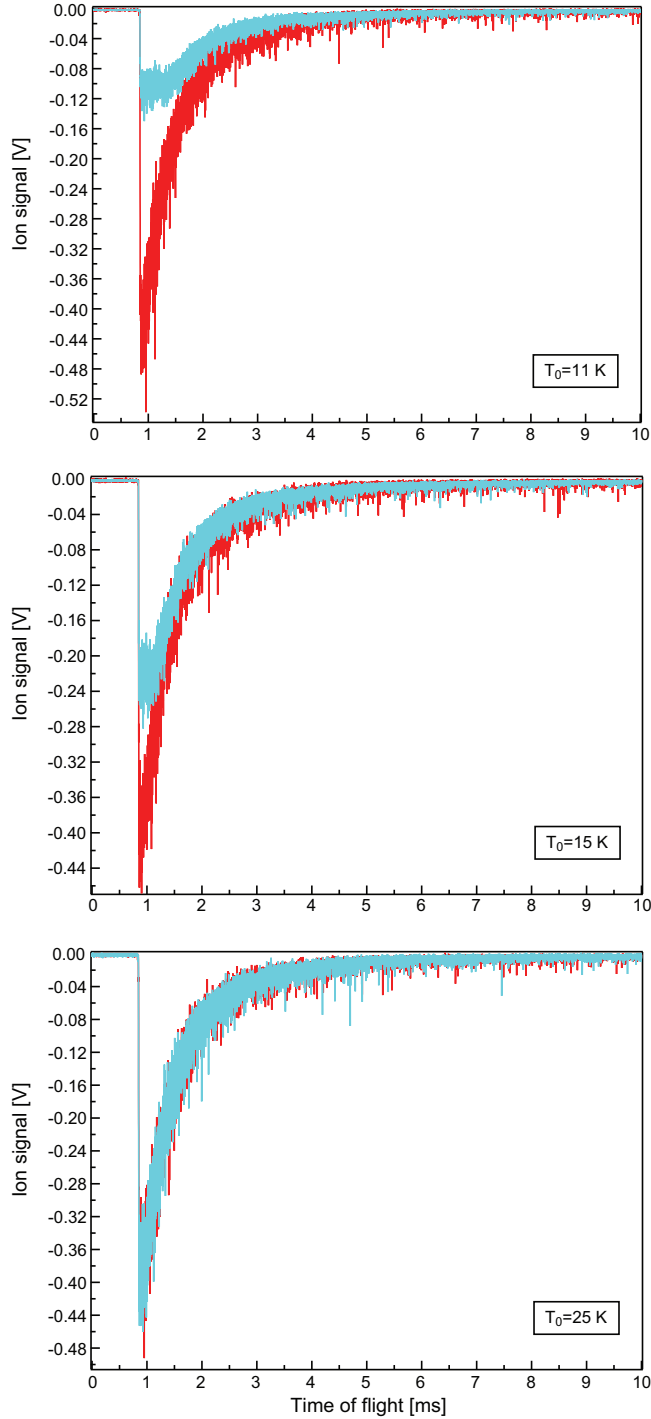
Figure 4.6: Depletion of ion trap by droplets produced by the Even-Lavie source as observed for different applied source temperatures (a) $T_0 = 11$ K, (b) $T_0 = 15$ K, (c) $T_0 = 25$ K, each at $P_0 = 40$ bar. He droplets are produced for 30 s at a repetition rate $f = 50$ Hz, and the valve opening times t_{pulse} are set to 15.5 μs in (a), 16.5 μs in (b), and 17.5 μs in (c). The trap content base ion yield (without He droplets) is shown in red, blue is the depleted ion signal.

droplets were sent through the trap for $t_{trap} = 30$ s at a repetition rate of $f = 4$ Hz. For each series (hence a particular source pressure P_0), the base trap content is measured and is shown as a red line in fig. 4.5 giving the normalized mean value (over different measurements) of the base ion signal for each applied source pressure. The red bars

in each panel represent the approximate errors in base ion signal which include the achievable accuracy of reading out the ion signal on the digital oscilloscope as well as statistical fluctuations of the ion signal over different measurements. For $P_0 = 20$ bar, the observed maximal depletion corresponds to ≈ 27 % of the base trap content, for $P_0 = 30$ bar, a depletion of ≈ 40 % is observed, and for 40 bar a depletion of ≈ 35 %. As a trend, it can be seen that the depletion is less pronounced when He droplets are produced at higher source temperatures T_0 and at lower gas pressures P_0. This agrees with the expectation that the droplet size decreases for expansions at higher source temperature and lower gas pressure and therefore, a reduced cross section for ion pickup should be seen under these conditions. A second reason might be a reduced droplet flux emitted from the nozzle at higher source temperatures.

Similarly, the depletion of the trap content by He droplets produced by the Even-Lavie source was measured. In fig. 4.6, this is shown for three different source temperatures, $T_0 = 11$ K (top), 15 K (center), and 25 K, all at a pressure $P_0 = 40$ bar. The trap was filled with protonated tryptophan ions, Trp^+. In red, the base trap content is given, and in cyan, the depleted trap content. He droplets were produced for 30 s at a repetition rate of $f = 50$ Hz, and the electric pulse lengths t_{pulse} were set to 15.5 μs, 16.5 μs, and 17.5 μs, respectively. Indeed, a depletion of the trap content is observed which is more pronounced for lower source temperatures T_0 and hence for larger sizes of the droplets produced. For $T_0 = 11$ K and 15 K, a depletion of about 75 % and 45 % of the base ion signal is observed, respectively, when He droplets traverse the trap, while for $T_0 = 25$ K, no depletion was observed. Presumably at this temperature, either no droplets are produced or they are not large enough to pick up and transport the stored ions.

Furthermore, the measured depletion can be used to determine the number of particles N contained in the trap. The number of ion-doped droplets per pulse is determined from the measured ion current of charged droplets doped with Trp^+ ions which are produced at a source temperature $T_0 = 16$ K with the calibrated *FEMTO* amplifier (see Ch. 4.3.2). The ion yield is determined to give ≈ 2000 doped droplets per pulse, assuming only the pickup of a single ion per droplet. Now, the depletion of 45 % of the trap content obtained when He droplets are produced at $T_0 = 15$ K is considered. This results in a number of $\approx 3 \cdot 10^6$ ions removed, implying an initial trap loading of $N \approx 7 \cdot 10^6$ particles.

4.2.2 Time–of–flight profiles of ion-doped He droplets

The first direct observation of ion-doped He droplets is the detection of an electrical current on a copper plate detector which is installed in the direction of flight of the He droplets after the quadrupole bender. The observed time-of-flight profiles show a dependence on the experimental parameters responsible for the generation and trapping of gas-phase ions in the hexapole trap as well as on the expansion conditions for He droplets. Therefore, the detection of the ion current is interpreted as a proof of principle for the pickup and transport of biomolecular ions by He droplets.

It is often difficult to detect heavy particles having high mass-to-charge ratios with standard charged particle detectors that rely on electron release from a surface upon ion impact as the first step (for example MCP's or Daly-type detectors) [153].

Alternatively, the direct ion current can be measured using a current-to-voltage amplifier. In order to detect the impinging ion-doped droplets as small single-charge currents, a strong amplification is required. Here, two types of amplifiers are used which are introduced together with the Daly detector in Ch. 3.1.2.

To detect the ion-doped droplets, the *Amptek* preamplifier together with the *Ortec–Brookdeal* amplifier was used in most measurements with the *Parker* General valve since it has a large amplification factor. Later, when the Even-Lavie valve had been installed in the He droplet source, the sensitive and fast conversion-type Daly detector [196] was available and was used for some of the measurements shown. For calibrated measurements of the ion current, the *FEMTO* amplifier was used.

Electric charge detectors

The current of ion-doped He droplets is detected using Faraday-type copper detectors of different areas and shapes. A wire ($\approx$ 1 mm thick), a plate (diameter $\approx$ 2.5 cm), and a detector in a "cone" shape (see fig. 4.7) are used. The at last-mentioned detector shape was chosen in order to maximize the collection of charges. It has a length of $\approx$ 5 cm and a maximum opening diameter of $\approx$ 1.5 cm.

Figure 4.7: Photo of the cone-shaped Faraday-type detector on a scale of $\approx$ 3:1 to the original.

With each detector the signal from ion-doped droplets is measured with both the *FEMTO* and the *Amptek* amplifier; the obtained time-of-flight profiles are shown in fig. 4.8, where those on the left side were recorded using the calibrated *FEMTO* amplifier and on the right side using the *Amptek* preamplifier together with the *Ortec-Brookdeal* amplifier at an amplification factor of 70 dB. From top to bottom, ion-doped He droplets are detected on a wire, on a plate, and with the cone detector. For each measurement, He droplets were generated at T_0 = 7.5 K, P_0 = 30 bar with the *Parker* General valve at a repetition rate of f = 4 Hz for t_{exp} = 15 s. They are doped with $Gram_{syn}^{+2}$ ions that are accumulated in the short trap for t_{acc} = 10 s. In all traces, an electromagnetic interference caused by the trigger pulse of the valve can be observed at early times. It is seen that the signal (peak) intensity decreases with decreasing area of the detector used, which is reasonable; furthermore, the peak shape changes (especially when the *Amptek* amplifier is connected). For the narrow Cu wire detector, a strong ringing is visible and one part of the signal becomes negative. This

Figure 4.8: Signal of ion-doped He droplets detected on Faraday-type metal detectors, measured using the calibrated *FEMTO* amplifier (in the panels on the left) at the maximal amplification of 10^{11} V/A and the *Amptek* preamplifier (in the panels on the right) with an amplification of 70 dB from the *Ortec-Brookdeal* frequency filter. He droplets are produced at $T_0 = 7.5$ K, $P_0 = 30$ bar with the *Parker* General valve and are doped with $Gram_{syn}^{+2}$ ions that are accumulated in the short trap for $t_{acc} = 10$ s.

ringing is reduced when detectors with larger areas are used and has almost vanished for the cone detector.

It is not fully understood why the signal shape is different depending on the shape of the detector and the amplifier used. Presumably, it can be excluded that this is a real physical effect due to the detected particles. It can rather be attributed to the electronics of the (pre)amplifiers used. In the case of the cone detector, its spatial extension in the flight direction might cause a spread in detection times of particles which have different radial positions within the beam profile. A particle moving along the beam central axis will probably enter more deeply into the cone detector and will thus be detected with a time delay compared to a particle that is moving further outwards in the beam. The latter would hit the detector more at its edge and thus would be detected earlier. With a length of 5 cm and a beam velocity of ≈ 250 ms^{-1}, this would lead to a temporal spread of ≈ 0.2 ms.

Another factor which possibly influences the shape of the ion signal is the capacitance of the detector ensemble employed. Different capacitances of the Faraday detectors might influence the amplifier response and lead to the observed signal shapes. This is more pronounced when using the *Amptek* preamplifier with the *Ortec-Brookdeal* filter. However, the capacitance dependence in the detection process will not be discussed further here.

Image charge detection

An experiment was performed to find out if it is possible to detect ion-doped He droplets *via* a non-destructive measurement that makes use of image charges induced on metal surfaces by nearby electric charges. For this purpose, a copper tube detector (inner diameter: 11 mm) is installed behind the bender in the direction of flight of the He droplets and centered radially to the beam axis. A grounded aperture with an opening diameter of 4 mm is installed in front of the tube to prevent direct impact of the ions on the tube detector.

The induced mirror charge is equal to the total charge Q of the ions that pass close to the detector, but the mirror charge has an inverse sign [197]. It should be proportional to the detector area and hence to the length of the tube, and inversely proportional to the detector capacitance and to the distance between the passing ion packet and the inner face of the tube.

For this experiment, He droplets that are produced at $T_0 = 7.5$ K, $P_0 = 30$ bar, $t_{exp} = 15$ s with a repetition rate of $f = 4$ Hz and an electric pulse length of $t_{pulse} = 220$ μs are doped with the doubly charged peptide Gram$_{syn}^{+2}$ that is accumulated for $t_{acc} = 15$ s in the short trap. Ion-doped droplets are detected *via* the image charge induced when they pass through the Cu tubes. Two different tube detectors were used, having the same inner diameter of 11 mm but different lengths (L$_1$=3 cm and L$_2$=6 cm). The time-of-flight profiles shown in fig. 4.9 were recorded using the *FEMTO* amplifier at its maximal amplification of 10^{11} V/A. 1500 time-of-flight profiles were averaged for the short tube and for the longer tube, 9000 averages were taken. The observed integrated signal allows for determining the number of induced image charges per droplet pulse through the amplification factor of 10^{10} V/A and gives for the shorter tube ≈ 500 and for the longer tube ≈ 1700 ion-doped He droplets per pulse. It can be seen that by doubling the
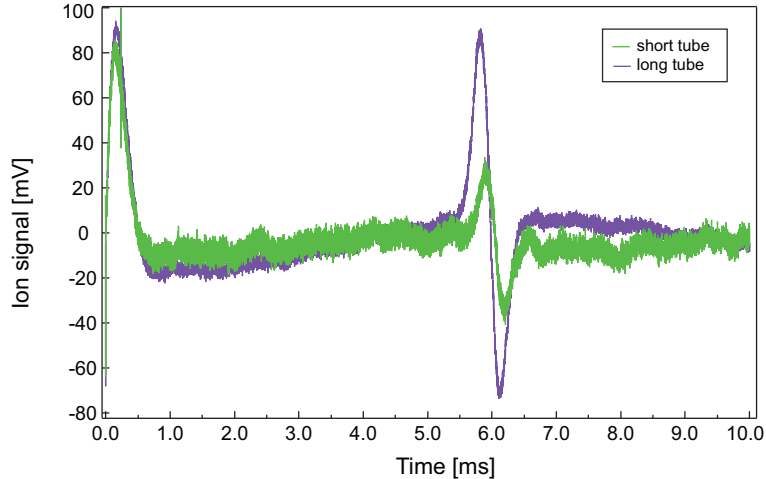
Figure 4.9: Image current signal of He droplets doped with doubly protonated Gram_{syn}^{+2} ions, measured with two tubes of different tube lengths and inner diameters: the short tube has a length of 3 cm, and the longer tube has almost twice this length; they both have an inner diameter of ≈ 11 mm. Transients of ion-doped He droplets detected by image current in tubes of different lengths. The He droplets were produced at $T_0 = 7.5$ K, $P_0 = 30$ bar.

tube length an enhancement of more than a factor of 2 of the signal intensity is achieved. With the (electric) pulse length t_{pulse} and the measured beam velocities, the longitudinal spread s_x of the droplet packet is determined. With the given source parameters, the beam velocity is $v_x \approx 195$ ms^{-1} , giving a longitudinal packet length of $s_x \approx 4.3$ cm. Thus, the packet is longer than the short tube and on passing through the tube, the packet cannot be entirely inside the tube at one time. As a consequence, with the short tube only a fraction of the pulse of charged droplets is detected per unit time, which results in a reduced signal intensity. In case of the longer tube, however, the whole packet can be measured at one time. Presumably, the non-linear difference in intensity in terms of the tube length can be attributed to the the ratio of tube length and packet length for the two tube detectors used.

Signal intensities of ion–doped He droplets

The results on ion-doped He droplets obtained by using the *Parker* General valve in the He droplet source are presented. The valve is operated at a repetition rate of 5 Hz with ≈ 220 μs long (electric) pulses. In fig. 4.10, the time-of-flight profiles measured for He droplets doped with Trp$^+$ ions (top panel) and CytC^{+17} ions (bottom panel) are shown. They were recorded using the calibrated *FEMTO* amplifier which allows for determining the number of ion-doped He droplets per pulse from the integrated intensity. This yields in the case of Trp$^+$ ions about 30 000 doped He droplets, and for CytC^{+17} about 470 doped droplets per pulse. The transients shown were not recorded on the same day, so expansion conditions, for example the gas pressure P_0, might slightly differ which could cause differences in the flight time (see fig. 4.8). In case of droplets doped Trp$^+$ ions, the time-of-flight profiles shown are averaged over 30 measurements and in case of CytC^{+17}-doped droplets over 500 measurements.

The dependence of the time of flight and peak intensity of ion-doped He droplets on the expansion parameters T_0, P_0 was studied. For varying source conditions, temporal profiles

(a)

(b)
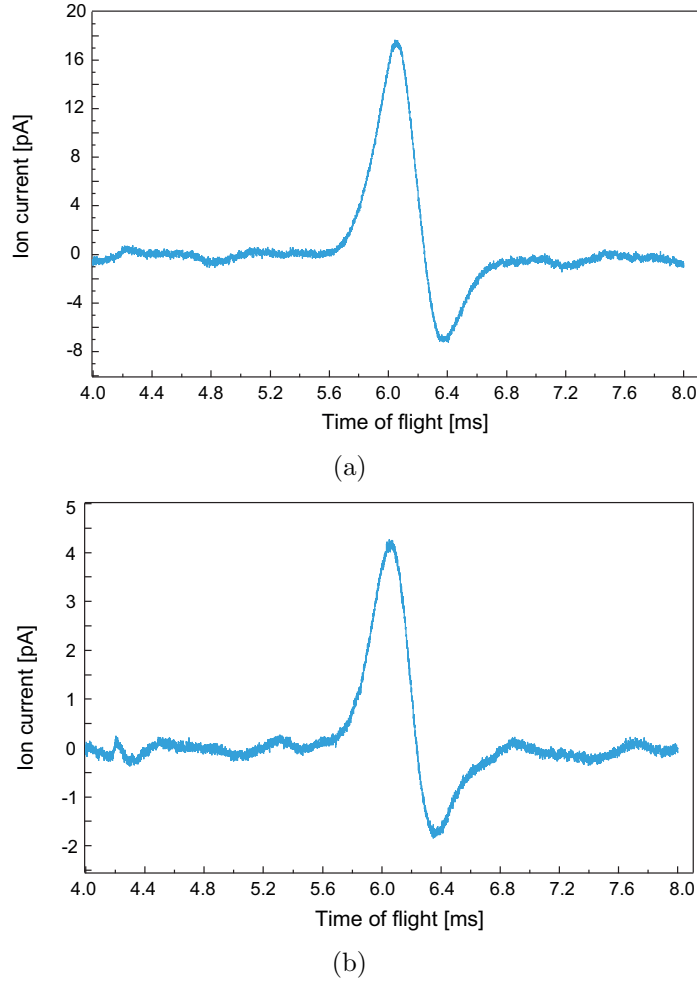
Figure 4.10: Time-of-flight profiles of He droplets produced by the *Parker* General valve at $T_0 = 8$ K, $P_0 = 30$ bar and doped with singly charged tryptophan (top panel), and cytochrome c ions in a charge state $+17$ (bottom panel). Traces are recorded using the calibrated *FEMTO* amplifier at an amplification factor of 10^9 V/A and the measured ion yield is directly displayed as an ion current. The signal of He droplets doped with Trp^+ ions corresponds to $\approx 30\,000$ doped droplets per pulse and the signal of droplets doped with $CytC^{+17}$ ions gives a number of ≈ 470 doped droplets per pulse.

of He droplets doped with $CytC^{+Z}$ ions in the charge state $Z = +14$ were recorded, and the results are shown in fig. 4.11. In the top panel, time-of-flight profiles of ion-doped He droplets are shown; they were obtained at varying source temperatures T_0 at a constant gas pressure $P_0 = 30$ bar. In the bottom panel, time-of-flight profiles are shown for doped He droplets produced at different gas pressures P_0 at a fixed source temperature, $T_0 = 7$ K. The ion signal appears at around 8 ms and has a width of ≈ 500 μs (FWHM). Upon increasing the temperature, the peaks shift to earlier times. At temperatures above 10 K, their intensity rapidly decreases and no doped droplets can be observed above 11.5 K. The measured beam velocities range from 201 ms^{-1} at 5 K to 290 ms^{-1} at $T_0 = 11.5$ K (given in the graph). The beam velocities are in agreement with velocities determined before for undoped He droplet fragments (see fig. 3.31 in Ch. 3.4.2) after electron impact ionization. The speed ratio $S = \frac{v}{\Delta v}$ of the He cluster beam is expected to be high, with values between 30–100, depending on the source conditions [15], as is known for cold cluster beams [58, 84, 113]. The velocity spread Δv_x (FWHM) of the time-of-flight profiles of

(a)

(b)
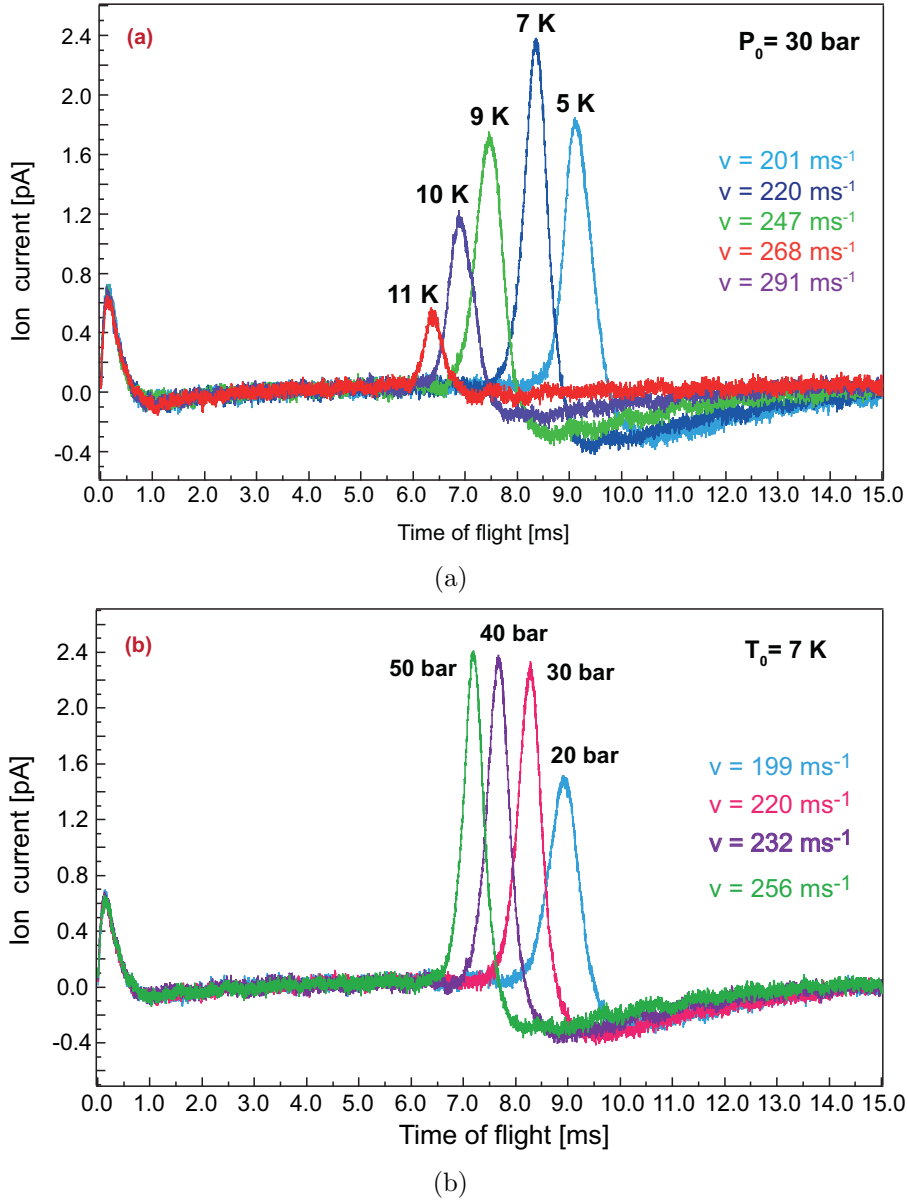
Figure 4.11: Time-of-flight profiles of He droplets produced by the *Parker* General valve. The measured current of ion-doped droplets is shown for varying expansion parameters T_0, P_0. The droplets are doped with $CytC^{+14}$ ions. In the top panel (a), the source temperature T_0 is varied from 5 K to 11 K at a fixed pressure of $P_0 = 30$ bar, and in the bottom panel (b), the temperature is kept at $T_0 = 7$ K and the gas expansion pressure P_0 is varied between 15 bar and 50 bar. It is observed that the ion signal maximum shifts to earlier arrival times for both increasing T_0 and increasing P_0. The corresponding mean beam velocities are denoted in the figures.

≈ 500 μs observed here is broad. However, it is possible that a considerable portion of the peak widths can be attributed to the time response of the current amplifier and also to the long pulse length of ≈ 200 μs which, in a first approximation, can be subtracted from the width. This results in a speed ratio of $\frac{v}{\Delta v} \approx 30$ at a beam velocity of 220 ms^{-1}. This value is smaller than expected for a cold cluster beam; the speed ratios determined for He cluster beams in pulsed expansions are observed to have values of around $S = 100$ [113]. However, the speed ratio S obtained here is more similar to those determined for cluster beams produced under the conditions of *"Regime 3"*, which have values of $S = 40$–60.

The gas dynamic properties in terms of dependence on different nozzle and expansion parameters and observed beam velocities are further discussed in Ch. 4.4.

(a)

(b)
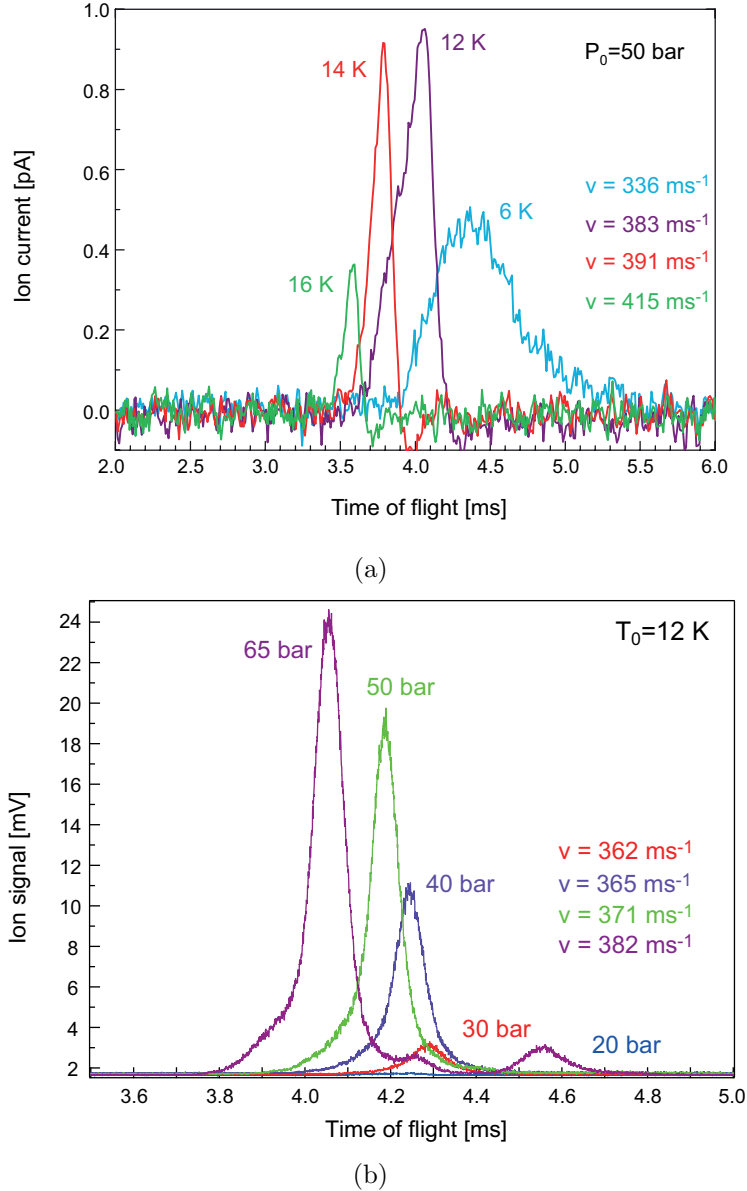
Figure 4.12: Time-of-flight profiles of ion-doped He droplets produced by the Even-Lavie valve as a function of the expansion parameters. The droplets are doped with Trp^+ ions. In (a), the source temperature T_0 is varied from 6 K to 16 K at a fixed pressure $P_0 = 65$ bar, and in (b), the temperature is kept at $T_0 = 12$ K and the gas expansion pressure P_0 is varied between 19 bar and 65 bar. The time-of-flight profiles in the top panel are recorded as ion currents from Faraday-type detectors using the *FEMTO* amplifier, whereas in the bottom panel, they are recorded using the fast conversion dynode-type Daly detector. It is observed that the signal maximum shifts to earlier arrival times for both increasing T_0 and increasing P_0. The corresponding beam velocities are quoted in the figures. The broadening of the peak for decreasing T_0 can probably be attributed to lower speed ratios in cluster beams with increasing cluster sizes.

The pickup of molecular ions in the hexapole trap was also observed when the Even-Lavie valve is used in the He droplet source. Time-of-flight profiles for ion-doped droplets

produced by the Even-Lavie valve were recorded as a function of the source temperature T_0 and gas pressure P_0 applied when holding the respective other parameter constant. They are shown in fig. 4.12. He droplets are produced at a repetition rate of $f = 50$ Hz with (electric) pulse lengths of $t_{pulse} = 18 \, \mu s$ at an initial stagnation pressure $P_0 = 65$ bar (top panel) and source temperature of $T_0 = 12$ K (bottom panel), respectively. The beam velocities are observed to increase for increasing source temperature and pressure. The speed ratio S is determined from the measured time-of-flight profiles. For the Even-Lavie droplet source, the electric pulse length and corresponding mechanical valve opening time is considerably shorter at only $\approx 15 \, \mu s$. The speed ratio as obtained from the measurements with the Faraday-type detector is found to be $S \approx 20$, but that obtained from measurements with the Daly detector has a much higher value of $S \approx 55$. Further discussion is given in Ch. 4.4.

Manipulation of charged droplets with electric fields

Having picked up an ion from the hexapole trap, a He droplet is electrically charged and can be manipulated by electrostatic forces.
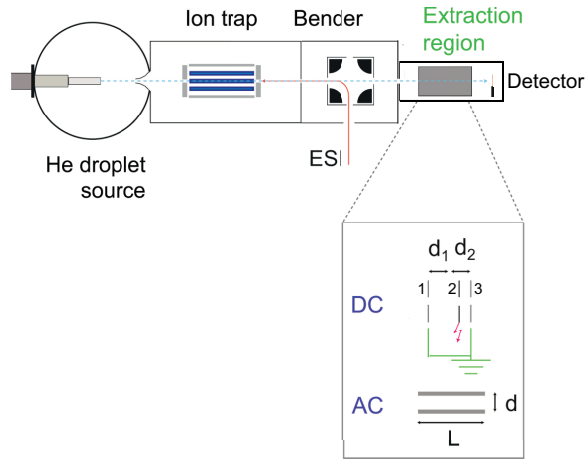
Figure 4.13: Sketch of the experimental setup for the extraction of ions from He droplets by applying high electric fields. In the inset, the geometries of the devices used to apply DC (top) or AC (bottom) electric fields are depicted.

Experiments were performed on ion-doped droplets to study whether it is possible to manipulate charged droplets with electric fields. Furthermore, it can be determined –linked to the theoretical considerations in Ch. 2.4– whether it is possible to extract an immersed ion from a He droplet by high electric fields. The setup used is shown in fig. 4.13. After ion pickup, the He droplets traverse the "extraction region" behind the bender where parallel or perpendicular-oriented electric fields (DC or AC) with respect to the droplet beam direction can be applied to two different metal plate assemblies. In the case of parallel DC electric fields, the installed device is a simple stack of three stainless steel plates (diameter 44 mm) with holes on the beam axis (diameter 4 mm) at a distance of $d_1 = 10$ mm between the two first plates and $d_2 = 5$ mm between the second and the third plate. The first and the third plate are grounded and a high voltage is applied to the second plate. This gives rise to an electric field between plate 2 and

plate 3, which has twice the strength compared to that between the first two plates due to the shorter spacing. To enhance the homogeneity in the electric field region, metallic meshes are glued onto the holes through which the ions and droplets pass. When an ion is extracted from the droplet in the high electric field region then it would be accelerated on an electron multiplier detector (ETP) that is installed behind plate 3. In this experiment, He droplets were produced at $T_0 = 7$ K and $P_0 = 30$ bar for 14 s at a repetition rate of 5 Hz in each cycle. $CytC^{+9}$ ions are accumulated for $t_{acc} = 9$ s in the trap. However, when parallel electric fields of field strengths up to 40 kV/cm are applied between the plate 2 and plate 3, no ions could be detected (not shown).

Then the electric field vector is rotated by 90° and rapidly alternating AC fields or DC electric fields are applied perpendicular to the beam direction between the two metal plates. The device used for this experiment consists of two parallel stainless steel plates of $L = 10$ cm length at a distance $d_y = 7$ mm from each other; the latter device will also be used for measuring the droplet size and size distribution *via* electrostatic deflection experiments (see Ch. 4.3.1). Time–of–flight profiles of the ion-doped droplets are measured by a Faraday-type copper detector that is installed further downstream behind the plates. In case an ion is extracted from a He droplet it would be accelerated towards the metal plates due to its light mass and could not be detected any longer as an electrical charge on the Faraday copper detector. Thus, an extraction of ions from the droplets would lead to a reduced signal intensity of ion-doped He droplets. In
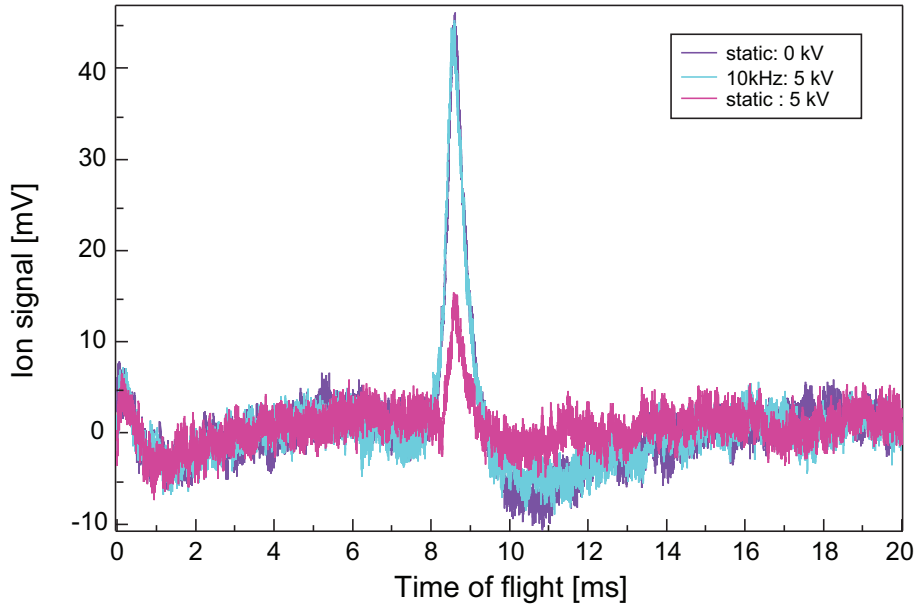
Figure 4.14: Resulting time–of–flight profiles of ion-doped droplets from AC extraction experiments. He droplets are produced at $T_0 = 7$ K, $P_0 = 30$ bar with the *Parker* General valve He droplet source for $t_{exp} = 10$ s. The ion-doped droplet current is measured on a copper Faraday-type detector that is installed behind the extraction region. In the time-of-flight profiles shown, the *Amptek* preamplifier with subsequent 70 dB amplification is used. He droplets are doped with $CytC^{+9}$ ions that were accumulated for $t_{acc} = 9$ s in the long trap.

the case of AC fields, two high-voltage switches are used and we test whether strong "shaking" of an ion inside a droplet might lead to a extraction of the ion from the droplet. The resulting time–of–flight profiles are shown in fig. 4.14. The purple curve is

recorded at zero electric field $|\vec{E}|$ and zero AC frequency. It serves as a static reference curve; similarly, the magenta curve serves as a static reference curve for an electric field strength of $|\vec{E}| = 7$ kV/cm. In cyan, the resulting time-of-flight profile for an electric field $|\vec{E}| = 7$ kV/cm with alternating polarity at a frequency of 10 kHz was applied to the metal plates. As can be seen in fig. 4.14, when rapidly changing AC fields are applied to the two plates, no change in the monitored time-of-flight profiles is detected as compared to the zero-field curve. However, applying static electric fields to the plates leads to a reduction of the signal intensity. This can be attributed to a deflection of the charged droplets from their original direction so they no longer reach the detector. The applied AC voltage, however, is changing so rapidly that on average, the electric forces in both directions cancel each other and no resulting force in one direction remains. Indeed, no reduction of charged droplets is observed in this case.

In conclusion, the observation of no detectable changes of signal intensities or peak shapes on applying static DC electric fields or AC electric fields is interpreted to imply that neither a moderate but steady pull, as with applied DC fields, nor a more rapid pull at high amplitudes, as with the AC fields, can lead to extraction of an embedded ion from a He droplet, at least not in the range of the field strengths and frequencies applied here. However, this can be seen as an experimental confirmation of the theoretical consideration of the magnitude of electric forces which are required to pull out an ion from a droplet in Ch. 2.4, at least in the range of experimental parameters applied here.

4.3 Droplet size and size distribution

The size and size distribution of a He droplet is an important quantity for studying both bare and doped droplets since most of the experiments require knowledge about the droplet sizes and size distributions. In the case of doped droplets, the cluster size and surface effects from the He environment often need to be considered for interpreting results from spectroscopic measurements on embedded dopant species. Performing action spectroscopy on doped He droplets can even put the number N_{He} of constituent He atoms into the role of the directly measured quantity when they are used as a "messenger" species for photon absorption. When the incident light is in resonance with a molecular transition, the dopant species absorbs photons and transfers the energy after excitation to the He droplet. The droplet releases this energy typically *via* thermal evaporation of He atoms from its surface. Hence, the light-induced change in the mass-to-charge ratio of the doped He droplet can be detected by mass spectrometry as a function of the incident wavelength in action spectroscopy.

It should be noted that measuring the size of He droplets is often difficult since a He droplet is a neutral and dissipative system which implies that any energetic or collisional impact leads to a change of the droplet mass and size. Several different methods have been employed for determining the droplet sizes and size distributions; most are applied to smaller clusters containing up to $\approx 10^4$ He atoms. One method is the diffraction of very small clusters composed of less than 100 He atoms by a nano-scale transmission grating, thus determining the cluster size by making use of the wave nature of the clusters [198–200]. Size distributions of clusters in the range of $N_{He} \approx 10^3$ He atoms could be obtained by deflection of a droplet beam *via* small-angle scattering at a second atomic

beam [201–203].

Measurements of droplet sizes are also performed in experiments on droplets doped with neutral species which subsequently become electrically charged within the droplets (for example by electron attachment, to produce negatively charged droplets [92]). Making use of the ability of He droplets to pick up any particle in a mechanical collision, their sizes can be determined by detecting the number of the embedded dopant particles either by electron impact ionization [183, 204] or by laser-induced fluorescence [113] in pulsed beam expansions. An alternative method for determining the sizes and size distributions of clusters containing up to $\approx 10^5$ He atoms is by measuring the attenuation of a cluster beam when ionized clusters are deflected out of the beam due to cluster fragmentation after bombardment with energetic electrons [205]. The sizes of electrically charged He clusters can be measured by, for example, a non-destructive technique making use of the image charge induced by the clusters. The cluster mass is determined by measuring the change in flight time upon applying a pulsed electric field to the charged droplet beam, which causes a mass-dependent change of the beam velocity. The charged droplets are detected by the image charge they induce on the inner face of a metal tube detector [206]. Large droplets composed of about 10^9 He atoms can even be detected optically using a microscope [90]. Another optical method is Rayleigh scattering, which is used in the group of Slenczka for determining the He droplet size [184]. The disadvantage of this method is that the droplet size is measured in a rather indirect way, since the signal of scattered light is a complicated function of the cluster size. Northby *et al.* determined the mean droplet sizes and size distributions of fragmented liquid beams produced in supercritical expansions. Helium cluster ions are created by crossing the cluster beam with an electron beam of 35 eV energy, giving positively charged clusters, and with an electron beam of 2 eV energy electrons, which gives negatively charged clusters. Their size is determined by stopping potentials as well as by electrostatic deflection in a perpendicular electrostatic field [85]. This is essentially the same method that we apply for determining the size of the He droplets produced with the *Parker* General valve in the He droplet source. The average sizes and size distributions of droplets formed by fragmentation of liquid beams has also been investigated. It is determined as a function of a dimensionless parameter related to the entropy in the liquid expansion, the surface tension, and the nozzle geometry by Knuth and Henne [86].

We determine the droplet sizes and size distributions by a direct method that makes use of the charged nature of ion-doped He droplets. These measurements involve electric fields which are applied in parallel or perpendicular direction to the beam of ion-doped droplets and exert forces on the charged droplets, causing them to change either the direction of their velocity (Ch. 4.3.1) or the absolute value of the velocity v_x (see Ch. 4.3.2).

4.3.1 Electrostatic deflection of ion-doped droplets

The masses of He droplets produced by the *Parker* General valve source are determined by electrostatic deflection in a homogeneous electric field. For an experimental measurement, a pair of oppositely-charged metal plates with a spacing of $d_y = 0.7$ cm and a length of $L_1 = 10$ cm is installed behind the trap and the bender (see fig. 4.15), about 120 cm downstream from the droplet source. Just in front of the plates, a 1.2 mm collimating
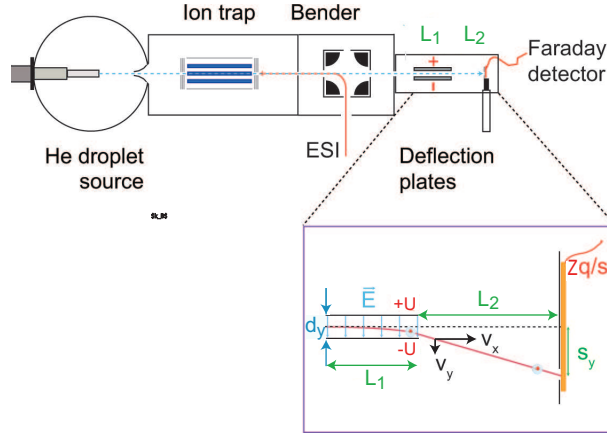
Figure 4.15: Scheme of the setup for the electrostatic deflection experiment. The entire experimental setup is shown in fig. 3.1. With mass-to-charge selected ions coming from the *ESI* source in the linear ion trap, He droplets traverse the trap and can pick up ions. Behind the bender, a pair of parallel metal plates is installed to perform electrostatic deflection experiments. The ion current is measured on a movable Faraday-type copper detector behind a 1.2 mm slit, and is detected by using the *Amptek* preamplifier followed by a 70 db amplification.

slit is located. Applying a voltage $\pm U$ to the plates causes a deflection s_y of the charged droplet beam which depends on the longitudinal beam velocity v_x, the droplet mass m, and droplet charge Zq according to:

$$s_y = \frac{Z\,q\,E\,L_1(L_1 + 2L_2)}{2mv_x^2} = \frac{Z\,q\,U\,L_1(L_1 + 2L_2)}{m\,d_y\,v_x^2} \qquad (4.2)$$

where $E = 2U/d_y$ the electric field strength.

The ion-current of the deflected droplet beam can be detected on a Faraday-type metal detector at a distance $L_2 = 50$ cm from the end of the deflection plates as a function of time of flight after valve opening (more precisely, the electronic trigger signal to the pulsed valve). In front of the detector, a movable 1 mm slit is placed. Time-of-flight profiles are recorded over a broad range of detector positions at an applied electric field of strength E, and the deflection of the ion-doped droplets is measured. Displaying the integrated intensity of the recorded ion signal *vs.* the respective detector position gives a so-called "deflection curve".

For the deflection measurements, droplets are doped with three different molecules: protonated Phe$^+$ ions, Gram$_{syn}^{+2}$ ions, and CytC^{+Z} ions in different charge states ($Z = +9$, $+14$ and $+17$). The experimental sequence employed is the one described in Ch. 4.2.2, see fig. 3.19. Ions are accumulated in the ion trap for $t_{acc} = 10$ s and are picked up by He droplets during the storage time of $t_{trap} = 15$ s. Typical expansion conditions in the deflection experiments are $T_0 = 8$ K, $P_0 = 30$ bar, $f = 5$ Hz, and an electric pulse duration of $t_{pulse} = 220$ μs.

When electric fields of sufficient strength $\vec{E}$ are applied to the deflection plates, it is observed that the intensity of the ion signal decreases at the detector position that yields maximal ion signal at zero electric deflection field. That means that the number of ion-doped He droplets reaching the detector is diminished as a consequence of the electrostatic force acting on the charged droplets between the deflection plates. Furthermore, when moving the detector in the respective direction of the deflected beam,
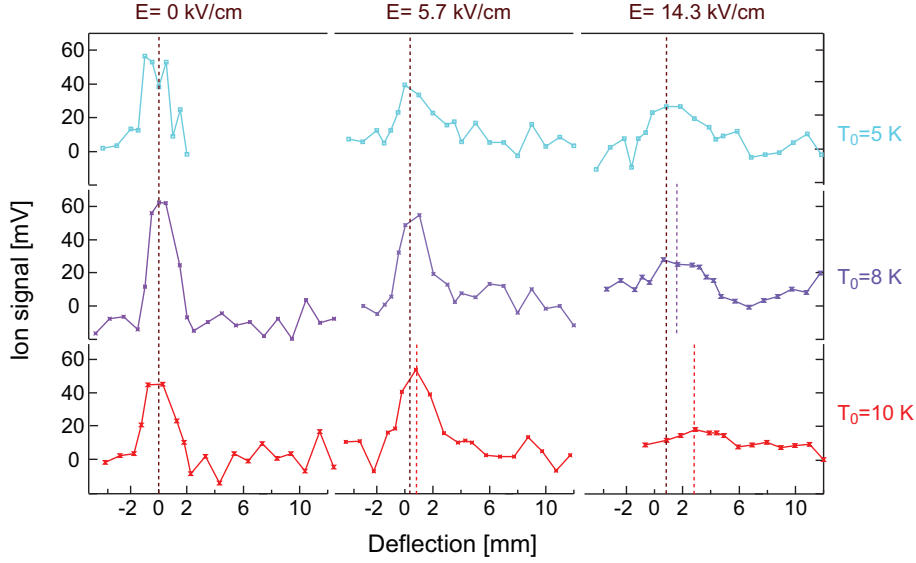
Figure 4.16: Electrostatic deflection of He droplets doped with doubly-charged Gram^{+2}_{syn} ions at three different expansion temperatures $T_0 = 5$ K (cyan), $T_0 = 8$ K (violet), and $T_0 = 10$ K (red). The short trap is used, and therefore, the measured signal-to-noise ratio is rather low. The vertical dashed lines are guides for the eye to indicate the (approximate) peak maximum at the respective electric field strength.

a shift of the signal peak maximum is observed, which is accompanied by a decreasing peak intensity and a broadening of the peak. This can be seen in fig. 4.16 and fig. 4.17. The latter two observations can be attributed to a certain distribution of He droplet sizes emitted by the droplet source and to the mass dependence of the electrostatic deflection (acceleration). Different masses are deflected into different angles which results in a broadening of the signal.

The dependence of resulting He droplet sizes on the applied expansion parameters T_0, P_0 is an important item of information. To obtain it, the deflection of He droplets doped with the doubly protonated synthetic peptide Gram^{+2}_{syn} ions was measured at three different expansion temperatures $T_0 = 5$ K, 8 K, and 10 K. The resulting deflection curves are shown in fig. 4.16. These measurements were performed using the short trap ($L = 14.5$ cm). The signal-to-noise ratio obtained is low due to a smaller total number of ions stored in the trap compared to the long trap. The deflection and hence the droplet sizes are determined by using eq. (4.2). It is difficult to detect a significant influence of the expansion temperature T_0 on the measured deflection under the given experimental conditions. Measurements of the droplet size dependence on the source temperature were also performed on ion-doped He droplets produced by the Even-Lavie valve installed in the He droplet source and are presented in Ch. 4.3.2.

The weak signal requires measurement at the maximal amplification of the *FEMTO* amplifier of 10^{11} V/A, which, in turn, enhances the sensitivity of the measurement towards any mechanical and electromagnetic disturbances present in the laboratory, leading to large fluctuations of the signal background. Furthermore, an average over a large number of measurement cycles (1500) is required to finally extract the deflected ion signal from the background signal. Another difficulty is given by the temperature fluctuations of up to ± 1 K that are observed when the He droplet source is running (see Ch. 3.1.5). Nevertheless, though the uncertainties may probably be high, it is presumed

that the correct order of magnitude for the droplet sizes can be determined. The droplet sizes obtained are determined to be $N_{He} \approx 2 \cdot 10^{10}$ He atoms for He droplets produced at $T_0 = 5$ K and 8 K. Due to the poor signal-to-noise ratio it is not possible to observe any difference in deflection. However, for $T_0 = 10$ K, a larger deflection is seen, resulting in a droplet size of $N_{He} \approx 6 \cdot 10^9$ He atoms. Hence, a size difference by around a factor of 5 is obtained. This is in agreement with the expectation that an increase in expansion temperature T_0 leads to the formation of smaller droplets as is known for continuous free-jet expansions [58]. Under the presumption that the space-charge limit is reached in the trap, the pickup of multiple ions has to be considered (see Ch 2.2.4). This was ignored in the first evaluation of the experimental results. The higher charge of multiply-doped He droplets would lead to a stronger deflection and thus to the conclusion that droplet masses obtained under the assumption of single pickup should represent a lower limit on the real droplet masses.

With the *Parker* General it is, in general, not possible to detect any signal from ion-doped He droplets when the source temperature T_0 is increased above 11.5 K (see fig. 4.12).

The weak signal and the low signal-to-noise ratio limit the applicable deflection voltages. A stronger electric field leads to a stronger peak broadening accompanied by a reduced peak intensity due to the mass distribution. Therefore, when applying higher voltages above $U = \pm 10$ kV to the deflection plates, it becomes difficult to extract the ion signal from the background fluctuations, even with a very large number of averaged measurements.

When the trap is replaced by the long trap, which has almost twice the length and larger orifices in the longitudinal trapping electrodes, the signal-to-noise ratio can be considerably improved. Together with a further optimization of the trapping and pickup conditions, such as a realignment of the He droplet source, we find an increase of the signal intensity by about a factor of 10 (see fig. 3.25 in Ch. 3.1.3). Deflection measurements on droplets doped with ions that are trapped in the longer trap are performed, and the results are shown in fig. 4.17. The integrated ion signal for the three charge states of CytC^{+Z} as well as protonated Phe$^+$ is displayed over the deflection s_y at a field strength of 5.7 kV/cm (diamonds) and with no deflection field applied (filled circles).

In order to quantify the observations, the curves in fig. 4.17 are fitted with a model. The curves with no field applied are fit to an instrumental function that contains the widths of the two slits as well as the absolute zero position. The model for the fits of the deflection curves contains the same instrumental function as well as a size distribution function of the droplets. For this purpose, a log-normal distribution was assumed, as has been shown in the literature to be applicable to He droplets [201]. Such a distribution is described by a mean size as well as by a width parameter. The width parameter σ, the standard deviation of the distribution of the logarithm of the droplet size, is kept constant at 1.0 for all CytC^{+Z} curves and at 0.58 for the Phe$^+$ curve. The resulting (arithmetic) mean droplet masses are $(2.3, 2.7$ and $3.2) \cdot 10^{12}$ amu for CytC +9, +14 and +17, respectively and $2.2 \cdot 10^{10}$ amu for Phe doped droplets; the respective size distributions are displayed in fig. 4.18.
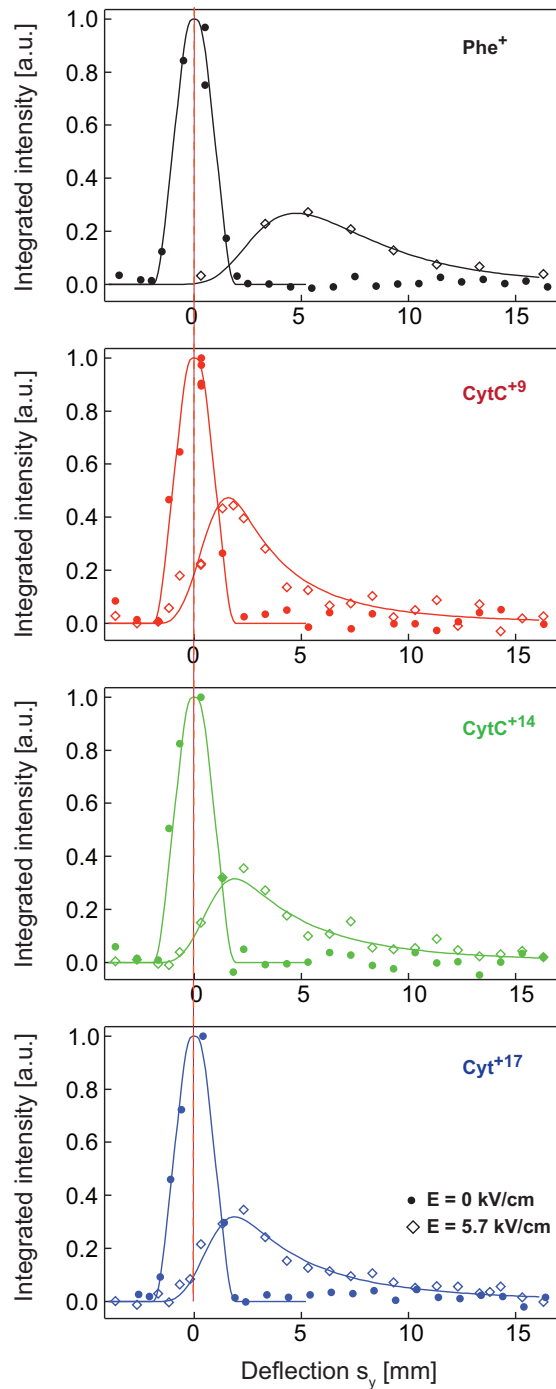
Figure 4.17: Deflection of He droplets doped with CytC^{+Z} ions (Z = +9, +14, +17) ions and Phe$^+$ ions measured at an electric field strength of $E = 5.7$ kV/cm (diamonds) and at zero field (filled circles). The integrated signal of ion-doped He droplets is displayed as a function of the deflection s_y measured. Also shown are the respective fitted curves (lines).
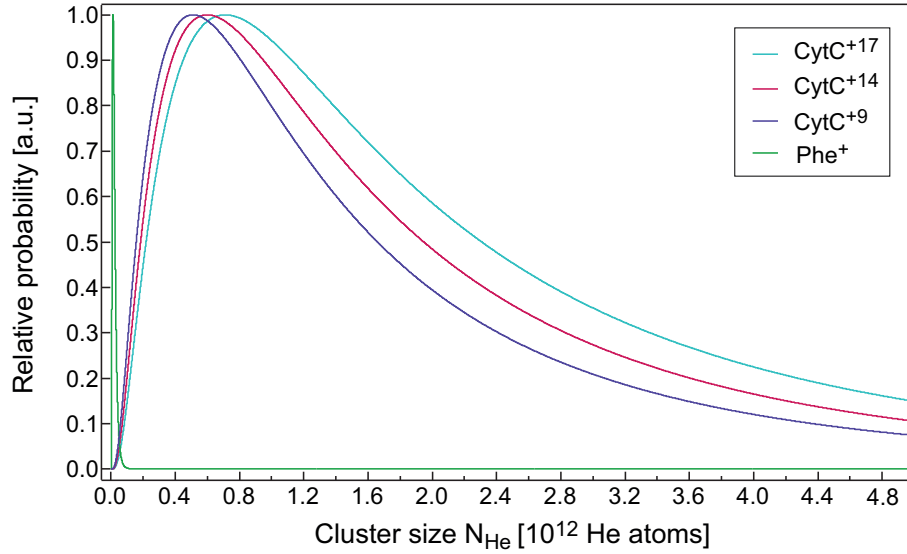
Figure 4.18: Log-normal size distribution of He clusters produced by the *Parker* General valve.

4.3.2 Acceleration of doped droplets

The second method employed to determine the sizes and size distributions of He droplets in a straightforward way is the application of an electric field in the parallel direction to the He droplet beam. This causes a (mass-dependent) acceleration of charged particles and therefore, a change in the beam velocity and arrival time at the detector. Practically, a voltage U_{acc} is applied to the hexapole ion trap and –depending on the polarity– leads to an acceleration or deceleration of the traversing ion-doped droplets.
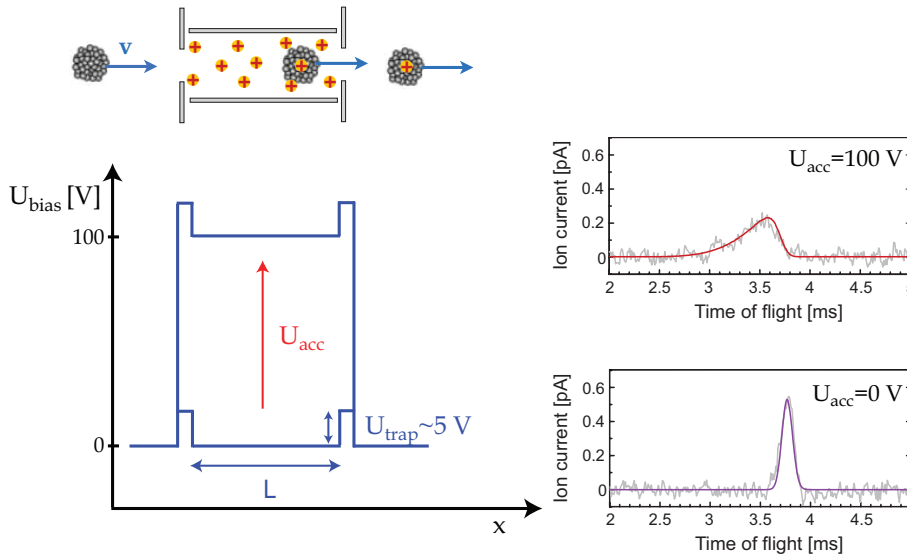
Figure 4.19: Experiment for acceleration of ion-doped He droplets by applying a bias voltage U_{acc} to the trap. He droplets that are passing through the trap of length L in the beam direction x and are doped with ions *via* pickup are accelerated by the electric field. This causes a shift in the measured time of flight compared to non-accelerated droplets produced under otherwise identical conditions. Since the acceleration is mass dependent, the change in the time-of-flight profile can be used to determine the mean sizes and the size distributions of the ion-doped droplets.

125

An illustration is shown in fig. 4.19. When a He droplet has picked up an ion, it is charged and can gain energy from the electric bias field. The energy of an accelerated ion-doped droplet $E_{ion+drop}$ is the sum of the kinetic energy of doped droplets at zero acceleration voltage $U_{bias} = 0$ V and the energy gained by the applied electric field $|\vec{E}|$. It is given by

$$E_{ion+drop} = \frac{1}{2}mv_0^2 + Z\,q\,U_{acc} \quad , \qquad (4.3)$$

where v_0 is the initial beam velocity of non-accelerated droplets, m the mass of the droplet+ion system, Zq the charge carried by the dopant ions, and U_{acc} the applied acceleration voltage.

This method was used to determine the size and size distribution of droplets produced by the Even-Lavie droplet source. The time of flight of ion-doped He droplets after valve opening was measured for a certain acceleration voltage U_{acc} applied and the change in flight time was determined. The comparison of the measured time of flight with that of non-accelerated ion-doped droplets at $U_{acc} = 0$ V as a reference flight time gives the droplet masses and thus sizes from eq. (4.3). The resulting time-of-flight profiles of He droplets accelerated by two different voltages are shown in fig. 4.20. The droplets are doped with Ang^{+2} ions and are accelerated by $U_{acc} = 100$ V and 500 V; they are shown together with the reference zero field profile. In both panels it can be seen that for increasing acceleration voltage U_{acc}, the peak maximum shifts to shorter flight times and simultaneously, the peak broadens and the peak intensity decreases. The latter can be attributed to a distribution of droplet masses. The "acceleration curves" shown in fig. 4.20 are further analyzed to derive the droplet mass and mass distribution or –equivalently– the size and size distribution of droplets. For mass determination, the longitudinal velocity distribution Δv_x in a pulse needs to be taken into account, since it has an influence on the measured flight times. Furthermore, the time-of-flight profiles can be influenced by the response function of the amplifier used and by the area and shape of the Faraday detector; it is possible that the longitudinal geometric dimensions of the detector cause a temporal spread of the recorded arrival times at the detector (see Ch. 4.2.2). However, it is observed that "acceleration curves" can be described well without taking into account the last two factors, and only the velocity distribution Δv_x present in an emitted droplet pulse is considered further. Comparing the two panels of fig. 4.20, especially the non-accelerated profiles for $U_{acc} = 0$ V, it can be seen that the temporal structure of a pulse of ion-doped droplets is different for the two source temperatures T_0 (at the same pressure $P_0 = 65$ bar). When droplets are produced at $T_0 = 14$ K, a single pulse is observed, whereas for the lower source temperature of $T_0 = 10$ K, the measured time-of-flight profile exhibits a bimodal structure. The pulse has two different components and the envelope curve is given by the sum of two pulses. Therefore, the velocity distribution Δv_x of time-of-flight profiles with single pulse structures is determined for non-accelerated beams from a fit with a single Gaussian and for time-of-flight profiles with double pulse structures by a bimodal Gaussian. The fitting curves yield the initial velocity v_0 and velocity distribution width Δv_x in the cluster beam.

The thus-obtained velocity distribution Δv_x is now used to determine the distribution of droplet masses in the accelerated beam. In principle, it is not evident that time-of-flight
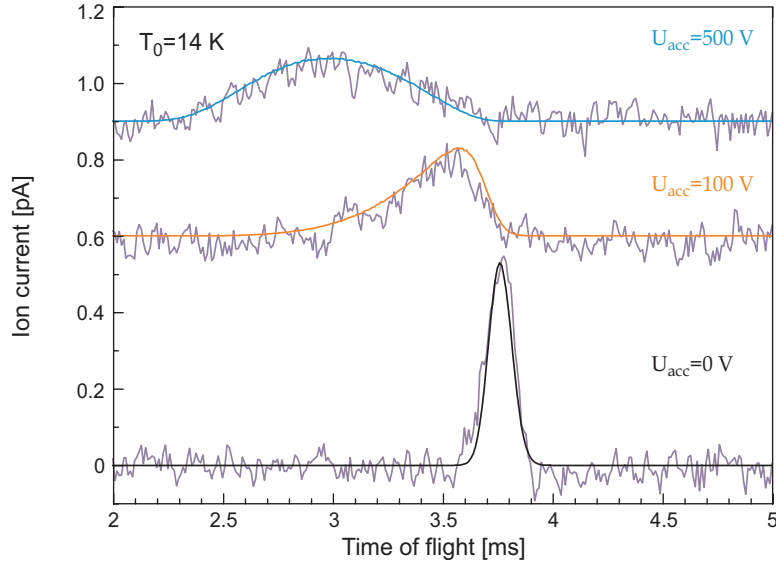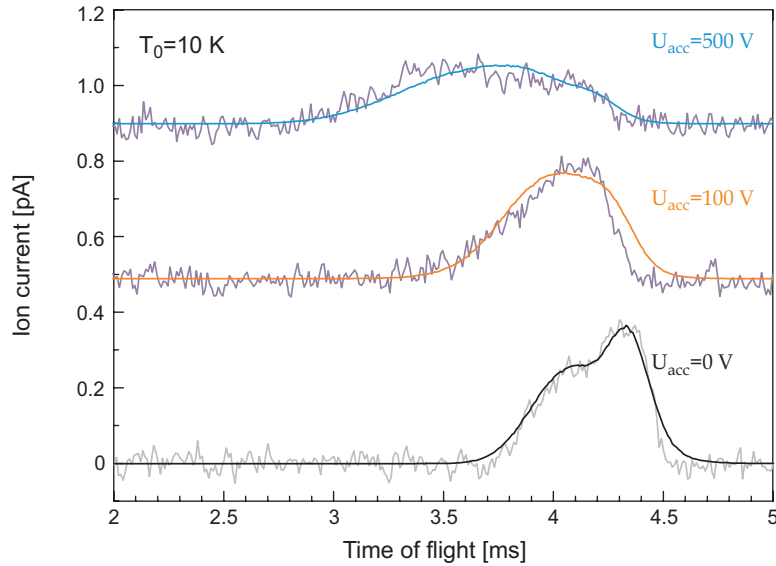
Figure 4.20: Time-of-flight profiles of accelerated ion-doped He droplets as detected on a Faraday-type copper detector using the *FEMTO* amplifier at an amplification factor of 10^{10} V/A. He droplets are produced by the Even-Lavie valve at $P_0 = 65$ bar and two different temperatures, $T_0 = 14$ K (top panel) and $T_0 = 10$ K (bottom panel). They are doped with Ang^{+2} ions. When an electric bias field is applied to the hexapole trapping voltage, it is observed that the peak maximum shifts to earlier arrival times and at the same time, the peak broadens and the peak intensity decreases. This is attributed to the mass distribution of droplets within a pulse.

profiles with a bimodal pulse structure necessarily have to result in a bimodal mass distribution as well. But it is observed that "acceleration curves" can indeed be better described with a bimodal mass distribution function when the corresponding velocity distribution is bimodal. Thus, the mass (and size) distribution can be described as the sum of a component with small droplets and a component with large droplets. This can be seen in fig. 4.21, where a normalized size distribution function is shown as the envelope curve (red curve) of a small (blue curve) and a large cluster component (green
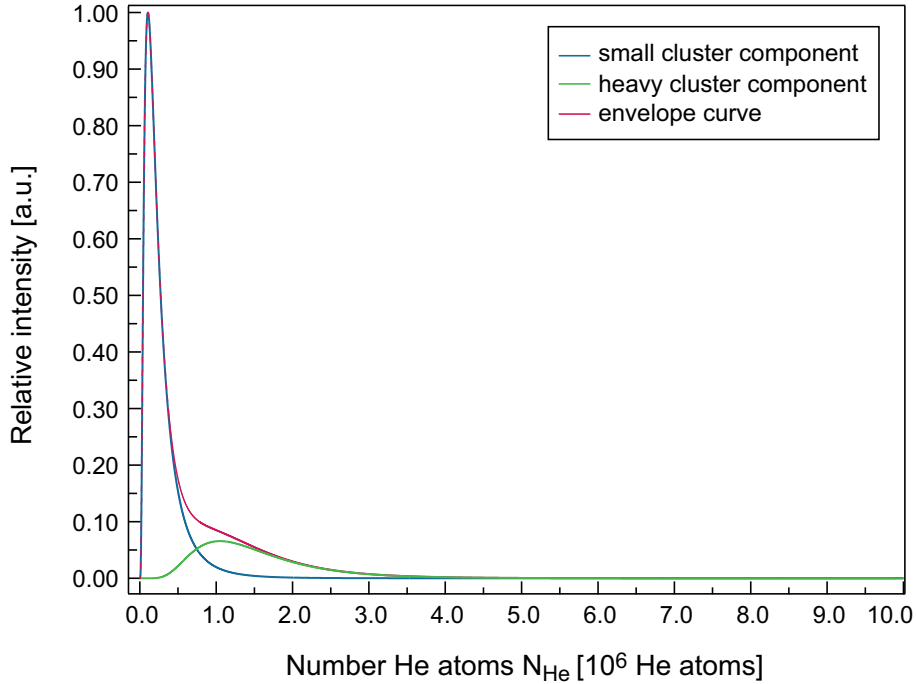
Figure 4.21: Bimodal size distribution of He droplets produced at a lower source temperatures $T_0 = 10$ K. The green curve represents the large-droplet component, the blue curve the small-droplet component, and the red curve is the envelope curve obtained as the sum of the two components.

curve). For elevated source temperatures, $T_0 \geq 10$ K, however, the "acceleration curves" obtained can be well described with a single-mode mass distribution function. Hence, the "acceleration curves" are fitted with a single log-normal distribution function to determine the mass distribution in cluster beams produced at higher source temperatures, corresponding to a single Gaussian velocity distribution, and with a bimodal log-normal distribution function for source temperatures $T_0 \leq 10$ K having a bimodal Gaussian velocity distribution.

To obtain information on the influence of the source temperature T_0 on the resulting droplet sizes, time-of-flight profiles of ion-doped He droplets which are accelerated by a voltage $U_{acc} = 100$ V were measured for different source temperatures T_0 applied . Furthermore, the droplet masses and mass distributions were determined for droplets doped with different dopant species. The resulting cluster sizes and size distributions for He droplets doped with two different species and produced at different source temperatures T_0 are shown in fig. 4.22. When He droplets that are produced at $P_0 = 65$ bar and $T_0 = 10$ K, 12 K, and 16 K are doped with Trp^+ ions, the resulting mean droplet sizes are determined to be $m_d = 1.7 \cdot 10^6$ amu for the large droplet component and $2.8 \cdot 10^5$ for the small droplet component at 10 K, as well as $2.1 \cdot 10^5$, and $5.2 \cdot 10^4$ amu at 12 K and 16 K, respectively, and only one component is needed for the fit. When, however, droplets produced at $P_0 = 65$ bar and $T_0 = 10$ K are doped with $CytC^{+10}$ ions, the resulting mean cluster mass is $m_d \approx 1.4 \cdot 10^6$ amu. The most probable droplet sizes are indicated in the caption of fig. 4.22.

Acceleration profiles are also recorded for He droplets doped with an atomic ion, Cs^+.

128
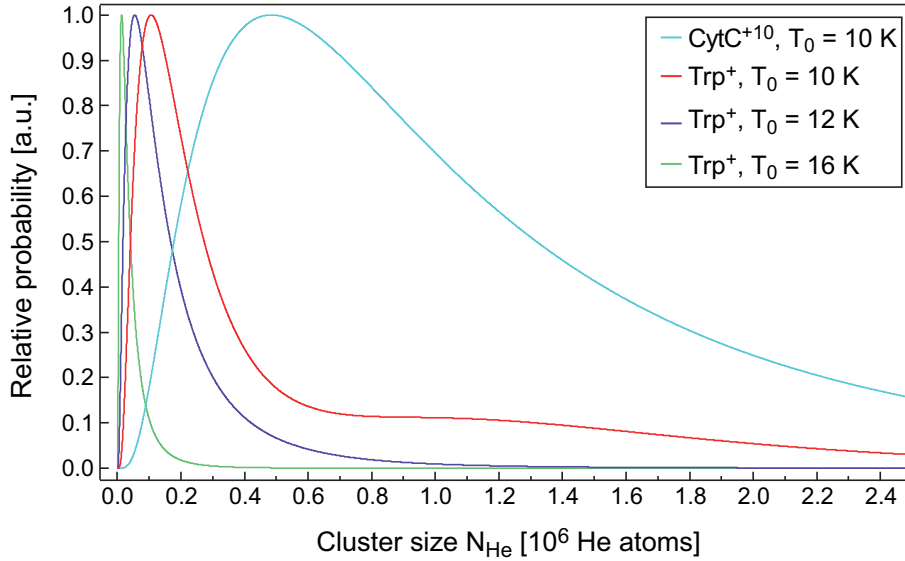
Figure 4.22: The cluster size distributions as determined by the acceleration measurements for He droplets produced by the Even-Lavie valve at different source temperatures T_0 which are doped with two different species are shown. It is observed that the most probable sizes of He droplets ($T_0 = 10$ K, $P_0 = 65$ bar) are considerably larger when they are doped with $CytC^{+10}$ ions consisting of $\approx 5 \cdot 10^5$ He atoms compared to He droplets doped with Trp^+ ions produced at $T_0 = 10$ K, 12 K, and 16 K, each at $P_0 = 65$ bar of $1 \cdot 10^5$, $5 \cdot 10^4$, and $1.2 \cdot 10^4$ He atoms, respectively. As expected, cluster sizes become smaller for higher T_0 and the distribution width becomes broader for increasing mean size.

As an atomic ion does not have any internal energy (rotational or vibrational) or heat capacity, the energy released after picking up an atomic ion should comprise only the collision energy and therefore, the resulting acceleration curves (not shown) most likely reflect the original cluster sizes and size distributions as emitted from the source for specific expansion parameters. The sizes and size distributions determined of droplets doped with Cs^+ ions are essentially the same as those of clusters doped with Trp^+ ions, produced at similar source parameters. This implies that the resulting mean sizes and size distributions of Trp^+ ion-doped clusters are also close to droplet sizes as emitted from the source.

Discussion cluster sizes

It turns out that the droplets produced by the two different sources vary in size over up to 6 orders of magnitude. Using the *Parker* General valve droplet source, the droplet sizes are found to be very large, and include droplets which contain more than 10^{11} He atoms, having geometric diameters of ≈ 4 μm. These sizes exceed by far the droplet sizes observed by other groups for similar temperature and pressure ranges [58, 85, 184, 201]. They are more similar to the sizes of droplets resulting from the breakup of a liquid He beam, which are produced at much lower temperatures of $T_0 = 1-4$ K [90]. Droplets produced by the Even-Lavie valve installed in the He droplet source appear to have sizes which are significantly smaller and thus of the same order of magnitude as droplet sizes reported in the literature for similar expansion conditions [113, 183, 184].
Firstly, experimental results on droplet sizes obtained for the *Parker* General valve droplet source are considered.
It is apparent that applying an electric field perpendicular to the flight direction x causes

the deflection profiles to shift and to broaden. The observed deflection should depend on the droplet mass and charge and the deflection should be more distinct for higher charges Zq. Comparing the differently charged CytC^{+Z} doped droplets (Z = 9, 14, 17) among themselves, an increased deflection with increasing charge is observed. Strikingly, when comparing droplets which are doped with the highly charged CytC^{+Z} ions to those doped with singly protonated Phe$^+$ ions, the opposite is observed. The increased deflection of the Phe$^+$ doped droplets must thus result either from a smaller droplet size or from a higher charge state.

In our initial publication [207], the first case is considered. The large difference in deflection observed and hence droplet size has been attributed to a large difference in droplet mass. It was argued that large ions with high internal energies of ≈ 30 eV require large droplet sizes in order to be picked up and cooled down. However, the experimental results obtained with droplets produced by the Even-Lavie droplet source can rule out this explanation, and it is observed that also droplets having modest sizes of $\approx 5 \cdot 10^5$ He atoms can still pick up large protein ions such as CytC^{+10}.

Therefore, the large difference in size can rather be attributed to a higher number of charges (Phe$^+$ ions) contained in a single droplet. When taking into account the pickup of multiple ions per droplet (see Ch. 2.2.4), the resulting deflection in an electrostatic field is of course increased as the deflection is linearly dependent on the charge, although the mean size of the droplets might be similar to that of droplets doped with CytC^{+Z} ions. From the electrostatic deflection experiments, the mean size of droplets doped with CytC^{+Z} ions is $N_{He} = 5 \cdot 10^{11}$ He atoms. This leads to the conclusion that about ≈ 100 Phe$^+$ ions might be picked up by a single He droplet. It is observed that Phe$^+$ ions can be produced by electrospray ionization rather efficiently and thus quickly reach the space charge limit in the trap. This would provide for a high particle density in the trap which is required for multiple pickup. It seems thus reasonable that a He droplet collides with more than one ion, in particular when the droplets have large collisional cross sections as in case of droplets composed of more than 10^{11} He atoms (corresponding to $\sigma = 1.3 \cdot 10^{-11}$ m^2). Furthermore, He droplets of this size are sufficiently large to allow for the ions to be located at large distances from each other so that they do not affect each other too much by Coulomb repulsion. A total charge Q_S of ≈ 100 Phe$^+$ ions contained on or in a 10^{12} He droplet is still below the Rayleigh limit, and no Coulomb explosion should occur.

For bare He droplets produced by the *Parker* General valve source, it is observed that the signal of fragment cluster ions (in particular the He dimer ion) disappears when the applied source temperature T_0 is higher than ≈ 11 K. All together, this indicates that the *Parker* General valve source itself can produce only droplets of very large sizes. A possible reason for the resulting enormous droplet sizes might be the large orifice diameter of 700 μm, which is however not much larger than the 500 μm used in the experiments of Vilesov in ref. [113], giving significantly smaller droplets (cf. table 4.1). In continuous expansions, the standard orifice opening is only 5 μm. It is known from beams of rare gas clusters (other than helium) that the cluster sizes scale with the orifice diameter by a scaling law: $P_0 D^q$, with $q >0$ (Ar: q=0.8) [82]. For He cluster beams, unfortunately, there is no scaling law given in the literature (to my knowledge). However, assuming a similar behavior for helium as for the other rare gases would indicate that nozzles having larger orifices result in larger droplet sizes at constant pressure P_0 applied. In addition, the nozzle employed here was machined out of copper (compared to stainless

steel as used in other experiments [113]) and has a longer 90° conical section, which might further promote the formation of large droplets.

A different possible explanation for the enormous cluster sizes is that small clusters are in fact produced in the expansion but they do not arrive at the ion trap. Possibly they are destroyed or scattered out of the beam before, for example by shock waves formed at the skimmer, while large droplets with high kinetic energies have a better chance to survive the shock waves. In the experiments using the *Parker* General valve source, the nozzle-to-skimmer distance is much shorter (≈ 5 cm) than in the experiments with the Even-Lavie source (≈ 20 cm). A short nozzle-to-skimmer distance promotes the formation of shock waves which can then interfere with the cluster beam.

Now, the results of the size determination of clusters produced by the Even-Lavie valve will be presented.

In fig. 4.23 (top panel), the time-of-flight profiles obtained with He droplets doped with different molecular species (Trp$^+$, Ang^{+1}, Ang^{+2}, CytC^{+10}) for zero acceleration voltage are shown, recorded with the calibrated *FEMTO* amplifier. The number of charges per pulse are determined to be 2000, 2000, 1000, and 11 ion-doped droplets. Thus, droplets doped with Trp$^+$, Ang^{+1}, or Ang^{+2} ions give equal numbers of charges per pulse. This allows for the conclusion that the charge density in the trap is the same for the three species (probably the space-charge limit) and that also the pickup efficiency by He droplets is similar. The only different ion yield is obtained for droplets doped with CytC^{+10} ions.

This difference is presumably caused by two main effects. First, the efficiency of ion production in the *ESI* process is not equal for different species. This can be compensated by the accumulation time according to the ion flux observed from the *ESI* source which is then $t_{acc} = 10$ s for Trp$^+$ ions and 60 s for Ang^{+1}, Ang^{+2}, and CytC^{+10} ions each, in order to account for different ion currents. The second effect is a cluster size effect. It appears that a minimal (geometric) droplet size is required to pick up and completely cool an ion of a certain size and internal energy in a He droplet. A possible reason is the physical dimension of a large protein that requires a lower limit for the geometrical size of the He droplets to allow a pickup and complete immersion within a droplet. It seems unlikely that a He droplet can pick up and cool a particle that has a larger geometric diameter than the droplet itself, and furthermore, that it could transport such a large particle out of the trap. The diameter of a CytC^{+Z} ion in solution in its native globular shape is indicated as ≈ 3.4 nm [208]. In the gas phase, however, and carrying multiple protons ($Z \approx 10$), the proteins are presumed to unfold due to electrostatic repulsion and adopt a more extended chain structure than a globule, with an extended length. Droplets composed of $N_{He} = (1 - 5) \cdot 10^5$ He atoms have a diameter of $\approx$ 20- 35 nm. To assure a full enclosure of a "cigar"-shaped long protein chain having a length of at least 3–4 nm, the He droplets should have a minimal size that is comparable to this diameter.

Another possible explanation is practically the same as the one we gave in ref. [207]. The geometric diameter would then set a lower limit for the pickup of dopant species in terms of the residence time and hence, the cooling time available of a dopant particle in a He droplet (in particular when the dopant is large and stores high internal energies). When, after the pickup, an ion enters the droplet at the relative velocity of the droplet+ion system, it will rapidly be decelerated to the Landau velocity of ≈ 60 ms^{-1} by the
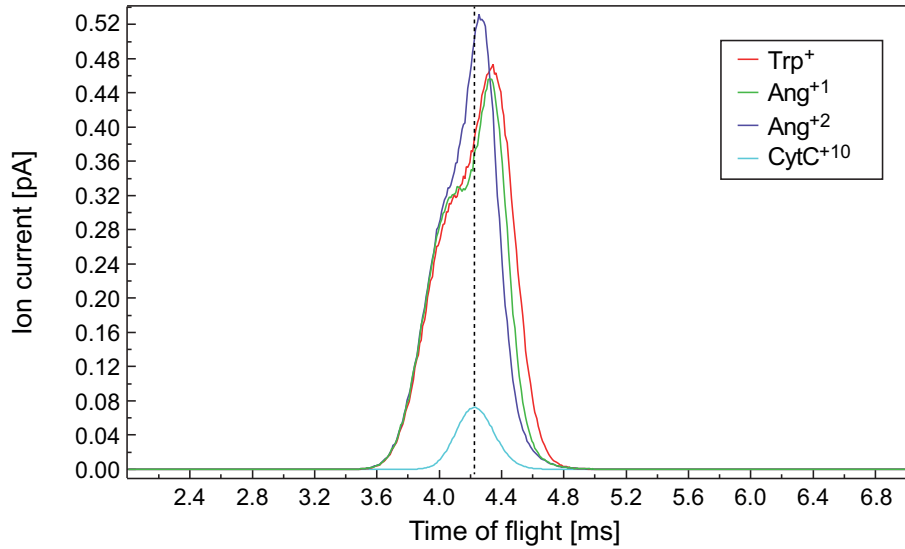
(a)
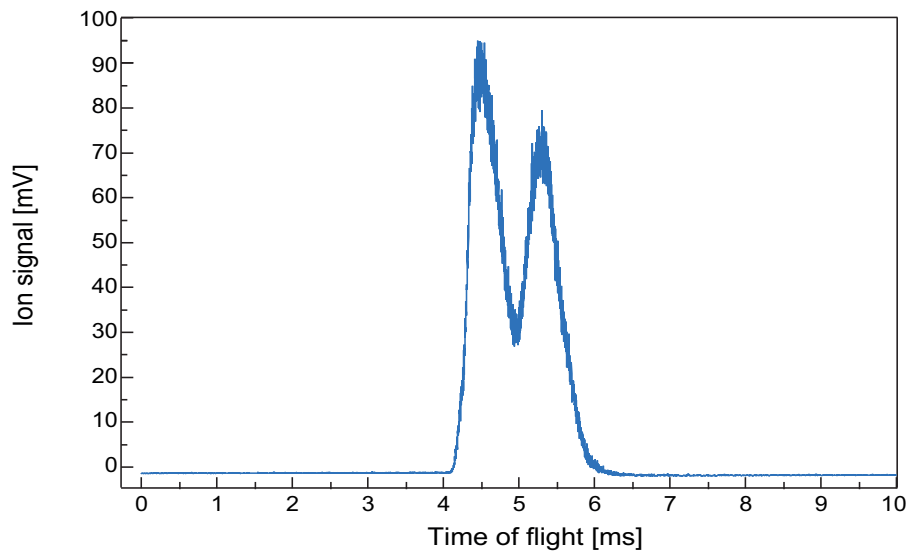
(b)

Figure 4.23: Time-of-flight profiles for He droplets produced by the Even-Lavie valve doped with different ion species. The top panel shows He droplet pulses (fits) expanded under identical source conditions ($T_0 = 10$ K, $P_0 = 65$ bar) which are doped with Trp^+ (red), Ang^{+1} (green), Ang^{+2} (violet), and $CytC^{+10}$ (cyan) ions. The time-of-flight profiles are recorded with the Faraday-type detector using the *FEMTO* amplifier at an amplification factor of 10^{10} V/A. It can be seen that the central velocity of all the pulses is approximatively the same. The black dotted line is a guide for the eye marking the center of the pulse of $CytC^{+10}$-doped droplets. The velocity distribution for droplets doped with Ang^{+2} or $CytC^{+10}$ ions shows only one component, that of droplets doped with Trp^+ or Ang^{+1} ions is bimodal. In the bottom panel, a time-of-flight profile of He droplets detected by the Daly detector is shown. These He droplets are produced at $T_0 = 7$ K, $P_0 = 30$ bar, and they are doped with Trp^+ ions. The dip in the central part of the peak can presumably be attributed to heavier droplets in the pulse which are detected with reduced efficiency by the (mass-dependent) conversion-type detector used.

frictional force exerted on it by the non-superfluid helium environment. A He droplet composed of $5 \cdot 10^5$ He atoms with a diameter of ≈ 35 nm is traversed in about 580 ps. If the heat transfer from a large protein to the droplet is considerably slower, then the

ion might be ejected from a smaller droplet before cooling is completed.

Therefore, the difference in signal intensity of droplets doped with different species would be due to the size distribution of the droplets. The low intensity of $CytC^{+10}$ ion-doped droplets observed (see top panel of fig. 4.23) could then be attributed to a small number of droplets in the distribution pulse having the minimum size required for picking up a large protein. Log-normal distributions can be very broad, with significant non-zero probability over a wide range of variables around the mean value. Hence, in the present log-normal size distribution, there is a much smaller number of droplets available for picking up large molecules (with high internal energies) than for smaller species (with lower internal energies) which can also be picked up by smaller droplets. Smaller ion-doped droplets should then have a significantly higher ion yield, even if the contribution to the signal of a singly-charged droplet is less than that of a multiply-charged ion contained in a large droplet.

While keeping in mind the mean droplet sizes determined from the fits (as shown in fig. 4.22), the time-of-flight profiles of He droplets doped with different molecular species are compared. They are produced under similar source conditions in the expansion. It can be seen in fig. 4.23 (top panel) that large droplets (doped with $CytC^{+10}$ ions) appear more in the central part of the pulse (on the time axis). This is confirmed when looking at time-of-flight profiles recorded with the conversion-type Daly detector, as shown in the bottom panel of fig. 4.23. A remarkable dip in intensity in the middle of the pulse is observed. Since the detection with this type of detector is mass-dependent and the sensitivity is usually lower for heavy particles, the observed dip presumably indicates that high masses are concentrated in the pulse center. On the other hand, smaller masses, which are detected with higher sensitivity, appear at times before and after the heavy particles in the pulse. The time-of-flight profiles of droplets doped with $CytC^{+10}$ ions are different from those of droplets doped with Trp^+, Ang^{+1}, or with Ang^{+2} ions. Although all have the same average velocity, the time-of-flight profiles of (large) $CytC^{+10}$-doped droplets are narrower. Therefore, it might be concluded that large droplets having narrower velocity distributions (larger velocity ratios) are presumably produced at expansion conditions which are most efficient in translational cooling in the expansion. Smaller droplets, on the contrary, exhibiting a larger velocity distribution can thus probably also be produced in "warmer" parts of the expansion process. Possibly, this might be related to the opening process of a pulsed valve. There, the best cooling would take place in the middle of the process, when the valve is fully opened and quasi-steady flow is attained in the pulsed nozzle expansion. Under these conditions of most efficient translational cooling, droplets of the maximum size with the smallest velocity spread would be produced. On the other hand, while the valve is being opened (or closed), i.e. with less efficient conditions for cooling, instead only smaller clusters might be produced, which then appear at earlier (or later) arrival times at the detector in a time-of-flight profile than the clusters of maximal size. The velocity distribution might then cause the peak to broaden, leading to a further separation of the arrival times of (differently sized) clusters which are produced at different stages of the valve opening process. However, since the detection takes place at a distance of about 1.5 m behind the nozzle, it is not possible to reconstruct the temporal profile of the pulse as emitted from the source. For this purpose, the time-of-flight profiles should be recorded at a detector which is installed close behind the nozzle.

In a bimodal velocity distribution, it is presumed that the large droplet compo-

nent arrives later at the detector than the small droplet component (see $U_{acc} = 0$ V curves in fig. 4.20). However, in the log-normal fits for the droplet mass distributions, there is no relation made between velocity and mass, and all components in the mass fits are performed with the same velocity distribution as obtained from the non-accelerated curves.

In case that large droplets would move more slowly than small droplets as also observed in ref. [92], this would contradict the expectation of uniform particle velocities for all sizes in a cluster beam expansion [2] (see Ch. 1.3.4). However, it seems that the distribution of droplets of different sizes is not homogeneous in a pulse, but rather the droplet masses and velocities seem to be correlated. A known feature for nozzle beams is a non-homogeneous distribution of particles of different sizes throughout the beam profile due to their different perpendicular velocity components v_y. Heavier particles with smaller perpendicular velocity components are then located closer to the beam axis, whereas light particles with larger perpendicular velocity components move more on the periphery of the beam [1, 2] and therefore are more readily scattered from the beam at the orifices which it passes through (see Ch. 1.3.4). This is observed when gas mixtures composed of gas particles with different sizes are expanded together, for example in seeded beams. If this conclusion can be transferred to cluster beams, then it would imply that large droplets are located more close to the beam axis.
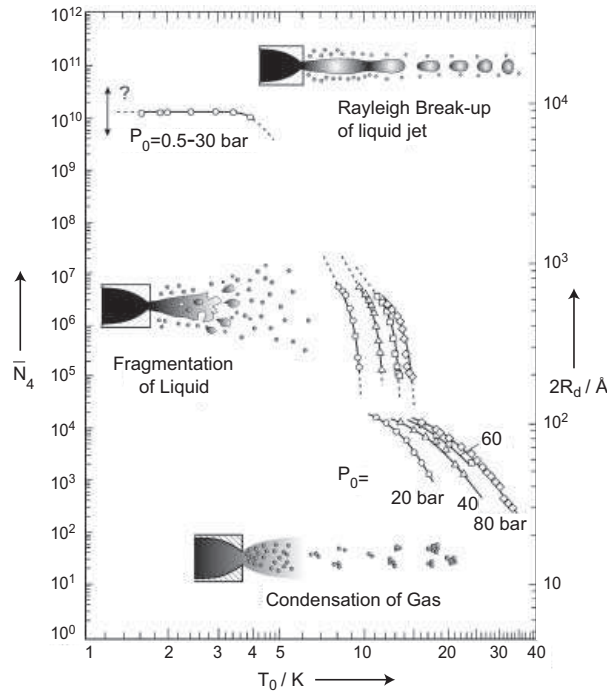
Figure 4.24: Droplet sizes and formation processes in dependence on the expansion parameters as measured for continuous expansions. On the left axis the cluster mean size $\bar{N}_4$ is shown, on the right axis the cluster diameter $2R_d$. The figure is taken from ref. [15] and shown modified.

The origin of the observed difference in droplet sizes might be assigned to different processes leading to cluster formation in the expansion. As discussed in ref. [58], droplets are formed on isentropes in the helium phase diagram (see fig. 1.7). The starting point of the isentropic expansion in the phase diagram and hence, the temperature and pressure at the crossing point of the respective isentropic line with the phase-separation line

between gaseous and liquid helium is determined by the initial source conditions T_0, P_0.

A possibility is that the *Parker* General valve exclusively leads to formation of clusters in or near "*Regime II*" (in the terminology of [58]), the so-called "supercritical regime", where the isentrope passes through or near the critical point (T_c, P_c). Droplets formed in this region are supposed to be large [58]. On the contrary, the Even-Lavie valve seems not to produce extremely large clusters. Possibly, the short pulse lengths at which the Even-Lavie valve is operated are not favorable to the formation of large clusters due to the short phase of quasi-steady flow during the opening process.

Whether the size distribution of clusters in a pulse can be described by a single or bimodal distribution depends on the source conditions applied. The second component of heavy droplets appears when the source temperature is decreased below 10 K at a constant gas pressure of $P_0 = 50$ bar. This might result from a change in the processes leading to cluster formation. The formation of clusters in certain mean size ranges N_{He} as a function of the source temperature T_0 for different gas pressures P_0 in continuous nozzle beam expansions is illustrated in fig. 4.24. The respective cluster formation processes invoked are indicated for the different ranges of applied source parameters (T_0, P_0).
Right around the point (10 K, 50 bar), there is a transition in the cluster formation processes. Increasing the source temperature or decreasing the source pressure will lead to cluster formation in "*regime I*" due to condensation of the expanded gas. On the other hand, when going to lower temperatures or higher pressures, the isentropes pass through a region on the low temperature side of the critical point in "*regime III*" and reach the phase separation line from the liquid side. Clusters are formed by fragmentation of a liquid beam into droplets due to Rayleigh oscillations, comparable to a "spray". The droplets formed are expected to be much larger, having almost uniform sizes on the order of magnitude of the nozzle orifice [86, 90, 209]. In pulsed sources, however, it is very difficult to reach the low temperatures required for this kind of expansions. The two regimes are separated by "*regime II*", where clusters are formed by a separation of the liquid and gaseous phases, due to cavitation as liquid "explodes" when brought into vacuum [58, 86]. The observed sizes of droplets produced by the Even-Lavie droplet source agree remarkably well with the mean droplet sizes indicated at the respective expansion parameters seen in fig. 4.24 for the "*regimes I + II*".

4.4   Gas dynamic properties of the He cluster beam

Beam intensities

The maximal mass flow rate G_{max}, the total beam intensity I_{tot}, and the centerline intensity I_0 are determined for both valves used in the He droplet source by means of eq. (1.10). At first, the values obtained for the *Parker* General valve are presented.
Switching on the He droplet source at specified operation parameters ($T_0 = 8$ K, $P_0 = 30$ bar) is accompanied by a background pressure rise in the source chamber by an absolute value ΔP from $P = 4 \cdot 10^{-7}$ mbar to $P = 3.3 \cdot 10^{-5}$ mbar, giving an approximate difference of $\Delta P \approx 3 \cdot 10^{-5}$ mbar.

The total mass rate of flowing gas G_{max} is determined for the observed background

pressure rise ΔP using eq. (1.10), cf. Ch. 1.3.3. The right side of the equation contains the throughput Q_t of gas particles in a chamber at a pressure P evacuated by a vacuum pump of pumping speed Z_p which is given here by (cf. eq. (3.2)):

$$
\begin{aligned}
Q_t &= Z_p \cdot \Delta P \\
&= 2.4\,\mathrm{m^3 s^{-1}} \cdot 3 \cdot 10^{-3}\, \frac{\mathrm{kg \cdot m}}{\mathrm{s^2 \cdot m^2}} \\
&= 7.2 \cdot 10^{-3}\, \frac{\mathrm{m^2 \cdot kg}}{\mathrm{s^3}} \quad .
\end{aligned}
\tag{4.4}
$$

This is inserted into eq. (1.10) together with an ambient temperature of $T = 300$ K, yielding a value for the maximal mass flow rate of $G_{max} = 1.2 \cdot 10^{-8}$ kg s^{-1}, referred to the mass of atomic helium.

With the mass flow rate G_{max}, the total flux I$_{\mathrm{tot}}$ and the centerline flux I$_0$ can now be determined using eq. (1.11) and eq. (1.12) to be $I_{tot} = 2.3 \cdot 10^{18}$ atoms $\cdot$ sr^{-1}s^{-1} and I$_0 = 1.4 \cdot 10^{18}$ atoms $\cdot$ sr^{-1}s^{-1}, respectively.

Likewise for the Even-Lavie He droplet source, the mass flow rate G_{max} and the beam intensities I$_{\mathrm{tot}}$ and I$_0$ are determined. At the expansion parameters T$_0 = 6$ K, P$_0 = 30$ bar, the pressure is observed to rise by $\Delta P = 4.8 \cdot 10^{-6}$ mbar, at a repetition rate of $f = 50$ Hz. For the mass flow rate, a value of $G_{max} = 1.9 \cdot 10^{-9}$ kg s^{-1} is obtained, and for the beam intensities, of $I_{tot} = 2.9 \cdot 10^{17}$ atoms $\cdot$ sr^{-1}s^{-1} and I$_0 = 1.7 \cdot 10^{17}$ atoms $\cdot$ sr^{-1}s^{-1}.

Beam velocities

The beam velocities are determined for both valves as a function of the respective expansion parameters T$_0$ and P$_0$. In fig. 4.25 and fig. 4.26, the observed beam velocities are displayed as a function of T$_0$ at fixed gas pressure P$_0$ and as a function of P$_0$ at fixed source temperature T$_0$, each for the *Parker* General valve source and for the Even-Lavie source.

First, results are presented for the *Parker* General valve, then for the Even-Lavie valve, and finally, these results are compared with each other.

It is expected that the beam velocity v_x is higher when the source temperature T$_0$ is increased. This is confirmed in the experiments (see fig. 4.12). The measured beam velocities range from 201 ms^{-1} at 5 K to 305 ms^{-1} at T$_0 = 11.5$ K. Similarly, the droplet velocities are observed to vary with pressure. At a fixed temperature of T$_0 = 7$ K, the velocity increases from 190 ms^{-1} at 20 bar to 240 ms^{-1} at P$_0 = 50$ bar; and below 20 bar, no ion signal of charged droplets is observed. For comparison, the expected beam velocities for a supersonic expansion of an ideal gas according to eq. (1.5) as well as the expected velocities obtained from the Bernoulli formula, eq. (1.7), are shown. It is valid for ideal liquids [90]. Here, a discharge coefficient of $C = 1.0$ is used and for ρ_0 the known values for the density of liquid helium at the respective temperatures and pressures (as available in ref. [159]) are inserted. Clearly, the ideal gas expression does not predict the observed pressure dependence, since it is not included in the ideal gas model. On the other hand, it can be qualitatively reproduced by the Bernoulli expression. However, the
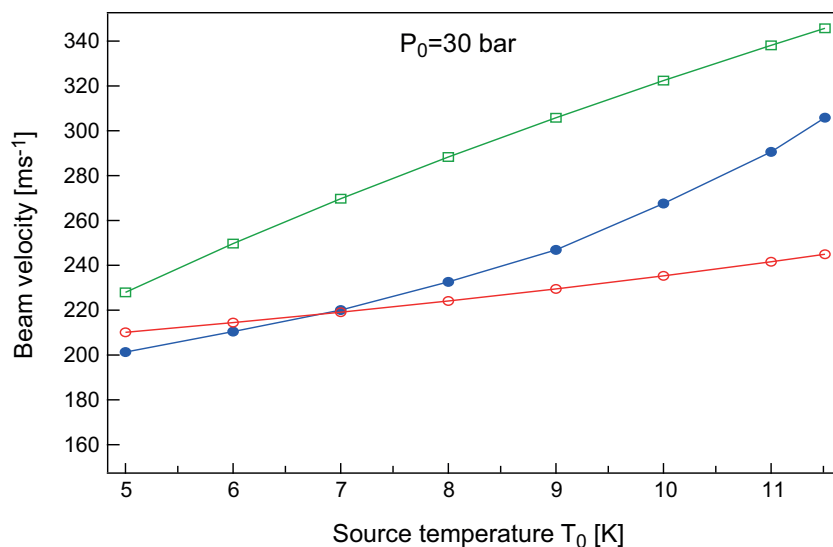
(a)
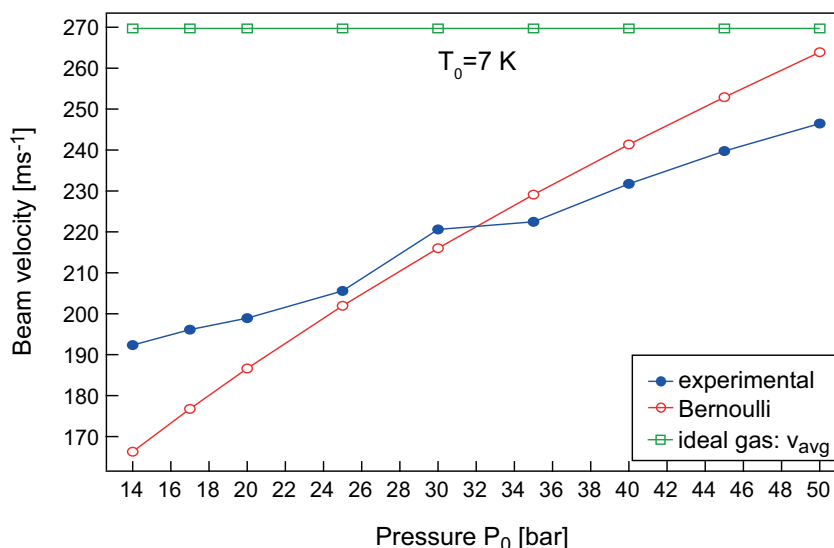
(b)

Figure 4.25: Measured velocities (blue points and curve) of ion-doped helium droplets as a function of (a) source temperature T_0 and (b) gas pressure P_0 for cluster beams formed using the *Parker* General valve. Also shown are predictions for an ideal He gas expansion (green solid curve) as well as a liquid expansion (red dashed curve) following the Bernoulli expression.

ideal gas expression does better in predicting the temperature dependence of the beam velocities. This results in a difference in velocity by a factor of 1.2 between calculated and experimentally obtained beam velocities. This difference can possibly be explained by the real expansion temperature present at the nozzle throat which is presumably higher than indicated by the temperature sensor. An increase in temperature for a pulsed valve in operation can be caused by heat production through moving parts or a less efficient cooling of the nozzle by the cryostat when the heat has to be transferred through a real material with a finite heat conductivity. In fig. 4.26, the beam velocity of He droplets produced by the Even-Lavie source is displayed as a function of source temperature T_0 (top panel) at a constant pressure of $P_0 = 65$ bar. In the bottom panel, the pressure
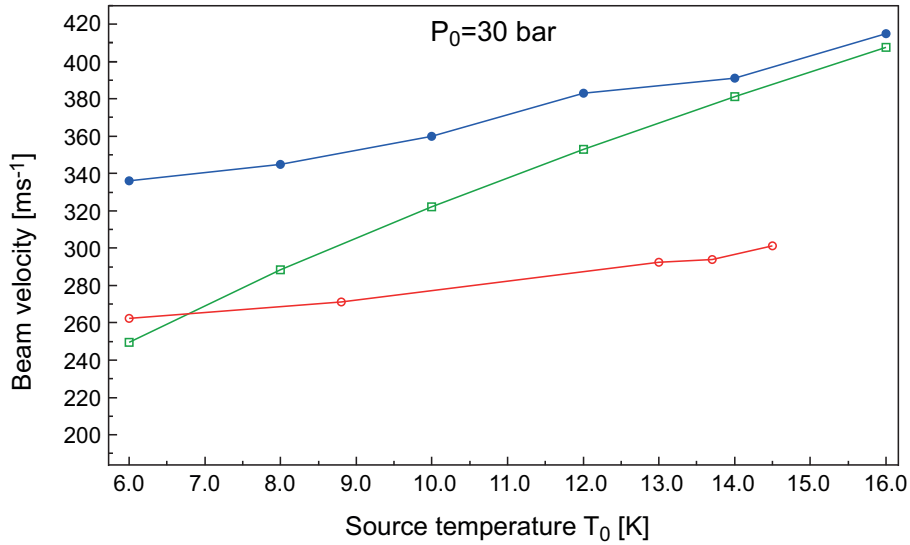
(a)
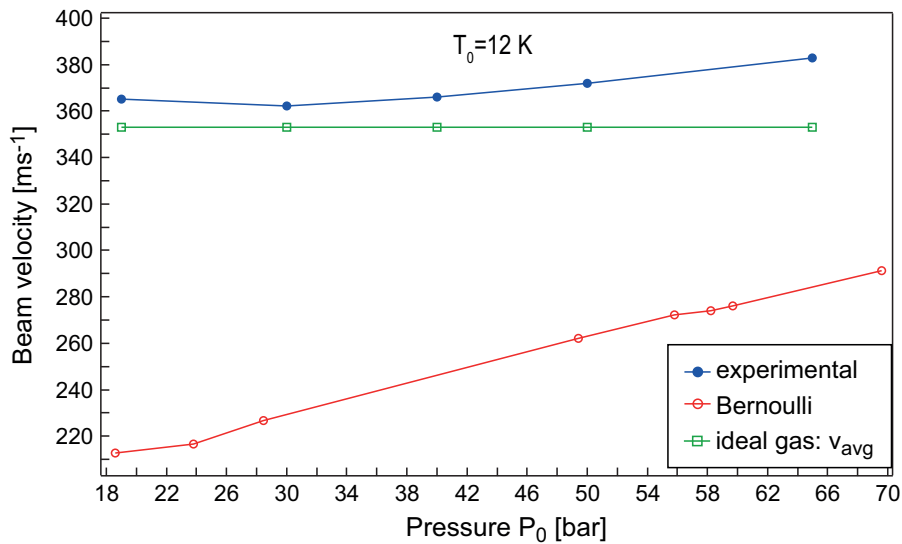
(b)

Figure 4.26: Measured velocities (blue points and curve) of ion-doped helium droplets as a function of (a) source temperature T_0 and (b) gas pressure P_0 for cluster beams formed using the Even-Lavie source. Also shown are predictions for an ideal He gas expansion (green diamonds) as well as a liquid expansion (red circles) following the Bernoulli expression.

dependence of the beam velocity is shown for a fixed $T_0 = 12$ K. As in fig. 4.25, the beam velocities determined for an ideal gas (green diamonds) and for an ideal fluid obtained by the Bernoulli equation (red circles) with $C = 1.0$ are also shown. We see that the beam velocity as a function of source temperature can be well approximated by the ideal gas expression, especially in the higher temperature range above $T_0 = 14$ K. There, the measured velocities and calculated values approach each other. The Bernoulli equation, in general, gives values for the beam velocity which are too small. The pressure dependence, however, basically cannot be described by either of the two models.

In conclusion, it appears that the observed beam velocities for droplet beams emitted from the *Parker* General valve droplet source agree more with velocities known from

liquid beam expansions [90]. The best agreement is observed for supercritical expansions in "*Regime II*" when droplets form by the separation of two phases due to cavitation [58]. In a related study by S. Grebenev [209], typical values of beam velocities in expansions obtained under similar conditions (P_0, T_0) are 50–250 ms^{-1} , which are close to the beam velocities of droplets produced by the *Parker* General valve droplet source determined here. For the source with the Even-Lavie valve, the observed beam velocities agree well with condensed beams as in "*Regime I*" for expansion temperatures $T_0 \geq$ 12 K and liquid beam expansions as in "*Regime III*" for lower source temperatures $T_0 \leq$ 10 K. Typical beam velocities are indicated as $\approx$ 500 ms^{-1} in both "*Regime I*" and "*Regime III*" [209].

An important question is the reason for the significant difference in velocity bet– ween cluster beams emitted from the two different pulsed He droplet sources. Under otherwise equal conditions, the observed beam velocities emitted from the droplet source with the Even-Lavie valve are significantly higher than those emitted from the source with the *Parker* General valve. For rare gas clusters, the nozzle diameter and geometry are known to influence the kinetic processes leading to cluster formation and growth (see Ch. 1.3.4) [82]. It is predicted for other rare gas cluster beams (not helium) that bigger nozzles make slower expansions which favors the cluster formation and yields larger clusters [82]. The orifice diameter D of the Even-Lavie valve (100 μm)[3] is seven

Table 4.1: Measured beam velocities v and droplet sizes N_{He} for different droplet sources under various expansion conditions by other groups as reported in literature.

Reference	P_0 [bar]	T_0 [K]	D [μm]	v[ms^{-1}]	N_{He} [He atoms]
Vilesov [113]	6–40	18–26	500	330–400	10^4–10^5
Buchenau [58]	8–20	5–20	5	170–300	10^4
Buchenau [84]	5–20	$\leq$20	5	200–400	10^3–10^6
Henne [92]	20	4–25	5	160–500	10^4–10^8
Slenczka [184, 185]	10–100	7–20	100	250–500	10^4–10^6
Kornilov [205]	1–100	6–20	5	250–450	10^3–10^5
Schilling [201]	20–80	4–30	5	$\leq$480	10^3–10^4
Toennies [90]	0.5–30	1.6–4.2	2	15–120	10^{10}–10^{12}
Northby [85]	10–80	6–18	5		10^3–10^5
Knuth [86]	8–20	5–10	5		10^4
Federmann [28]	20	10	5		$2 \cdot 10^4$
Ellis [183]	8–20	10–16	600		$5 \cdot 10^4$
Hagena [82]	0.1–16	120–450	1.5–15		$5 \cdot 10^2$–10^4 (Ar)
Grebenev [209]	20	12–24	5	350–500	10^2–10^4
Grebenev [209]	20	8–11	5	50–250	10^8
Grebenev [209]	20	2.6–7	5	350–500	10^6–10^8

times smaller than the orifice of the General valve (0.7 mm). Thus the higher beam velocities of the cluster beams emitted from the Even-Lavie source can probably be attributed to the smaller nozzle orifice diameter and the different geometry, compared

---

[3]The nozzle orifice diameter is indicated to be 100 μm; practically, however, the Kapton foil that is placed in front of the nozzle has a diameter of only 60 μm.

to the *Parker* source. The difference in beam velocity is presumably also related to the difference in cluster sizes since slow expansions are known to favor cluster growth [82].

In table 4.1, an overview of cluster sizes and beam velocities (if available) as obtained for nozzle beam expansions under various source conditions in other groups is given. Most of them are determined for continuous expansions, except for ref. [113, 183–185], and most of the nozzles employed have much smaller orifice diameters. The results we obtained for the cluster sizes in the case of the *Parker* source are similar only to the ones reported in ref. [90], however the expansion conditions under which the clusters are obtained there are quite different to the ones we applied. Also, the beam velocities they observe are significantly lower. They agree better with those observed in ref. [58] and ref. [209] in which, however, the cluster sizes as reported are much smaller. Therefore, transferring any results from literature in order to find explanations for the processes taking place in the expansions from the *Parker* droplet source must be done with caution. In the case of the Even-Lavie source, however, the cluster sizes as well as the beam velocities observed are in good agreement with those reported, for example, in ref. [184, 185] as well as in ref. [113], even though in the latter they use a nozzle with a larger orifice. Therefore, it seems reasonable to interpret our observations in a similar way as it is done in the literature mentioned.

4.5 Summary

In this Chapter, the experimental results on the charged He droplets produced in a pulsed expansion are presented. Non-doped He droplets are charged by electron impact ionization, and the cluster fragment ions are detected in a quadrupole mass spectrometer. The droplets are doped *via* pickup of ions from the hexapole ion trap and are detected as an electric current of single charges on Faraday-type metal detectors. The sizes and size distributions of the emitted droplets are determined for the two different sources. The beam intensities are determined and the dependence of the beam velocity on the source parameters are studied.

Chapter 5

Conclusion and outlook

In the framework of this thesis, a new experiment has been set up, which allows the investigation of large mass-to-charge selected biomolecules at sub-kelvin temperatures. It provides the opportunity to gain fundamental insights into the properties of even large species such as proteins or biomolecular complexes and, using spectroscopic techniques, to obtain detailed information on the investigated systems.

In the experimental setup, an electrospray ion source is combined with mass-selective techniques for gas-phase ions, a linear ion trap, and a pulsed He droplet source. The nature and properties of the particles investigated, such as their charge state and the translational as well as the internal temperature, can be controlled by several experimental parameters. In this way, the molecules are in a well-defined state at the moment of laser interrogation. Selected charge states of ions produced by electrospray ionization are accumulated in a hexapole ion trap. While stored in the trap, the ions can be picked up by superfluid He clusters traversing the trap. The experimental approach is conceptually similar to the pickup of neutral particles from a gas cell. However, the crucial difference from those kinds of experiments results from the explicit use of the high kinetic energy of heavy He droplets so that ions can leave the trap only when they are picked up and transported by He droplets. Loaded droplets can then be further studied by diverse experimental techniques.

It is shown that ions over a wide range of sizes, including large proteins composed of more than 1000 atoms, can be efficiently incorporated into superfluid He droplets by the pickup technique. The ion yield of doped droplets obtained is promising for spectroscopic investigations of the charged droplets in the future. For example, for (multiphoton) spectroscopic measurements as in "action spectroscopy", only a few ions per pulse suffice.

The experiment was performed on biomolecules as dopant species which can be classified into three categories in terms of particle size: single amino acids composed of ≈ 15 atoms, peptides composed of ≈ 100 atoms, and large proteins composed of ≈ 1000 atoms. The number of atoms composing a molecule defines its number of degrees of freedom and thus the internal energy contained in the molecule. This energy is transferred to the droplet after the pickup and leads to a rise of the droplet temperature to almost above the λ-transition temperature (depending on the mass and thus the heat capacity of the He droplet), which is followed by a rapid cooling of the ion+droplet system down to the equilibrium temperature of the droplet of ≈ 0.37 K. The efficiency of the heat transfer is determined by the overlap of the density of (excited) states of

the ion (which is greater for large molecules) and the density of internal states of the droplet. The result is that the initial cooling rate is faster, the greater the amount of energy deposited into the droplet.

A linear hexapole ion trap is used as a pickup cell. The oscillating RF voltage for radial trapping is supplied by standard radio equipment using a tunable coil for matching the resonance frequency. Longitudinally, the ions are trapped by a low trapping potential of 2–10 eV. In this thesis, experimental results are presented which were obtained by using two different hexapole traps. The main difference between them is their rod length. The first version of the trap has rods which are 14.5 cm long, while the advanced version has rods of approximately double that length. Exchanging the traps together with a realignment of the He droplet source with respect to the experimental main axis was observed to yield an increase of the ion signal by about a factor of 10. High ion densities up to the space charge limit can be reached in the trap. This is observed in the time-of-flight mass spectrometer after dumping the trap and measuring the signal of liberated ions. The filling of the trap can be controlled by the accumulation times, which are adjusted to the flux of ions produced by the *ESI* source. To facilitate trapping, the ions must be translationally cooled *via* collisions with He buffer gas atoms. Thereafter, they can be stored in the trap for several minutes without significant losses.

Two different pulsed droplet sources have been characterized, one equipped with a *Parker* General valve (series 99), the other with an Even-Lavie cryogenic valve. They are different in design and demand different operation parameters as well as expansion parameters.

The *Parker* General valve has a custom-built copper faceplate with an orifice diameter of 0.7 mm which is about a factor of 10 larger than the orifice diameter of the Even-Lavie valve ($\approx 100\,\mu$m). The duty cycles are also rather different. The *Parker* valve is usually operated at a 5 Hz repetition rate. The other valve emits much shorter pulses which allows a higher repetition rate of 50 Hz. Cluster formation is observed when the source with the *Parker* valve is operated at temperatures T_0 between 4.5 K–10.5 K and pressures P_0 between 15–50 bar, and for the droplet source with the Even-Lavie valve for T_0 between 6–20 K and P_0 between 30–65 bar.

The production of He droplets has been confirmed for both sources by mass spectrometry. Fragment ions of undoped He clusters are observed up to clusters of 20 He atoms in the mass range detected. In the case of the droplet source with the Even-Lavie valve, the additional occurrence of water clusters up to an order of $(H_2O)_5$ is observed; these are missing in mass spectra from the source with the *Parker* General valve. The absence of water cluster ions is attributed to the large sizes of the clusters produced by the first source (see Ch. 4.3). One possibility is that a large droplet size can either favor the aggregation of many water molecules in the droplet and lead to large water clusters having sizes which are beyond the detectable mass range. Alternatively, dopant species embedded in very large droplets could have a reduced probability for ionization or detection [98]. Usually, the signal of the He dimer He_2^+ as the fragment ion with highest abundance is monitored as an indicator for the efficiency of cluster formation as a function of the applied source conditions P_0, T_0.

The first indicator for the successful removal of ions from the trap by He droplets and thus, the proof of principle for the ion-pickup technique was the observed dimin-

ishing of the trap content after the passage of He droplets through the trap. When He droplets traverse the loaded trap for a definite time period, a subsequent measurement of the trap content reveals that it has been depleted relative to a "basis" trap content; this is obtained under the same experimental conditions and measured after the same storage time, but without the previous passage of He droplets. The degree of depletion is dependent on the applied expansion parameters at the droplet source (P_0, T_0), on the number of traversing droplet pulses, as well as on the initial trap filling, because the pickup probability is determined by the particle density in the collision cell.

The ion-doped droplets were then directly detected as an electric current of charges impinging on a Faraday-type metal detector, with a peak current of up to 20 pA. The ion yield (in the case of the long trap) is determined to be $\approx$ 30 000 per pulse when droplets produced by the *Parker* He droplet source are doped with singly protonated amino acids (for example Trp^+ ions), and $\approx$ 470 per pulse when they are doped with large multiply-charged proteins (for example $CytC^{+17}$ ions). In the case of the Even-Lavie valve, the intensities obtained were $\approx$ 2 000 Trp^+ ion-doped droplets per pulse, but only about 10 per pulse when the droplets were doped with $CytC^{+10}$ ions. These ion intensities approximately agree with the observed number of ions removed in the depletion experiments.

For both He droplet sources, the size and size distributions of the emitted droplets were determined, as well as the dependence of the droplet sizes and longitudinal beam velocities on the applied expansion parameters. The results obtained from the two sources reveal large differences with the droplets produced by either one of the sources having sizes which vary over up to six orders of magnitude under the same expansion conditions (P_0, T_0). The sizes and size distributions of the He droplets are determined by applying parallel or perpendicular electric fields to the charged droplet beam. The deflection of the beam from the straight direction (by perpendicular electric fields) or the change in flight time (by parallel electric fields) with respect to zero field measurements is observed. With the resulting values, the masses of droplets doped with ions of a specific m/q ratio were determined.

For the *Parker* General valve source, the droplet sizes and size distributions were determined by the droplet beam deflection technique. The deflection in a perpendicular electrostatic field was measured for droplets doped with Phe^+ ions and with $CytC^{+Z}$ ions in different charge states, $Z = 9$, 14, 17. The mean size of the droplets was found to be larger than $N_{He} = 10^{11}$ constituent He atoms. The size distributions can be described by log-normal distributions.

A large difference in deflection is measured when He droplets are doped with Phe^+ ions or with $CytC^{+Z}$ ions. When the pickup of only one ion per droplet is assumed, this would lead to a difference in droplet size by two orders of magnitude, depending on the embedded dopant species.

It is shown that the pickup of more than one ion per droplet must be considered when on the one hand, a high particle density is present in the trap and, on the other hand, large droplets with large geometric cross sections are provided. The probability for the pickup scales linearly with the particle density n, the geometrical cross section of the colliding particles (which is mainly determined by the droplet size), and the length of the trap. Furthermore, a large droplet is able to contain a greater number of charges without fragmenting due to Coulomb repulsion.

The pickup of ≈ 100 Phe$^+$ ions could explain the observed large deflection of Phe$^+$-doped droplets as compared to CytC^{+Z}-doped droplets. This total charge would result in a deflection of the observed magnitude of a droplet having the same sizes N_{He} such as the droplets doped with a protein.

The sizes and size distributions of droplets produced by the Even-Lavie valve were determined by measuring the change in velocity when accelerating the ion-doped droplets in an electric field. The "acceleration" measurements revealed that at higher source temperatures than $T_0 = 10$ K ($P_0 = 65$ bar), the velocity distribution Δv_x can be described by a single Gaussian and the size distribution by a single-mode log-normal distribution. At temperatures $T_0 \leq 10$ K, however, a second component of slower particles appears, leading to a bimodal Gaussian velocity distribution. Then, the size distribution can be well described by a bimodal log-normal distribution with a small and a large droplet component. The mean size of Trp$^+$-doped droplets produced at $T_0 = 10$ K was determined to be $N_{He} = 1.7 \cdot 10^6$ He atoms for the large droplet component and $2.8 \cdot 10^5$ for the small droplet component, as well as $N_{He} = 2.1 \cdot 10^5$ and $5.2 \cdot 10^4$ He atoms when droplets are produced at higher source temperatures, $T_0 = 12$ K or 16 K, respectively.

When droplets are doped with a protein ion, the measured droplet sizes are significantly larger than the sizes of droplets doped with smaller ions, such as a single amino acid. Picking up, cooling, and transporting large proteins with high internal energies seems to require larger droplets than those needed for small dopant particles.

The dependence of the velocities of the cluster beam on the applied expansion parameters was studied. The result is that the beam velocities increase for increasing T_0 and increasing P_0 , and decrease for decreasing T_0 or P_0. At $P_0 = 30$ bar, upon variation of T_0 from 5–11.5 K, the velocities of beams emitted from the *Parker* General valve increase from 200–300 ms^{-1} ; and at a fixed temperature of $T_0 = 7$ K, an increase of P_0 from 15–50 bar results in beam velocities of 190–250 ms^{-1}. For the Even-Lavie droplet source, the cluster beams produced at a fixed $P_0 = 30$ bar and different temperatures T_0 from 6–16 K yield beam velocities of 340–410 ms^{-1} , and those emitted at a fixed $T_0 = 12$ K at varying source pressures $P_0 = 20$–65 bar have velocities of 360–380 ms^{-1}. Thus, with equivalent source parameters P_0 and T_0, it is observed that cluster beams emitted from the Even-Lavie droplet source are considerably faster than the beams emitted from the *Parker* General valve source. This is attributed to the different nozzle geometries, which affect the kinetics of isentropic free-jet expansions, and to the smaller orifice diameter of the Even-Lavie valve, since smaller nozzles are known to produce faster beams [82].

Regarding the observed difference in beam velocities and in behavior in dependence on the expansion parameters (P_0, T_0) applied, it appears that the processes leading to cluster formation in the beams emitted from the two sources are fundamentally different. While clusters produced by the Even-Lavie source seem to form *via* condensation at higher source temperatures T_0 (*regime I*) and result from breaking-up liquid beams at low source temperatures (*regime II*), those produced by the *Parker* droplet source seem also to form in liquid expansions; the droplet sizes observed indicate *regime III* expansions, however, the low temperatures required might not be reached in pulsed

expansions. The range of the applicable expansion parameters P_0, T_0 together with the enormous droplet sizes and the low beam velocities are indicators of supercritical expansions. Furthermore, the observation of vanishing of the He dimer ion signal at expansion temperatures $T_0 \geq 11$ K is indicative that the *Parker* droplet source might, in general, not produce small clusters. This can be an inherent property of the nozzle expansion using this source, leading to the formation of very large clusters exclusively; another possibility is that smaller droplets are produced in the expansion but they do not reach the trap for some reason. Possibly, small clusters are scattered from the beam or destroyed before reaching the trap, for example by shock waves forming at the skimmer. The short nozzle-to-skimmer distance (≈ 5 cm) in the experimental setup with the *Parker* droplet source is advantageous for the formation of shock waves, whereas the nozzle-to-skimmer distance in the setup with the Even-Lavie valve is considerably enhanced, and therefore, the probability of shock wave formation is much reduced in the case of the Even-Lavie source.

Cluster sizes on the order of magnitude as produced by the *Parker* General valve source make it difficult to further investigate the doped droplets, because particles of such high m/q ratios are beyond the detection sensitivity range of most standard charged particle detectors such as MCPs.

One possibility to obtain (useful) information from experiments performed on the doped droplets is to eliminate most of the constituent He atoms before detection. For example, trapping the doped droplets and storing them in a trap at elevated temperatures would lead to evaporation of many He atoms from the droplet in a sufficient time window. However, trapping (charged) particles of very high kinetic energies requires a large experimental effort. Alternatively, removing He atoms from a cluster could also be achieved by mechanical collisions. For example, sending the beam of charged droplets through a grid would lead to a "stripping" of He atoms from the cluster. However, for this purpose meshes are needed having wire diameters that are narrower or at least comparable to the geometric dimensions of the droplets themselves. Grids in the nanometer size ranges are not commercially available and are complicated to fabricate. Thus, this is not a possibility which can easily and quickly be realized.

Alternatively, information on the dopant species can be obtained if it could be extracted from the droplet by laser excitation. This would enable the detection of the bare ion after laser interrogation. However, it is predicted from the experiments performed by Gspann and Drabbels that an ejection process of ionized or vibrationally-excited ions from a He cluster decreases rapidly with the cluster size.

Finally, the difficulties of dealing with such large-sized droplets could be avoided when the new droplet source was installed. The Even-Lavie valve source was observed to produce much smaller droplets, which may enable the performance of spectroscopic experiments on the charged droplets directly, to gain useful and detailed information on the embedded particles. Furthermore, this significantly facilitates the manipulation of the charged beams by (for example) electric fields, allowing further investigation of the doped droplets or deflecting them to an off-axis detector. In the detection process, use could be made of the dissipative nature of the droplets, for example by the messenger technique. The loss of He atoms as a function of the incident laser wavelength could be measured and would give an absorption spectrum of the respective dopant species.

Outlook

The experimental setup presented in Ch. 3 can be enhanced in order to further investigate the charged droplets or the embedded dopant particles. One possibility would be to perform spectroscopic measurements using multi-photon techniques with for example, a high-fluence FEL as IR light source, as is currently being constructed at the Fritz-Haber Institute. After interrogation of the charged droplets with laser light, they could be analyzed in a time-of-flight mass spectrometer.
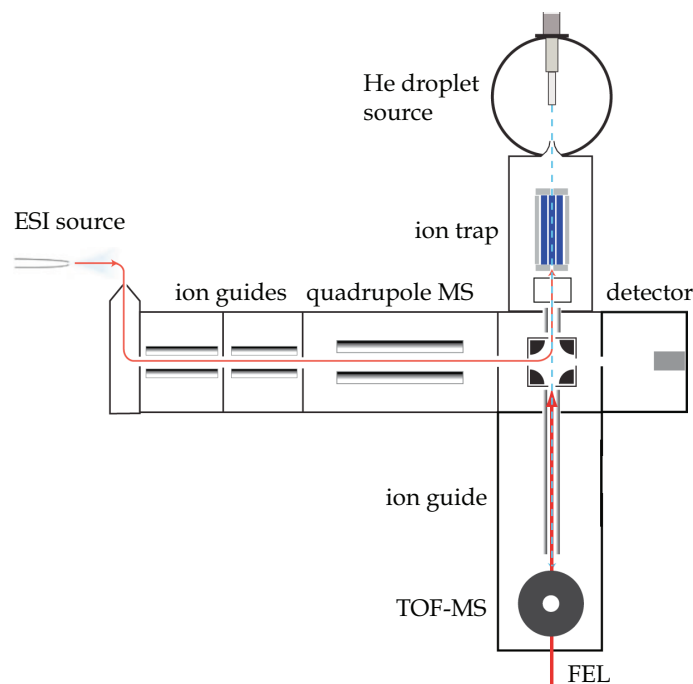
Figure 5.1: Scheme of a new experimental setup designed for performing spectroscopic measurements on ion-doped He droplets produced by the Even-Lavie valve.

There are already first results from successful spectroscopic measurements of this type. For performing these measurements, the experimental setup was modified. After the quadrupole bender, two metal plates were installed which can be set to an electric potential and are followed by two meshes at the exit. The first mesh is at the same voltage as the two plates, while the second mesh is grounded. This potential difference serves to accelerate passing ions. Between the two plates, a multi-pass cell composed of two parallel but slightly displaced prisms is installed. A laser beam incident from the perpendicular direction to the droplet beam can be reflected approximately 7 times, each time crossing the beam of ion-doped droplets. In fig. 5.2, the electronic spectrum of Fe–Heme$^+$ ions which were picked up and cooled in He droplets and irradiated by laser light in the wavelength range between $\approx$ 375–410 nm is shown. Fe–Heme$^+$ ions (Hemin, molecular weight: 617 g/mol) is the metal core contained in cytochrome c. The black curve shows a non-accelerated charged droplet beam ($U_{acc} = 0$ V), produced at $T_0 = 16$ K and $P_0 = 65$ bar, and the red curve shows the charged droplet beam after acceleration by a voltage of $U_{acc} = 50$ V. The blue curve reflects the accelerated charged beam after laser irradiation (using a multi-pass cell). The green curve, finally, is the difference between the

blue and red curves. A fast peak appears upon laser irradiation and is interpreted as the signal of bare Fe–Heme$^+$ ions after ejection from the droplets. Simultaneously, the signal of ion-doped droplets is observed to be depleted. The wavelength-dependent spectrum in fig. 5.2 confirms that the measured spectrum is that of the electronic transition $S_2 \leftarrow S_0$, the so-called Soret band. This band is intrinsically rather broad, since the excited state is known to have a very short lifetime due to ultra-fast internal conversion of the absorbed energy, causing the electronic transition to relax on a time scale of femtoseconds.
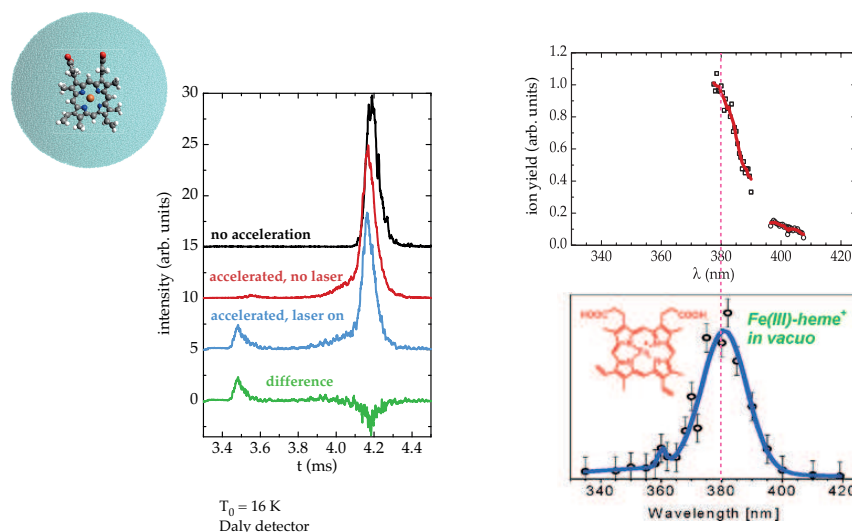
Figure 5.2: First spectrum: Electronic transition $S_2 \leftarrow S_0$ (Soret band) of Fe–Heme$^+$ in He droplets ($P_0 = 65$ bar, $T_0 = 16$ K). The spectrum on the bottom right is taken from ref. [210]. The ions are ejected from the droplets upon laser irradiation at wavelengths between 375–410 nm. For further explanation, see text.

The range of species to be investigated can be expanded by exchanging the *ESI* source by an alternative ion source. A laser ablation source, for example, would enable metal-cluster ions cooled in He droplets to be studied. The use of a nano-electrospray ionization source would enable the investigation of new interesting species such as large proteins and protein complexes. This technique is known to be able to transfer the species of interest very gently into the gas phase, due to charge reduction in the production process, so that the produced molecular ions are mostly present in the gas phase in their native structure. Furthermore, it allows the use of minimal sample quantities and is, therefore, convenient for the investigation of rare or expensive molecules which are not readily available.

The influence of the solvent could be directly studied when solvent molecules are added one by one after electrospray ionization. The change in the intrinsic molecular properties, for example the structure, upon solvent attachment could then be monitored in the resulting spectra.

The setup can rather flexibly be combined with various experimental techniques. To further develop control over the particle properties before pickup, the experiment can be combined with, for example, an ion mobility setup. The whole initial part of the Qtof would then be replaced by a nano-*ESI* source with a mass spectrometer and a drift tube with an entrance and an exit funnel. In this way, the experiment would provide

for separation of different conformers of ions having the same mass-to-charge ratio and as such, enable the investigation of cold mass-to-charge- and conformer-selected large biomolecules.

Cooling the entire region from the ion trap to the detection region to cryogenic temperatures of about 10 K will largely reduce the incorporation of residual gas particles in the He droplets which perturb the spectral results. Instead, a controlled pickup cell for neutral particles can be installed behind the ion trap to obtain ion-neutral complexes simultaneously picked up in the He droplets which can then be investigated.

Bibliography

[1] G. Scoles, *Molecular beams* (Oxford University Press, New York, 1988), Vol. 1.

[2] H. Pauly, *Atom, Molecule and Cluster Beams 1* (Springer Verlag, Berlin, 2000), Vol. 1, 2.

[3] D. H. Levy, Science **214**, 263 (1981).

[4] M. Smits, C. A. de Lange, S. Ullrich, T. Schultz, M. Schmitt, J. G. Underwood, J. P. Shaffer, D. M. Rayner, and A. Stolow, Rev. Sci. Instrum. **74**, 4812 (2003).

[5] T. R. Rizzo, Y. D. Park, and D. H. Levy, J. Chem. Phys. **85**, 6945 (1986).

[6] E. G. Robertson and J. P. Simons, Phys. Chem. Chem. Phys. **3**, 1 (2001).

[7] R. E. Haufler, Y. Chai, L. P. F. Chibante, M. R. Fraelich, R. B. Weisman, R. F. Curl, and R. E. Smalley, J. Chem. Phys. **95**, 2197 (1991).

[8] M. S. de Vries and P. Hobza, Ann. Rev. Phys. Chem. **58**, 585 (2007).

[9] L. Jiang, T. Wende, R. Bergmann, G. Meijer, and K. R. Asmis, J. Am. Chem. Soc. **132**, 7398 (2010).

[10] J. A. Stearns, O. V. Boyarkin, and T. R. Rizzo, J. Am. Chem. Soc. **129**, 13820 (2007).

[11] A. Svendsen, U. J. Lorenz, O. V. Boyarkin, and T. R. Rizzo, Rev. Sci. Instrum. **81**, 073107 (2010).

[12] B. Roth, A. Ostendorf, H. Wenz, and S. Schiller, J. Phys. B **38**, 3673 (2005).

[13] D. Offenberg, C. B. Zhang, C. Wellers, B. Roth, and S. Schiller, Phys. Rev. A **78**, 061401 (2008).

[14] T. E. Gough, M. Mengel, P. A. Rowntree, and G. Scoles, J. Chem. Phys. **83**, 4958 (1985).

[15] J. P. Toennies and A. F. Vilesov, Angew. Chem. Int. Ed. **43**, 2622 (2004).

[16] J. P. Toennies and A. F. Vilesov, Ann. Rev. Phys. Chem. **49**, 1 (1998).

[17] F. Stienkemeier and K. K. Lehmann, J. Phys. B **39**, R127 (2006).

[18] M. Y. Choi, G. E. Douberly, T. M. Falconer, W. K. Lewis, C. M. Lindsay, J. M. Merritt, P. L. Stiles, and R. E. Miller, Int. Rev. Phys. Chem. **25**, 15 (2006).

[19] M. Barranco, R. Guardiola, S. Hernandez, R. Mayol, J. Navarro, and M. Pi, J. Low Temp. Phys. **142**, 1 (2006).

[20] S. Goyal, D. L. Schutt, and G. Scoles, Phys. Rev. Lett. **69**, 933 (1992).

[21] M. Hartmann, R. E. Miller, J. P. Toennies, and A. Vilesov, Phys. Rev. Lett. **75**, 1566 (1995).

[22] K. K. Lehmann and G. Scoles, Science **279**, 2065 (1998).

[23] C. Callegari, K. K. Lehmann, R. Schmied, and G. Scoles, J. Chem. Phys. **115**, 10090 (2001).

[24] R. E. Zillich, K. B. Whaley, and K. v. Haeften, J. Chem. Phys. **128**, 094303 (2008).

[25] S. Grebenev, M. Hartmann, M. Havenith, B. Sartakov, J. P. Toennies, and A. F. Vilesov, J. Chem. Phys. **112**, 4485 (2000).

[26] A. Lindinger, J. P. Toennies, and A. F. Vilesov, J. Chem. Phys. **110**, 1429 (1999).

[27] S. Denifl, F. Zappa, I. Mahr, J. Lecointre, M. Probst, T. D. Mark, and P. Scheier, Phys. Rev. Lett. **97**, 043201 (2006).

[28] J. D. Close, F. Federmann, K. Hoffmann, and N. Quaas, Chem. Phys. Lett. **276**, 393 (1997).

[29] S. Müller, S. Krapf, T. Koslowski, M. Mudrich, and F. Stienkemeier, Phys. Rev. Lett. **102**, 183401 (2009).

[30] T. Doppner, T. Fennel, T. Diederich, J. Tiggesbäumker, and K. H. Meiwes-Broer, Phys. Rev. Lett. **94**, 013401 (2005).

[31] A. J. Nelson, S. Toleikis, H. Chapman, S. Bajt, J. Krzywinski, J. Chalupsky, L. Juha, J. Cihelka, V. Hajkova, L. Vysin, T. Burian, M. Kozlova, R. R. Faustlin, B. Nagler, S. M. Vinko, T. Whitcher, T. Dzelzainis, O. Renner, K. Saksl, A. R. Khorsand, P. A. Heimann, R. Sobierajski, D. Klinger, M. Jurek, J. Pelka, B. Iwan, J. Andreasson, N. Timneanu, M. Fajardo, J. S. Wark, D. Riley, T. Tschentscher, J. Hajdu, and R. W. Lee, Opt. Exp. **17**, 18271 (2009).

[32] K. J. Gaffney and H. N. Chapman, Science **316**, 1444 (2007).

[33] C. Gnodtke, U. Saalmann, and J. M. Rost, Phys. Rev. A **79**, 041201 (R) (2009).

[34] J. C. H. Spence and R. B. Doak, Phys. Rev. Lett. **92**, 198102 (2004).

[35] C. Tanford, Science **200**, 1012 (1978).

[36] R. L. Baldwin, Mol. Phys. **371**, 283 (2007).

[37] M. Yamashita and J. B. Fenn, J. Phys. Chem. **88**, 4451 (1984).

[38] B. T. Ruotolo and C. V. Robinson, Curr. Opin. Chem. Biol. **10**, 402 (2006).

[39] J. L. P. Benesch, B. T. Ruotolo, D. A. Simmons, and C. V. Robinson, Chem. Rev. **107**, 3544 (2007).

[40] M. Karas and F. Hillenkamp, Anal. Chem. **60**, 2299 (1988).

[41] B. Domon and R. Aebersold, Science **312**, 212 (2006).

[42] K. Thalassinos, S. E. Slade, K. R. Jennings, J. H. Scrivens, K. Giles, J. Wildgoose, J. Hoyes, R. H. Bateman, and M. T. Bowers, Int. J. Mass Spectrom.nt **236**, 55 (2004).

[43] C. Wu, W. F. Siems, G. R. Asbury, and H. H. Hill, Anal. Chem. **70**, 4929 (1998).

[44] J. B. Fenn, M. Mann, C. K. Meng, S. F. Wong, and C. M. Whitehouse, Science **246**, 64 (1989).

[45] M. S. Wilm and M. Mann, Int. J. Mass Spectrom. **136**, 167 (1994).

[46] P. Kebarle, J. Mass Spec. **35**, 804 (2000).

[47] J. Oomens, B. Sartakov, G. Meijer, and G. v. Helden, Int. J. Mass Spectrom. **254**, 1 (2006).

[48] M. Okumura, L. I. Yeh, and Y. T. Lee, J. Chem. Phys. **83**, 3705 (1985).

[49] K. R. Asmis and J. Sauer, Mass Spectr. Rev. **26**, 542 (2007).

[50] Bergmann-Schäfer, *Gase, Nanosysteme, Flüssigkeiten* (de Gruyter, Berlin, New York, 2006).

[51] L. Landau, J. Phys.–USSR **5**, 71 (1941).

[52] D. R. Tilly and J. Tilly, *Superfluidity and superconductivity*, 3 ed. (IOP Publishing LTD, Bristol, 1994).

[53] K. R. Atkins, Phys. Rev. **116**, 1339 (1959).

[54] S. Grebenev, J. P. Toennies, and A. F. Vilesov, Science **279**, 2083 (1998).

[55] L. Pitaevskii and S. Stringari, Z. Phys. D **16**, 299 (1990).

[56] M. Hartmann, J. P. Toennies, A. F. Vilesov, and G. Benedek, Czech. J. Phys. **46**, 2951 (1996).

[57] G. N. Makarov, Physics-Uspekhi **51**, 319 (2008).

[58] H. Buchenau, E. L. Knuth, J. Northby, J. P. Toennies, and C. Winkler, J. Chem. Phys. **92**, 6875 (1990).

[59] D. M. Brink and S. Stringari, Z. Phys. D **15**, 257 (1990).

[60] M. V. R. Krishna and K. B. Whaley, J. Chem. Phys. **93**, 6738 (1990).

[61] A. F. Vilesov, Chem. Phys. Lett. **235**, 596 (1995).

[62] H. Kamerlingh Onnes, Commun. Phys. Lab. Univ. Leiden **105**, 3 (1908).

[63] E. W. Becker, R. Klingelhöfer, and P. Lohse, Z. Naturforsch. A **16**, 1259 (1961).

[64] J. A. Northby, J. Chem. Phys. **115**, 10065 (2001).

[65] M. A. Weilert, D. L. Whitaker, H. J. Maris, and G. M. Seidel, J. Low Temp. Phys. **98**, 17 (1995).

[66] R. Fröchtenicht, J. P. Toennies, and A. F. Vilesov, Chem. Phys. Lett. **229**, 1 (1994).

[67] M. Hartmann, F. Mielke, J. P. Toennies, A. F. Vilesov, and G. Benedek, Phys. Rev. Lett. **76**, 4560 (1996).

[68] K. Nauta and R. E. Miller, J. Chem. Phys. **111**, 3426 (1999).

[69] M. Y. Choi and R. E. Miller, J. Am. Chem. Soc. **128**, 7320 (2006).

[70] R. Lehnig and A. Slenczka, J. Chem. Phys. **122**, 244317 (2005).

[71] R. Lehnig and A. Slenczka, J. Chem. Phys. **118**, 8256 (2003).

[72] J. Tiggesbäumker and F. Stienkemeier, Phys Chem Chem Phys **9**, 4725 (2007).

[73] N. X. Truong, P. Hilse, S. Gode, A. Przystawik, T. Doppner, T. Fennel, T. Bornath, J. Tiggesbaumker, M. Schlanges, G. Gerber, and K. H. Meiwes-Broer, Phys. Rev. A **81**, 013201 (2010).

[74] N. Pförtner, A. F. Vilesov, and M. Havenith, Chem. Phys. Lett. **343**, 281 (2001).

[75] F. Stienkemeier, J. Higgins, W. E. Ernst, and G. Scoles, Phys. Rev. Lett. **74**, 3592 (1995).

[76] F. Stienkemeier, J. Higgins, C. Callegari, S. I. Kanorsky, W. E. ERnst, and G. Scoles, Z. Phys. D **38**, 253 (1996).

[77] P. Claas, G. Droppelmann, C. P. Schulz, M. Mudrich, and F. Stienkemeier, J. Phys. Chem. A **111**, 7537 (2007).

[78] A. Sassara, G. Zerza, and M. Chergui, J. Chem. Phys. **29**, 4997 (1996).

[79] S. Smolarek, A. M. Rijs, J. S. Hannam, D. A. Leigh, M. Drabbels, and W. J. Buma, J. Am. Chem. Soc. **131**, 12902 (2009).

[80] J. Harms, M. Hartmann, B. Sartakov, J. P. Toennies, and A. F. Vilesov, J. Mol. Spectr. **185**, 204 (1999).

[81] W. Christen, K. Rademann, and U. Even, J. Phys. Chem. A **114**, 11189 (2010).

[82] O. F. Hagena and W. Obert, J. Chem. Phys. **56**, 1793 (1972).

[83] L. W. Bruch, W. Schöllkopf, and J. P. Toennies, J. Chem. Phys. **117**, 1544 (2002).

[84] H. Buchenau, J. P. Toennies, and J. A. Northby, J. Chem. Phys. **95**, 8134 (1991).

[85] T. Jiang and J. A. Northby, Phys. Rev. Lett. **68**, 2620 (1992).

[86] E. L. Knuth and U. Henne, J. Chem. Phys. **110**, 2664 (1999).

[87] E. L. Knuth, J. Chem. Phys. **107**, 9125 (1997).

[88] H. Lamb, *Hydrodynamics*, 6 ed. (Univ. Press, Cambridge, 1953).

[89] R. A. Granger, *Fluid mechanics* (Dover publications inc., New York, 1995).

[90] R. E. Grisenti and J. P. Toennies, Phys. Rev. Lett. **90**, 2345011 (2003).

[91] E. L. Knuth, F. Schünemann, and J. P. Toennies, J. Chem. Phys. **102**, 6258 (1995).

[92] U. Henne, Ph.D. thesis, Max-Planck-Insitut für Strömungsforschung, Göttingen, 1996.

[93] J. H. Moore, C. C. Davis, and M. A. Coplan, *Building a Scientific Apparatus*, 3 ed. (Perseus books, Cambridge University Press, Massachusetts, YEAR).

[94] A. Phillips and P. V. E. McClintock, Phys. Rev. Lett. **33**, 1468 (1974).

[95] T. Ellis, C. I. Jewell, and P. V. E. McClintock, PHys. Lett. A **78**, 358 (1980).

[96] M. Buzzacchi, D. E. Galli, and L. Reatto, Phys. Rev. B **64**, 094512 (2001).

[97] N. Halberstadt and K. C. Janda, Chem. Phys. Lett. **282**, 409 (1998).

[98] M. Ovchinnikov, B. L. Grigorenko, K. C. Janda, and V. A. Apkarian, J. Chem. Phys. **108**, 9351 (1998).

[99] D. Bonhommeau, M. Lewerenz, and N. Halberstadt, J. Chem. Phys. **128**, 054302 (2008).

[100] F. X. Gadea and I. Paidarova, Chem. Phys. **209**, 281 (1996).

[101] R. Ahlrichs, H. J. Bohm, S. Brode, K. T. Tang, and J. P. Toennies, J. Chem. Phys. **88**, 6290 (1988).

[102] S. Smolarek, N. B. Brauer, W. J. Buma, and M. Drabbels, J. Am. Chem. Soc. **132**, 14086 (2010).

[103] A. Scheidemann, B. Schilling, and J. P. Toennies, J. Phys. Chem. **97**, 2128 (1993).

[104] B. E. Callicoatt, D. D. Mar, V. A. Apkarian, and K. C. Janda, J. Chem. Phys. **105**, 7872 (1996).

[105] M. Lewerenz, B. Schilling, and J. P. Toennies, J. Chem. Phys. **102**, 8191 (1995).

[106] T. Ruchti, K. Förde, B. E. Callicoatt, H. Ludwigs, and K. C. Janda, J. Chem. Phys. **109**, 10679 (1998).

[107] D. Bonhommeau, N. Halberstadt, and A. Viel, J. Chem. Phys. **124**, 024328 (2006).

[108] B. E. Callicoatt, K. Forde, L. F. Jung, T. Ruchti, and K. C. Janda, J. Chem. Phys. **109**, 10195 (1998).

[109] P. W. Stephens and J. G. King, Phys. Rev. Lett. **51**, 1538 (1983).

[110] K. K. Lehmann and J. A. Northby, Mol. Phys. **97**, 639 (1999).

[111] M. Hartmann, R. E. Miller, J. P. Toennies, and A. F. Vilesov, Science **272**, 1631 (1996).

[112] A. Bondi, J. Phys. Chem. **68**, 441 (1964).

[113] M. N. Slipchenko, S. Kuma, T. Momose, and A. F. Vilesov, Rev. Sci. Instrum. **73**, 3600 (2002).

[114] M. A. Duncan, Int. J. Mass Spectrom. **200**, 545 (2000).

[115] private communication with B. Sartakov.

[116] C. H. Spink and I. Wadso, J. Chem. Thermodyn. **7**, 561 (1975).

[117] A. V. Kustov and V. P. Korolev, Russian J. Phys. Chem. A **81**, 193 (2007).

[118] M. Fink, R.-D. Heuer, H. Kleinpoppen, K.-P. Lieb, N. Risch, and P. Schmüser, *Bergmann Schaefer, Lehrbuch der Experimentalphysik 4* (de Gruyter, Berlin, New York, 2003).

[119] private communication with B. Friedrich.

[120] R. Guardiola, O. Kornilov, J. Navarro, and J. P. Toennies, J. Chem. Phys. **124**, 084307 (2006).

[121] O. Kornilov, J. P. Toennies, R. Guardiola, and J. Navarro, J. Low Temp. Phys. **138**, 235 (2005).

[122] E. Coccia, E. Bodo, F. Marinetti, F. A. Gianturco, E. Yildrim, M. Yurtsever, and E. Yurtsever, J. Chem. Phys. **126**, 124319 (2007).

[123] E. Yurtsever, E. Yildirim, M. Yurtsever, E. Bodo, and F. A. Gianturco, Eur. Phys. J. D **43**, 105 (2007).

[124] M. Rossi, M. Verona, D. E. Galli, and L. Reatto, Phys. Rev. B **69**, 212610 (2004).

[125] P. W. Atkins, *Physikalische Chemie*, 5 ed. (VCH, Heidelberg, 1996).

[126] H.-J. Butt, K. Graf, and M. Kappl, *Physics and chemistry of interfaces* (Wiley-VCH Verlag, 69469 Weinheim, Germany, 2003), Vol. 1.

[127] A. D. Koutselos, E. A. Mason, and L. A. Viehland, J. Chem. Phys. **93**, 7125 (1990).

[128] K. T. Tang and J. P. Toennies, J. Chem. Phys. **66**, 1496 (1977).

[129] J. A. Stratton, *Electromagnetic theory (Pure and applied physics)* (MacGraw Hill, New York, 1941).

[130] H. Namaizawa, J. de Phys. **39**, 72 (1978).

[131] M. W. Cole and R. A. Bachmann, Phys. Rev. B **15**, 1388 (1977).

[132] M. Born, Z. Phys. **1**, 45 (1920).

[133] R. Kunz, *Molecular modelling für Anwender* (Teubner, Stuttgart, 1997).

[134] B. Jayaram, J. Phys. Chem. **98**, 5773 (1994).

[135] L. Onsager, J. Am. Chem. Soc. **58**, 1486 (1936).

[136] M. Born, Z. Phys. **45**, 1 (1920).

[137] C. J. Cramer and D. G. Truhlar, Chem. Rev. **99**, 2161 (1999).

[138] G. P. F. B. and H. Stassen, Pure Appl. Chem. **76**, 231 (2004).

[139] P. W. Atkins, *Einführung in die Physikalische Chemie*, 4 ed. (Wiley-VCH Verlag, Weinheim, 2006).

[140] J. C. Kotz, P. Treichel, and J. R. Townsend, *Chemistry and chemical reactivity* (Thomson Brooks/Cole, Belmont, USA, 2009), Vol. 2.

[141] C. di Paola, F. Sebastianelli, E. Bodo, I. Baccarelli, F. A. Gianturco, and M. Yurtsever, J. Chem. Theory Comput. **1**, 1045 (2005).

[142] J. Harms, J. P. Toennies, and F. Dalfovo, Phys. Rev. B **58**, 3341 (1998).

[143] F. Dalfovo, Z. Phys. D **29**, 61 (1994).

[144] E. Widmann, I. Sugai, T. Yamazaki, R. S. Hayano, M. Iwasaki, S. N. Nakamura, H. Tamura, T. M. Ito, A. Kawachi, N. Nishida, W. Higemoto, Y. Ito, N. Morita, F. J. Hartmann, H. Daniel, T. Vonegdi, W. Schmid, J. Hoffmann, and J. Eades, Phys. Rev. A **51**, 2870 (1995).

[145] F. J. M. Mofers, G. Casteleijn, and Y. K. Levine, Biophys. Chem. **16**, 9 (1982).

[146] D. Alvarez-Paggi, D. F. Martin, P. M. DeBiase, P. Hildebrandt, M. A. Marti, and D. H. Murgida, J. Am. Chem. Soc. **132**, 5769 (2010).

[147] C. J. Grebenkemper and J. P. Hagen, Phys. Rev. **80**, 89 (1950).

[148] C. E. Chase, E. Maxwell, and W. E. Millett, Physica **27**, 1129 (1961).

[149] P. R. Antoniewicz, G. T. Bennett, and J. C. Thompson, J. Chem. Phys. **77**, 4573 (1982).

[150] J. D. Jackson, *Electrodynamics*, 3 ed. (John Wiley & Sons, New York, 1999).

[151] J. Gspann and H. Vollmar, J. Low Temp. Phys. **45**, 343 (1981).

[152] W. K. Lewis, R. J. Bemish, and R. E. Miller, J. Chem. Phys. **123**, 141103 (2005).

[153] J. Gspann, Surf. Sci. **106**, 219 (1981).

[154] W. K. Lewis, B. E. Applegate, J. Sztaray, B. Sztaray, T. Baer, R. J. Bemish, and R. E. Miller, J. Am. Chem. Soc. **126**, 11283 (2004).

[155] K. Winkler, J. R. Lindner, V. Subramaniam, T. M. Jovin, and P. Vohringer, Phys. Chem. Chem. Phys. **4**, 1072 (2002).

[156] G. D. Stein, Surf. Sci. **156**, 44 (1985).

[157] K. Nauta and R. E. Miller, J. Chem. Phys. **113**, 9466 (2000).

[158] R. J. Donelly and C. F. Barenghi, J. Phys. Chem. ref. Data **27**, 1217 (1998).

[159] R. W. Hill and O. V. Lounasmaa, Phil. transactions of the royal society of London series a-mathematical and physical sciences **252**, 357 (1960).

[160] *The observed properties of liquid helium at the saturated vapor pressure* (Department of Physics, University of Oregon, 1371 East 13th Avenue, Eugene, Oregon 97403–1274 USA, http://pages.uoregon.edu/rjd/vapor8.htm, YEAR).

[161] K. K. Lehmann, J. Chem. Phys. **119**, 3336 (2003).

[162] C. E. Klots, J. Chem. Phys. **83**, 5854 (1985).

[163] C. E. Klots, Z. Phys. D **5**, 83 (1987).

[164] K. K. Lehmann and A. M. Dokter, Phys. Rev. Lett. **92**, 173401 (2004).

[165] D. Eichenauer, A. Scheidemann, and J. P. Toennies, Z. Phys. D **8**, 295 (1988).

[166] V. Weisskopf, Phys. Rev. **52**, 0295 (1937).

[167] M. Hartmann, N. Pförtner, B. Sartakov, J. P. Toennies, and A. F. Vilesov, J. Chem. Phys. **110**, 5109 (1999).

[168] S. Frauendorf, Z. Phys. D **35**, 191 (1995).

[169] M. Hartmann, R. E. Miller, J. P. Toennies, and A. F. Vilesov, Phys. Rev. Lett. **95**, 15669 (1995).

[170] A. A. Ramos, H. Yang, L. E. Rosen, and X. Yao, Anal. Chem. **78**, 6391 (2006).

[171] Ardara, *Ardara Technologies Product Bulletin PB_2701A* (Pennsylvania 15615 USA, http://ArdaraTech.com, 2009).

[172] *SIMION* Version 8.0.4, *Industry standard charged particle optics simulation software* (Scientific Instrument Services, Inc., http://simion.com, 2003–2008).

[173] N. R. Daly, Rev. Sci. Instrum. **31**, 264 (1960).

[174] *FEMTO* Messtechnik GmbH, *Datasheet DLPCA-200* (Paul–Lincke–Ufer 34, D-10999 Berlin, Germany, http://www.femto.de, 2009).

[175] *AMPTEK* INC., *A250 Application notes* (14 DeAngelo Drive, Bedford, Massachusetts 01730 USA, http://www.amptek.com, 2004).

[176] D. Gerlich, Advances in chemical physics **82**, 1 (1992).

[177] D. J. Douglas, A. J. Frank, and D. M. Mao, Mass Spectr. Rev. **24**, 1 (2005).

[178] V. V. K. R. Rao and A. Bhutani, Int. J. Mass Spectrom. **202**, 31 (2000).

[179] M. A. Röttgen, K. Judai, J.-M. Antonietti, U. Heiz, S. Rauschenbach, and K. Kern, Rev. Sci. Instrum. **77**, 013302 (2006).

[180] N. Lavie and U. Even, *The Even-Lavie valve, Type E.L-5-C-C-2009 operating manual* (School of chemistry, Tel Aviv University, www.even-lavie-valves.com/index.html, 2011).

[181] Lake Shore Cryotronics, Inc. (http://www.lakeshore.com).

[182] P. H. Corporation, *Pulse valve, Vacuseal(r), Flange with cone 99S4-99B07*.

[183] S. F. Yang, S. M. Brereton, and A. M. Ellis, Rev. Sci. Instrum. **76**, 104102 (2005).

[184] D. Pentlehner, R. Riechers, B. Dick, A. Slenczka, U. Even, N. Lavie, R. Brown, and K. Luria, Rev. Sci. Instrum. **80**, 043302 (2009).

[185] D. Pentlehner, Ph.D. thesis, Dissertation Universität Regensburg, Regensburg, 2010.

[186] K. Strupat, Methods Enzymol. **405**, 1 (2005).

[187] P. Kupser, K. Pagel, J. Oomens, N. Polfer, B. Koksch, G. Meijer, and G. von Helden, J. Am. Chem. Soc. **132**, 2085 (2010).

[188] Protein data base (no. 1HRC).

[189] http://www.uniprot.org/uniprot/P00004#section_seq (2010).

[190] J. Oomens, N. Polfer, D. T. Moore, L. van der Meer, A. G. Marshall, J. R. Eyler, G. Meijer, and G. von Helden, Phys. Chem. Chem. Phys. **7**, 1345 (2005).

[191] I. D. Williams, B. Merron, R. J. H. Davies, I. G. Hughes, and V. Morozov, Application of accelerators in research and industry, Pts 1 and 2 **475**, 561 (1999).

[192] M. Rabrenovic, C. J. Proctor, T. Ast, C. G. Herbert, A. G. Brenton, and J. H. Beynon, J. Phys. Chem. **87**, 3305 (1983).

[193] J. L. Collier, B. J. Goddard, D. C. Goode, S. Marka, and H. H. Telle, Measurement science and technology **7**, 1204 (1996).

[194] P. W. Stephens and J. G. King, Bulletin of the Am. Phys. Soc. **24**, 372 (1979).

[195] R. A. Haefer, *Kryo–Vakuumtechnik* (Springer Verlag, Berlin, Heidelberg, New York, 1981).

[196] E. P. Suurmeij and A. L. Boers, J. Phys. E-Sci. Instr. **3**, 624 (1970).

[197] W. H. Benner, M. J. Bogan, U. Rohner, S. Boutet, B. Woods, and M. Frank, J. Aerosol Science **39**, 917 (2008).

[198] W. Schöllkopf and J. P. Toennies, Science **279**, 2083 (1994).

[199] O. Kornilov and J. P. Toennies, Europhysics **38**, 22 (2007).

[200] W. Schöllkopf, J. P. Toennies, T. A. Savas, and H. I. Smith, J. Chem. Phys. **109**, 9252 (1998).

[201] M. Lewerenz, B. Schilling, and J. P. Toennies, Chem. Phys. Lett. **206**, 381 (1993).

[202] J. Harms, J. P. Toennies, and F. Dalfovo, Phys. Rev. B **58**, 3341 (1998).

[203] J. Harms, J. P. Toennies, M. Barranco, and M. Pi, Phys. Rev. B **63**, 184513 (2001).

[204] A. M. Ellis and S. F. Yang, Phys. Rev. A **76**, 016106 (2007).

[205] O. Kornilov and J. R. Toennies, Int. J. Mass Spectrom. **280**, 209 (2009).

[206] S. R. Mabbett, L. W. Zilch, J. T. Maze, J. W. Smith, and M. F. Jarrold, Anal. Chem. **79**, 8431 (2007).

[207] F. Bierau, P. Kupser, G. Meijer, and G. von Helden, Phys. Rev. Lett. **105**, 133402 (2010).

[208] N. Mirkin, J. Jaconcic, V. Stojanoff, and A. Moreno, Proteins-structure function and bioinformatics **70**, 83 (2008).

[209] S. Grebenev, Ph.D. thesis, Georg-August Universität zu Göttingen, Göttingen, Bochum, 2000.

[210] M. K. Lykkegaard, A. Ehlerding, and P. Hvelplund, J. Am. Chem. Soc. **130**, 11856 (2008).

List of Figures

Acknowledgement

und Lieblingstierfreund sowie der großen Community der (Exil– und Adoptiv)Marburger, mit denen ich schon seit vielen Jahren das Vergnügen habe, Zeit verbringen zu dürfen. Herzlichen Dank an Ferdi für das schönste "Kottröpfchen" unter der Sonne.

Seit der Uni begleiten mich Jasmin, Jana, Philip, Sara, Philipp, Carsten, Fabian, Volker, Thomas, Christoph und Nuria, stellvertretend für meine Ubriasmus–Freunde. In Wannseezeiten kamen hinzu Ben, dem ich fürs Korrekturlesen und die gute kanadisch–japanische Freundschaft danke, Elias der kleine Hobbit, Christian Dr. Kotze, Onkel Lord der Suppenkönig, Kevin und Nadine und der Rest des leider verstorbenen Kochkreises. Danke an meine "jüngsten" Mitbewohnerinnen Ruth, Evelyn, Claudia und natürlich an meine pelzigen Gefährten und Seelenwärmer Paula und Kasimir..

Die Familie ist die mitunter wichtigste Basis, und ich bin äußerst froh, dass ich meine habe. Meinen Eltern danke ich aus tiefstem Herzen für alle Liebe und niemals endende Unterstützung aller Art. Ebensolchen Dank an meine Schwestern Andrea und Sandra, die mir sehr nahe stehen und auch beide nicht ganz fachfremd sind, sowie an Felix, die beiden Kleinen und Holger.

Christophe danke ich für die Unterstützung in den letzten Monaten, die psychologische Aufbauarbeit, Croques– Monsieur, seine Liebe, einfach alles.

Publication list

Publikationen

M. Rossi, V. Blum, P. Kupser, G. v. Helden, F. Bierau, G. Meijer, and M. Scheffler,
*Secondary structure of Ac–Ala$_n$–LysH+ Polyalanine peptides (n=5, 10, 15) in vacuo:
Helical or not?*, J. Phys. Chem. Lett. **24**, (2010), p. 3465

F. Bierau, P. Kupser, G. Meijer, and G. v. Helden, *Catching proteins in liquid helium droplets*
Phys. Rev. Lett. **105**, (2010) p. 133402

K. Pagel, P. Kupser, F. Bierau, N. C. Polfer, J. D. Steill, J. Oomens, G. Meijer, B. Koksch,
and G. v. Helden, *Gas–phase IR spectra of intact α–helical coiled coil protein complexes*
Int. J. Mass Spectr. **283**, (2009) p. 161

Lebenslauf

Der Lebenslauf ist aufgrund datenschutzrechtlicher Gründe in der Online-Ausgabe nicht verfügbar.